Universidad de Sevilla
Departamento de Física Atómica, Molecular y Nuclear

Non-destructive techniques for *in situ* studies of easel paintings: development and application of a confocal X-ray micro-fluorescence system

PhD Thesis by
Kilian Laclavetine

Doctoral program of Nuclear Physics

Supervisors
Prof. Miguel Ángel Respaldiza Galisteo
D. Francisco Ager

Sevilla, 2015

Universidad de Sevilla
Departamento de Física Atómica, Molecular y Nuclear

Técnicas no destructivas para el estudio *in situ* de pinturas de caballete: desarrollo y aplicación de un sistema de micro-fluorescencia de rayos X confocal

Tesis doctoral presentada por
Kilian Laclavetine

Programa de doctorado de Física Nuclear

Dirigida por
Prof. Miguel Ángel Respaldiza Galisteo
D. Francisco Ager

Sevilla, 2015

A mes parents,

Suzy et Jean François,

Pour leur soutien constant,
Pour leur amour éternel,
Pour m'avoir permis d'être un rêveur.

“Los hombres desaparecemos unos tras otros, y las generaciones se suceden como las olas de polvo que levanta el viento en los caminos; pero las acciones y la memoria de cada uno de los que producen males o bienes, deben quedar en los demás como recuerdo imborrable, para que sirvan de estímulo o de escarmiento, y para que los que nos sucedan sigan o se desvíen de este, o de aquel camino…”

Diccionario universal de historia y geografía: v. I, p. III-IV. México, Tipografía de Rafael, Librería de Andrade, 1853-1856.

Declaration of the author of this dissertation:
Aware of legal responsibility for making untrue statements I hereby declare that I have written this dissertation myself and all the contents of the dissertation have been obtained by legal means.

Declaration of the thesis Supervisor:
This dissertation is ready to be reviewed.

Disclaimer:
Reference to any companies or specific commercial products was not intended as an advertisement.

PREFACE

This work was supported by the Junta de Andalucía project P09-HUM4544 named: *"Análisis de la Colección Pictórica de los Siglos XV-XVI del Museo de Bellas Artes de Sevilla Mediante Técnicas Nucleares no Destructivas"* leaded by Prof. Miguel Ángel Respaldiza Galisteo.

During this PhD thesis, several foreign internships have been made:

The study of "Martirio de San Hipólito" at the National Museum of History in Chapultepec was made in September 2011 in Mexico (supported by AUIP grant) while the study of the "Virgen de las Uvas" was made in October 2013 at the Metropolitan Cathedral of Mexico (supported by CONACyT CB2012-179601 project).

The study of experimental paint multilayer samples by infrared reflectography and the study of stratigraphic micro-samples by optical microscopy were made at the Institute of Aesthetic Research of the National Autonomous University of Mexico (IIE-UNAM) in January 2013.

Finally, the CXRF study of experimental paint multilayer samples at the Center for Research and Restoration of Museums of France (C2RMF), Museum of Louvre in Paris, was made between September and December 2012 with the supervision of Dr. Thomas Calligaro.

ACKNOWLEDGEMENTS

Those officials' acknowledgements are presented using three languages:

- Le français, ma langue natale que j'aime et respecte,
- En español, idioma que adopte hace siete años mezclando sus versiones mexicana, colombiana e ibérica,
- In English, language elected for this PhD thesis.

Agradezco a todos los miembros del CNA y de la Universidad de Sevilla (US) por ofrecer las condiciones para el buen desarrollo de esa investigación.

Agradezco el Prof. Miguel Ángel Respaldiza por haberme integrado al proyecto y haberme autorizado a cursar mi doctorado. Doy las gracias al Dr. Francisco Ager por haberme apoyado en el manejo de los diferentes equipos. Agradezco ambos por tomar la dirección de esa tesis doctoral.

Agradezco la Dra. Anabelle Kriznar por su apoyo constante, su participación a los diferentes estudios y su amabilidad. Doy las gracias al resto del grupo, la Dra. Inés Ortega, la Dra. Blanca Tubio y la Mtra. Ana Isabel Gómez sin olvidar la Dra. Simona Scrivano que tiene un lugar especial en esos agradecimientos.

Deseo gratificar José Luis Benjumea del Taller mecánico de la Facultad de Física de la US por su inestimable trabajo, su amistad y su disponibilidad. Agradezco Dr. Victorino Franco de la Facultad de Física de la US por haberme iniciado al uso de LabVIEW y por su apoyo constante. Agradezco Dr. Fernando Castaño Castaño de la Escuela de Ingeniero de la US por su colaboración, su profesionalismo y su apoyo imprescindible.

Gracias a la directora del Museo de Bellas Artes de Sevilla, Mª del Valme Muñoz Rubio, por su apoyo incondicional y las facilidades otorgadas para los estudios en el Museo durante estos 4 años, así que el apoyo para el estudio de la "Virgen del Valle".

Gracias a Ignacio Hermoso Romero, Roció Izquierdo y Lourdes Páez por hacer posible este trabajo en el recinto del Museo. Gracias a Fuensanta de la Paz, Mercedes Vega y Alfonso Blanco por su ayuda, su apoyo y su escucha. Gracias a todos los empleados del Museo, en particular al personal de seguridad y de mantenimiento por su amabilidad y profesionalismo.

Agradezco el Cabildo de la Catedral de Sevilla por permitir y apoyar el estudio de la "Virgen del Valle". Agradezco igualmente su colaboración al Instituto Andaluz de Patrimonio Histórico (IAPH).

Deseo gratificar la colaboración y el apoyo del Dr. Joaquín Arquillo así que la participación de sus estudiantes del Taller de Restauración de la Facultad de Bellas Artes de la US. Gracias a M°Angeles Fernández Laó, Luna Méndez Robles, Rocío Martínez Vázquez, Carmen Hermoso Humanes, por las confecciones de las multicapas pictóricas experimentales.

Fue posible el estudio del "Martirio de San Hipólito" gracias a la autorización del entonces director del Museo Nacional de la Historia (MNH), el historiador Salvador Rueda Smithers y a la generosa colaboración y la asistencia del personal investigador del taller de restauración del Museo, los restauradores Raúl Arce y Alejandro Ramírez, perteneciendo al Consejo Nacional para la Cultura y las Artes (CONACULTA) y al Instituto Nacional de Antropología e Historia (INAH). Agradezco las facilidades otorgadas por esos responsables. Además, agradezco el apoyo recibido del Arq. Raúl Delgado Lamas, Director General de Sitios y Monumentos del CONACULTA (DGSMPC), al Arq. Enrique Varela Argote Residente de Estudios y Proyectos en la Catedral – DGSMPC y a Monseñor Manuel Arellano Rangel, Canónigo Deán de la Catedral Metropolitana, para el estudio de la "Virgen de las Uvas", que se exhibe en la Sala Capitular de la Catedral Metropolitana de la ciudad de México.

En cuanto al estudio de ambas obras, fue planteado y coordinado dentro de las actividades del proyecto CONACyT CB2012-179601 "Historias de pincel: metodología interdisciplinaria para el estudio de la técnica pictórica, materiales y conservación en la pintura de la Nueva España", cuyo responsable académico es la Dra. Elisa Vargaslugo Rangel, investigadora emérita del Instituto de Investigaciones Estéticas (IIE-UNAM) de la Universidad Nacional Autónoma de México (UNAM).

En esa iniciativa debo agradecer al grupo de investigación de la UNAM:

- Para el IIE-UNAM: Dr. Pedro Ángeles Jiménez, Mtra. Elsa Arroyo, Lic. Eumelia Hernández, Mtro. Ricardo Alvarado, Pasante Elizabeth Vite, Mtra. Sandra Zetina y Mtra. Tatiana Falcón.
- Para el Instituto de Física de la UNAM (IFUNAM): Dr. José Luis Ruvalcaba Sil, Lic. Dulce María Aguilar, Dr. Edgar Casanova, Dr. Pieterjan Claes, Fis. María Angélica García Bucio, Mtra. Mayra Dafne Manrique Ortega, Mtro. Alejandro Mitrani y Fis. Malinalli Wong Rueda.
- Para el Instituto Nacional de Investigaciones Nucleares (ININ): el Dr. Manuel Espinosa Pesqueira.

Agradezco la Mtra. Elsa Arroyo por haberme ofrecido el uso de sus facilidades en el Laboratorio de Diagnóstico de Obras de Arte del IIE-UNAM. Gracias por sus sugerencias y su ayuda. Deseo gratificar la Lic. Eumelia Hernández por su amistad y su colaboración en el estudio con IRR de las multicapas pictóricas experimentales. Doy las gracias al Ing.

Quím. Víctor Santos Vázquez por su inestimable ayuda en la preparación de las estratigrafías de micro-muestra y el estudio por microscopio óptico de las muestras experimentales.

Je remercie Marie Lavandier et Michel Menu, pour m'avoir permis de faire mon stage doctoral au C2RMF. Un grand merci à Myriam Eveno et Thomas Calligaro pour leur encadrement, leur soutien et leur gentillesse ; pour leur relecture, leurs corrections et leurs conseils ainsi que pour l'enseignement de l'usage du logiciel PyMCA.

Un grand merci à Ina Reiche et Katharina Müller pour l'enseignement des bases du fonctionnement de l'équipement LouX^{3D}. Je remercie vivement Laurent Pichon pour son aide immense, indispensable et précieuse tout au long de ce stage et au-delà. Merci à l'équipe AGLAE, Claire Pacheco, Quentin Lemasson, Brice Moignard et Thierry Dusautoir pour leur disponibilité constante, leur amabilité et leur efficacité. Un merci à tous les membres du C2RMF et du Musée du Louvre.

J'ai une pensée remplie de joie et d'affection pour mes camarades du C2. Pedro Campos pour les discussions hispano-brésiliennes et sa gentillesse. Manon Castelle et son accent chantant ainsi que nos nombreux fous-rires. Céline Daher et sa passion pour les maisons closes françaises de l'avant-guerre. Victor Gonzales et ses minutes Wikipedia. Anita Hayem Ghez et sa bonne humeur communicative. Carlotta Santoro et ses "ma compètement fous injections".

I want to thanks D. Paweł Wróbel from the Faculty of Physics and Applied Computer Science of the AGH University of Science and Technology of Krakow (Poland) for his fructuous collaboration.

Agradezco Hayley Anne Salvo, Rikki Archibald, Jérôme Hay y Alejandro Mitrani así que Lorena Forero Artunduaga, José Ignacio Troya Guerrero, Steve Church, Justin Bannister, Cristina Battaglia y Ziad Abou-Haidar para sus correcciones del inglés.

Thanks to people from Goodfellow. Thanks to Thanos J. Pantazis, Claire Hald and Mark Leblanc from Amptek Inc. Thanks to Carolina López, Juanjo Mañas, Toni Ruiz and Gerard Ester from Infaimon. Thanks to David Castrillo from Hamamatsu Photonics.

Agradezco Ramón Arroyo Barroso y Enrique por el diseño del logo del µXRF-CONCHA.

CONTENT

INTRODUCTION

Archaeometry is a field of discipline developed during the last century, which consists in the application of sciences (physics, chemistry, geology, biology, etc.) to cultural heritage studies of archaeological artifacts and artworks. On the one hand, archaeometry was brought about by the advent of new technology yet, on other hand, by the natural evolution of archaeology, art history and other historical sciences. Indeed, those research areas need to test the veracity of the bibliography, in order to obtain new information and clues confirming or refuting the hypotheses presented within and to revisit what we know about our past. The key resides in trans-disciplinary research, which allows for studying new perspectives and hypotheses and for testing old ones.

Following from that, within the world of physics applications there are basically two main areas of study: dating techniques (14C, K/Ar, thermoluminescence, etc.) and material characterization techniques, sometimes called archaeophysics (Fig. 1).

In the case of easel painting characterization studies, the main goals of interdisciplinary collaboration with art historians and conservator-restorers is to characterize the artist's palette and technique, and locate previous restoration interventions and reintegration zones in order to help conservator-restorers work and to confirm the authorship of some paintings, on the basis of material and aesthetical study [1].

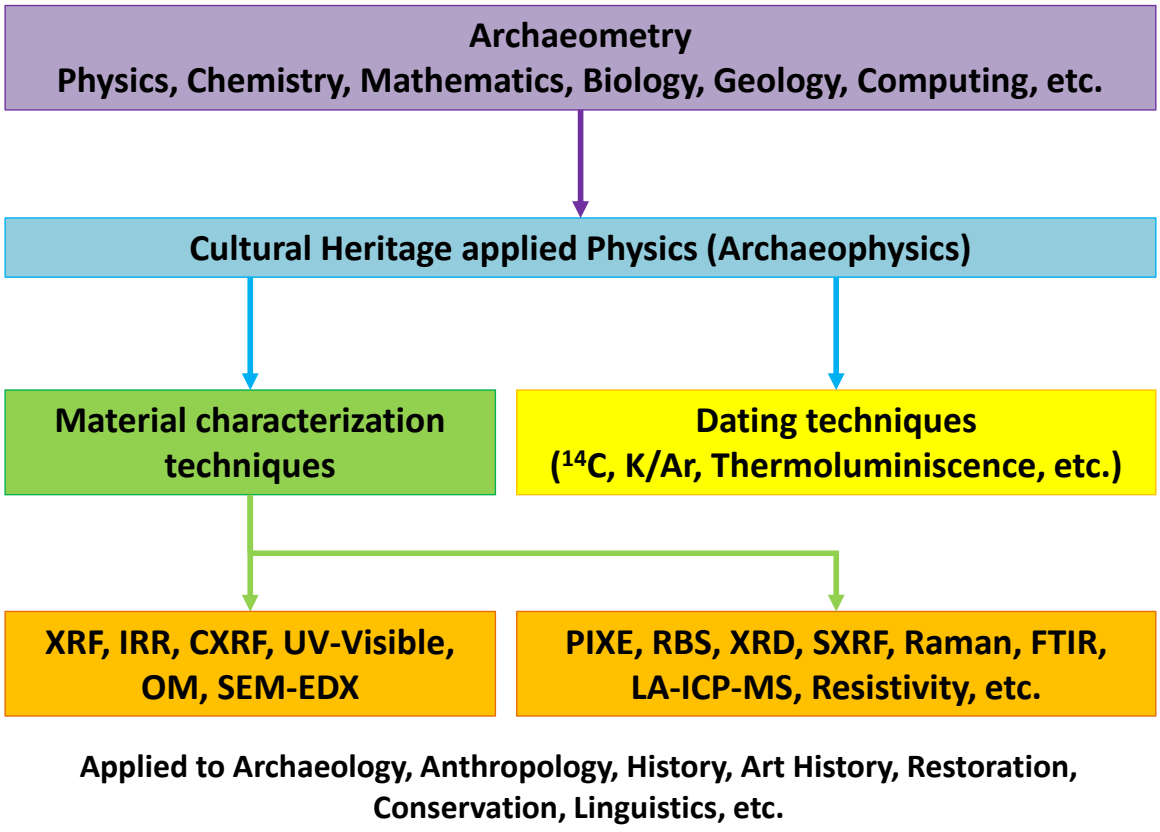

Fig. 1. Archeometry and several techniques involving applied physics.

The contribution of this thesis to achieve these goals is focused on the complementary application of two spectroscopic techniques:

- X-ray fluorescence spectroscopy (XRF) [2],
- Confocal X-ray micro-fluorescence (CXRF) [3].

Along with two imaging techniques:

- UV-induced visible fluorescence photography [4],
- Infrared reflectography (IRR) [4, 5].

All these techniques have the advantage of being non-destructive and non-invasive to allow the analysis of unique and fragile artifacts. In the last twenty years, these non-destructive techniques have been highly demanded within the cultural and historical heritage world whose main objective is the long-term preservation and integrity of artwork.

Some of those techniques (XRF, UV, and IRR) have been applied for several decades in the study of paintings, providing universally accepted results. In the case of IRR it is noteworthy that it remains undeveloped at a very basic level of diagnosis [6]. This work proposes to adapt IRR to the study of large artworks and delve deeper into the analysis of pigments. Moreover, the CXRF is a relatively new technique with the first application and subsequent publication of a pictorial heritage happening as recently as 2009 [7]. It is one of the most recent non-invasive techniques in the field of cultural heritage studies. The confocal X-ray micro-fluorescence is gaining considerable interest because it can provide compositional and spatial information that are typically obtained using standard micro-invasive and/or micro-destructive techniques (e.g. scan electron microscope in combination with energy dispersive X-ray spectroscopy (SEM-EDX)), without the need for sampling [8, 9]. In particular, CXRF extends the capabilities of the micro X-ray fluorescence to the depth profiling of multilayered materials. Due to the novelty of this developing technique, its abilities remain to be clearly defined.

This work focuses not only on the methodological application of these four techniques, but also presents the mechanical engineering and computing developments made during this PhD. A large effort has been made to provide several *in situ* scientific setups (e.g. μXRF-CONCHA and X-Panda systems) which seek to study artwork directly in places of exhibition, so that artwork is not moved unnecessarily. Internationally renowned and well-funded laboratories, such as the *Centre de recherche et de restauration des musées de France* (C2RMF) in the Louvre Museum of Paris [10, 11], usually grant permission to move artwork for study (requiring large funding for insurance rates, the capacity to solve complex administrative requirements, the necessary funds to cover the high cost of transporting delicate artwork to adequate facilities prepared for the reception and storage of artwork during the study, etc.). However, in many other cases, the development of *in situ* studies is crucial.

Those scientific setups developed during this PhD made possible an international collaboration between the University of Seville, the Fine Arts Museum of Seville and the Universidad Nacional Autónoma de México (UNAM) about to research artwork by Alonso Vázquez, an important painter from Seville [12]. Vázquez was active in the second half of the 16th century and in the first decade of the 17th century. In 1603 he travelled to New Spain (modern-day Mexico) as a member of the Viceregal Court. There, he left paintings as well, though regrettably his works, discovered on the other side of the Atlantic, are decontextualized and unsigned. The main goal of this research is to

characterize the technique used by Vázquez and to confirm the authorship of some paintings in Mexico, using material study.

We begin by explaining the different techniques applied in this thesis, and the function of the main components. Then, we will present the work done in the instrumental development and characterization of each setup and the design and operation of the corresponding acquisition programming software. We will discuss the different components of each portable device, their capabilities and their advantages for the study of paintings. Next, we will detail the results of the intercomparison of three CXRF setups, the LouX^{3D} system at the C2RMF laboratory [11], the CXRF set-up at AGH University of Science and Technology in Krakow [13] and the μXRF-CONCHA system developed at the Centro Nacional de Aceleradores (CNA) in Seville. The aim is to check the reliability of the new Seville device and to compare the performance of each CXRF setup. Finally, we will describe the methodology applied in the corpus study of seven pieces of artwork attributed to the painter Alonzo Vázquez. We will illustrate with emblematic examples the contribution of each technique in this global study. Finally, we will compare the artworks attributed to Vázquez during his period in Mexico and his previous period painting in Seville. The technique of the artist and his palette in terms of inorganic pigments will be shown amongst other information provided by the archaeometric investigation. In conclusion, the attribution by historian of art of five of those paintings will be discussed based on the material study.

Chapter 1. Spectroscopic and multispectral imaging techniques applied to *in situ* studies of easel paintings

The first chapter of this thesis presents the theory behind four different techniques for material characterization of artwork. It also illustrates the experimental development incurred for the UV-induced visible fluorescence photography and part of the infrared reflectography.

1.1. X-ray fluorescence spectroscopy (XRF)

1.1.1. XRF principals

X-rays are part of the electromagnetic spectrum and were discovered and described by W.C. Röntgen in 1895 [14, 15]. Only a portion of this spectral range, between 1 and 100 keV, is used in energy-dispersive X-ray spectroscopy (EDS). One of the EDS method is named X-ray fluorescence (XRF), is a non-destructive characterization method based on the interactions of X-rays with matter [16]. Those interactions can be divided into two categories: dominant photoelectric absorption and scattering (cf. Chapter 1.2.7). More specifically, XRF uses the emission produced by photoelectric effect of characteristic X-rays of elements composing a material. This secondary X-ray emission is produced when a material is irradiated by a primary X-ray beam [17]. This technique needs an X-ray beam to illuminate the object of interest and an X-ray detector to collect the signal emitted by the irradiated item. For this thesis, an X-ray tube and a silicon drift detector (SDD) were used.

The emitted X-rays are specific to each element that exists in nature, thus allowing for their identification and as a result a deduction of the likely constituents of the analyzed material (Fig. 2) [18]. This noninvasive technique allows users to execute qualitative and semi-quantitative multi-elemental analysis in a short period of time. This method is highly sensitive and able to detect even trace or minor elements. Quantitative analysis may also be performed with high accuracy [19] and allows for the analyzing of artwork without physical contact or causing visible damage to the studied areas with respect to the experimental conditions usually employed in this case study [20].

In principle, this technique permits the identification of all chemical elements, except for hydrogen and helium, which do not produce X-ray fluorescence. However, other light elements may be difficult to measure due to several reasons (the matrix effect on the item studied, absorption by the air or absorption by the detector window), which limit the study of all elements with a higher atomic number than 13 (Aluminum, Al). Nevertheless, the analysis can be extended to sodium (Na, $Z = 11$) using thin polymer detector window and helium atmosphere between the sample and the X-ray detector [21, 22]. In higher energy range, the limitations are related with energy of exciting radiation (intensity of primary beam for energies above the absorption edge of element) and detector thickness.

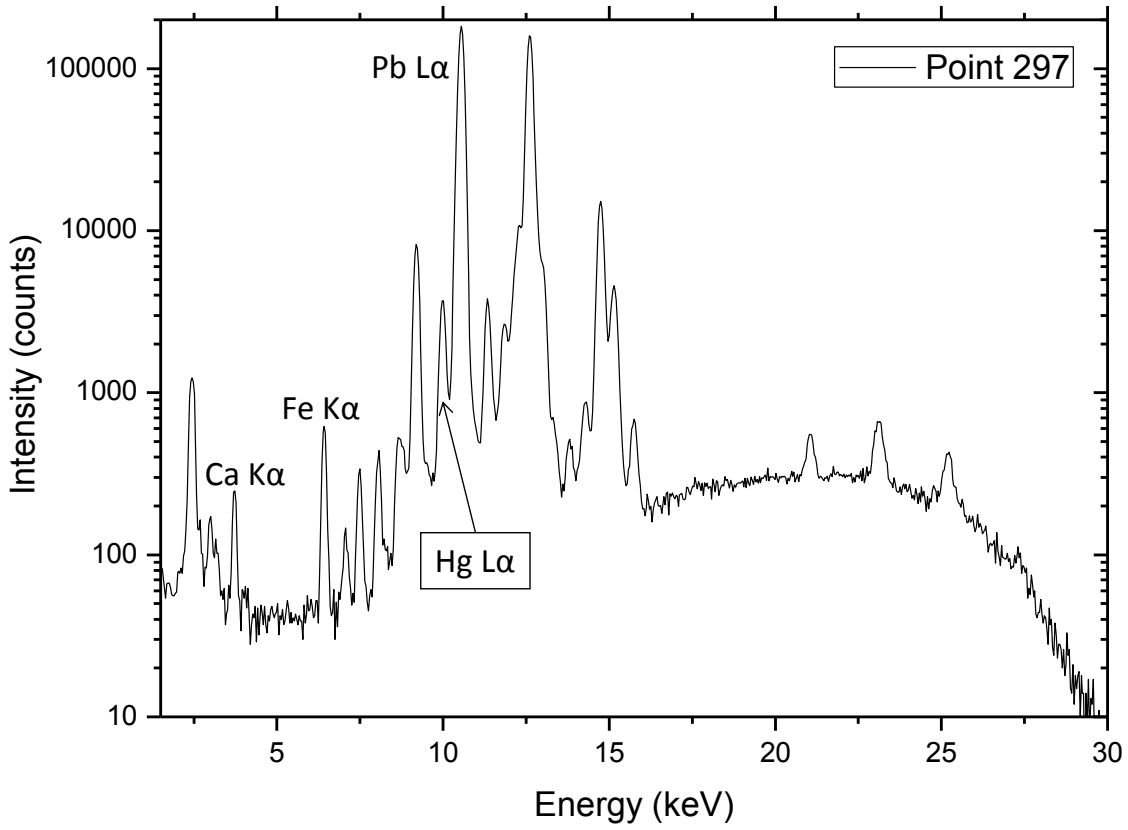

Fig. 2. XRF spectrum with characteristics elements peaks of a red pigment (from Sagrada Cena) in logarithmic scale.

Inducing the photoelectric effect requires the incident photon energy to exceed the binding energy of the electron. Therefore, the identification of elements also depends on the energy of the X-ray beam produced by the X-ray tube (cf. Chapter 1.1.2). When a photon of sufficient energy interacts with an atom there is a certain probability that some of its electrons are ripped off from the inner shells, thus ionizing the atom which is then in an unstable state (Step 1, Fig. 3). After ejection, the electrons from the outer shells fill the internal voids allowing the atom to return to a stable energy configuration. Consequently, the difference in energy between the shells involved in the electron transition process is emitted in X-ray photons (Step 2, Fig. 3).

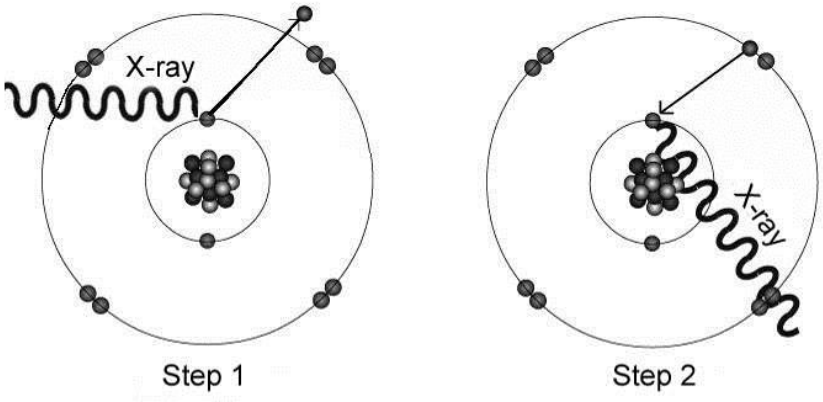

Fig. 3. XRF based on photoelectric effect [23].

Competing with the photoelectric effect, the scattering process is minor but unwanted in XRF (Fig. 4) (also see Chapter 1.2.7). Scattering is a process defined by the interaction of photons with matter which results in the photons changing their trajectory. When photon energy remains unchanged, coherent (Rayleigh) scattering takes place. This can only be done if photons are scattered by bound atomic electrons. On the other hand, incoherent (Compton) scattering takes place when photons interact with electrons with negligible binding energy. In the case of incoherent scattering, electrons can be considered free. During inelastic scattering, part of the photon energy and momentum is transferred to the electron which is recoiled, decreasing photon energy.

With respect to atom deexcitation, the Auger effect is an alternative way to remove excess energy. It consists in the ejection of one of fewer bounded electrons. This effect dominates in low Z elements, for which the energy differences between levels are smaller. In XRF, the Auger effect is an unwanted effect which decreases the intensity of characteristic radiation.

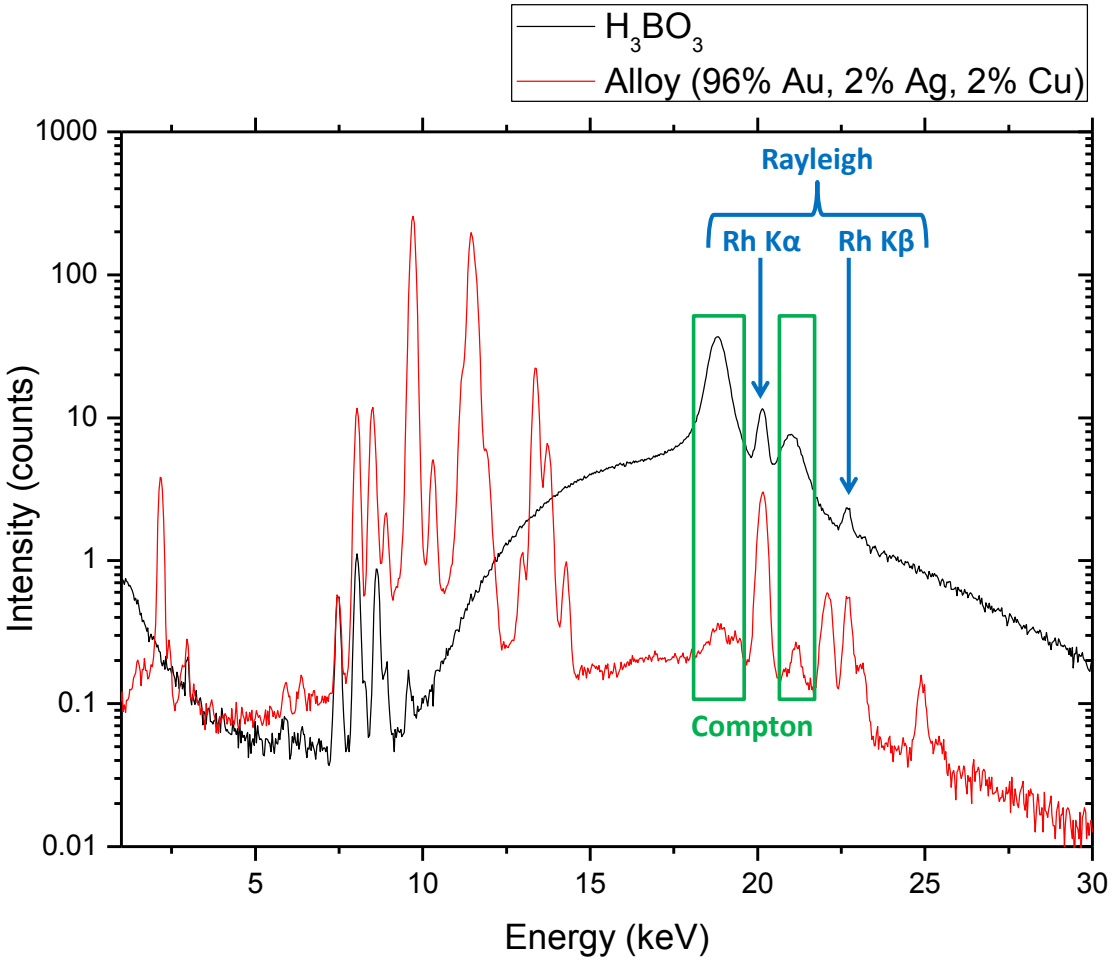

Fig. 4. Rayleigh and Compton scattering. XRF spectrum of two different materials is presented. In the gold standard spectrum (in red), the Rayleigh effect is observable while in the boric acid pellet spectrum (in black) the contribution of the Compton effect is higher [24].

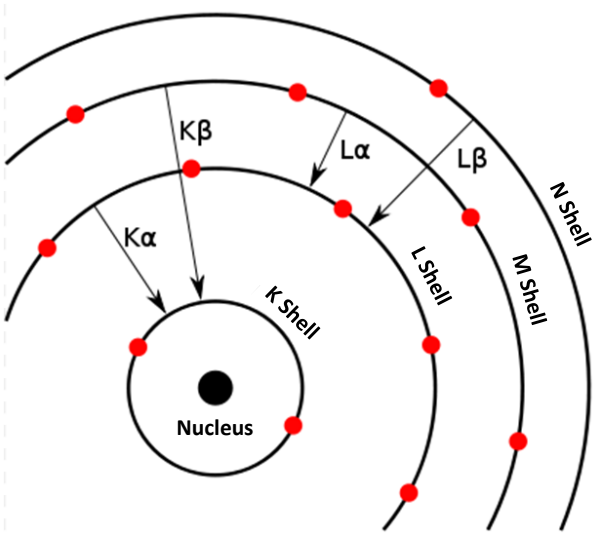

Fig. 5. Scheme of the principals transitions allowed by the selection rules of quantum theory between different shells of an atom.

The selection rules of quantum theory dictate the processes allowed in transition (Fig. 5). The nomenclature of the emitted X-rays is based on conventional rules (Siegbahn notation, Table 1).

In Siegbahn notation, the first capital letter (e.g. K, L, M) refers to the shell (from the Bohr model) from which an electron is initially expelled. The Greek letters and numbers are used to distinguish X-rays. These references are linked to the orbital from, which the electron fills the originally created hole. The X-rays emitted wavelength depends on the atomic number Z of the excited atoms. The wavelength of each X-ray is related to Z as described by Moseley's law, where λ is the wavelength and, k_1 and k_2 are constants [25]:

$$\lambda = \frac{k_1}{(Z - k_2)^2} \quad (1)$$

Table 1 shows the correspondence between the Siegbahn notation and the IUPAC notation (International Union of Pure and Applied Chemistry) used in PyMca software (cf. Appendix V) [26].

Table 1. Correspondence between the Siegbahn and the IUPAC notations.

Siegbahn notation	IUPAC notation
$K\alpha_1$	$K\text{-}L_3$
$K\alpha_2$	$K\text{-}L_2$
$K\beta_1$	$K\text{-}M_3$
$L\alpha_1$	$L_3\text{-}M_5$
$L\beta_1$	$L_2\text{-}M_4$
$M\alpha_1$	$M_5\text{-}N_7$

Each element in the Periodic Table (except for hydrogen and helium) emits X-rays with specifics wavelengths, which characterize that element. This specific radiation can be detected and displayed graphically on an X-ray spectrum (Fig. 2).

As the wavelengths and energies of the emitted X-rays identify the elements contained in the sample, the peak areas of the signals of each element are related to the concentration of this element in the analyzed volume of the sample [27, 28].

The XRF technique has been used since the sixties in the study of archaeological and historical objects [29]. Now, it is widely used because of its potential in archaeometry for scientists, conservator-restorers, archaeologists and art historians. The literature reveals that XRF analysis remains to be one of the primary techniques used to identify and characterize a great variety of archaeological and art history materials. Metallic objects (including coins) and ceramics occupy more than 50% of applications, but materials of minerals, stone, bone, ivory, painted surfaces (paints, mural painting, sculpture) and glasses are also studied [30].

XRF analysis allows for the direct analysis of solids without destructive or invasive and time consuming preparation of samples [17]. Moreover, it leaves the artifact untouched and available for analysis via other methods. Furthermore, with the recent miniaturization of X-ray sources and the development of a thermoelectrically cooled semiconductor for X-ray detectors, portable XRF systems have been commercialized and are now available for *in situ* analysis. These portable systems allow to study cumbersome, fragile and/or valuable items avoiding the cost and risk related to the transfer to a laboratory for analysis. Although, when the strategy study is methodologically and ethically acceptable, it remains possible to extract a micro-sample of the artifact. Nevertheless, it should be noted that the number of accessible objects for archaeometry studies has increased exponentially since the advent of these mobile XRF devices. They provide access to unique items which cannot be damaged using other techniques or cannot leave their storage or exposition rooms to be analyzed in laboratory.

At present, the XRF technique is a well-established method, though its scope and limitations are well known and understood. Analysis via XRF is cost effective and efficient, requiring only a few minutes per spectrum. A great advantage of this method is its ability to measure concentrations or, at least, its capacity to evaluate the presence of major, minor and trace elements.

Accurate quantitative analysis without sample preparation can be difficult because of the X-ray interfering effects (cf. Chapter 1.2.7) which are often not easy to correct. Quantitative study is even less so easy in cultural heritage studies due to the fact that the objects present superficial alterations (corrosion, etc.). Furthermore, the concentrations measured with XRF reflect the composition of the material near the surface. Due to the attenuation in the material, only the X-rays emitted from the first layers of the surface can reach the detector. Fig. 6 illustrates the subsequent volume of the sample involved in the analysis for each element of a bronze object. In the Fig. 6, X (50%) and X (90%) represent the depth from where 50% and 90% of the X rays emitted by the sample are originated. While the primary X-ray beam penetrates deeply into the sample, only a small depth from the surface gives a signal recorded by the X-ray detector. The emission depth depends on the kind of atomic element being analyzed, the type of electronic transition (Kα and Lβ emission respond differently in Fig. 4), and the density and composition of the sample.

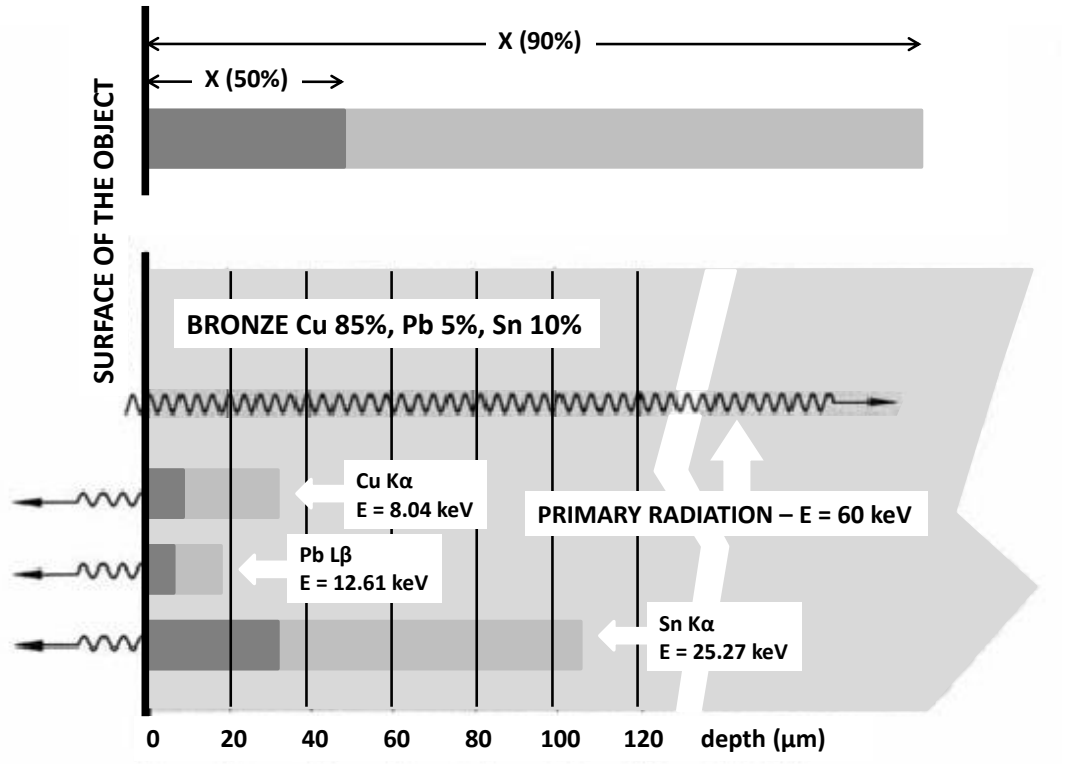

Fig. 6. Scheme of a cross section of a bronze representing the depths penetration and emission of X-rays in it [30].

Another difficulty with surface analysis is that most cultural heritage objects studied have been altered over time. Their surface composition can vary drastically from its original and unaltered composition. These constraints are significantly decreased when the artifact can be sampled and prepared to obtain a precise quantification.
Both X-ray beam diameter and scanned areas are generally a few millimeters large. It should be specified that the area analysis depends on:

- the size of the incident beam exciting the analyzed surface,
- the angular configuration between the detector and the X-ray source,
- the properties of the detector,
- the distance from the device to the sample and,
- the angle of the analysis with respect to the surface of the sample.

The operation of both X-ray tube and silicon drift detector (SDD) are below.

1.1.2. X-ray source

In an X-ray tube, X-ray photons are generated by electron irradiation of a target producing the X-ray emission by bremsstrahlung radiation and X-ray fluorescence of the anode. The X-ray tube generates an X-ray beam by a process involving electrons produced by a hot cathode (usually a tungsten filament) and accelerated by electrical potential with velocities reaching 100 kV. These electrons then collide with an anode. In our case, the anode is a metal target composed of tungsten, but the target can be made of other elements of high purity [31]. Upon collision, the electrons are slowed by the constituent atoms of the target, converting partially or fully its kinetic energy into X-rays. The kinetic energy lost by the slowed electrons differs from one collision to another

which explains that the energy of the X-ray photons emitted varies continuously within a substantial range. The X-ray spectrum produced by this collision is composed of a continuous bremsstrahlung radiation and characteristic lines of the target material (Fig. 7). This X-ray spectrum has several characteristic features [26]:

- Maximum energy of photons E_{max} depends on tube voltage:

$$E_{max} = eV_0 \quad (2)$$

- Maximum bremsstrahlung photon intensity is observed at the energy of approximately 2/3 E_{max}
- Total photon intensity I is proportional to the product of the applied current i to the applied voltage V_0 and the atomic number Z of the target material [26]:

$$I \approx iZV_0(V_0 + 16.3Z) \quad (3)$$

The bremsstrahlung can be modified using filters at the exit of the X-ray tube. In our case, a 1 mm thick aluminum filter of high purity was used. The aluminum filter reduces the low energy of the continuum and almost entirely removes the tungsten L peaks from the anode. Fig. 7 shows the phenomena induced by the use of this filter in the analysis of boric acid pellet with X-Panda device (cf. Chapter 2.5.1).

Several parameters can characterize X-ray tubes, which the total power being one of them. The total power is related to the total emitted photon flux. X-ray tubes can be divided into high and low power devices. For the sake of this work, low power air-cooled X-ray tubes were used (cf. Chapters 2.1, 2.2 and 2.5). Their maximum power is lower than 100 W.

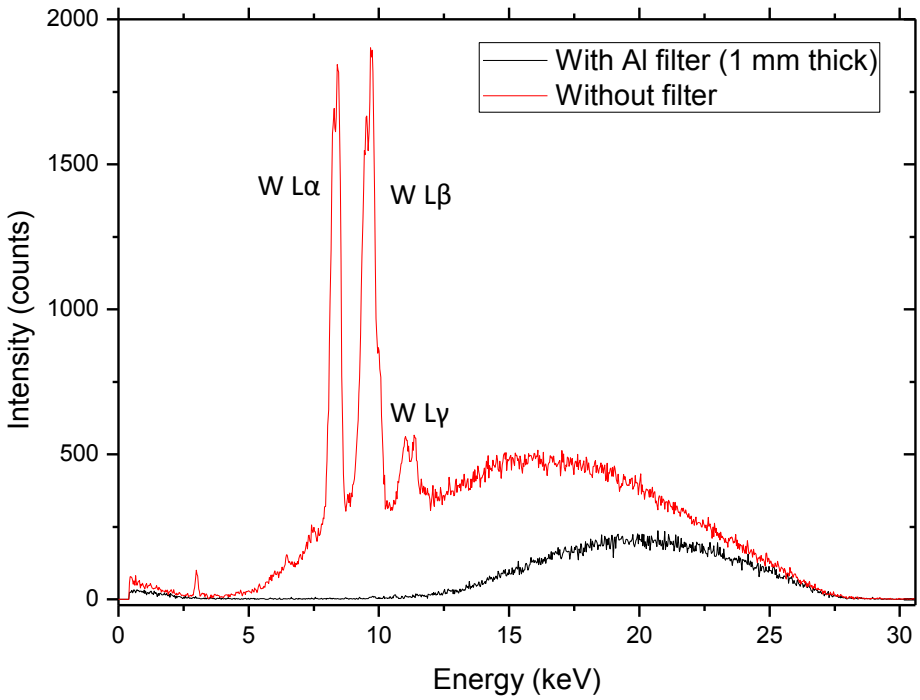

Fig. 7. X-ray spectra of a boric acid pellet, obtained with the Mini-X tube with a W anode, at 30 kV and 120 µA for 60 s, with and without an Al filter showing the bremsstrahlung continuum emission and the characteristic lines.

1.1.3. SDD X-ray detector

This paragraph describes the operation of the silicon drift detector (SDD). The main characteristics of the X-ray detector are:

- Active area;
- Quantum efficiency;
- Energy resolution;
- Peak to background ratio;
- Maximum count-rate.

The active area determines the solid angle of the radiation emitted from the sample to be registered and defines the total detection efficiency.

Quantum efficiency depends on two factors: at higher energies it grows in conjunction with detector thickness and at low energies is connected to entrance window thickness.

Energy resolution depends on the total noise produced in the detector volume and by the detector electronics. Consequently, the output resolution (expressed in FWHM) can be written as [32]:

$$FWHM_{output}^2 = FWHM_{detector}^2 + FWHM_{electronics}^2 \quad (4)$$

The detector volume noise is connected to the Poisson statistics of charge production process, which occurs in detector volume and increases in relation to the energy of detected radiation [32]:

$$FWHM_{detector} = 2.35\sqrt{F\varepsilon E} \quad (5)$$

where F is the Fano factor, which describes the deviation from Poisson statistics, ε is the mean energy required to produce an electron-hole pair and E is the energy of incident photons.

Electronic noise can be caused by thermally generated leakage currents in the detector volume. Thus, the resolution degrades in accordance with detector size. It can also be introduced at the first stage of pulse processing. This effect is avoided by cooling the input transistor of the preamplifier along with the detector.

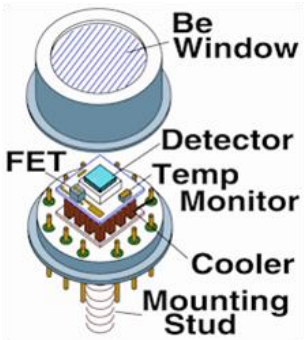

Fig. 8. Components of a SDD detector [33].

The silicon drift detector (SDD) is widely used nowadays in XRF applications. The SDD concept was introduced in 1984 by Gatti and Rehak [34] and in 1985, Rehak *et al*.

proposed an SDD optimized for X-ray spectroscopy [35]. Later, in 1987, Kemmer *et al*. improved its design significantly [36]. Even nowadays, investigation in the area of SDD is still very active [37-40].

The SDD is highly sensitive to 1 to 30 keV X-rays. The lower limit of detection is due to the incapacity of the radiation with an energy below 1 keV to pass through the Be detector window (Fig. 8) [39]. The upper limit of detection is fixed by the silicon crystal thickness.

The SDD provides better performance than conventional planar detectors by using a special type of photodiode, functionally similar to a planar photodiode but with a specific electrode structure. The small surface of the anode provides the major advantage, meaning a much lower capacitance than a planar diode with the same area, resulting in better energy resolution and higher count rates. Also, it presents less electronic noise than an equivalent planar detector, especially for short measurement times. It provides the SDD with better energy resolution for moderate count rate and even better for high count rate. Its great advantage is that the low energy peaks can be measured with high count rate and only a small loss in resolution.

The SDD photodiode cathode is composed of a p-type silicon cathode and an n-type silicon anode (Fig. 9). X-ray photons enter the photodiode and generate electron-hole pairs. Around the very small central anode, a series of concentric derivation electrodes which are negatively polarized create an electric field. That focuses the electrons in the central anode, which is directly connected to the FET (field-effect transistor) (Fig. 9). Optimal resolution is obtained by stabilizing the system and cooling it electrically (using the Peltier effect) to less than 15 ºC. Moreover, with this design, the active volume of the diode can be expanded, thus adding more derivation electrodes without modifying the small size of the area of the central anode, i.e. without changing the input capacitance. Due to its unique electrode structure, a very high active area is available without degradation of performance.

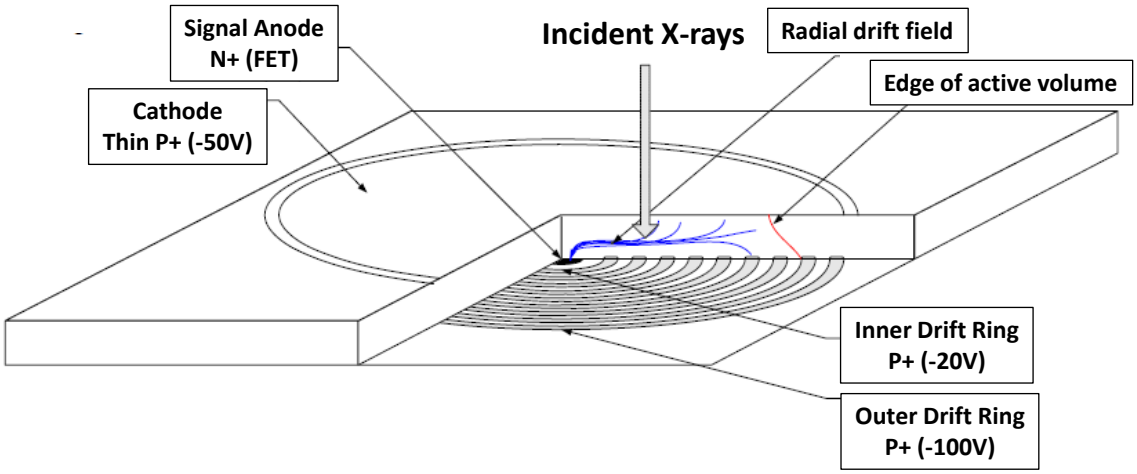

Fig. 9. Scheme of the Amptek SDD design [33].

Besides, the electronics of the signal processing is almost identical to that of planar silicon detectors. As presented in Fig. 10, the anode is connected to a charge sensitive preamplifier and to the pulse processor, which detects the pulse and measures its amplitude. The bottom right of Fig. 10 illustrates the pulse form in each step of the signal process.

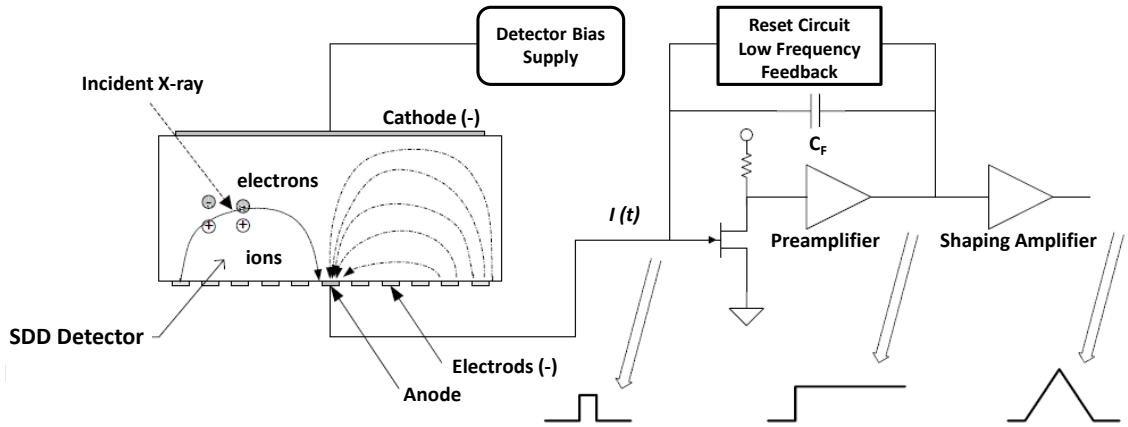

Fig. 10. Scheme of the SDD electronics of the signal processing [33].

1.2. Confocal X-ray fluorescence (CXRF) spectrometry

1.2.1. CXRF spectrometry principals and historical background

As explained previously, X-ray primary radiation is employed to induce the emission of characteristic X-ray radiation in XRF. This characteristic X-ray emission is not only generated superficially but also emerges from extended depths (several tens to hundreds of micrometers) below the surface of the material. This phenomenon is exploited by confocal μ-XRF [1].

CXRF extends the potential of the technique known as micro X-ray fluorescence (μ-XRF) to depth profile of multilayer materials. The μ-XRF technique consists of the placement of a polycapillary X-ray lens at the exit of micro-focus X-ray tube, with 45º between the excitation and detection channels and 90º between the excitation channel and the surface of the sample (Fig. 11). Meanwhile, in CXRF, an additional polycapillary lens at the entrance of the X-ray detector is employed to limit the space from which X-ray photons can be detected (Fig. 11) [41]. In the case of CXRF, the excitation channel forms an angle of 45° with respect to the surface of the irradiated object and 90° with respect to the detector channel. A study from Bjeoumikhov *et al*. determined that this angle configuration procures the best depth resolution [42].

Several μXRF devices are commercially available (Artax [43] or M6 JetStream [44] from Bruker, for example). Nevertheless, at present, CXRF setups are not commercially available.

Confocal micro-X-ray fluorescence is a non-destructive technique that can provide depth-resolved information about elemental composition and it has proven its suitability in the investigation of stratified structures in microscales [3, 45-47]. A probing micro-volume (called confocal volume) is defined by the overlap of the foci of both X-ray lenses [11]. By scanning materials through this micro-volume, one can obtain intensity profiles reflecting the local elemental composition variation versus depth or versus a lateral coordinate (with a resolution in the range of 3 to 10 μm for most CXRF setups) [1]. The maximum depth of analysis is limited by absorption effects (cf. Chapter 1.2.7) and usually does not exceed 1 mm in low-Z matrices or tens of microns in heavy-Z matrices.

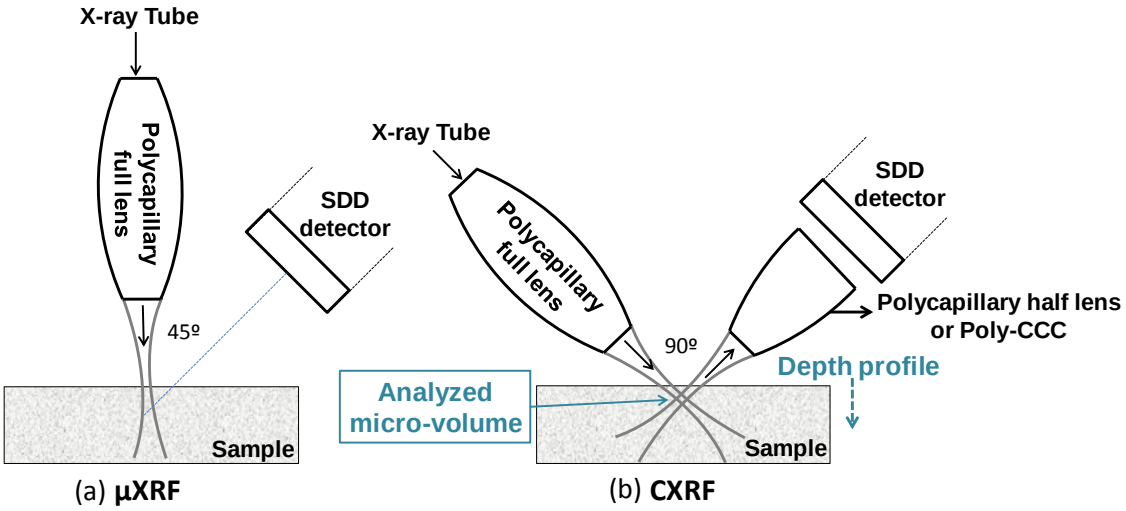

Fig. 11. Configuration of µXRF (a) and CXRF technique (b).

CXRF is associated with another technique named Synchrotron X-ray fluorescence (SXRF). In SXRF, a synchrotron monochromatic beam is used for the excitation channel instead of a polychromatic micro focus X-ray tube beam (CXRF). The idea is similar but the results obtained present differences. Indeed, Kanngießer *et al*. [48, 49] compared the sensitivity of table-top and synchrotron setup. These two techniques can be used to perform confocal studies. Nevertheless, this work only focuses on CXRF study.

In the late 1980s the quick development of capillary optics took place. The transport abilities of capillaries were presented by Rindby in 1986 [50]. The use of capillary optics opened up the possibility to create efficient laboratory micro-XRF setups. The first laboratory spectrometers utilizing capillary optics were presented in 1989 by Carpenter [51] and Rindby [52]. In 1990 Kumakhov [53, 54] introduced the polycapillary X-ray lens as a new method of focusing X-rays. Due to the high intensity gain it became the widest spread X-ray focusing device. The configuration of the confocal micro-XRF system was decided upon in 1993 by Gibson and Kumakhov [41].

In 2000, Ding *et al*. presented the first experiment with a CXRF setup for three dimensional elemental analyses (Fig. 12) [8]. Up until now, several CXRF setups have been presented worldwide. At the International Atomic Energy Agency (IAEA) [55] and Vienna University of Technology, both in Austria [56], at Beijing Normal University in China [8], at C2RMF (*Centre de recherche et de restauration des musées de France*) in France [11], at the Technical University of Berlin, Germany [48], at Osaka City University in Japan [57, 58], at AGH University of Science and Technology in Poland [59] and at Los Alamos National Laboratory in New Mexico, USA [60, 61].

CXRF is a relatively novel technique and may appear under different names in scientific publications. This fact may difficult the visibility of the technique. Sometimes, the name used focuses on the 3D ability of the technique for example “3D micro-X-ray fluorescence” [9] or “confocal 3D XRF” [7]. Acronyms such as 3D-XRF will be not used in this work as it results in a misuse of language. On one hand, CXRF can provide depth-resolved information (3D analysis) but other X-ray emission based techniques can do it as well as:

- classic XRF and µXRF [21, 62-66],
- PIXE and RBS [64],
- µPIXE [67, 68].

On the other hand, in the study of paintings, CXRF is mostly used to obtain depth profiles (1D study) or 2D profiles [3, 69, 70]. 3D study of paintings can be very time-consuming and does not provide additional information respect to 2D analysis.

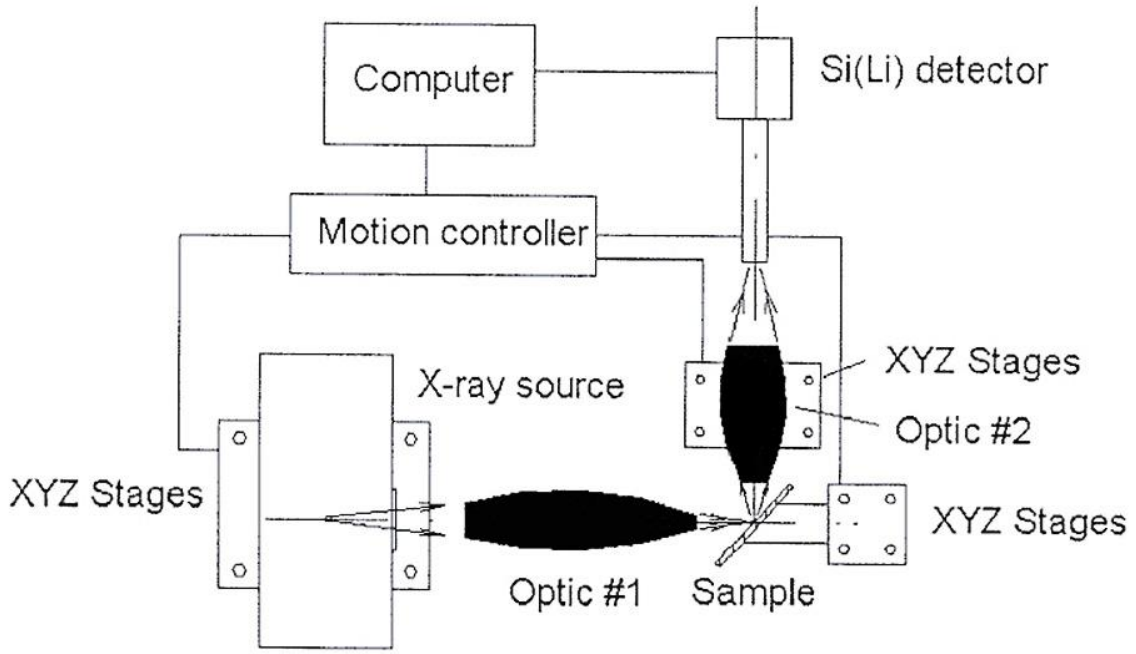

Fig. 12. Diagram of the experimental setup of the first CXRF system [8].

1.2.2. CXRF application in Cultural Heritage

Most of the published confocal studies in Cultural Heritage were performed in synchrotron installations (SXRF) [27, 45-47, 71, 72]. The significance of confocal micro X-ray fluorescence has increased quickly in the last decade. The numerous applications have proven that this method is now a well-established tool for non-destructive imaging of three-dimensional distributions of chemical elements within sampling. This method became especially useful for testing multi-layered systems in micrometer scale. In the study of artwork, it is becoming a strong non-destructive alternative to the classical scanning electron microscopy supplemented with energy-dispersive X-ray spectroscopy (SEM-EDX) applied to cross section micro-samples [73].

In 2003, the first publication of depth analysis on 18th century Mughal miniature paintings by means of SXRF by Kanngießer *et al.* took place [9]. In 2005, Kanngießer *et al.*, again, published the first CXRF study of experimental paint layers [48]. In 2009, the first CXRF depth analysis applied in Cultural Heritage of Japanese lacquerware 'Tamamushi-nuri' was published by Nakano and Tsuji [7]. In 2012, the first CXRF study of Renaissance paintings was published by Reiche *et al.* [11]. In this study, the CXRF depth profiles obtained on the paintings were related to lateral CXRF scans on cross-sections. The cross sections were prepared from samples taken next to the analyzed points, in order to better evaluate the performance of CXRF depth profiling for the analyses of paint layers. The cross-sections were also studied by optical microscope (OM) and SEM-EDX in order to compare the results to those obtained by CXRF [11]. Beside the analysis of paint layers, the study of other objects of Cultural Heritage was also

performed. For example, Mantouvalou *et al.* [49] studied Medieval reverse paintings on glass and Dead Sea scrolls [74].

Moreover, CXRF was also used in other interesting fields:

- analysis of biological samples as seeds or little fish [58, 69, 75, 76],
- studies of solid/liquid interfaces [76],
- studies of the elemental distribution in pharmaceutical tablets [77, 78],
- density measurements in ultra-low density materials [79].

Some other applications are also possible, such as the 3D elemental imaging of microSD card [80] or the depth elemental imaging of multi-layered automotive paint fragments and microchips [69].

1.2.3. Micro-focus X-ray tube

Due to the use of X-ray optics for focusing the beam, CXRF needs a micro-focus X-ray tube as an excitation source. Indeed, those micro-focus low-power X-ray tubes (with a typical spot size of about 50×50 μm^2) make the combination with polycapillary lenses possible. The first micro-focus X-ray tube was developed for X-ray radiography in 1953 [81]. The first micro-focus X-ray tube with an electromagnetic focalization system was described by Arndt *et al.* in 1998 [82].

Those tubes may also be employed for XRF. One of the most common uses is for the so-called macro-XRF technique. Using a small spot size and high intensity beam, this technique consists in obtaining the cartography of paintings, for example, with an exposure time per point that is extremely short (10 seconds) which allows the scanning of a large area with a small step (1 mm) [10, 83].

From the X-ray optics point of view the brilliance is a much more important parameter than total photon flux. The brilliance is a measure of quality of the X-ray source [84, 85]. Brilliance is related to the concentration of photons and takes four factors into account:

- Number of photons produced per second (N_P),
- The angular divergence of the photons (θ_P), or how fast the beam spreads out,
- The cross-sectional area of the beam (A_P),
- The photons falling within a bandwidth (BW) of 0.1% of the central wavelength or frequency.

The resulting formula is:

$$Brilliance\,(\mathrm{s^{-1}.mm^{-2}.mrad^{-2}}) = \frac{N_P\,(photons.s^{-1})}{\theta_P\,(mrad^2) * A_P\,(mm^2) * 0{,}001 * BW\,(photons)} \quad (6)$$

The greater the brilliance, the more photons are concentrated on a spot. The increase of brilliance can be achieved by increasing the total power of the X-ray tube or by decreasing the size of the focal spot.

The reduction of the focal spot size can be achieved by the focusing of the electron beam by magnetic lenses. Increasing the total power of the X-ray tube enhances the heat load on the anode which is limited by thermal conductivity and cooling efficiency. Consequently, the higher power load reduces the durability of the tube.

In a typical micro-focus side-window X-ray tube with total power of 50 W, the focal spot with an area of 100 μm^2 can be produced. In this case, the anode power load can

reach values greater than 1 kW/mm^2 meaning that the brilliance can be higher despite the low total power of the tube. For this reason, low power X-ray tubes have become very popular. Moreover, low power tubes are more compact than high power tubes as the size of the cooling system as well as the high voltage power supply are smaller. Their small size makes them particularly suitable for transportable setup.

The design of a micro-focus side-window X-ray tube with electromagnetic focalization is illustrated in Fig. 13. X-ray photons are generated by electron irradiation of a target producing the X-ray emission by bremsstrahlung radiation and X-ray fluorescence of the anode. The X-ray tube generates an X-ray beam by a process involving an electron beam produced by an electron gun, accelerated by electrical potential, and electromagnetically focused before colliding with a target. The electron gun consists of a Wehnelt electrode and an indirectly heated activated dispenser cathode. The advantage of the dispenser cathode is that it is mechanically stable and, due to the lower power consumption and operating temperature, it has a greater lifetime than heated filament cathodes. The electrons are accelerated from the cathode, held at a high negative potential, towards the grounded anode. They pass through a hole in the anode before being electromagnetically focused [86].

Micro-focus low-power X-ray tube with high brilliance coupled to a polycapillary lens allows to obtain a reduced beam focal spot size with high intensity. For this reason, both elements are essential for CXRF.

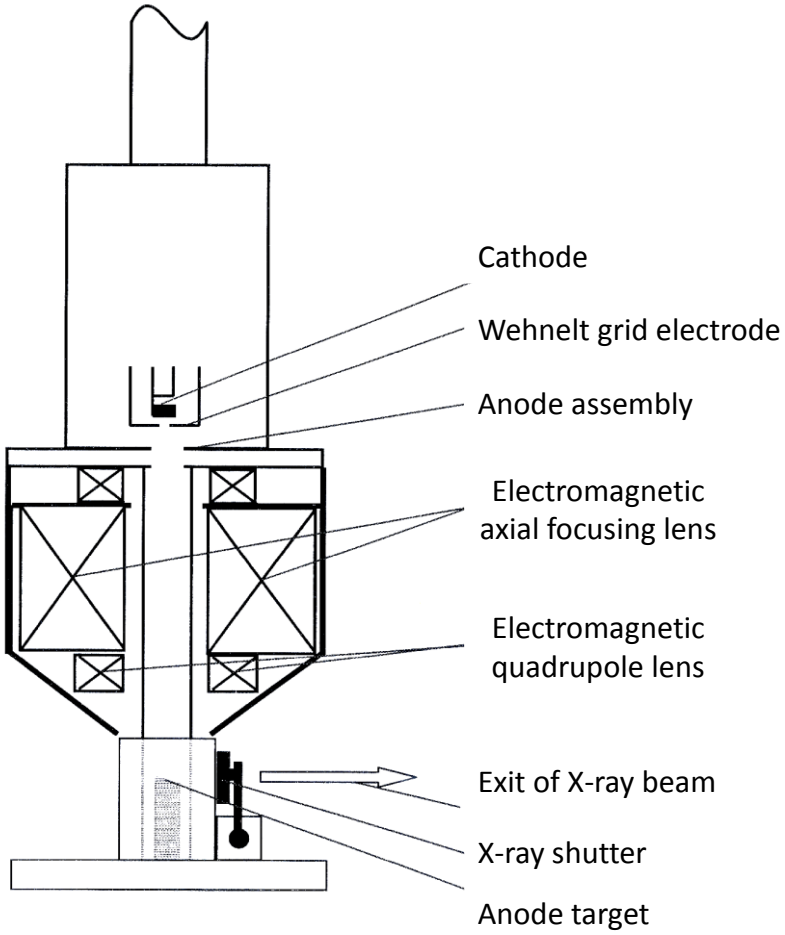

Fig. 13. Schematic drawing of an electromagnetically focused micro-focus X-ray tube [86].

1.2.4. Polycapillary lenses and polycapillary collimators

The main goal of focusing optics is to capture the radiation emitted in a large solid angle and concentrate it in a very small spot. Polycapillary lens is one kind of X-ray focusing device. It consists of large amounts of hollow glass channels (from several thousands to hundreds of thousands, each working as a waveguide) (Fig. 14). It collects photons in a large solid angle transporting them by multiple reflections inside every channel and focusing the beam in a small spot with a higher density radiation. Bent capillaries transport the radiation and also change the direction of the beam. The radiation emitted from the source point is transported by capillaries which have openings that are oriented towards the source.

In the case of polycapillary full-lens, the arrangement of channels changes from divergent into convergent, so that the radiation can be refocused into a focal spot as shown in Fig. 15.

Another group of focusing devices is called polycapillary collimators. They can be made of bent (polycapillary half-lenses) or straight channels (polycapillary conical collimators or poly-CCC). The main role of polycapillary half-lenses is to make the divergent radiation beam parallel whereas poly-CCC is able to guide and collimate divergent radiation (see Fig. 15 b and c). They are used in front of the X-ray detector to complete the CXRF configuration.

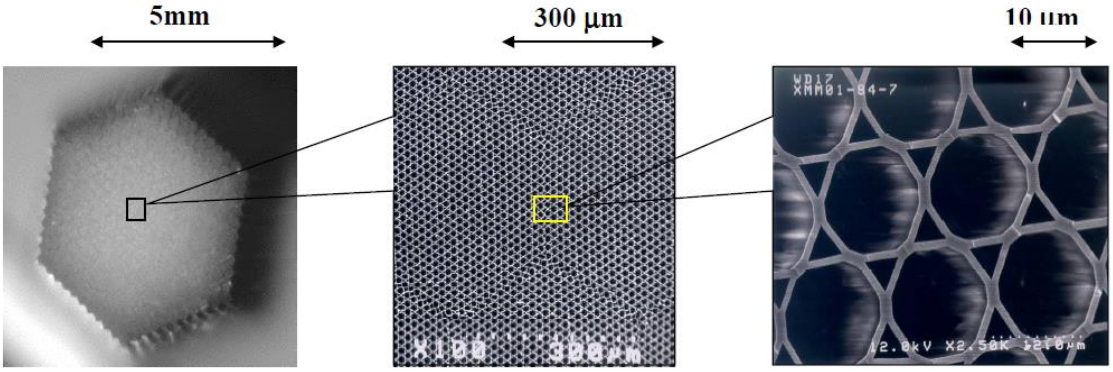

Fig. 14. Microchannel makeup of polycapillary optics [87].

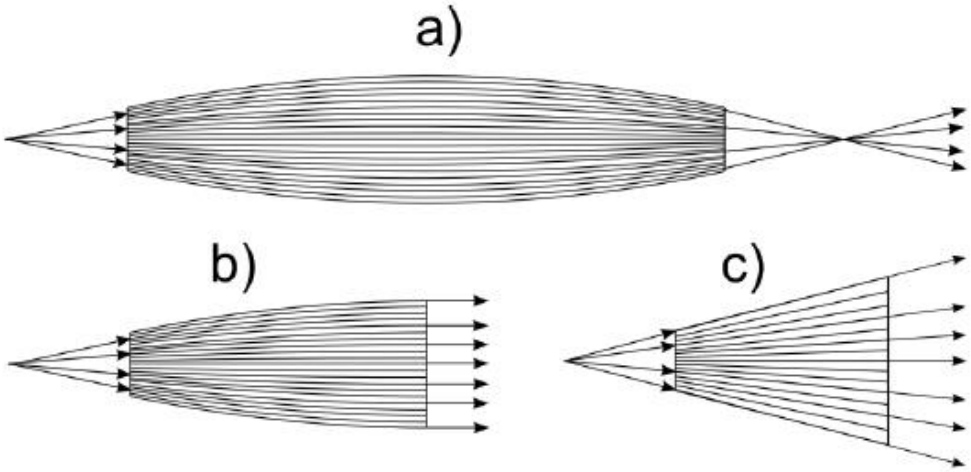

Fig. 15. Schemes of polycapillary full-lens (a), polycapillary half-lens (b) and polycapillary conical collimator (poly-CCC) (c) [13].

There are several important parameters that describe the performance of the X-ray optics:

- The size of the output beam or focal spot size *S* defines the achievable spatial resolution of the spectrometer. The X-ray beam formed by the focusing device reveals uneven distribution of intensity across the beam. Usually it can be approximated by a Gaussian function. In this case the size of the beam is defined by the Full Width at Half Maximum (FWHM) of the Gaussian.
- The gain is a useful parameter which is used to describe the X-ray lens. It is a dimensionless factor that defines the increase of beam intensity in comparison with a pinhole collimator with an internal diameter equivalent to this of the polycapillary lens. This parameter is defined as the number of X-ray photons by unit of surface, by unit of time (Appendix II and VI).
- The working distance or output focal distance *f* defines the distance between the optics and the focal spot. For short working distances the sample has to be put very close to the optics. This parameter is crucial for depth profiling of a sample – for short working distances the maximum accessible probing depth and the security of the measurement are reduced. In the Cultural Heritage study, the selection of the working distance is critical.

1.2.5. X-ray optic principals

Total External Reflection (TER) occurs when X-ray radiation strikes the internal surface of a capillary at an angle which is smaller than the critical angle (θ_c) (Fig. 16, a). Because it is a very small number (10^{-5}-10^{-6}) in the X-ray energy range, the angle of total reflection is very small (several mrad). The X-ray photons are then transported by reflection along the length of the tube without any losses. Meanwhile, those X-rays that do not fulfill this condition are absorbed into the walls of the capillary (Fig. 16, b).

θ_c is a function of the density of reflective material and the energy of the incident radiation. For borosilicate glass, θ_c is determined by the X-ray energy through the formula [88]:

$$\theta_c(mrad) \approx \frac{30}{E(keV)} \quad (7)$$

The size of the output beam *S* can be roughly estimated by the following equation [88]:

$$S(\mu m) \approx 2 f(mm)\theta_c(mrad) + d_{out}(\mu m) \quad (8)$$

where *f* is the working distance (or output focal distance) and d_{out} is the channel diameter of the capillary at the output end of the optic, which is very small compared with *S* and can be neglected.

Combining the equations 7 and 8 and neglecting d_{out} gives:

$$S(\mu m) \approx \frac{60 f(mm)}{E(keV)} \quad (9)$$

Because the critical angle (θ_c) changes with energy (eq. 7), for lower energies (higher θ_c), more photons can be accepted and thus emitted. For this reason capillary works as a low-pass filter.

According to equation 9, the focal spot size S is energy dependent. Consequently, for a determined working distance f, S is smaller for higher energies. This property will explain the variation of the depth resolution with X-ray energy (cf. Chapter 1.2.6).

The energy dependence of transmission of X-rays through the polycapillary with bent channels results connected to the curvature. The curvature radius R is related to the critical angle (θ_c) as followed [89]:

$$\theta_c^{\,2} \geq \frac{2d}{R} \approx \theta^2 \quad (10)$$

where d is the channel diameter.

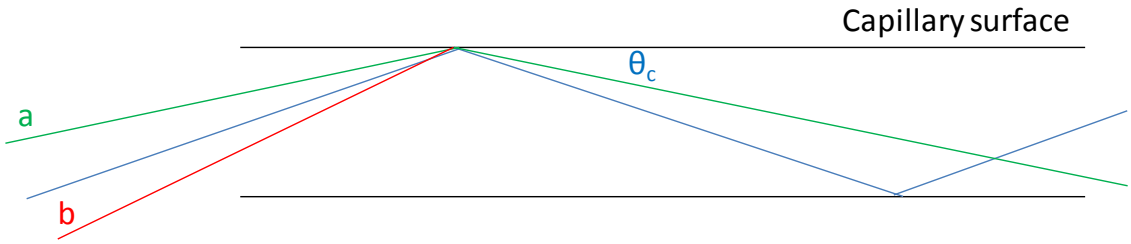

Fig. 16. Conditions of Total External Reflection. X-rays with incidence angles θ smaller than the critical angle (θc) are reflected (a). On the contrary, X-rays are absorbed (b).

The great advantages of these devices are the simple manufacturing process (low cost) and broad band transmittance. Because of its compact size, focalizing properties and ability to produce high-flux of polychromatic beams, they have become very popular especially for polychromatic X-ray tube purposes. The greatest advantage of polycapillaries is the acceptance of a large solid angle of emitted radiation.

1.2.6. Depth resolution and depth profile

As previously explained, a probing micro-volume is defined by the overlap of the foci of both polycapillary lenses (Fig. 17).

The characterization of the CXRF setup is achieved by defining the depth resolution [49, 57, 70, 90]. The depth resolution is represented as a function of the X-ray energy. The FWHM of several depth profiles of elemental thin films are represented versus the respective X-ray energy. It is obtained measuring depth profile of a series of thin foils. The foils had to be thinner than the depth resolution in order to prevent the absorption effect (cf. Chapter 1.2.7). Then, the FWHM of the depth profile of the Kα or Lα radiation of those elements (in μm) is represented versus the energy of emission of the chemical element composing the foil (in keV) (Fig. 18). For every in-depth scan measured, the estimated error applied to the FWHM values is half of step size.

The depth resolution is energy dependent, being smaller for higher energies (Fig. 18). This means that, in multilayered samples, the depth resolution is slightly different depending of the chemical element excited by the X-rays.

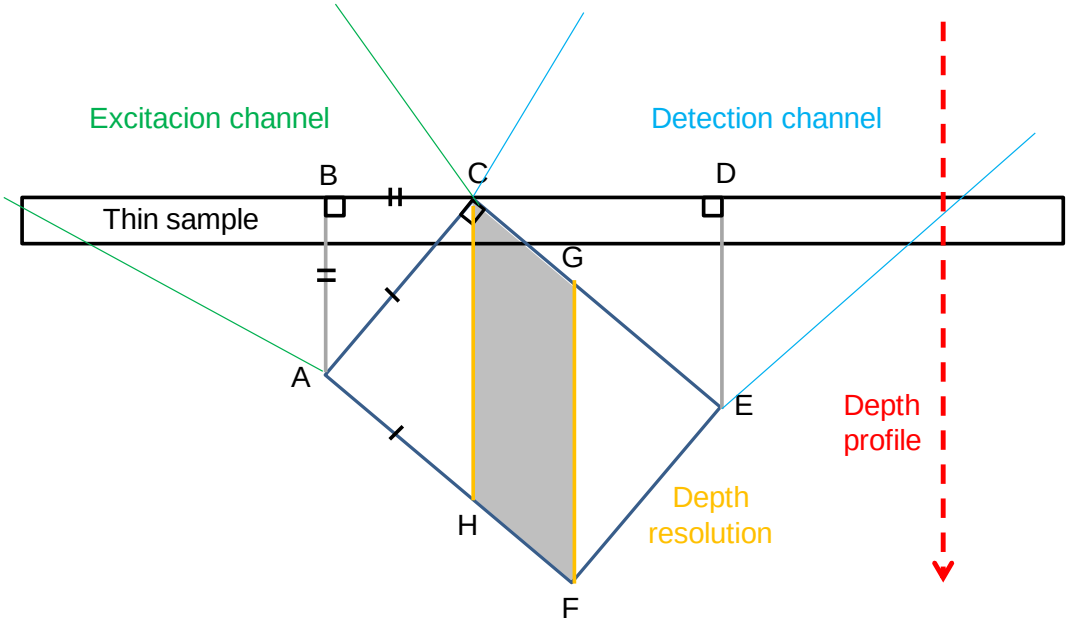

Fig. 17. Simplified scheme representing the depth resolution defined by the overlap of the foci of both X-ray polycapillary lenses.

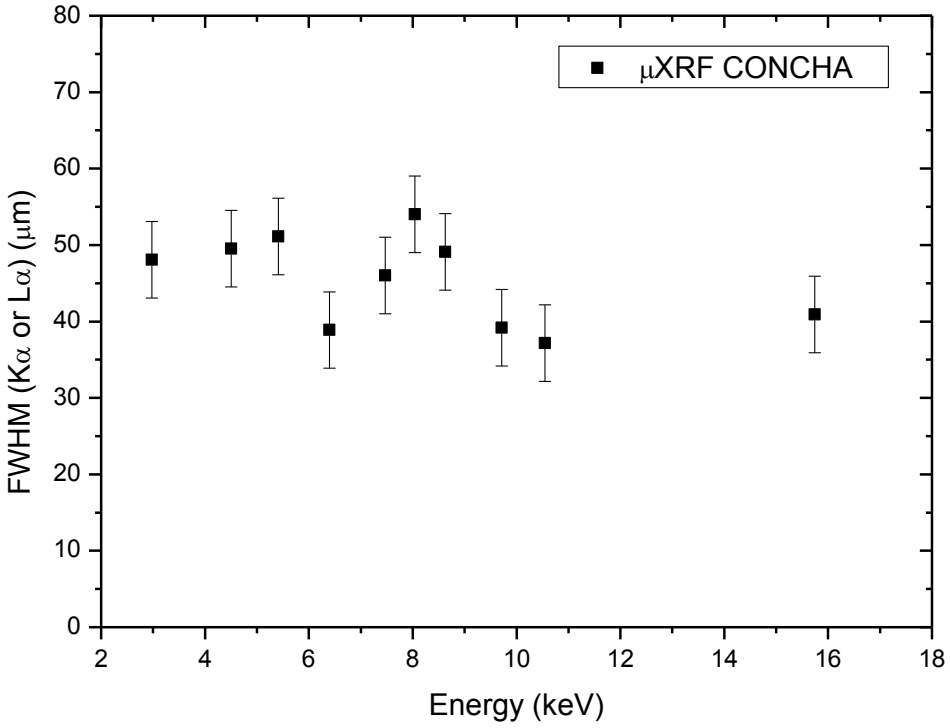

Fig. 18. Depth resolution of the μXRF-Concha set-up as a function of the emitted energy. The FWHM of several depth profiles of elemental thin films is represented versus the respective X-ray energy.

Depth profile is obtained by scanning materials through the probing micro-volume. The path of the scanning is crucial. The motorized movement has to be accurate with a precision below 1 µm. The simplest depth profile represents the intensity evolution of a characteristic peak area of one chemical element (in counts) (e.g. Cu Kα peak) in function of the proximity of the CXRF device to the sample (i.e. depending on the depth) (in µm) (Fig. 19). The characteristics of the depth profile shape depend on chemical composition, density and thickness of the analyzed material.

The depth profile of a thin foil (Fig. 19) can be fitted using a Gaussian function. The FWHM of the Gaussian corresponds to the depth resolution. In the case of a multilayered sample, the centroid of each Gaussian, Xc, of each chemical element in the sample determines the chemical composition and sequence of each layer (cf. Chapter 3.3).

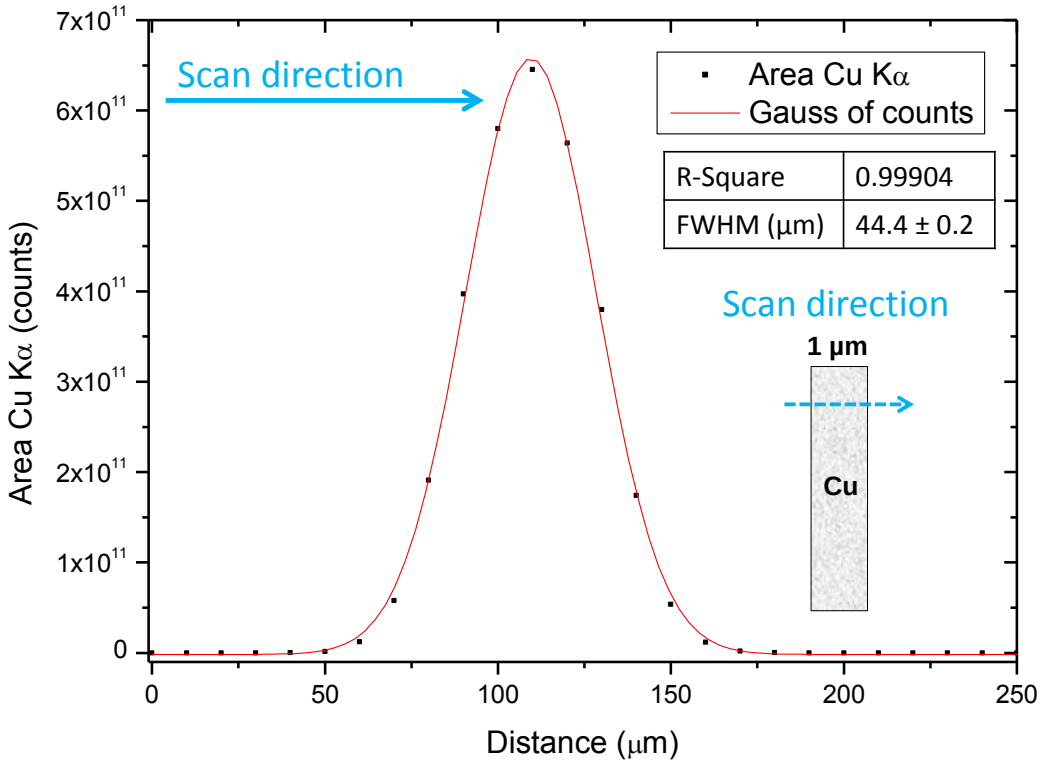

Fig. 19. Depth profile of a thin foil (Cu, 1 µm thick, 10 µm steps and 120 s per spectrum).

1.2.7. X-ray interfering effects

Two main interfering effects can be distinguished as absorption and enhancement effects.

The absorption effect occurs when either primary or secondary X-rays are absorbed within the sample. When X-ray passes through a sample of thickness *D*, the primary intensity I_0 is reduced to *I* according to the Lambert-Beer law:

$$I = I_0 e^{-\mu_{lin} D} = I_0 e^{-\mu \rho D} \quad (11)$$

where μ_{lin} is the linear absorption coefficient, μ is the mass absorption coefficient and ρ is the density of the medium.

In the energy range from several hundreds of eV to several tens of keV, there are three main phenomena responsible for absorption of X-rays: photoelectric absorption, coherent and incoherent scatterings. The mass absorption coefficient μ is defined as the probability of those phenomena normalized by the number of atoms in a given mass of material and can be expressed as a sum of mass absorption coefficients corresponding to each interaction process:

$$\mu = \mu_{\mathrm{F}} + \mu_{\mathrm{inc}} + \mu_{\mathrm{coh}} = (\sigma_{\mathrm{F}} + \sigma_{\mathrm{inc}} + \sigma_{\mathrm{coh}}) \frac{\mathrm{N_A}}{\mathrm{A}} \quad (12)$$

where μ_F, μ_{inc} and μ_{coh} are the mass absorption coefficients respectively for photoelectric absorption, incoherent and coherent scatterings; σ_F, σ_{inc} and σ_{coh} are cross sections for photoelectric absorption, incoherent and coherent scatterings, N_A is Avogadro's number and A is the atomic mass of the element composing the matter.

The mass absorption coefficient depends on energy but also on the chemical element. This coefficient for a multi-element attenuator μ_{total} can be expressed as a weighted average:

$$\mu_{total} = \sum_{i=1}^{n} W_i \mu_i \quad (13)$$

where W_i and μ_i are weight fraction and mass absorption coefficient for element i.

As can be seen, the absorption effect limits the maximum probing depth from which the signal can be registered. For any given element the attenuation length can be defined as a probing depth from which the registered intensity drops to 36.7% of the maximum value [91]. The attenuation length depends on the overall composition of the sample. It decreases for samples with a higher atomic number and density and increases with the energy of X-ray emitted.

The enhancement effect emerges when characteristic X-ray radiation from one chemical element can excite other elements present in the sample. In these cases, some X-ray peaks reveal higher intensities as they are excited by both primary and secondary radiations. This effect is significant when the fluorescence radiation of an element can excite other elements present in high concentrations.

The study of the enhancement effect in CXRF geometry was done by Sokaras and Karydas [68]. The fluorescence intensity produced by primary and secondary radiations for different matrices was calculated. As expected by the calculation, they observed the strongest enhancement effect for an alloy sample consisting of 50 % iron and 50 % copper (the enhancement reaches 40 %). For samples with diluted elements in a light matrix, this effect is significantly reduced while, for low concentrations (<10 %), it can be ignored.

Those phenomena can drastically affect the CXRF multilayered paintings results. The Gaussian shape of the depth profile and the information obtained from this Gaussian are modified.

In the case of the absorption effect, the information of some layers is completely absorbed by upper layers and cannot be detected. For detected sublayers, the intensity measured from the depth profile may decrease due to the contribution of the absorption effect (Fig. 20).

Obviously, the absorption effect increases with depth and affects more the deepest part of the depth profile. Consequently, the decreasing part of the depth profile is shorter than the increasing part which deforms the original Gaussian shape of the profile. Applying a Gaussian fit to this distorted depth profile gives a lower value of the maximum and of the FWHM of the Gaussian curve. In the case of the FWHM, this means that the depth resolution is smaller due to the absorption effect (see Table 21, Chapter 3.3.3). If interfering effects are ignored, the maximum of the Gaussian has to appear at the center of the analyzed layer which would be useful to measure the distance between different layers. Nevertheless, due to the fact that the absorption effect modifies the value of the maximum of the depth profile of each layer, it is difficult to determine precisely the paint layer depth or deducing its thickness from those.

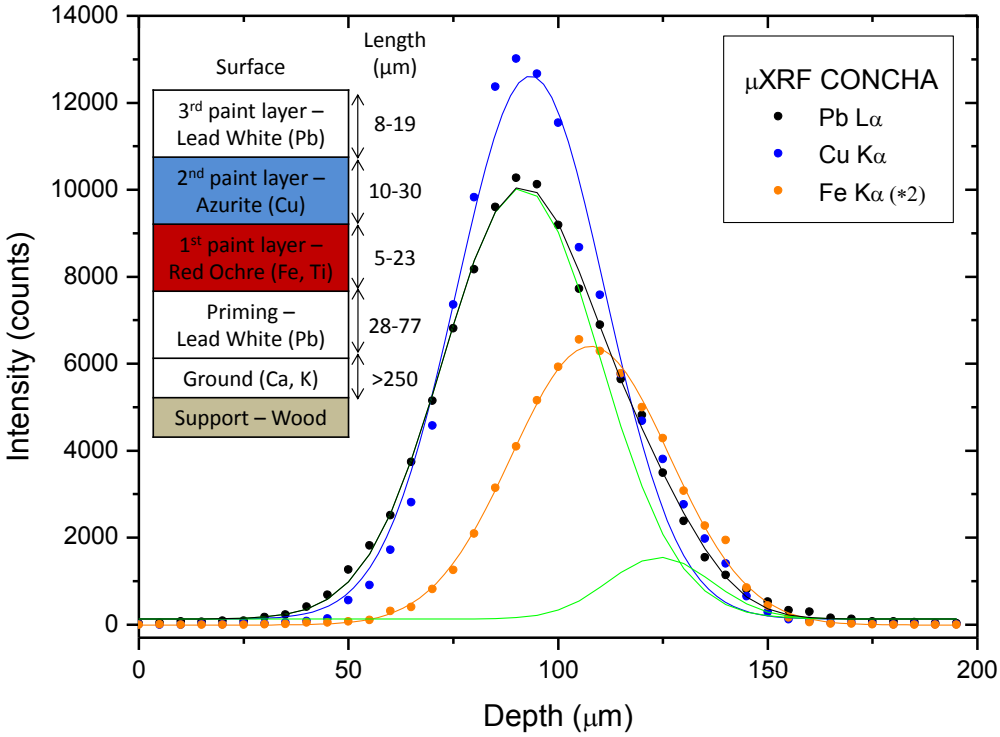

Fig. 20. Depth profile of a five-layer sample. The decrease of the area with the depth of the layer illustrates the absorption effect.

The enhancement effect appears when a layer is composed of an element the fluorescence of which can excite the elements from other layers. Consequently, the elements from the upper layers, once excited, appear together with the element composing the lower layer. The enhancement effect produces artefacts in the depth profile which do not correspond to the real position of the element analyzed or the real chemical composition of the layer.

For unknown multilayered paintings, the contribution of those phenomena may difficult the interpretation of the CXRF results.

1.2.8. CXRF quantitative analysis

Several quantitative methodologies have been developed for both SXRF and CXRF techniques over the last few years [45, 48, 57, 91-97].

To compensate for the absorption effect, the entire composition of the sample has to be taken into account. This is especially difficult in the case of the presence of unknown and undetectable elements (so called dark matrix). The correction of this effect is further complicated in the case of polychromatic excitation where different mass absorption coefficients for different energies as well as the spatial energy distribution of primary X-ray beam have to be taken into account. It should be noted that the energy distribution of the primary beam changes inside the sample due to absorption effects. This "beam hardening" is caused by the fact that soft X-rays are always more strongly attenuated than hard X-rays. This means that the depth resolution will decrease at higher probing depths.

In actual quantitative methodologies proposed, the density of the sample matrix as well as the density of the element (or compounds that contain the given element) have to be known in order to convert the local densities into concentrations. Also, all calculations performed are based on the assumption that the composition and density of the dark matrix is known. All of this information is not available just using CXRF study of Cultural Heritage objects like old paintings. The use of other techniques would be necessary in order to determine the information required. At present, CXRF quantitative analysis methodology of unknown multilayered material is not available.

Nevertheless, CXRF study of old paintings does not need this kind of information for it to be valuable. The qualitative results provide complementary information to the classical study of stratigraphic micro-samples by SEM-EDX in a nondestructive way. These results give access to depth compositional profiles of the pictorial layers for the purpose of identifying the inorganic pigments palette and techniques used by the artist. The interests of CXRF study of antique paintings resides in the definition of the chemical composition of every layer composed by inorganic pigments and the sequence of these layers.

1.3. UV-induced visible fluorescence photography

In 1801, physicist Johann Wilhelm Ritter observed that invisible rays just beyond the violet end of the visible spectrum darkened silver chloride-soaked paper more quickly than violet light itself. What he was discovered is known today as ultraviolet (UV) radiation (Fig. 21).

Indeed, the first technique applied in our methodology for the study of paintings is ultraviolet-induced visible fluorescence photography. This technique consists in the illumination of a painting by UV light and recording the induced fluorescence effect emitted by the painting using a photographic camera. In UV fluorescence photography, a visible cut-off filter is placed in front of the UV source which absorbs all of the radiation in the visible spectrum, allowing only the desired ultraviolet light to pass and reach the item in question. Many materials, including painting materials, absorb invisible UV radiation and transform part of the energy received into radiation emission in the visible spectrum. The visible light is not reflected but emitted by the artwork. When the UV is absorbed without emission, the observed area appears quite obscure in contrast to the fluorescent areas. In some cases, a second UV cut-off filter is placed in front of the camera lens allowing only the desired visible fluorescence to be recorded by the camera.

Finally, in order to prevent sunlight or lighting from adversely effecting results, it is necessary to work with the camera in a dark room.

The most useful UV band in the examination of artwork is 360 nm (known as near UV). Today, almost all painting analysis begins with UV examination, which quickly and cheaply provides useful information that can be used to determine the next appropriate analysis technique or conservation approach [98].

In our case, we use up to four handheld UV lamps, selected depending of the size of the artwork, and a digital camera (model D3100 from Nikon with AF-S DX 18-55 mm and AF-S DX 55-200 mm VR lenses). The four handheld UV lamps are 6 Watt UV lamps (model UVGL-55 from Ultra-Violet Products Ltd (UVP) [99] which combine long (365 nm) and short waves (254 nm). Using a hand held UV lamp is a convenient and effective way to scan an entire painting. In order to illuminate the painting, lamps can be moved manually in front of the item or fastened to a tripod thanks to specific pieces manufactured at the mechanic workshop of the Faculty of Physics of the University of Seville.

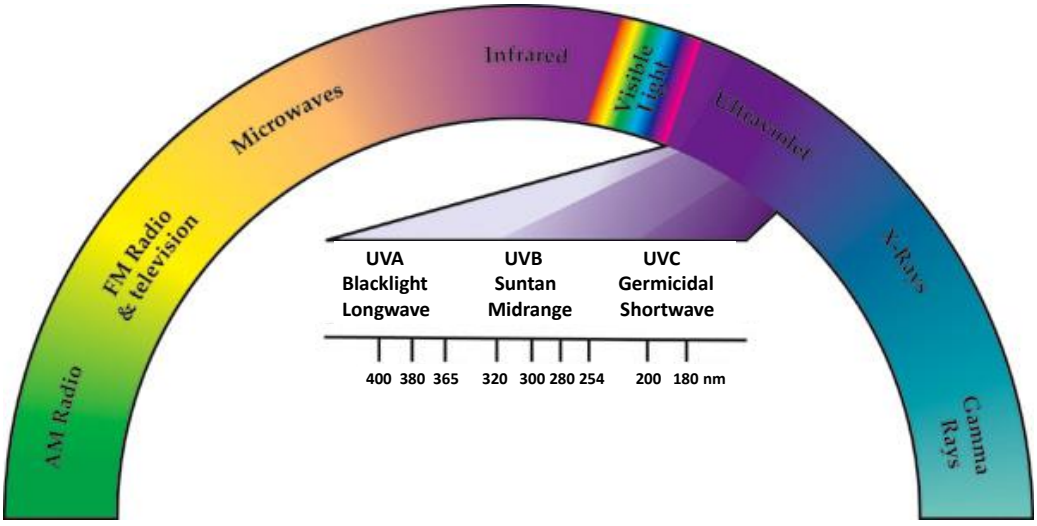

Fig. 21. Electromagnetic spectrum showing the spectral regions of the UV radiation. [99].

The UV-induced visible fluorescence photography objective is to localize prior restoration interventions on the painting in order to avoid the restored areas during further posterior analysis (XRF, CXRF, etc.). Indeed, this technique can expose the presence of old natural resin varnishes, as these often fluoresce under UV light while newer varnishes do not. It is also possible to identify overpainting, repairs and floating signatures which usually appear as dark spots in contrast to the original fluorescent areas (Fig. 22). This is of particular interest to this work as the authenticity of the original inscriptions or signatures can be confirmed [98].

In addition, bluish-white spots indicate the presence of lining compound, dark bluish-violet indicates picture repair putty, and very small blue dots are dust. Finally, a chartreuse haze indicates old varnish.

Nevertheless, UV examination has some limitations. In fact, very old over-paintings or retouchings executed in the past and examined with UV light can be difficult to distinguish as they tend to fluoresce after eighty to a hundred years. Furthermore, it may take more than 10 years for the resin composing an artwork to be chemically altered to the point that UV radiation provokes visible fluorescence. Thus, the uniform fluorescence of the painting layer does not have to exclude past interventions [98].

Finally, certain pigments also have specific fluorescence signatures, such as zinc white (which has been used in ground preparations since the 19th century) which appears yellow. Certain pigments and binders can fluoresce with very precise colors under UV, however this identification technique must be used very carefully as many factors can influence the fluorescence color observed, such as impurities that can may even cause fluorescence to diminish or disappear [100].

In conclusion, based on UV-induced visible fluorescence photography, a specific interest can be done on some fluorescence observed areas during located analysis (XRF, CXRF, etc.) in order to define their chemical specificities.

Fig. 22. Photography of a detail of "San Pedro Nolasco despidiéndose de Jaime I el Conquistador" (a) and the same detail in UV-induced visible fluorescence photography (b).

1.4. Infrared reflectography (IRR)

Infrared (IR) radiation was first detected by astronomer Sir William Herschel in 1800. He discovered that many molecules have both vibrational and rotational resonances in the infrared and, as a result, are good absorbers. Therefore, IR is often mistakenly referred to as heat waves.

Since the J.R.J. Van Asperen de Boer thesis, infrared reflectography (IRR) has become a classic image registration method in the technical examination of art [5]. This technique reveals the presence of preparatory drawings made of carbon black (infrared no-reflective material) and the artist's process of execution and changes in the composition (*pentimenti*) as well. It also provides information that helps to deduce the nature of some pigments present on the artwork's surface [6, 101].

Indeed, images under IR radiation have been employed, for many years, during the material study of artwork, mainly in the restoration field, but also as an important tool from the history of art perspective. The IRR technique permits users to visualize a painting by registering its response in the infrared spectrum, invisible to the human eye. It has the advantage of being both nondestructive and noninvasive.

Infrared radiation extends from the nominal red edge of the visible spectrum at 700 nm to 1 mm. At present, different IRR cameras are available with detectors which are able to record a specific part of the IR spectra (Fig. 23). The reflection intensity of the IR light by a painting registered by an IRR camera depends not only on the wavelength range of the IR radiation recorded by the sensor camera but also on the thickness of the painting layer as well as the kind of materials present and its quantities.

During the present studies, the excitation of the paintings were achieved with two halogen light reflectors (800W with intensity regulation control) placed on either side of the artwork. To achieve the most homogeneous illumination, in the case of Seville, two tripods were placed at a distance of 1 m from each side of the 2D motion device (cf. Chapter 2.3), both at an angle of 45º with respect to the surface of the painting (Fig. 24). Those conditions were applied for all artworks studied in order to homogenize the results obtained.

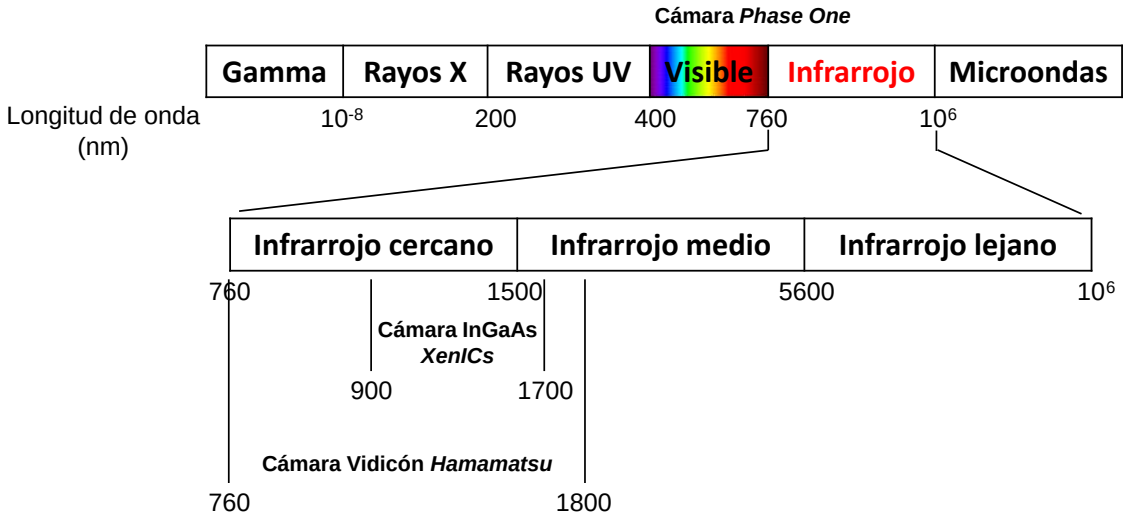

Fig. 23. Specific part of the IR spectra registered by each IRR camera.

Fig. 24. Position of the tungsten lights in order to obtain the most homogeneous illumination.

During this work, three different technologies of IRR cameras were used:

- two InGaAs cameras, the *Xeva-XS-512* model in Seville and the more recent *Xeva-1.7-640* model in Mexico (both from Xenics) (Fig. 25),
- a Si-CCD camera (model Power Phase from Phase One) (Fig. 26),
- an infrared vidicon camera (model C2741-03 with a 25 mm tube diameter (model N2606-06) from Hamamatsu Photonics K.K.) (Fig. 26).

The difference between both Xenics cameras is the resolution. The *Xeva-XS-512* has a resolution of 320×256 pixels while the resolution of the *Xeva-1.7-640* is 640×512 pixels.

To define the IR range of each camera, the sensor response division scheme has been chosen [102]. This scheme divides the band based on the response of various detectors. In this case, near-infrared ranges from 0.7 to 1.0 µm (0.7 µm being the approximate end of the response from the human eye to 1.0 µm being that of silicon) while short-wave infrared is defined as 1.0 to 3 µm (1.0 µm being cut-off of silicon to 3 µm being cut-off of the MWIR atmospheric window). The last division belongs to InGaAs, which covers up to 1.8 µm (Table 2).

Now, the different technologies of IRR cameras are presented and explained.

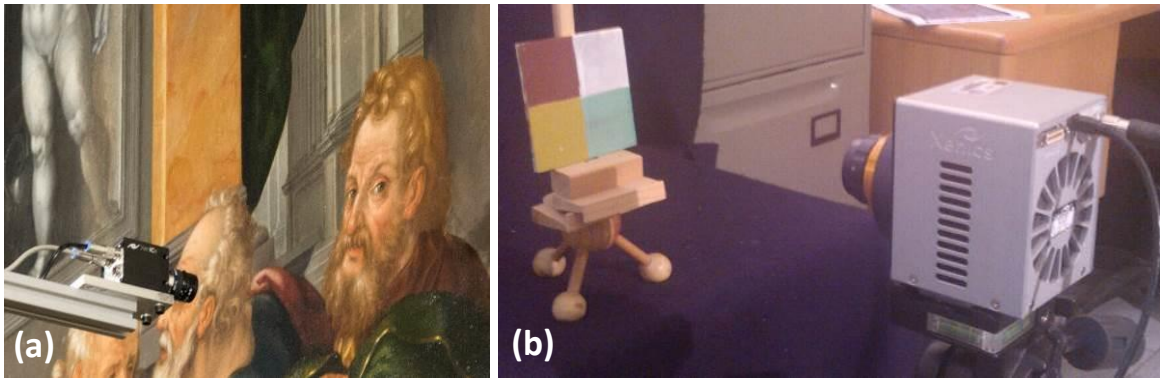

Fig. 25. The Xeva-XS-512 model in Seville (a) and the Xeva-1.7-640 model in Mexico (b).

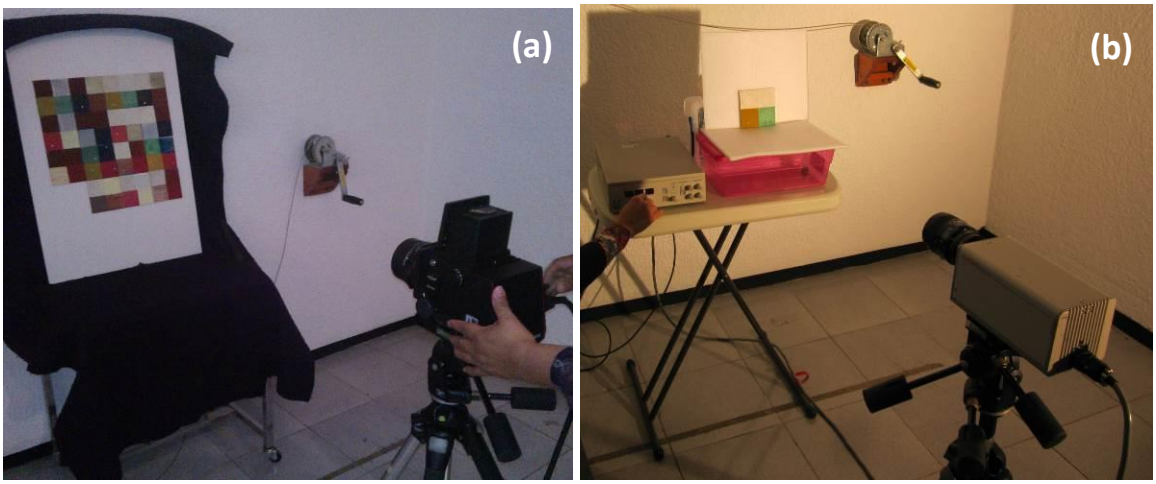

Fig. 26. Si-CCD camera (model Power Phase) (a) and infrared vidicon camera (model C2741-03) (b), both in Mexico.

Table 2. Classification of the different technologies of IRR cameras based on the sensor response division scheme.

Technology type	Responsivity range (nm)	Sensor response division scheme
Si-CCD	300-1000	near-infrared
Vidicon	400-2200	near-infrared and short-wave infrared
InGaAs	900-1700	short-wave infrared

1.4.1. Si-CCD detector

The charge-coupled device (CCD) was invented in 1969 at AT&T Bell Labs by Willard Boyle and George E. Smith [103] who were awarded the Nobel Prize in Physics in 2009 [104].

In a CCD for capturing images, there is a photoactive region and a transmission region. Fig. 27 illustrates the electrode structure defining an individual CCD sense element.

Image generation can be divided into four stages: charge generation through photon interaction with the device's photosensitive region, collection and storage of the liberated charge, charge transfer, and finally charge measurement.

When an image is projected through a lens onto the two-dimensional capacitor array (the photoactive region), each capacitor accumulates an electric charge proportional to that of the light intensity present in that location. Once the array has been exposed to the image, a control circuit causes each capacitor to transfer its contents to its neighbor (operating as a shift register). The last capacitor in the array dumps its charge into a charge amplifier, which converts the charge into voltage. By repeating this process, the controlling circuit converts the entire contents of the array in the semiconductor to a sequence of voltages. In a digital device, these voltages are then sampled, digitized, and usually stored in memory. During readout, the collected charge is subsequently shifted along the transfer channels under the influence of voltages applied to the gate structure. The bucket brigade for rainfall measurement analogy aids in visualizing the concept of serial readout of a CCD. It is very well illustrated (Fig. 28) by K.R. Spring, T.J. Fellers and M.W. Davidson [105].

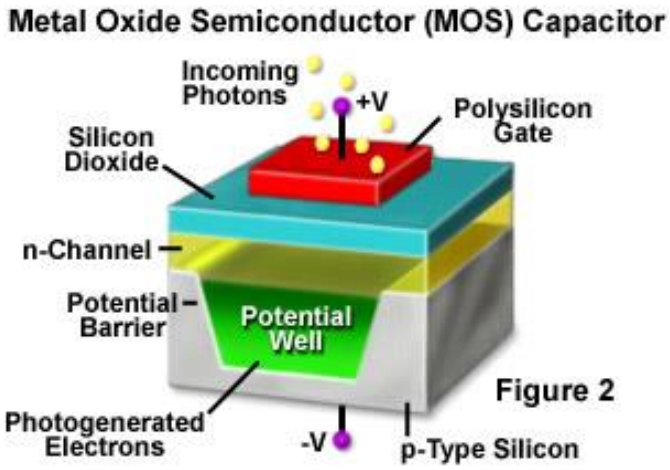

Fig. 27. Electrode structure defining an individual CCD sense element [106].

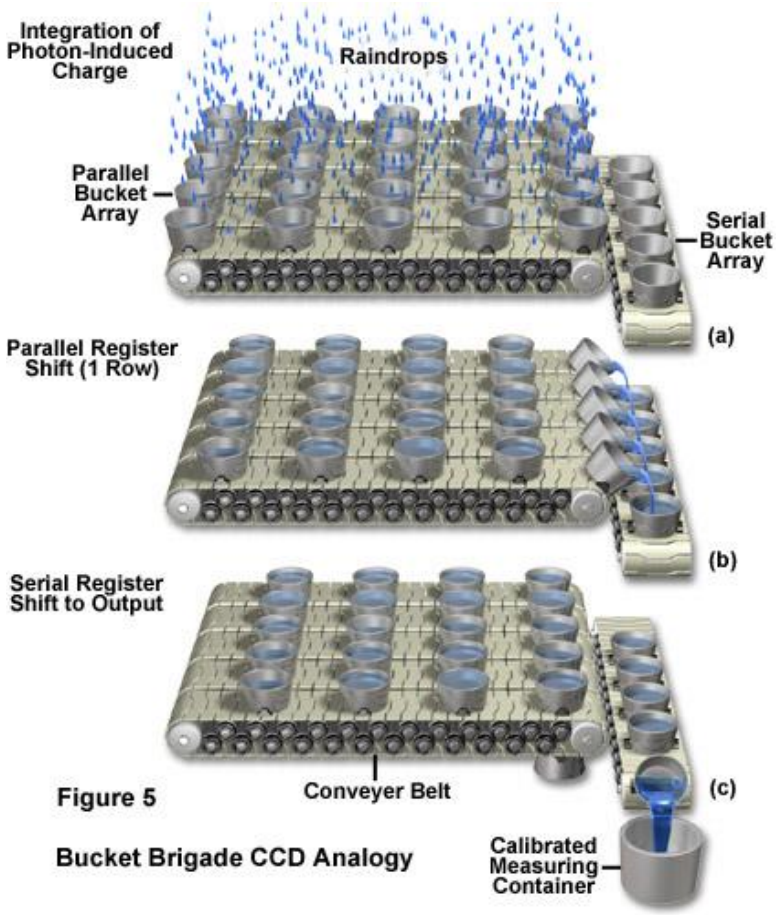

Fig. 28. The bucket brigade for rainfall measurement analogy aids in visualizing the concept of serial readout of a CCD [106].

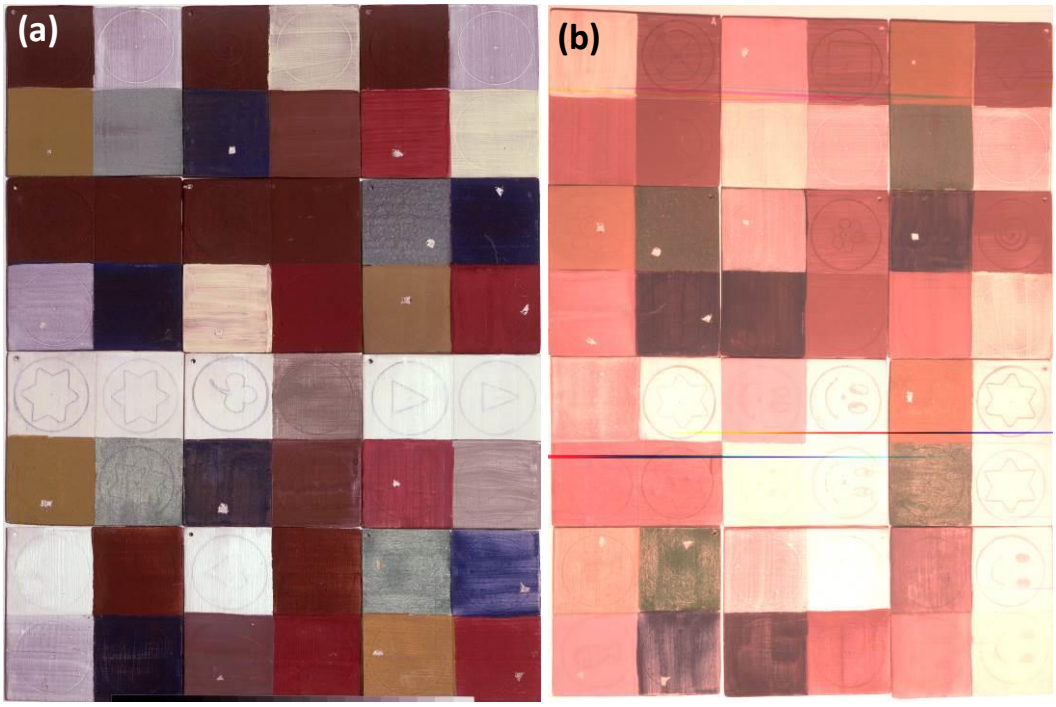

Fig. 29. Image capture by a Si-CCD camera with an IR cut-off filter (a) and without IR cut-off filter (b). The last image is redder than the normal one.

In the case of the CCD Power Phase camera, this technology works with scanning back. A digital scan back uses one array per RGB component. This translates to a triple sensor matrix layered vertically in a holder. The main advantage of using this technology to analyze artwork is the extremely high quality images obtained. This translates to a tremendously accurate color reproduction, as every pixel is measured individually for red, green and then blue, and allows to print in very large sizes without loss of detail. The downside of capturing images using a Power Phase camera is the amount of time needed to achieve a scan (from several seconds to minutes). A second inconvenience is the necessity to work connected to a computer due to the huge file sizes (hundreds of megabytes or even gigabytes) each scan produces.

During this study, the Power Phase camera used had a sensor size of 7000×7000 pixels with a resolution of about 36 megapixels, 12 bit. It consisted of a trilinear CCD camera which was able to register a wide spectrum from ultraviolet to near-infrared including visible light (from 300 to 1000 nm). Consequently, in order to obtain visible photography, specific cut-off filters had to be used which prevented IR and UV radiations from reaching the CCD and thus appearing in the captured image. In the case of IRR image captures (cf. Chapter 3.2), it is important to note that a UV cut-off filter but not an IR cut-off filter were used allowing IR radiation to reach the CCD. The image captured in this way was redder than a normal one (Fig. 29). Nevertheless, no visible cut-off filter was used during this study meaning that both visible spectrum radiations and near-infrared radiations are registered on the image. This imaging method will be referred as visible-IR imaging. Generally, in IRR, the images are represented using a grey scale established depending of the wavelength range measured by the detector. So, after capturing the image, the computing process consisted in a conversion of the visible-IR image in a grey scale to make it appears IRR image-like. Nevertheless, registering only the near-infrared radiations might be achieved using a visible cut-off filter to prevent the visible spectrum radiations from reaching the CCD.

1.4.2. InGaAs detector

InGaAs photodiodes were invented in 1977 by Pearsall [107]. Indium gallium arsenide (InGaAs) is a ternary alloy composed of indium, gallium and arsenic. It is used as a semiconductor with applications in electronics and optoelectronics which provide excellent photosensitivity in the IR. Among them, its principal application is as an infrared detector. The spectral response of an InGaAs photodiode is shown in Fig. 30. Infrared InGaAs detectors offer a specific spectral range which varies depending of the fraction of indium in the ternary compound.

The second important innovation was the engineering of InGaAs focal-plane arrays (FPAs) present in InGaAs cameras. An InGaAs FPA consists of a two-dimensional photodiode array (PDA) (itself comprising an indium phosphide (InP) substrate, an InGaAs absorption layer, and an ultrathin InP cap) that has been indium bump bonded to a readout integrated circuit (ROIC) (Fig. 31). As in a CCD, in an InGaAs FPA, the two-dimensional array detects incident light and then generates and collects charge. The ROIC clocks and converts the collected charge to voltage and then transfers the resulting signal to off-chip electronics.

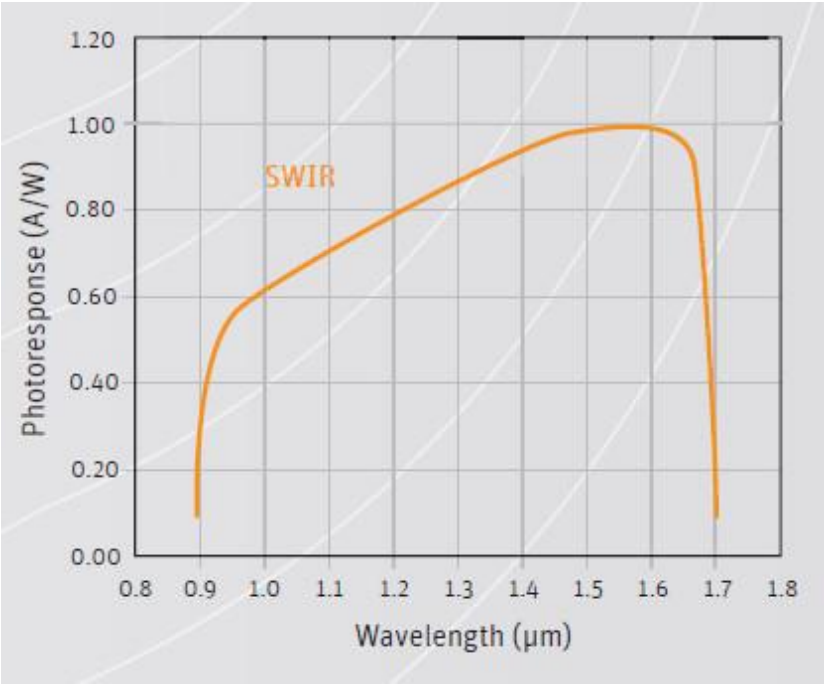

Fig. 30. The spectral response of an InGaAs photodiode [108].

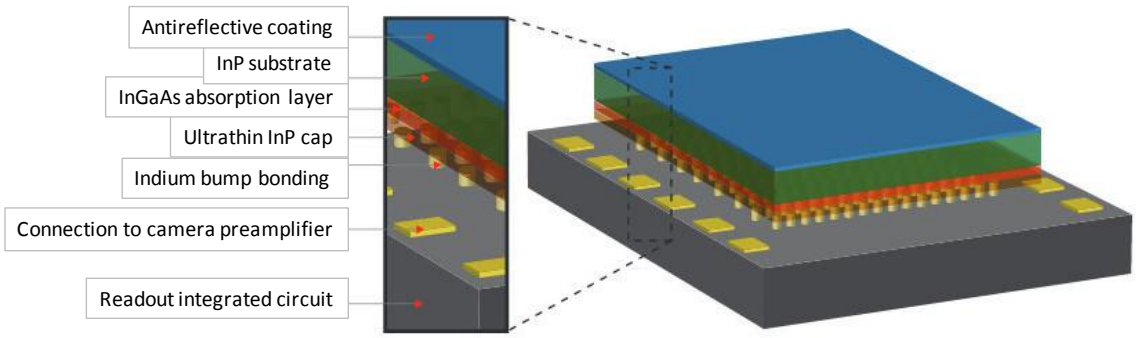

Fig. 31. An InGaAs FPA is a two-dimensional photodiode array (InP substrate, InGaAs absorption layer, ultrathin InP cap) indium bump bonded to a readout integrated circuit [109].

While Si-CCD cameras cannot offer sensitivity beyond 1100 nm (Fig. 32), InGaAs cameras provide sensitivity over short-wave infrared range due to its lower bandgap. Nevertheless, this bandgap is also responsible for much higher dark current (thermally generated signals) compared to those produced by Si-CCDs. As a result, scientific InGaAs FPA cameras require deep cooling (i.e. down to -90°C) in order to minimize this unwanted noise source.

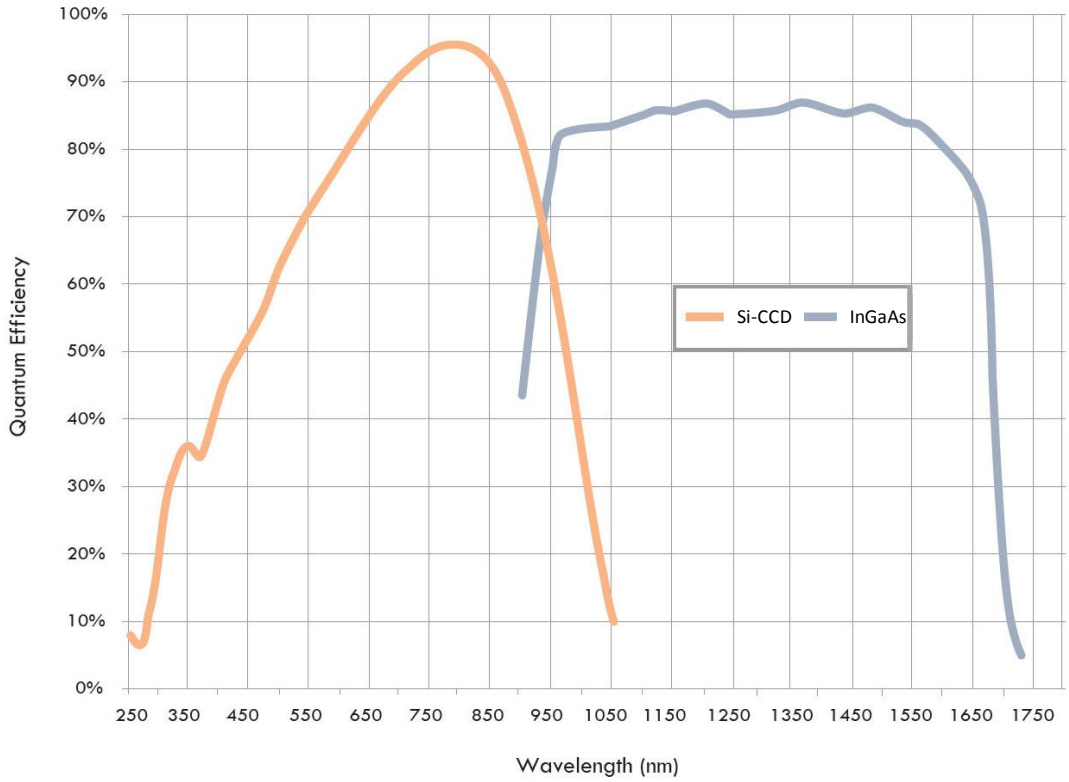

Fig. 32. InGaAs FPAs provide better QE above 900 nm than Si-CCD technology [109].

Due to a very complex manufacturing process, almost every InGaAs FPA has a small percentage of defective pixels classified as non-uniform, dark, and bright. A non-uniform pixel demonstrates greater or lesser photosensitive response than the surrounding pixels. Its response, though linear, differs from the average response demonstrated by the rest of the device's array. A dark pixel, meanwhile, is unresponsive to light and appears black in an image. Finally, a bright pixel is a pixel that saturates independently of incident light and appears as a white spot in an image (Fig. 33). While pixel defects are inevitable when dealing with InGaAs FPA devices, it is necessary to apply a defect-correction algorithm built into the camera's acquisition software or hardware.

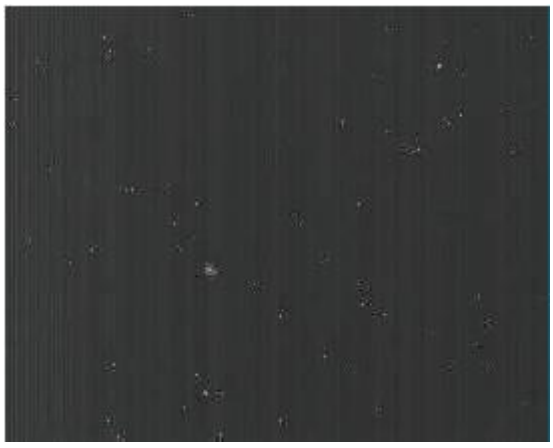

Fig. 33. The occurrence of bright pixels with the *Xeva-XS-512* model in Seville.

Finally, the reflectograms measured by InGaAs cameras are small images and the equipment must be placed near the painting in order to give good results. Depending on the size of the artwork in question, the result can be tens to thousands of images that must then be integrated into a single image. The complexity of obtaining complete IR images of large format easel paintings increases proportionally with the number of reflectograms needed. Precise control of lighting is also necessary to ensure an accurate capture of the painting under the same conditions throughout the reflectrographic study [110]. In this perspective, two different capture methods were used: a 2D motion device and a rotating motion device (cf. Chapter 2.4).

1.4.3. Infrared Vidicon detector

A Vidicon tube is a video camera tube design in which the target material is a photoconductor (Fig. 34). The Vidicon was developed in the 1950s at RCA by P. K. Weimer, S. V. Forgue and R. R. Goodrich.

The infrared Vidicon is composed of two main components [111].

Firstly, there is a photoconductive target - an electrode that stores a pattern of charges corresponding to the input image. It is the PbO-PbS pyroelectric photoconductive target that is sensitive to a broad range of wavelengths (400 to 2200 nm) (Fig. 35). While PbS is sensitive to infrared, PbO provides high sensitivity in the visible region. This precise combination of two substances gives the tube its spectral response characteristics. Usually, the IR-Vidicon is used for infrared only, with a visible cut-off filter.

Secondly, there is the electrode section made of an electron gun, an accelerating electrode, two focusing and deflecting electrodes and a field mesh (Fig. 34). The electron gun directs the thermionic electrons from the cathode into a tight beam, which is further narrowed by passage through a small aperture. The electron beam has the high current density needed to read the stored image efficiently. The various electrodes and coils accelerate the beam, focus and deflect it onto the target. The coils aim at changing the trajectory of the electron beam through the electron gun in order to scan the entire surface of the target. The optimum angle at which the beam should strike the target is 90º, so a collimation lens is provided between the focusing electrode and field mesh.

When scanned by the electron beam, the photoconductive target generates a signal current. The fluctuating voltage coupled with a video amplifier is used to record the input image. The electrical charge produced by an image will remain in the faceplate until it is scanned or until the charge dissipates.

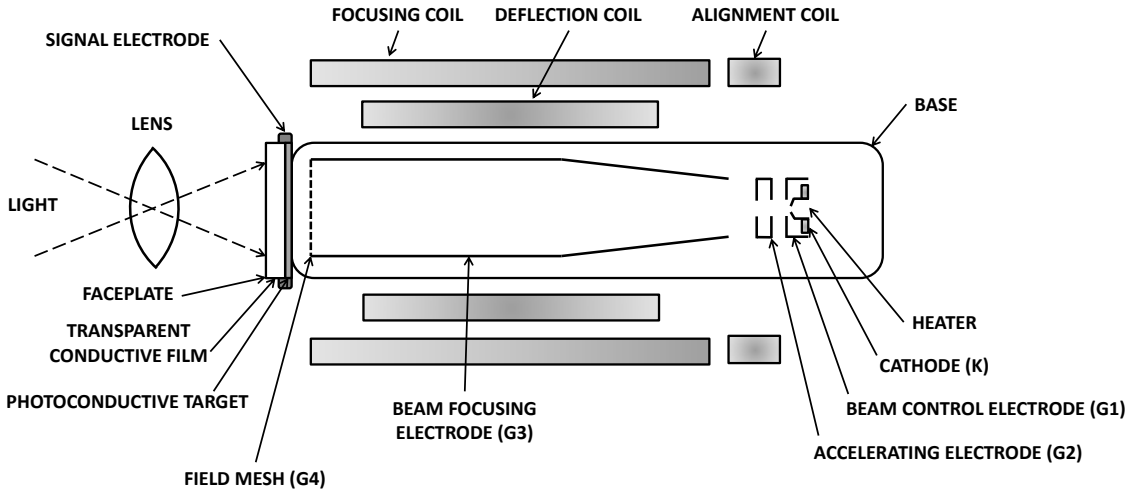

Fig. 34. Scheme of an infrared Vidicon detector.

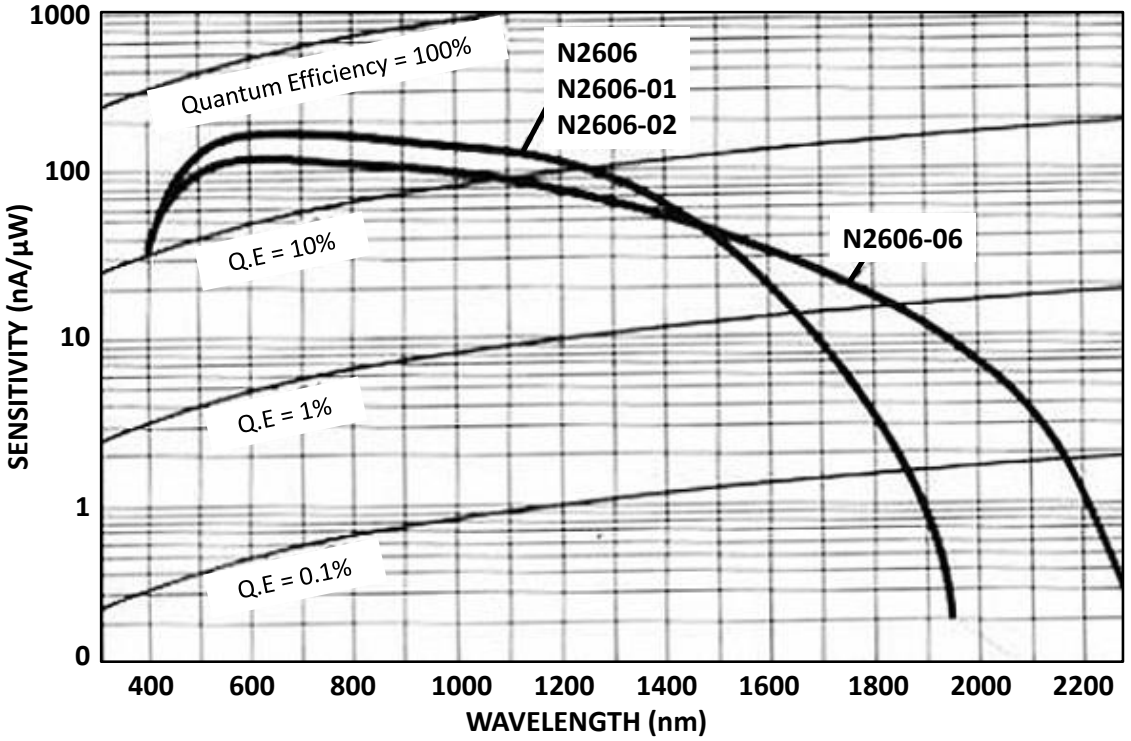

Fig. 35. Typical spectral response of infrared Vidicon detector model N2606-06 [111].

Chapter 2. Experimental setups

Part of the instrumentation used in the case of UV and IRR techniques has already been presented in Chapters 1.3 and 1.4. The rest of the equipment used and designed during this investigation is described below. First, the μXRF-CONCHA system will be described and characterized. Then, the characteristics of the three confocal micro X-ray fluorescence setups used for the intercomparison study of Chapter 3.3.3 will be reviewed. In continuation, the 2D motion device that makes possible the 1D, 2D and 3D studies by means of CXRF, IRR and XRF of large paintings at the Fine Arts Museum of Seville will be introduced. After that, two IRR image capturing methods and three different software programs used for the assembly of multiple IRR images will be presented. This chapter concludes with the description of the three different XRF devices used during the Alonso Vázquez project with special attention placed on the characterization of the new portable XRF system designed during this PhD thesis called X-Panda.

2.1. μXRF-CONCHA system, CXRF device for *in situ* analysis

2.1.1. Description of the set-up

The Micro X-Ray Fluorescence Confocal for Cultural Heritage Analysis (μXRF-CONCHA) system consists of a micro-focus X-ray source (IMOXS, Institute for Scientific Instruments (IfG)) [112, 113] (cf. Appendix I) and a silicon drift detector (super SDD, model X123SDD, Amptek) (Fig. 36). It is completed with two polycapillary X-ray lenses, a full lens at the exit of the X-ray source and a half lens at the entrance of the detector (both from IfG) (Fig. 37, 38 and Table 3) (cf. Appendix II).

Fig. 36. General view of the μXRF-CONCHA set-up analyzing "San Pedro Nolasco despidiéndose de Jaime I El Conquistador".

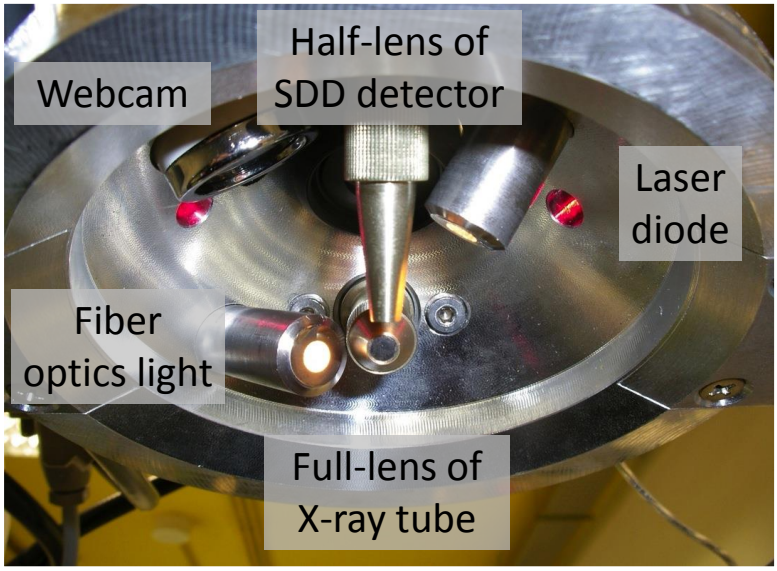

Fig. 37. Measuring head of the μXRF-CONCHA device.

Table 3. Characteristics of the μXRF-CONCHA set-up.

CXRF set-up		**μXRF-CONCHA - Seville**	
Excitation channel		**Detection channel**	
X-ray tube anode	W		
Manufacturer/model	IfG/iMOXS MFR	Manufacturer/model of detector	Amptek/Super 123SDD
Maximum power (W)	30	Si crystal thickness (μm)	500
Maximum voltage (kV)	50	Resolution at 5.9 keV (eV)	138
Maximum intensity (μA)	600	Detector active area (mm^2)	25
Polycapillary lens	Full lens	Polycapillary lens	Half-lens
Focus spot size (μm)	17-29	Focus spot size (μm)	19-36
Focal distance (mm)	7.3 ± 0.1	Focal distance (mm)	6.5 ± 0.1

The X-ray source (279×57×115 mm, approximately 3.5 kg) is composed by a low-power 30W side window X-ray tube with a tungsten anode cooled with air and working together with a control unit (165×280×420 mm, approximately 8 kg) (cf. Appendix I). It can be operated at a maximum voltage and current of 50 kV and 600 μA respectively and provides a 50×50 $μm^2$ beam spot at the entrance of the full lens, which is directly fastened to the exit of the X-ray source. The beam is focused with a polycapillary X-ray full lens. The lens has a nominal working distance of 7.3 ± 0.1 mm and a nominal focal spot diameter of 28 μm FWHM at W-Lα energy (8.40 keV). Finally, the tube includes a built-in shutter for switching on and off the X-ray output.

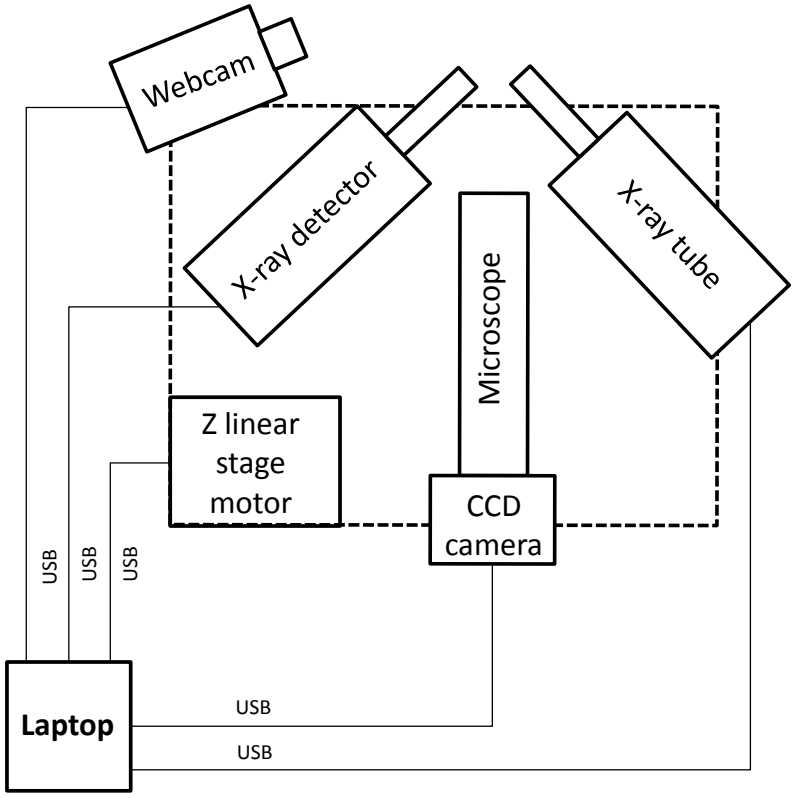

Fig. 38. Scheme of the μXRF-CONCHA device.

The active area of the SDD Si crystal is 25 mm^2 with an active thickness of 500 μm. It is sealed with a 12.7 μm Be window. The resolution of the detector measured is 138 eV for the Mn-Kα line (FWHM of the peak at 5.9 keV) (cf. Appendix III). The detector includes an integrated pre-amplifier, a pulse processor and an internal power supply. More details on the characteristics of the X-123SDD model detector are provided in Appendix IV.

The head of the SDD is interlocked with the half lens through a metallic piece allowing XY movement respect to the conical support (Fig. 36). The positions of both half lens and SDD can be optimized in order to obtain the highest depth resolution (cf. Chapter 1.2.6). The half lens has a nominal working distance of 6.5 ± 0.1 mm and a nominal focal spot diameter of 33 μm FWHM at W-Lα energy.

The X-ray source and the X-ray detector are positioned at 45° with respect to the surface of the analyzed sample. The working distance from the set-up to the sample is indicated by means of two laser diode modules (Micro LDM Laser Diode Modules model, Edmund Optics) with a beam size below 50 μm at the optimum focusing position). A CMOS color camera (model EO-0413C, with 752×480 pixels) coupled to a zoom imaging lens (model VZM 1000i, with a primary magnification from 2.5x to 10x), both from Edmund Optics, are placed in front of the sample. They allow to observe the sample surface and to detect when the laser diodes are focused. Finally, a webcam (model LifeCam Cinema, Microsoft) permits a general view of the sample and safety control during the study (Fig. 36).

All these components (X-ray tube, detector-half lens, microscope, laser diode modules and webcam) are fastened to a conical support made by IfG. The conical support have been adapted by Jose Luis Benjumea Acevedo at the workshop of the Physics Faculty of Seville in order to be fastened to a 210 mm range linear stage motor from OWIS (model

LIMES 80-200-HSM) which has a load capacity of 150 N (roughly 15 kg) with a positioning error inferior to the micrometer (Fig. 36).

The set-up was designed to be able to perform elemental mapping by moving the measuring head (X-ray tube and detector) versus the sample. This system is complete with the addition of a specific 2D motion device which will be presented later (cf. Chapter 2.3). At present, none CXRF set-up working in this configuration are commercially available.

The X-ray tube, SDD, microscope, webcam and motion motor are connected to a computer via USB (Fig. 38). Different in-house developed LabVIEW programs control the detector and the motion motor. National Instruments LabVIEW system design software and development environment for graphical programing language allows data acquisition, automation and measurement control [59, 114-116]. These programs, developed in order to automatize some routine tasks, are called according to their purpose:

- "1_Working_distance_Adjustment" is used to find the working distance of the X-ray tube-full lens system;
- "2_Depth_profile_Acquisition" allows obtaining a depth profile.

The objectives and operation of each routine will be fully described later on (cf. Chapter 2.1.2).

2.1.2. Set-up characterization and tune-up

It is really important, but difficult, to properly tune up a CXRF set-up. In this thesis, a strategy was proposed and applied to optimize the system. The complexity of the adjustment lies in the positioning the two polycapillary X-ray lenses in the optimal position with micrometric precision. For all the following experiments, the X-ray voltage and current were 50 kV and 600 µA, respectively.

First, it is necessary to center the full lens in front of the exit of the X-ray source to provide the optimum beam intensity at the exit of the full lens. Consequently, the full lens is adjusted in front of the X-ray source exit (Fig. 39) by maximizing the count rate obtained from a thick bronze standard. This manipulation has to be done out of the CXRF support to allow the access to the different Allen screws. After this adjustment, the X-ray source together with the full lens has to be carefully mounted on the CXRF support (Fig. 40).

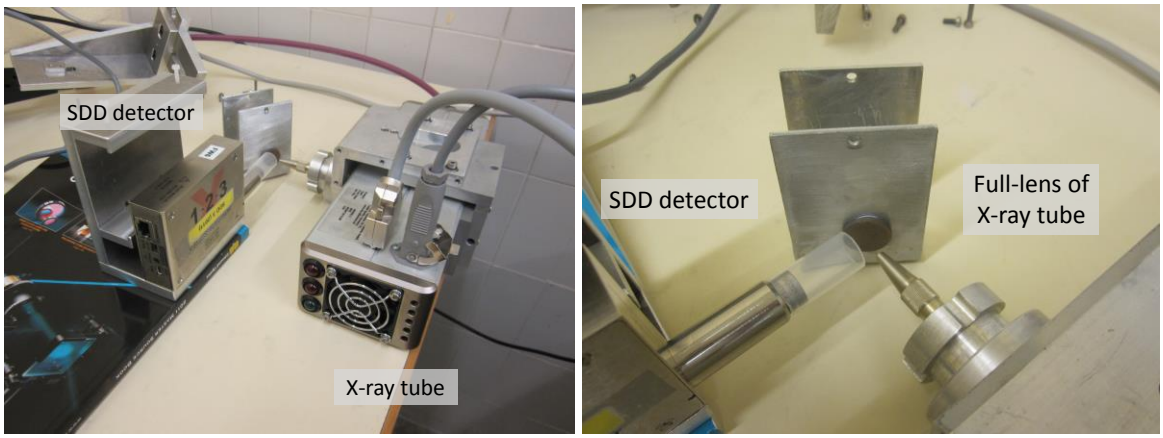

Fig. 39. Two views of the device configuration used to adjust the full-lens in front of the X-ray tube.

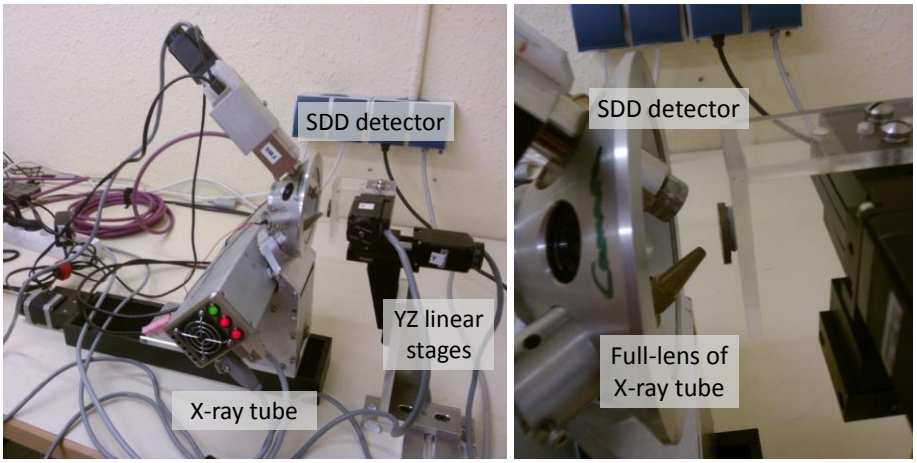

Fig. 40. CXRF device mounted without the half lens in front of the detector.

Then, the position of the X-ray beam focus has to be determined. The orientation of the two laser diodes has to be adjusted to pinpoint the working distance of the X-ray tube on the analyzed surface. To find the optimal working distance, the SDD is used without the half lens (Fig. 40). In front of the head set-up, a motorized support with two 10 mm range linear stages (resolution of 0,156 µm) from Standa (model 8MT173-10-240mA) (Fig. 40). It scans horizontally over an iron blade. A series of lateral profiles modifying the distance (Z) between the blade and the head of the CXRF set-up are performed searching the smaller FWHM from the Fe Kα lateral profile which corresponds to the optimal focal distance to the full lens.

To perform this experiment, the "1_Working_distance_Adjustment" LabVIEW routine is used (Fig. 41). It controls the lateral Standa motion and saves each spectrum of the lateral profiles. The user has to choose, for each lateral scan, the name of the folder to save the spectrum files, the number of analyzed points, the distance between each pitch, and the measurement time. The program starts recording the spectrum at the initial position. Then, it performs a loop including two steps, changing the position and then recording the spectrum. All the developed LabVIEW routines automatically record the name of the spectrum incremented using the date and the spectrum number. It is important to note that Amptek SDD is controlled with a previous firmware (FW5) for compatibility reasons with LabVIEW at that time.

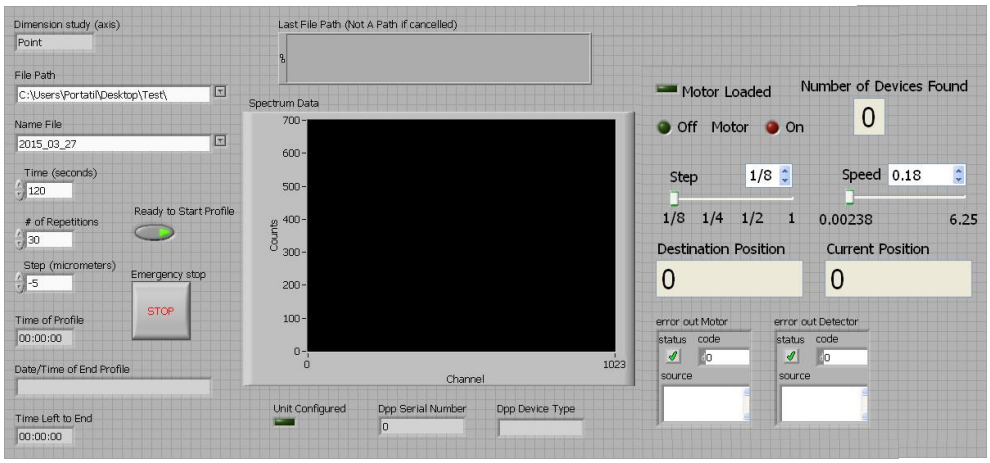

Fig. 41. Front panel of "1_Working_distance_Adjustment" LabVIEW routine.

In total, five lateral scans were performed. Each scan was composed of 30 spectra taken with 10 μm step size and a counting time of 5 s per point. The evolution of the lateral diameter size of the beam versus Z distance is presented in Fig. 42. The smallest FWHM measured were 49 ± 5 μm.

The lateral beam profile in the focal spot position is presented in Fig. 43 as well as its derivative.

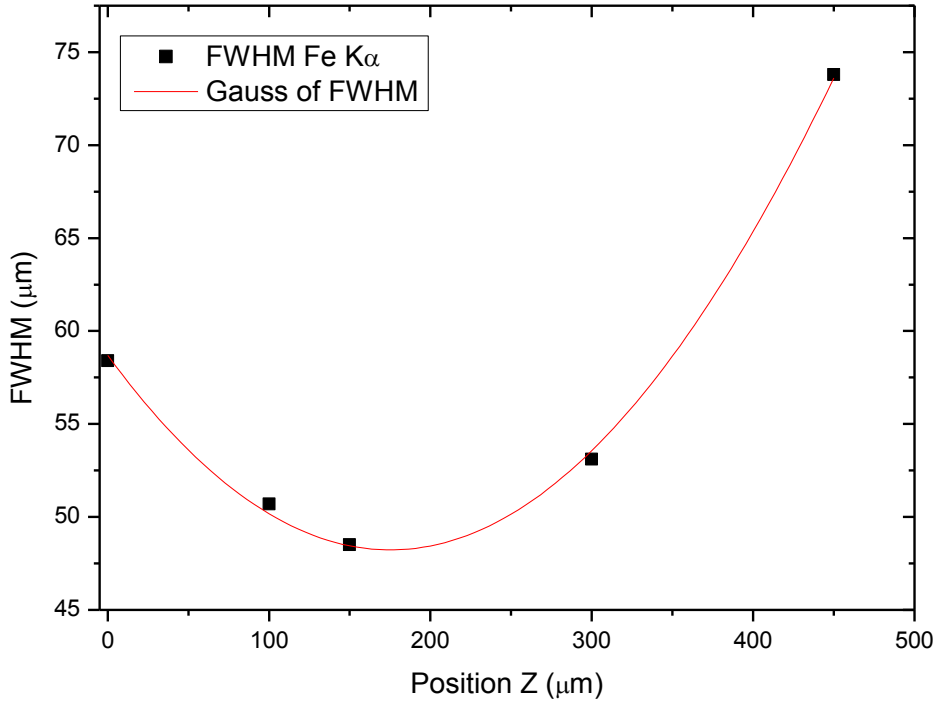

Fig. 42. Evolution of the lateral diameter size of the beam versus Z distance.

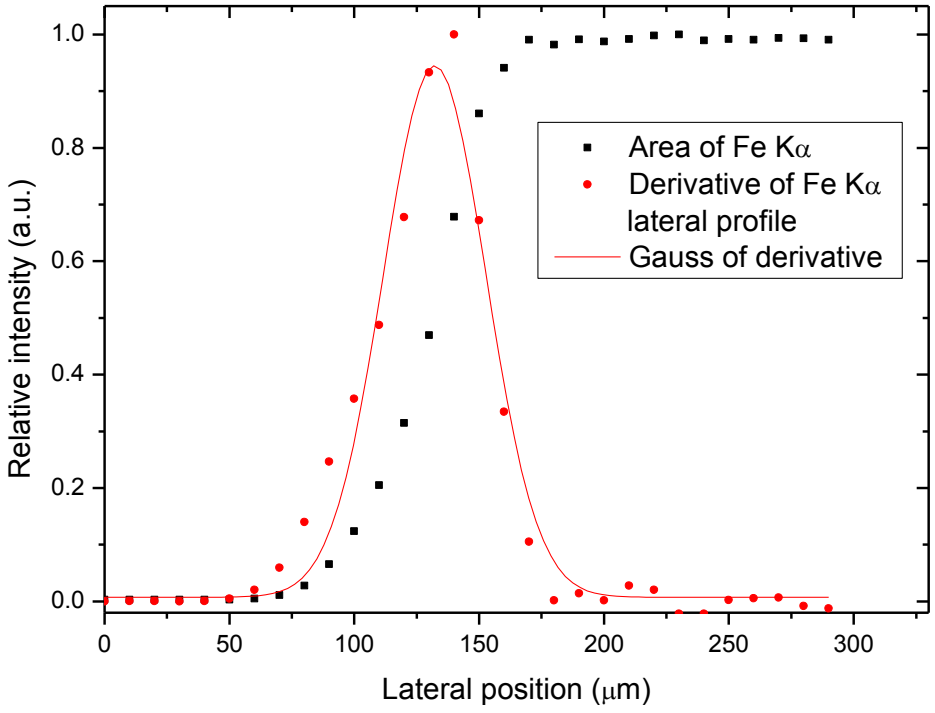

Fig. 43. Lateral beam profile in the focal spot position and derivative of the profile.

Once the focal distance is found, the position is pinpointed with the two laser diodes. Then, the impact point of the X-ray beam is visualized using a scintillator in a dark room environment before pinpointing the laser diodes to the exact location. Thereafter, the CMOS camera coupled to its zoom imaging lens is adjusted according to its working distance (35 mm ± 1 mm) using the bronze standard for observation.

Then, the half lens is fastened to the SDD (Fig. 37) and the optimal position of the half lens had to be found in order to finish the installation of the CXRF set-up. To align the confocal geometry, a series of measures positioning the bronze standard in the focus of the primary X-ray beam were done modifying the position of the detector-half lens looking at the maximum count rate. At the maximum count rate corresponds the optimal position of the optics, and thus the smaller depth resolution.

Once the confocal geometry is established, the characterization of the CXRF set-up is achieved. Then, the lateral resolution of the confocal volume has to be determined using the same "1_Working_distance_Adjustment" LabVIEW routine. It scans horizontally over a copper grid (model T200-CU, from Electron Microscopy Sciences). It is a grid with 125 µm pitch, 113 µm hole and 12 µm bar (Fig. 44). A lateral profile is performed measuring the FWHM from the Cu Kα at the focal distance (Fig. 45). The scan was composed by 79 spectra taken with 5 µm step size and a counting time of 120 s per point. The results in Table 4 show a lateral resolution about approximately 34 ± 3 µm.

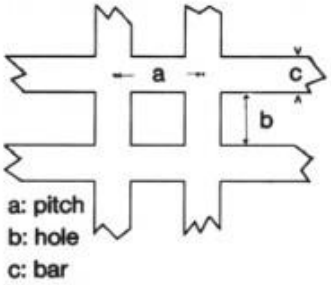

Fig. 44. Scheme of a copper grid.

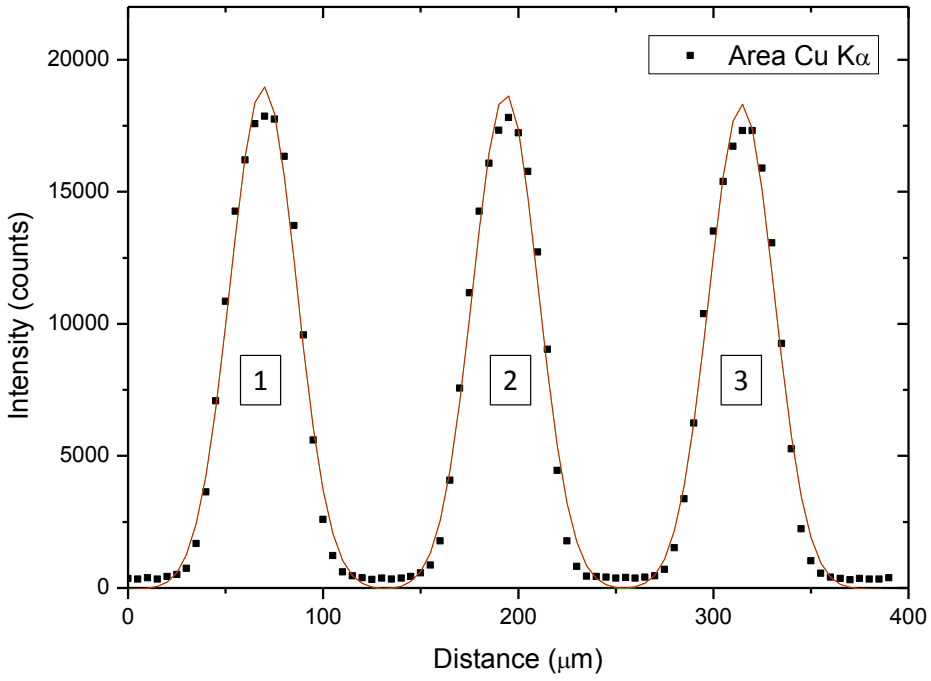

Fig. 45. Lateral profile of a copper grid in the focal spot position.

Table 4. Results of lateral profile of a copper grid in the focal spot position.

Bar	FWHM (μm)	Xc (μm)	Distance between bars (μm)
1	34 ± 3	69 ± 3	124 ± 3
2	34 ± 3	193 ± 3	122 ± 3
3	34 ± 3	315 ± 3	

Consequently, depth profile of a series of thin foils (1 μm thick) of different chemical elements (Ti, Cr, Fe, Ni, Cu, Zn, Zr, Ag, Au and Pb) (from Goodfellow) is measured to define the depth resolution of the CXRF set-up (Fig. 46). From now on, the depth profile of the 1 μm Cu thin foil will be used as a reference so as to verify the calibration of the set-up every time.

To achieve this experiment, "2_Depth_profile_Acquisition" LabVIEW routine is used (Fig. 47). It performs spectra acquisition of the depth profile controlling the OWIS motion. The program input consists of the name of the folder to save the spectrum files, the number of analyzed points, the pitch distance and the measurement time. It starts recording the spectrum at the initial position so that it performs a loop including two steps, changing the Z position and then recording the spectrum. The difference with "1_Working_distance_Adjustment" routine resides in the control of OWIS motor instead of Standa motor.

Each scan was composed by 30 spectra taken with 10 μm step size and a counting time of 120 s per point. The evolution of the depth resolution versus secondary fluorescence energy is presented in Fig. 46 (repetition of Fig. 18).

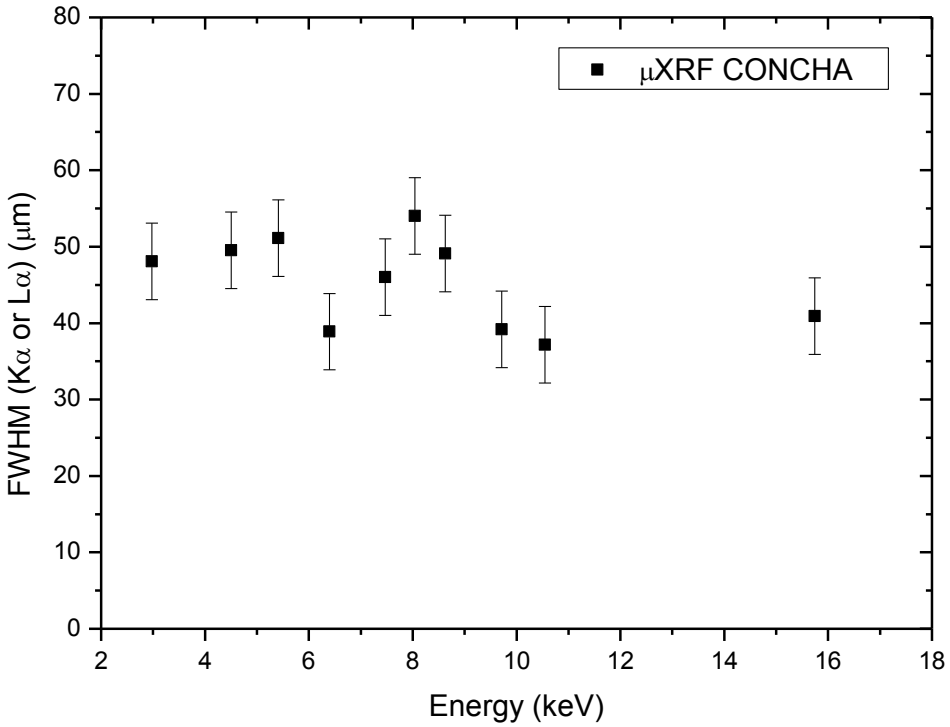

Fig. 46. Depth resolution of the μXRF-Concha set-up as a function of the emitted energy (repetition of Fig. 18).

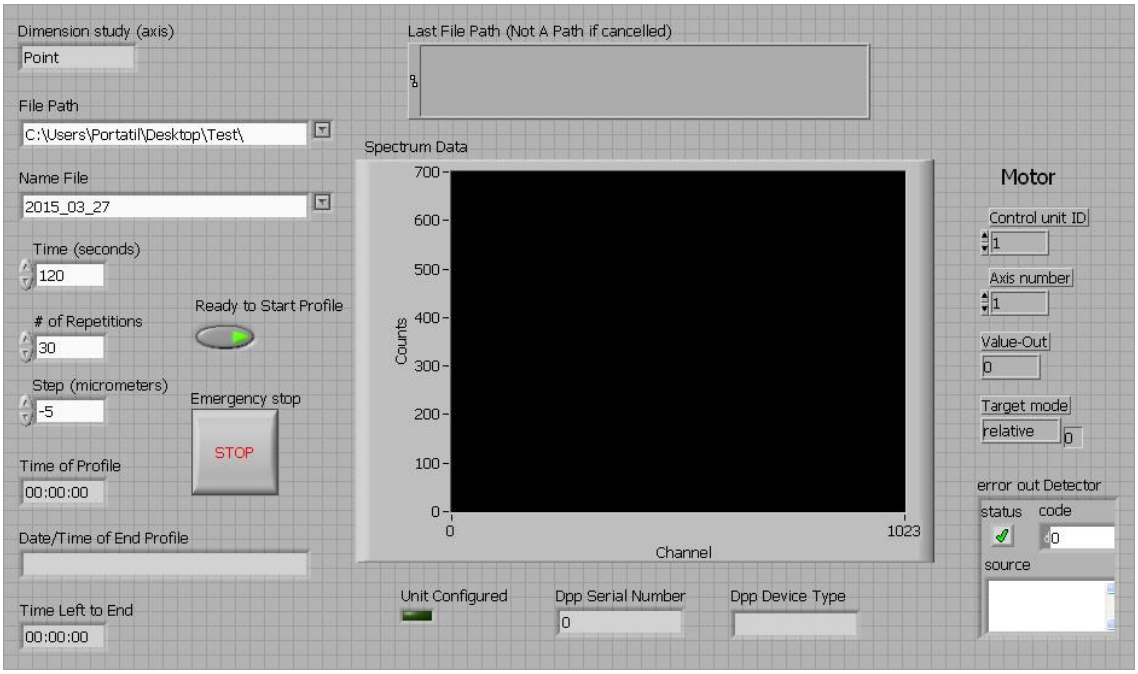

Fig. 47. Front panel of "2_Depth_profile_Acquisition" LabVIEW routine.

Besides, using the same "2_Depth_profile_Acquisition" LabVIEW routine, a series of Cu thin foils (from Goodfellow) of different thicknesses (1, 5, 10, 15, 20, 25, 30, 34, 40, 45, 50, 75 and 100 µm) were analyzed to determine the capability of the CXRF technique in measuring the thickness of copper foils and also to illustrate the absorption effect (cf. Chapter 1.2.7).

Each scan was composed by 30 spectra taken with 10 µm step size and a counting time of 120 s per point. The evolution of the height of the Gaussian curve versus thickness of foils is presented in Fig. 48.

The results show that it may be possible to determine the thickness of a copper single layer thinner than 20 µm. Beyond 20 µm, the self-absorption effect in a copper foil prevents the secondary X-ray fluorescence from escaping the sample and reaching the detector. The total counts registered by the detector reach a limit value that remains constant for all copper foils thicker than 20 µm. Consequently, the information about thickness is lost. This phenomenon can be modeled in the case of this kind of simple sample and the equation giving the relation between Gaussian height and thickness can be achieved easily. Nevertheless, for more complex unknown samples, such as cultural heritage samples, thickness estimation is a challenge.

In this way, simulations have been performed by Pawel Wrobel, in a collaboration study, on two experimental paint multilayers made during this PhD thesis (about experimental samples, see Chapter 3.1) [117]. The results show that, in order to simulate the thickness of each layer, density and composition must be known. So, the ability to measure the thickness of a multilayered sample based only on CXRF results without any previous knowledge of the density and composition of each layer remains impossible.

Another focus can be proposed on the measurement of thickness layers. Nondestructive techniques such as conventional transmission computer micro-tomography (µ-CT) [118], micro-beam X-ray fluorescence computed tomography (µ-XRFCT) [119] or *in situ* nuclear magnetic resonance (NMR) [120-122] can be considered in order to offer complementary information to CXRF study.

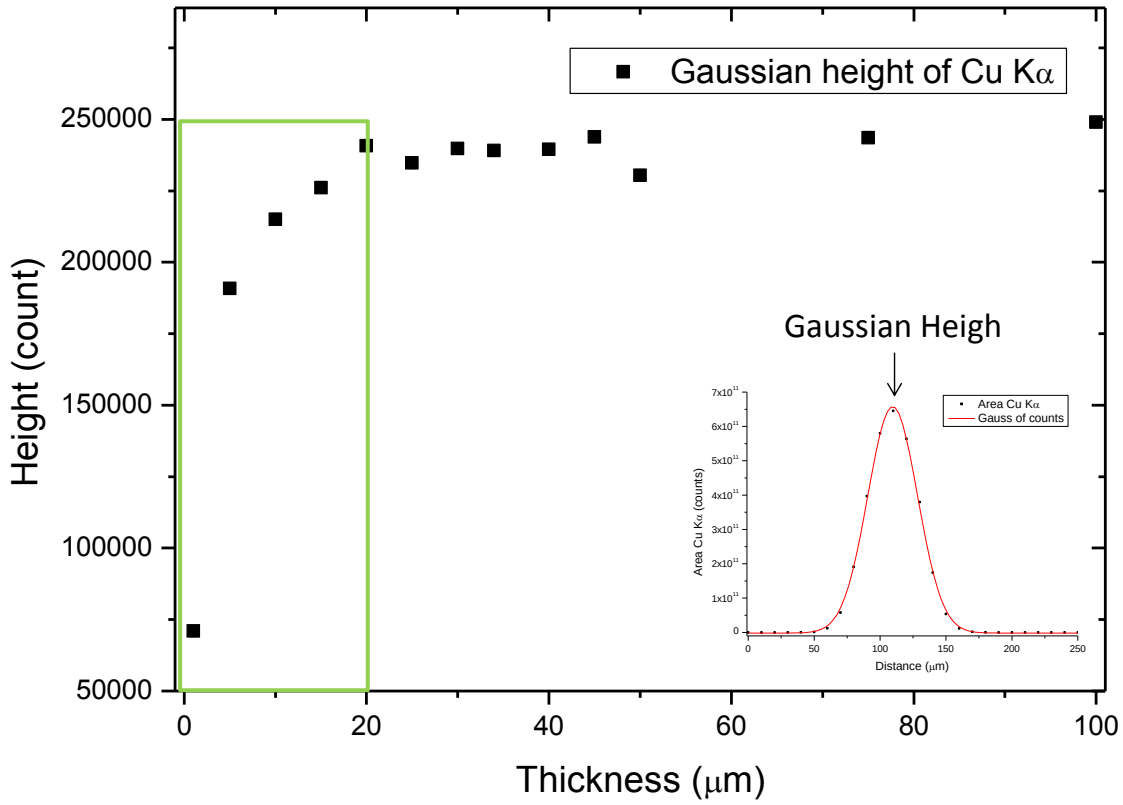

Fig. 48. Evolution of the height of the Gaussian curve versus the thickness of Cu foils (error included in the points).

2.1.3. Data treatment

Each depth profile produces a several tens of spectra that have to be analyzed. All CXRF data were processed with the free software PyMca. It was developed by the "Software Group of the European Synchrotron Radiation Facility (ESRF)" and distributed under GNU General Public License [123]. The PyMca Toolkit is a collection of tools for visualization and analysis of energy-dispersive X-ray fluorescence data. The version used here was "PyMca Application Version 4.4.1". This software proposes a lot of advantages. It allows automatic analysis of a group of spectra and permits a visualization of the sum of spectra which allows for better and faster recognition of all the chemical elements presents. Each tool, like the data analysis routines, can be used independently. Nonetheless, its manipulation is uneasy therefore the methodology used to make the complete treatment of the data is explained in Appendix V. This appendix presents the use of PyMca software and its sub-programs to analyze depth or lateral profiles scans (1D) respectively obtained with all CXRF setups used during this investigation.

2.2. LouX^{3D} system and CXRF set-up at AGH University of Science and Technology

Intercomparison of three confocal micro X-ray fluorescence systems will be made in Chapter 3.3.3 for the non-destructive characterization of experimental paint layers. In this

third chapter the results obtained using three CXRF systems are presented: the LouX3D at the C2RMF laboratory in Paris [11], the CXRF set-up at AGH University of Science and Technology in Krakow [59] and, the µXRF-CONCHA previously presented. The CXRF set-up at AGH University of Science and Technology in Krakow was designed and characterized by Pawel Wrobel in his PhD thesis. The LouX3D set-up was designed and firstly characterized by Ina Reiche and Katarina Müller. As part of the intercomparison study, the LouX^{3D} was newly characterized using the same thin foil standards and the same methodology applied to the µXRF-CONCHA system in Seville (cf. Chapter 2.1.2). Hereafter, the main features of this device and the results obtained are presented.

The LouX^{3D} system consists of a micro-focus X-ray source (IMOXS, IfG) [112, 113] and a SDD Rontec X Flash (series 4, model 4010, Bruker AXS) (Fig. 49, 50 and Table 5). It is complete with a full lens at the exit of the X-ray source and a Poly-CCC lens at the entrance of the detector (both from IfG) (see specifics in Appendix VI).

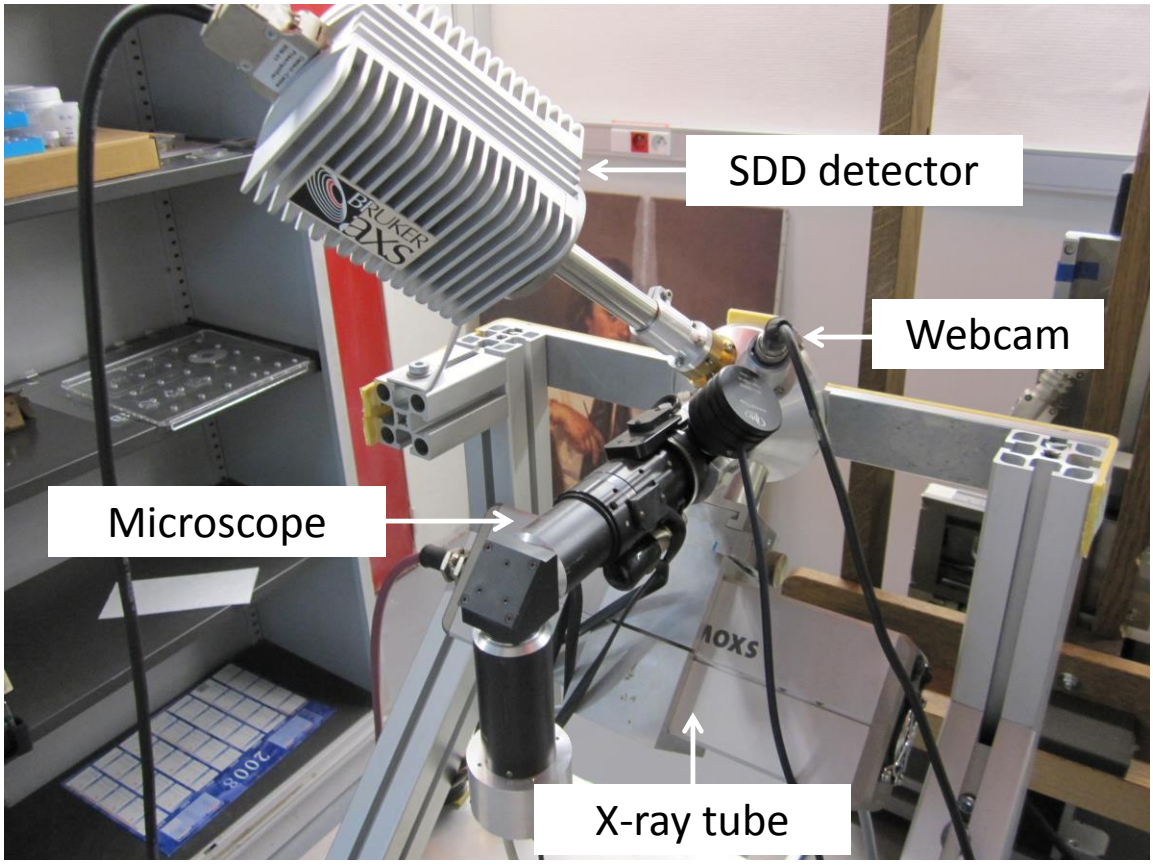

Fig. 49. General view of the LouX3D set-up.

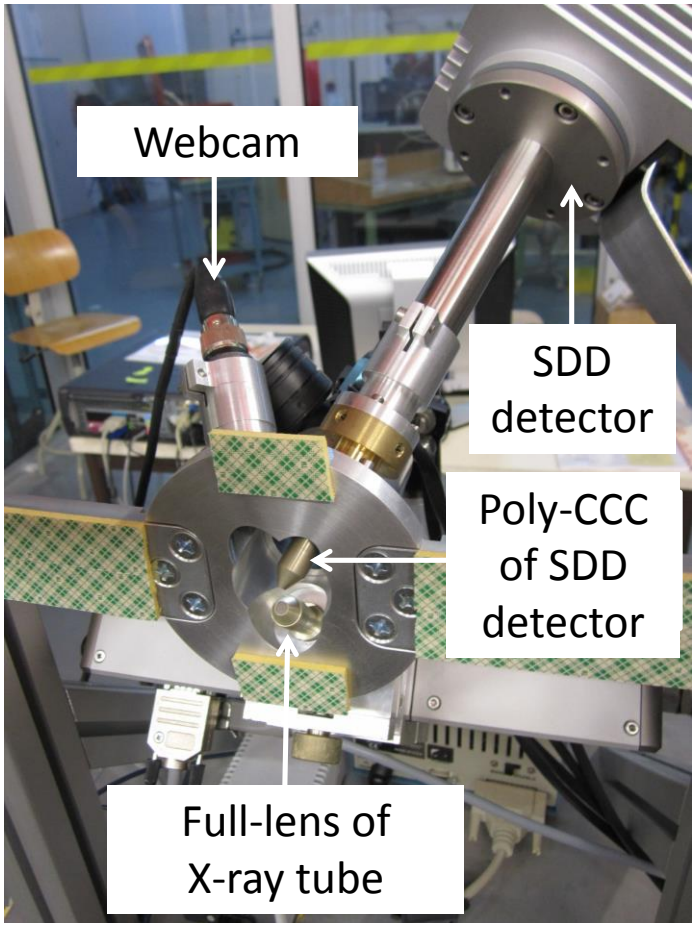

Fig. 50. Head analysis of the LouX3D device.

Table 5. Characteristics of the LouX3D device.

CXRF set-up		**LouX^{3D} - Paris**	
Excitation channel		**Detection channel**	
X-ray tube anode	Rh		
Manufacturer/model	IfG/iMOXS MFR	Manufacturer/ model of detector	Bruker AXS/ SDD Rontec X Flash
Maximum power (W)	30		
Maximum voltage (kV)	50	Si crystal thickness (µm)	450
Maximum intensity (µA)	600	Detector active area (mm^2)	10
Polycapillary lens	Full lens	Polycapillary lens	Poly-CCC
Focus spot size (µm)	29-45	Focus spot size (µm)	40 (Cr Kα and Fe Kα)
Focal distance (mm)	11 ± 0.1	Focal distance (mm)	6.2

The X-ray source is similar to the one used with the µXRF-CONCHA. The only difference is that the X-ray tube works with a rhodium anode. It can be operated with maximum voltage and current of 50 kV and 600 µA respectively and provides a 50 μm^2 beam spot at the entrance of the full lens which is directly fastened to the exit of the X-ray source. This beam is focused with the polycapillary X-ray full lens. The lens has a nominal working distance of 11 ± 0.1 mm and a nominal focal spot diameter of 29 µm FWHM at Rh-Kα energy (20.17 keV). Finally, the tube disposed of an integrated shutter module for switching on and off the X-ray output.

The active area of the SDD Si crystal is 10 mm^2 for an active thickness of 450 µm. The head of the SDD is interlocked to the Poly-CCC which has a nominal working distance of 6.2 mm and a nominal focal spot diameter of 40 µm FWHM at Fe-Kα energy (6.40 keV).

The X-ray source and the X-ray detector are positioned at 45° with respect to the surface normal of the analyzed sample. A microscope (with a primary magnification from 2.5x to 10x) from Opto is placed in front of the sample allowing the observation of its surface. Finally, a webcam permits preview visualization of the sample and safety control during the study.

All these components (X-ray tube, detector, microscope and webcam) are fastened to a motionless tabletop support made by IfG. In this device, the sample support in front of the CXRF head set-up is motorized, allowing the movement in the XYZ directions. The sample support is moved by three 100 mm mid-travel steel linear stage motors from Newport (from Newport Micro-Controle Klinger, model UTS100). These motors have a 200 N maximum horizontal load capacity (approximately 20 kg) and a 50 N maximum vertical load capacity (approximately 5 kg) for a uni-directional repeatability of 1 µm. These are the limitations, which have to be considered when studying artwork.

X-ray tube, detector, microscope and the three motion motors are connected to a computer via USB. The device is controlled by a software called "Louvre0" developed by IfG [112]. The software version used is dated October 19, 2007. It allows single measurements, 1D, 2D and 3D analysis. The use of the "Louvre0" acquisition software is detailed in Appendix VII.

The characterization of the LouX^{3D} set-up was achieved by measuring the same series of thin foils (1 µm thick) of different chemical elements (Ti, Cr, Fe, Ni, Cu, Zn, Zr, Ag, Au and Pb) with the same condition as with the µXRF-CONCHA to define the depth resolution of the device (Fig. 51). Consequently, each scan was composed by 30 spectra taken with 10 µm step size and a counting time of 120 s per point.

In the case of the data from the CXRF set-up at the AGH University of Science and Technology, the depth resolution was measured by Pawel Wrobel [13]. The characterization was obtained by measuring a different series of thin foils of different chemical elements (Table 6). Each scan was obtained with 50 kV, 1 mA and it is composed by spectra taken with 2.5 µm step size.

The evolution of the depth resolution versus secondary fluorescence energy of the three CXRF setups is presented in Fig. 51.

As mentioned before, all the CXRF data were processed with the PyMCA software. The methodology is slightly different to that used with the µXRF-CONCHA device and it will be explained with more detail in Appendix V.

Table 6. Series of thin foils used to measure the depth resolution in the case of the AGH CXRF device.

Chemical element	Thickness (μm)	Counting time (s)
Ti	6	1
Mn	15	1
Fe	5	1
Co	8	1
Ni	7.5	1
Cu	7	1
Zn	~0.025	1
Zr	66	2.5
Sn	250	3
Pb	120	3
Au	~0.025	30

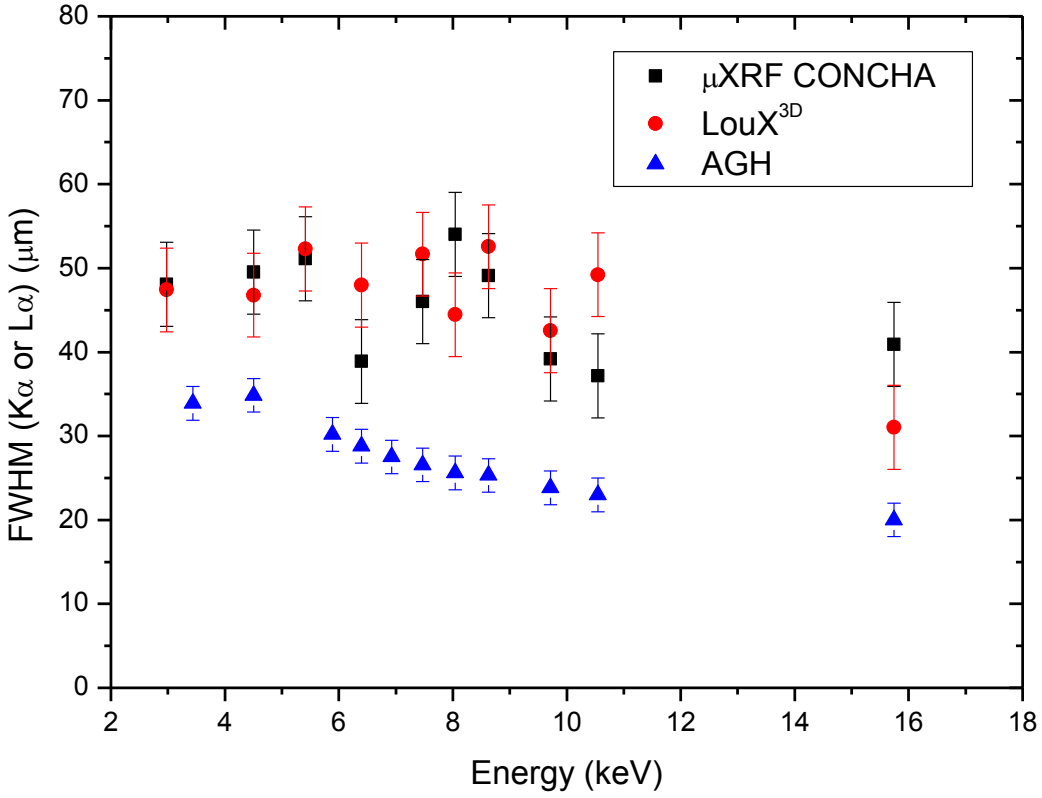

Fig. 51. Depth resolution of the three CXRF setups as a function of the emitted energy.

Finally, Table 7 summarizes the specifications of each CXRF set-up with respect to the intercomparison of the three devices presented later in Chapter 3.3.3.

Table 7. Characteristics of the three CXRF setups.

CXRF set-up	μXRF-CONCHA - Seville	LouX^{3D} - Paris	AGH - Krakow
Excitation channel			
X-ray tube anode	W	Rh	Mo
Manufacturer/model	IfG/iMOXS MFR	IfG/iMOXS MFR	XOS/Powerflux PF X-Beam
Maximum power (W)	30	30	50
Maximum voltage (kV)	50	50	50
Maximum intensity (μA)	600	600	1000
Polycapillary lens	Full lens	Full lens	Full lens
Focus spot size (μm)	17-29	29-45	13 (Mo Kα)
Focal distance (mm)	7.3 ± 0.1	11 ± 0.1	4.4 ± 0.3
Detection channel			
Manufacturer/model of detector	Amptek/Super 123SDD	Bruker AXS/SDD Rontec X Flash	Ketek/VITUS-SDD (AXAS-V)
Si crystal thickness (μm)	500	450	450
Resolution at 5.9 keV (eV)	138	NC	139
Active area (mm^2)	25	10	10
Polycapillary lens	Half-lens	Poly-CCC	Poly-CCC
Focus spot size (μm)	19-36	40 (Cr Kα and Fe Kα)	28 (Fe Kα)
Focal distance (mm)	6.5 ± 0.1	6.2	4.4 ± 0.3

2.3. 2D motion device at the Fine Arts Museum of Seville

The characteristics of the 2D motion device used at the Fine Arts Museum of Seville are as follows. This device can operate several different scientific setups like μXRF-CONCHA in a vertical plane parallel to the artworks surface. It allows for reaching a point of analysis anywhere in the painting and makes 1D, 2D and 3D study possible for CXRF, IRR and XRF techniques. In the case of the μXRF-CONCHA, the device is set up with the OWIS Z motion motor fastened to the head support (Fig. 52). Also, it allows the installation of the IRR camera and the installation of the XRF system called X-Panda (presented in Chapter 2.5.1). Initially made by Optimind, the device has been highly modified during this investigation. This customization has been made in collaboration with Jose Luis Benjumea Acevedo from the workshop of the Faculty of Physics and Fernando Castaño Castaño from the School of Engineering, both from the University of Seville.

Fig. 52. The 2D motion device with the μXRF-CONCHA set-up together with the OWIS Z motion.

Several structural modifications have been made:

- Improvement of the safety and stability of the system adding wheels.
- Modification of the counterweight compartment allowing the adjustment of the counterweight with respect to used scientific set-up weight.
- Connectivity between the head of the 2D motion device and the different scientific setups (XRF, CXRF, IRR).
- Ability to modify the elevation of the head analysis so that the study of the part of an artwork located very near to the ground and up to five meters high can be made if necessary (Fig. 53).

Fig. 53. Ability of the 2D motion device to modify the elevation of the head analysis.

The horizontal (X) and vertical (Y) movements are produced by two motors (model M07184-STD and model AF63-/4B-7 13./T11 from TMT) controlled by a variable frequency drive (VFD004L21D from Delta). The limit switches in the four directions are detected by four detectors placed at the end of each run (model PS31W-CS11R1-T00 from Carlo Gavazzi). The positions X and Y are measured independently with potentiometric sensors).

Some improvements have been achieved:

- Modification of the movement detection system to enhance the precision of horizontal/vertical movements so that they can be controlled separately.
- New electronics allowing the motion to be controlled by computer.
- New hardware and software for the analytical techniques.

In-house LabVIEW sub-program called "2D_Motion_Control" was developed by Fernando Castaño Castaño (Fig. 54). The sub-program allows communication with the 2D motion device and the use and control of the position (X,Y) of the head device by the user. It permits movement of different setups at a regular distance in the plane (XY) and allows achieving:

- lateral profile, 2D or 3D analysis with µXRF-CONCHA,
- matrix of IRR images with InGaAs camera,
- lateral profile or also 2D mapping analysis with X-Panda device.

In order to reach the point analysis or some particular position, the user can move the device using both the LabVIEW routine or a joystick.

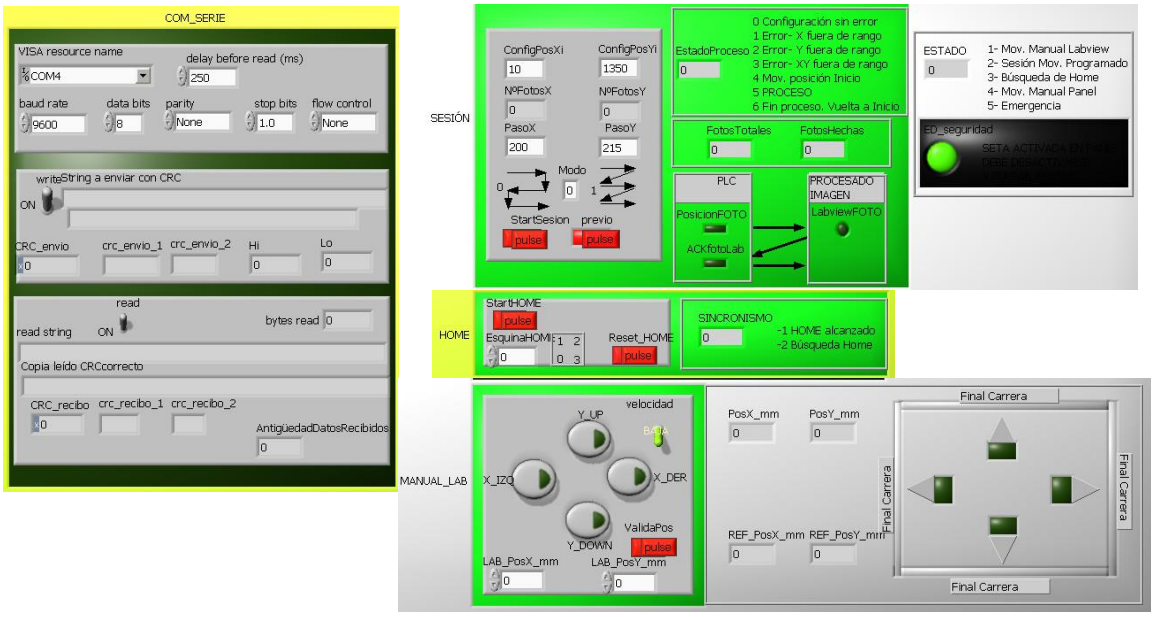

Fig. 54. Front panel of "2D_Motion_Control" LabVIEW routine.

2.4. IRR motion systems and mosaic production software

The characteristics of the InGaAs technology were previously presented (cf. Chapter 1.4.2). During the international collaboration project, done particularly with Eumelia Hernández from the IIE (Instituto de Investigaciones Estéticas) of the UNAM, it seems interesting to make a comparative study between two image capturing methods and three different software programs for the assembly of multiple images.

2.4.1. IRR images capturing methods

In Seville, the IRR device is called PIRR (Portable InfraRed Reflectography). It consists of an InGaAs camera (*Xeva-XS-512* model from Xenics) coupled to the customized 2D motion device presented before (cf. Chapter 2.3) (Fig. 55). The device moves the camera in a plane parallel to the artwork surface.

An in-house LabVIEW routine called "IRR_matrix_Acquisition" allows the achievement of a matrix of IRR images (Fig. 56). It controls the 2D motion device and saves each image of the mosaic. The user has to choose the name of the folder receiving the image files, the number of images taken in horizontal and in vertical, the scan path (serpentine or zigzag) and the distance between each image. The pitch between images

has to be adjusted according to the distance between the camera and the painting and has to be evaluated before the acquisition process. "IRR_matrix_Acquisition" uses two sub-programs to move the camera and save the image. First of all, the main program creates a folder with the name chosen by the user and the sub-program "2D_Motion_Control" moves the device to the initial position. Then, the main program performs a loop between the two sub-programs. The first sub-program saves the image and "2D_Motion_Control" moves the device to the next position. At the end of the loop, "2D_Motion_Control" moves the device back to its original position.

This set-up has the advantage of producing a mosaic assembly without significant deformation and it has been used *in situ* at the Museum of Fine Arts of Seville. It reaches more than 4 meters in height, avoiding, in most cases, the necessity of moving the painting from the exhibition site. Therefore, the resulting robustness and weight are very important and do not allow an easy deployment in the field. Moreover, the images are saved automatically. The average acquisition time is about 9-10 s per image.

Fig. 55. IRR study of "San Pedro Nolasco redimiendo cautivos" with 2D motion set-up (a) and study of "Virgen de las Uvas" with Gigapan system (b).

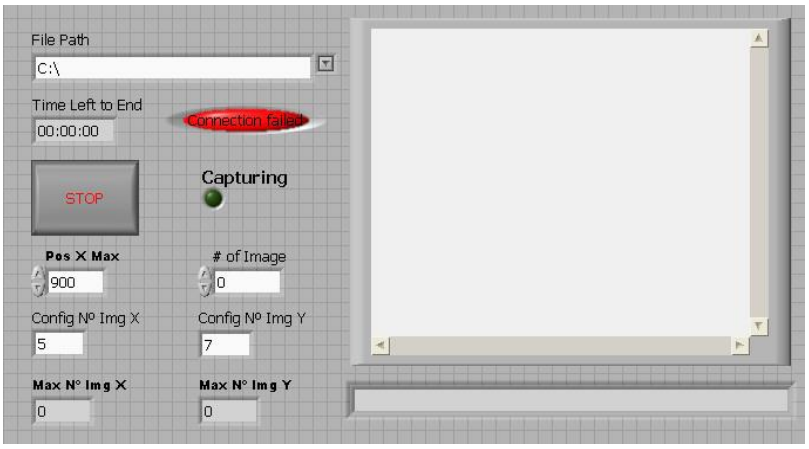

Fig. 56. Front panel of "IRR_matrix_Acquisition" LabVIEW routine.

In Mexico, the InGaAs camera was coupled with Gigapan Epic Pro, a commercial motion device (Fig. 55) [124]. This device allows the capture of a series of photos of an artwork from a fixed point giving the proper angle, so that the set of photos cover the entire painting. As a result, during the mosaic production process, in addition to stitching the pictures together, the software must be able to correct the angular deformation effect resulting from this specific process (Fig. 60 and Fig. 61).

This set-up has the advantage of being lightweight and can be deployed *in situ* for the study of artworks at specific locations: museums, churches, archaeological sites, etc. The bigger the object studied the more pronounced the angular deformation. This fact makes the acquisition process more complex so the large format capture methodology had to be improved and refined. For paintings higher than 3 meters, photo acquisition is divided into sections to minimize foreshortening. After assembly and correction of each section, they are joined together in order to generate the complete mosaic. The images are saved manually. The acquisition time is about 20 to 25 s per image.

Gigapan Epic Pro set-up turns out to be very convenient for *in situ* studies of paintings. For large format paintings, the 2D motion system is the most suitable system, as it allows the generation of a mosaic of several images with very few deformations. Gigapan equipment needs more careful and elaborated methodology to provide the same result. However, due to its robustness, weight and dimensions, the actual 2D motion system does not allow for easy deployment in the field in situations where workspace can be limited. It is important to specify that, in both cases, the exposure control is a key in the success of final assembly.

2.4.2. Mosaic production software

The reflectograms measured with the InGaAs cameras are small images and the equipment must be placed at a short distance from the painting. Depending on the size of the artwork in question, the result can be tens to thousands of images that must then be integrated into a single image. Obtaining complete IR images of large format easel paintings complicates proportionally to the number of reflectograms needed and depends highly of the capacity of the software used [110].

For the assembly of the mosaics, the software programs selected were VARIM (*Visión Artificial aplicada a la Reflectografía de Infrarrojos Mecanizada* or Artificial Vision applied to Mechanized Infrared Reflectography, version 1.0.7), Kolor Autopano Giga (Version 2.4.6) and Microsoft ICE (Microsoft Image Composite Editor, version 1.4.4.0). Subsequently, the characteristics, advantages, options and efficiency of the software packages for images assembly were evaluated.

VARIM is a freeware developed by the "Grupo de Aplicación de Telecomunicaciones Visuales" from the "Universidad Politécnica de Madrid" and the "Instituto del Patrimonio Histórico Español" (IPHE), nowadays known as the "Instituto del Patrimonio Cultural de España (IPCE)" [125]. It has the ability to take the IRR images and compose them automatically at the same time. During the present study, only the stitch function of the software was handled manually. In this case, the user has to find three points of concordance between two consecutive photos to put them together (Fig. 57) and repeat as many times as necessary until the full mosaic of the artwork is obtained.

Autopano Giga 2.4.6 from the Kolor Company is a commercial software with an available trial version. It allows a rich variety of corrections: color, saturation, alignment, etc. This software requires RGB mode images (Fig. 57), nevertheless, the InGaAs camera acquisition software records images into PNG format. That fact forces the previous conversion of all the images into 8-bit JPEG format in RGB mode. This can be achieved using commercial software like Adobe Photoshop in order to be able to stitch the photos together with Autopano Giga.

Finally, Microsoft ICE is a freeware. It allows stitching the images taken with different scan paths (serpentine or zigzag), correcting the effects of deformation (2D motion or rotating motion), and also controlling the overlapping (Fig. 58).

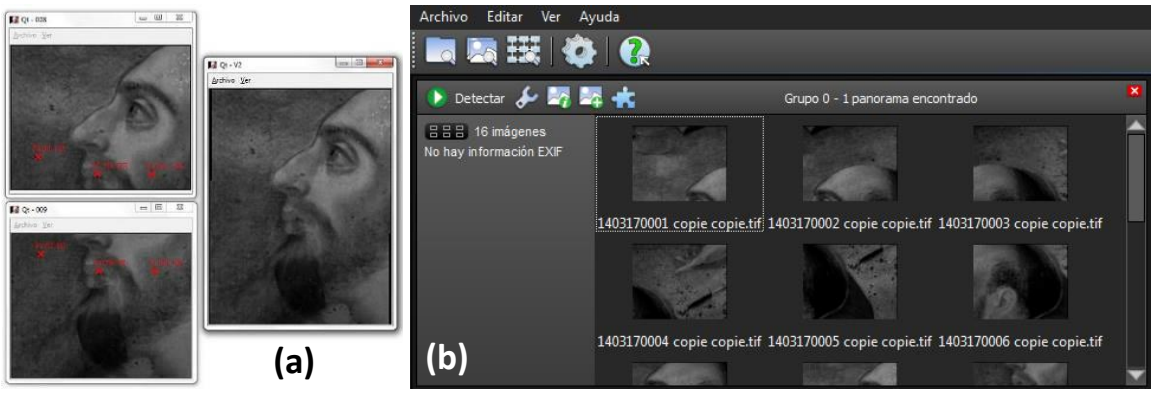

Fig. 57. Screen capture of the manual stitch process with VARIM (a) and stitch process with Autopano Giga (b).

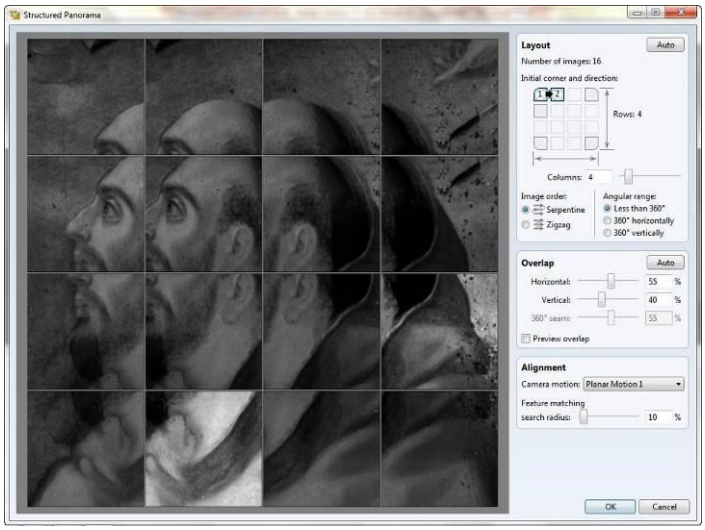

Fig. 58. Stitch process with Microsoft ICE.

The objective is now to evaluate the efficiency of the different software, by means of obtaining a final assembly using a single painting as example for each set-up (PIRR from Seville and Gigapan Epic Pro from Mexico).

2.4.3. Stitching methods for images obtained with the 2D motion device

In this example, a detail from the painting by Alonso Vazquez “San Pedro Nolasco redimiendo cautivos” of the Fine Arts Museum from Seville was studied. It is a 16 images mosaic assembly obtained for a distance of 18 cm between the painting and the IRR camera (Fig. 59). In the case of ICE software, the “planar motion 1” mode was selected for the camera motion and 10% for feature matching search radius.

A difference in the brightness of the neck area was observed between VARIM mosaic and the others (Fig. 59, white square). There is an image brighter than the others. Indeed, for some unknown reasons, InGaAs camera sometimes captures images using a different contrast and VARIM software do not corrects exposure for those images unlike ICE and

Autopano Giga. Comparing the three final assemblies, Autopano Giga provides a clearer picture in order to deduce the nature of some pigments present on the artwork's surface. The automatic brightness compensation results in a balanced image where the IR reflection contrasts can be interpreted more accurately.

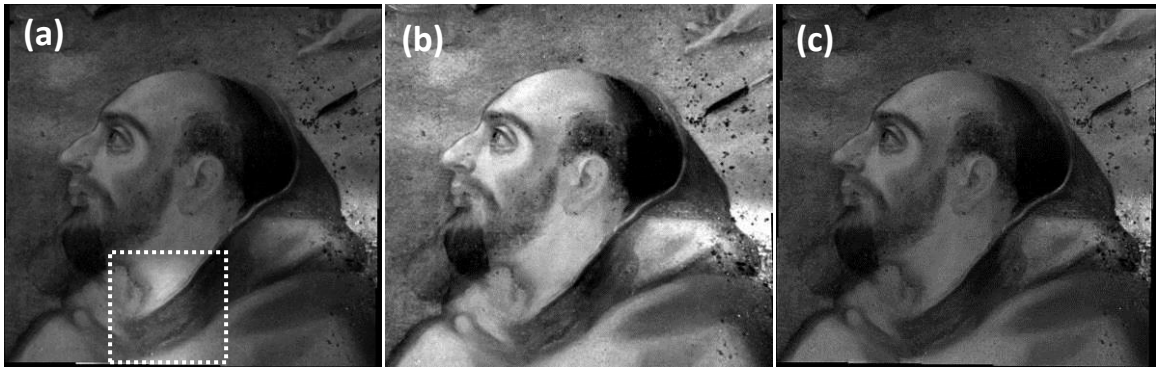

Fig. 59. Mosaic assembly result obtained with VARIM (a), Autopano Giga (b) and ICE (c).

2.4.4. Stitching methods for images obtained with the Gigapan system

In this example, the "Virgen de las Uvas" attributed to Alonso Vazquez from the Metropolitan Cathedral of Mexico was studied. 30 images for the mosaic assembly were captured within a distance of 110 cm between the painting and the IRR camera. In the case of ICE software, the "rotating motion" mode was selected for the camera motion and 30% for feature matching search radius. The "Projection Perspective" option was selected in order to correct the deformation. In the following figures, the results obtained with each software without correction (Fig. 60) and with correction (Fig. 61) are shown.

VARIM software (Fig. 60) had some difficulties in stitching the more distorted part of the picture (left and right side of the paintings) producing an artificial duplication of some parts of the mosaic. Although VARIM proposes several correction options, it was impossible to use them in order to obtain the mosaic assembly without the deformation effect. In this case, ICE and Autopano Giga produced the best results. This last one also has the advantage of allowing exposure compensation in areas with too much contrast. Consequently, it eases the observation of contrasting areas on the IRR image of the artwork to aid in the detection of certain pigments (Fig. 61).

Fig. 60. Mosaic assembly result obtained with VARIM (a) and ICE (b).

Fig. 61. Mosaic assembly result obtained with ICE with projection perspective (a) and with Autopano Giga with correction effect (b).

2.4.5. Comparison of the efficiency of the software results

Consequently, the efficiency of the software in the final assembly of IRR images was evaluated, comparing them by means of different variables (like time of acquisition, digital correction features, etc.), and creating a ranking based on a numerical scale (Table 8).

Table 8. Efficiency comparison and rating.

Software	VARIM	Autopano Giga	ICE
Total time for 2D motion assembly (16 images)	7 min	2 min	2 min
Assembly speed (1 = slow, 3 = fast)	1	3	2
Total time for rotation motion assembly (30 images)	16 min	3 min	8 min
Assembly speed (1 = slow, 3 = fast)	1	3	2
Total time for rotation motion assembly with correction (30 images)	X	5 min	13 min
Assembly speed (1 = slow, 3 = fast)	1	3	2
Facility of use (1 = difficult, 3 = easy)	2	1	3
Possibility to work with the original PNG image format without necessity of conversion (1 = no, 3 = yes)	3	1	3
Necessity to modify mosaic assemblies with Photoshop (1 = necessary, 2 = eventually for publication, 3 = not necessary)	2	3	2
Photos exposure compensation (1 = hazardous changes, 2 = no change, 3 = controlled modification)	2	3	1
TOTAL (average of 10)	**5.7**	**8.1**	**7.1**

The ICE program is the best in terms of quality/time. It provides enough information for the preliminary interpretation of the technical aspects of the artwork. It is especially suitable in order to control the quality acquisition process during field work, where time is often limited. Autopano Giga software provides the highest quality mosaics, but needs previous conversion of PNG photos using other commercial software, such as Adobe Photoshop. It would be suitable for the production of higher quality material for publication. VARIM provides high quality results, nonetheless, its manual mode performance is very time-consuming. It is a very efficient freeware for photos taken without regard to distance, as a case in point, when the camera is used with a basic tripod.

Finally, Microsoft ICE and Autopano Giga are very efficient for the correction of angular deformations. This deformation is the consequence of the rotated motion used by Gigapan system while acquiring images.

2.5. XRF setups used during Alonso Vazquez Project

The archaeometry research group of the *Centro Nacional de Aceleradores* at the University of Sevilla (CNA-US) has developed wide expertise in *in situ* cultural heritage analysis by the use of XRF portable systems. This technique has been used to study a wide variety of artefacts and museum objects as well as artworks of several kinds: statues

[126, 127], easel paintings [128, 129], coins [130], bronzes [131], gold jewelry [132], glassware [133], etc.

During the Alonso Vazquez project, the XRF study of the different artworks in Seville and Mexico were managed through the use of three different XRF devices. In this section, the X-Panda set-up will be detailed. The two others setups will be also briefly described: an old one designed as the "Museum XRF device" from the CNA and the SANDRA system from Mexico.

2.5.1. Description of the X-Panda set-up

During this PhD thesis, a new portable XRF system adaptable to the 2D motion system from the Fine Arts Museum of Seville has been designed for *in situ* study of paintings. X-Panda is a Spanish acronym for "Equipo de rayos X Portátil de Análisis No Destructivo para el Arte" meaning "Portable XRF set-up for the non-destructive analysis of art" (Fig. 62).

The set-up consists of an X-ray source (Mini X model, Amptek) and a SDD (model X123SDD, Amptek) (more specifics respectively in Appendix VIII and IV) [33]. It is completed with two laser diode modules and a webcam for the positioning and inspection of the surface sample.

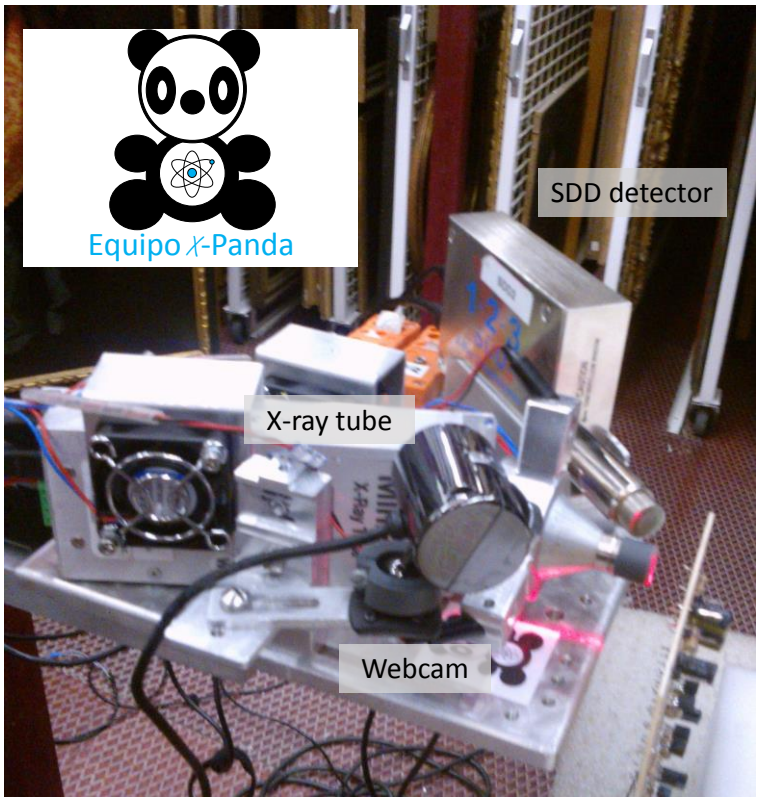

Fig. 62. General view of the X-Panda device.

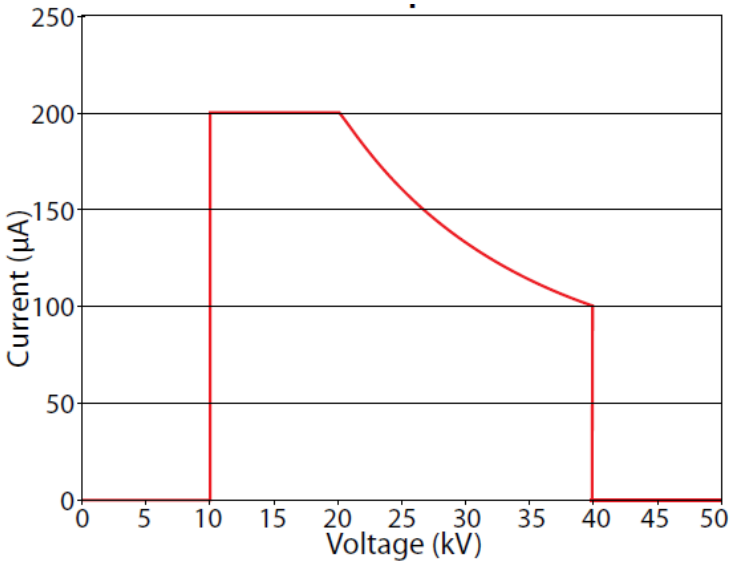

Fig. 63. Isopower curve of the Mini-X 4W X-ray tube (From Amptek, 2011).

The X-ray source is composed by a low-power 4W X-ray tube with tungsten anode, a 500 µm Be window and an internal power supply unit. It can be operated with maximum voltage and current of 40 kV and 200 µA (Fig. 63). Its maximum operating temperature is 50°C. To avoid reaching this temperature, it is possible to use two small fans placed around the Mini X run by USB. The X-ray tube is controlled via USB with "Mini-X Controller Software" (version 1.0.0.8, copyright © Amptek Inc.). This software allows the turning on and off of the X-ray tube and setting the working voltage and the current passing through the filament.

The diameter of the primary X-ray beam is reduced using an in-house designed tungsten collimator made from a tungsten rod from Goodfellow and processed by the *Mecanica de Precision* company [134] with a 2 mm diameter hole.

A 1 mm thick aluminum filter is placed at the exit of the collimator, fixed by a grey plastic piece in order to reduce the low energy of the continuous bremsstrahlung radiation and almost entirely remove the tungsten L peaks from the anode. If necessary, another plastic piece can be used fixing a 1 mm thick aluminum filter together with a thick tungsten collimator (with a 1 mm diameter hole) providing a smaller incident X-ray beam. The latter has never been used during this study.

Two laser diode modules (Micro LDM Laser Diode Modules model, Edmund Optics) pinpoint the working distance from the set-up to the sample (Fig. 64). This working distance has been fixed to 10 ± 0.1 mm. Consequently, the surface of the irradiated sample is a disc of 2.9 ± 0.3 mm diameter and the beam aperture from the exit of the collimator has been estimated to be 2,5 ± 0.5 ° [135].

The active area of the SDD Si crystal is 7 mm^2 with an active thickness of 450 µm. It is sealed with a 25,4 µm Be window. The resolution of the detector measured is 148 eV for the Mn-Kα line (FWHM of the peak at 5.9 keV). More details on the characteristics of the X-123SDD model detector are provided in Appendix IV.

To complete the description of the device, the geometry of irradiation-detection channels has to be described. Like the other two XRF devices, irradiation is normal to the surface of the analyzed sample and the detection angle is 45° (Fig. 64). This arrangement permits the study of any kind of material with greater penetration, making it less sensitive to the heterogeneity of the surface but more sensitive to the matrix effects.

Finally, a CMOS color camera from Woxter (model i-Cam 60) allows the saving of images from the position of each measurement, controlling the safety of the study, observing the irradiated region of the sample and selecting the region of interest (Fig. 63). The camera is attached to the side of the XRF system and can be easily dismantled or moved if its presence hinders the analysis.

All of these components (X-ray tube, SDD, laser diode modules and webcam) are fastened to a support designed and conceived at the workshop of Physics Faculty from US by Jose Luis Benjumea Acevedo. The support can be fastened to the 2D motion system together with the Z linear motion from OWIS presented previously (cf. Chapter 2.3) or it can be coupled to a manual XYZ motion system [135]. Finally, a removable L-shaped bracket can be fastened to the support in order to be able to study small samples easily (like standards used for calibration) (Fig. 64).

The idea behind the design of this device is to provide a robust set-up allowing for evolution and versatility. Each component can be removed quickly and easily. The device only takes ten to fifteen minutes to be fully assembled and ready to operate.

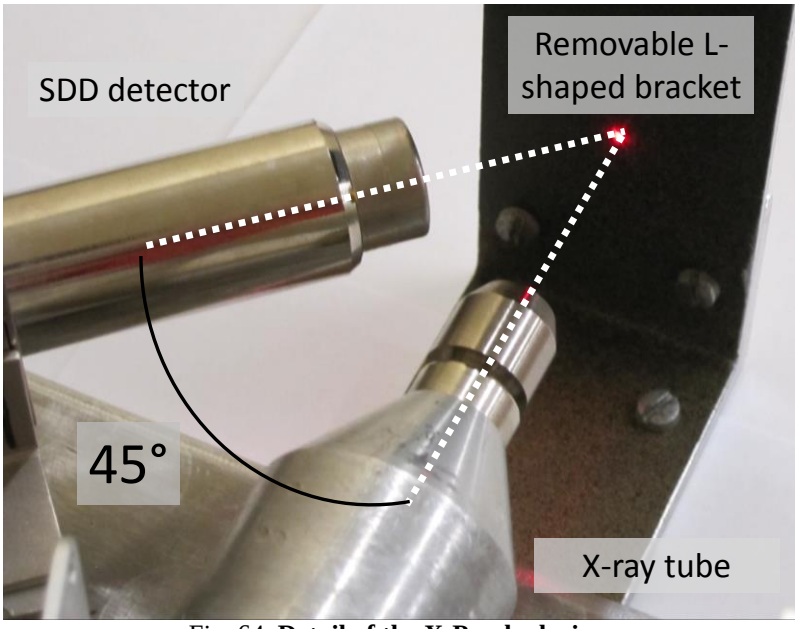

Fig. 64. **Detail of the X-Panda device.**

An in-house LabVIEW routine called "XRF_Acquisition" can be used when X-Panda works in connection with the 2D motion system (Fig. 65). It allows the acquisition of punctual spectrum, 1D or 2D analysis. "XRF_Acquisition" controls the 2D motion device and saves each image and spectrum. The user has to choose the name of the folder receiving the files, the number of spectra taken horizontally and vertically, the type of path processes (serpentine or zigzag), the distance between each spectrum and the acquisition time. First of all, the user has to move the 2D motion device to the initial position and has to place the X-Panda at the working distance from the sample using OWISoft (Version 2.71 by OWIS GmbH) which controls the OWIS motion motor. Then, "XRF_Acquisition" calls two sub-programs, moving the X-Panda device and saving the spectrum and the webcam image. First, the main program creates a folder with the name chosen by the user. Then, the main program performs a loop between the two sub-programs. The first sub-program saves the spectrum and the image. Then, "2D_Motion_Control" moves the device to the next position. At the end of the loop, "2D_Motion_Control" moves the device back to its original position. Like with

"1_Working_distance_Adjustment" LabVIEW, Amptek SDD is controlled with FW5 firmware. Finally, the evolution, in real time, of the detected spectral signals is available in logarithmic or linear scale.

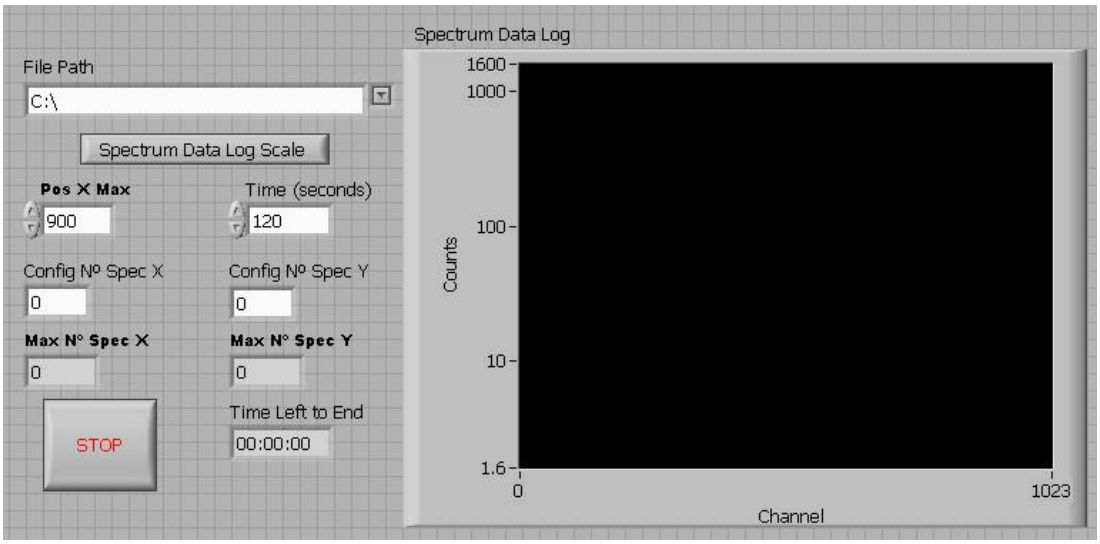

Fig. 65. Front panel of "XRF_Acquisition" LabVIEW routine.

2.5.2. Description of the "Museum XRF device" and the SANDRA system.

Now, the "Museum XRF device" and the SANDRA system will be briefly presented. The detailed characteristics of the three XRF setups are shown in Table 9.

The "Museum XRF device" used in Seville consists of a W X-ray source (RX38 model, EIS S.L.) and an SDD detector (Fig. 66). It is complete with a positioning system made by two laser diode modules [129].

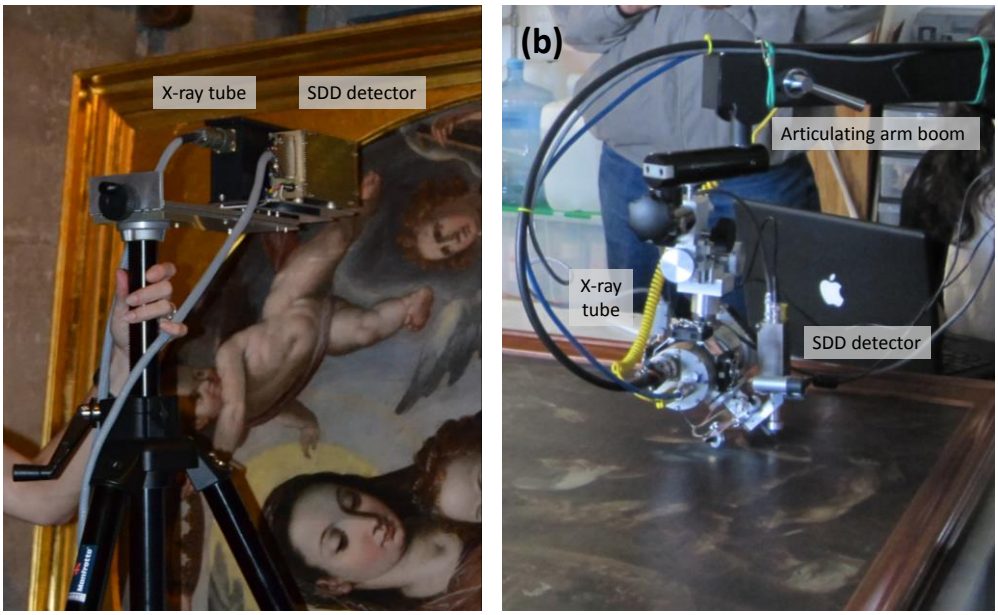

Fig. 66. "Museum XRF device" during "Virgen del Valle" study (a) and SANDRA setup during "Martirio de San Hipólito" study (b).

In Mexico, SANDRA is a Spanish acronym for *Sistema de Analisis No Destructivo por RAyos X* meaning System for Non Destructive Analysis using X-rays. This portable X-ray system was developed at the Physics Institute of the UNAM (IFUNAM, Mexico). For this study, it was composed by a 75W Mo X-ray tube (XTF5011 model, Oxford Instruments) and a Si-PIN detector (XR-100-CR model, Amptek) (Fig. 66).

The X-ray tube is powered by a high voltage power supply XLG50P100 from Spellman and manually controlled by a console. The maximum operating temperature is 50°C. To avoid reaching this temperature, three small fans and a main fan at the bottom of the X-ray tube provide the necessary cooling. For safety reasons, the temperature is monitored by a thermocouple. Finally, a security LED turns on when the X-ray tube is working and a shutter can stop the X-ray beam at any time.

The X-ray beam diameter is determined by a lead collimator. The beam diameter is inferior to 1.2 mm. Two laser diode modules pinpoint the working distance from the set-up to the sample. This working distance has been fixed to 8 mm. To improve the data recorded and to observe the irradiated region on the sample, a webcam with medium resolution is used.

The head of the device is mounted on an XYZ manual motion support allowing movements about 3 cm in each direction to smoothly reach the region of interest on the surface of the sample. The SANDRA system is mounted on an articulating arm boom stand ensuring high mobility and flexibility (Fig. 66). This XRF device can not only be used for analysis on vertical and horizontal planes but also can be tilted as necessary. For more details about the SANDRA set-up, please refer to [136].

Table 9. Characteristics of the three XRF setups.

XRF set-up	X-Panda - Seville	"Museum XRF device" - Seville	SANDRA - Mexico
Excitation channel			
X-ray tube anode	W	W	Mo
Manufacturer/model	Amptek/ Mini-X	EIS S.L./RX38	Oxford Instruments/ XTF5011
Maximum power (W)	4	10.5	75
Maximum voltage (kV)	40	30	50
Maximum intensity (μA)	200	350	1500
Be window thickness (μm)	500	150	125
Collimator	W	W	Pb
Collimator inner diameter size (mm)	1.5	1	1
Filter	Al	Al	None
Filter thickness (mm)	1	1	None
Beam diameter spot (mm)	2.9 ± 0.3	3	< 1.2
Working distance (mm)	10 ± 0.1	12	8
Detection channel			
Active area (mm^2)	7	7	6
Si crystal thickness (μm)	450	450	500
Resolution (eV)	148	140	180
Be window thickness (μm)	25,4	127	0.5
Manufacturer/model	Amptek/ 123SDD	EIS S.L.	Amptek/XR-100-CR

2.5.3. Data acquisition and processing

With both XRF setups, the signals processed by the digital pulse processor are acquired via USB and displayed on the laptop thanks to the ADMCA software (ADMCA Analog and Digital Acquisition, version 2.0.0.0, copyright © 1998-2010, Amptek Inc.) (Fig. 67). This software allows controlling the onset and duration of data acquisition and the visualization in real time of the detected spectral signals presented in logarithmic or linear scale.

During this study, ADMCA software was used to record the data and perform a qualitative assessment of the elemental composition of the analyzed area, reading the energy at which the different peaks appear. Prior to this it is necessary to perform an energy calibration recording a spectrum belonging to a composition's known standard (bronze standard in this case). Once the spectrum is obtained, the energy value of some of the characteristic peaks from the standard has to be entered in order to calibrate the energy scale, allowing the software to assign an energy value to each channel of the multichannel. This procedure has to be performed each time a new session of ADMCA is started. This previous analysis of the same standard also allows for checking the stability of the set-up. It was done for the three XRF devices at the beginning and at the end of each day of study.

Finally, all the spectra measured with these three XRF devices have been analyzed with PyMCA. The methodology is slightly different than that which was used with the CXRF data and is detailed in Appendix V.

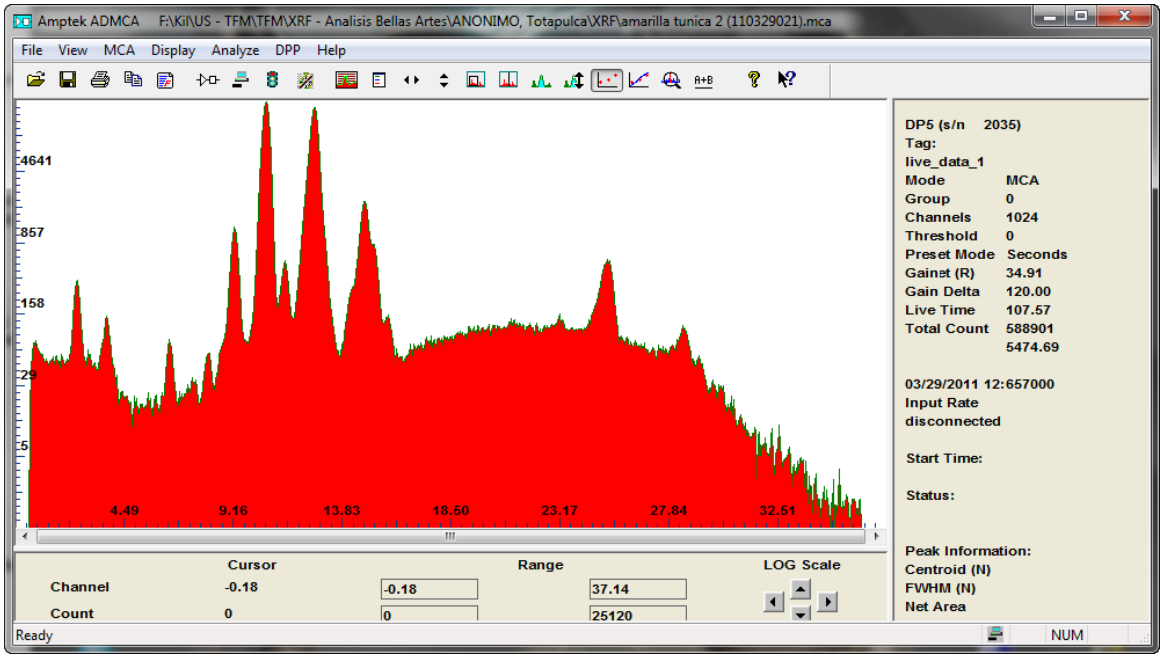

Fig. 67. Graphical user interface of ADMCA software showing a spectrum in logarithmic scale.

Chapter 3. IRR and CXRF studies of experimental paint multilayers

Prior to the application of the different techniques to the study of the 16th century artworks from the Alonso Vazquez project, it was decided to develop a series of experimental paint multilayers made like that of old paintings and to analyze them with IRR and CXRF. The methodology applied to produce those experimental samples will be detailed. Then, those experimental paint multilayers were observed with four IRR cameras in order to compare the results obtained. The objectives were to:

- evaluate the performance of the different cameras,
- define the kind of information obtained by each camera,
- set the specific IR reflectivity of each material,
- evaluate the accuracy of a first diagnosis of the nature of the pigments present based on IRR images; to do so, discrimination of different pigments with the same color was tried,
- identify the influence of overlapping layers of different materials.

Finally, the CXRF abilities in the study of controlled multilayered samples were tested using the µXRF-CONCHA set-up. Thereafter, the results were compared with those obtained using two other CXRF systems. The aim of these measurements was to compare the composition and sequence information obtained analyzing the same experimental paint layers using the three different setups and determined if any inherent differences appear between the three devices.

3.1. Making of experimental paint multilayers

A series of experimental paint multilayers made like that of old paintings were prepared by students at the restoration workshop of the Faculty of Fine Arts of Seville. The objective was to produce multilayer samples using one pigment by layer and typical recipes used in the 16th century. The methodology has been established following suggestions from Elsa Arroyo from the IIE-UNAM. Since 2008, her interdisciplinary group has developed an important knowledge of developing reference standards like 16th century paintings in order to support their investigation [137]. The produced samples consist of a series of up to four layers of six different inorganic pigments on top of a ground layer (Fig.73). The methodology applied to produce those experimental samples is detailed as followed:

- Preparation of the wood support
- Application of the ground layer
- Application of two different kinds of priming layers
- Application of the paint layers

3.1.1. Preparation of the wood support

First, the wood supports were prepared. Twelve squares of 100 cm^2 of balsa wood were cut with a saw. The edges were grounded and one side of the support was diagonally marked with a saw blade as shown in Fig.68. Then, the wood supports were wet with hot water on a bristle brush and allowed to dry for one day. Afterwards, a mixture of rabbit glue and water (1 to 3 ratios) was applied and allowed to dry for another day. To do so,

the rabbit glue was previously soaked in water and then heated in a water bath before its application to the wood (Fig. 68).

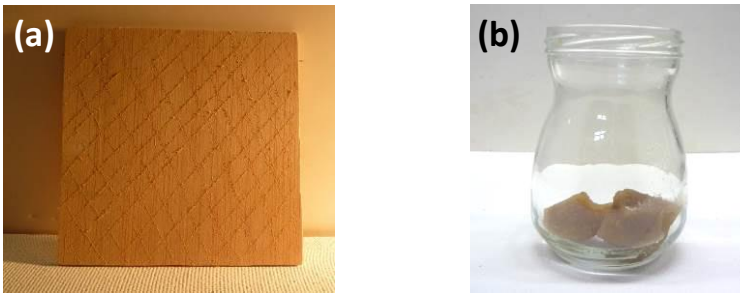

Fig. 68. Wood support diagonally marked with a saw blade (a) and rabbit glue processed (b).

3.1.2. Application of the ground layer

The second step consisted in the application of the ground layer. The preparation of the stucco was made by melting 2/3 of water for 1/3 of rabbit glue and adding calcium sulfate until saturation. The rabbit glue was previously prepared with pentachlorophenate as a fungicide. The supports were covered with several layers of this mixture each one being applied in the opposite direction to the previous and respecting drying time between each layer application (Fig. 69). At the end of the process, the stucco surfaces were sanded with wet sandpaper in a circular action. Each support was etched dividing its surface into four squares. Then, a circle was etched into each square and sketched with soft graphite. Within each circle, a different design was drawn with soft graphite (Fig. 70 and Table 10).

Fig. 69. Wood supports with several layers of stucco.

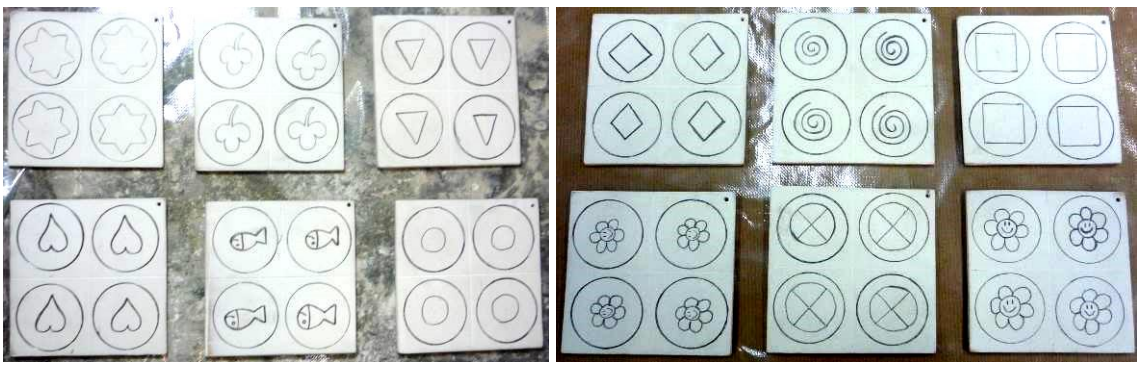

Fig. 70. Different designs drawn with soft graphite inside circle.

Table 10. Different designs drawn with soft graphite inside circle.

Support name	Design
B1	Star
B2	Clover
B3	Triangle
B4	Circle
B5	Heart
B6	Fish
R1	Diamond
R2	Spiral
R3	Square
R4	Flower
R5	Circle with X inside
R6	Flower

3.1.3. Application of the priming layers

The application of two different kinds of priming layers was the third step. The mixture was applied using specific brushes (Escoda® 2234 nº12 of natural hair and Van Gogh® 361 Light ox hair - royal Talens) (Fig.71). On the six first supports, white lead was applied as a priming layer. They were marked with the letter "B" and given a number between 1 and 6. The carbonate lead was bound with purified linseed oil (product 027 Talens®, 20 mL) and cobalt siccative (TITAN®, 0,5 mL). Two priming layers were applied to the supports B4, B5 and B6. The priming layer on B1 is more diluted while those on B2 and B3 are slightly opaque (Fig.71). Red iron oxide was applied on the six other supports as priming layer (hematite). They were marked with the letter "R" and given a number between 1 and 6. The red primer was prepared by mixing 3 mL linseed oil, 0,5 mL of cobalt siccative and completed with hematite pigment to nearly saturation. The result was a thicker and more opaque primer than the white primer as shown in Fig.72.

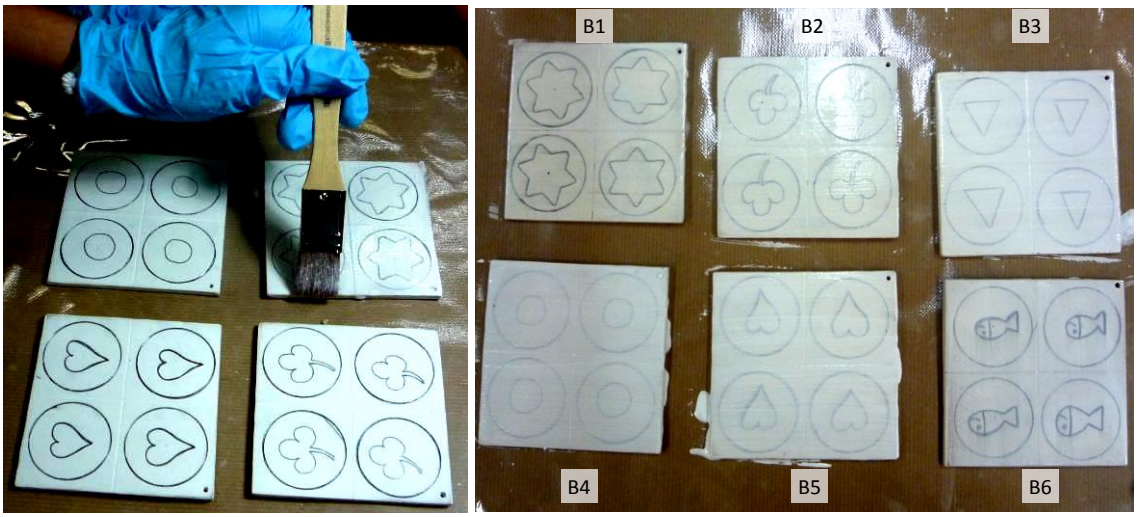

Fig. 71. Application of the white primer.

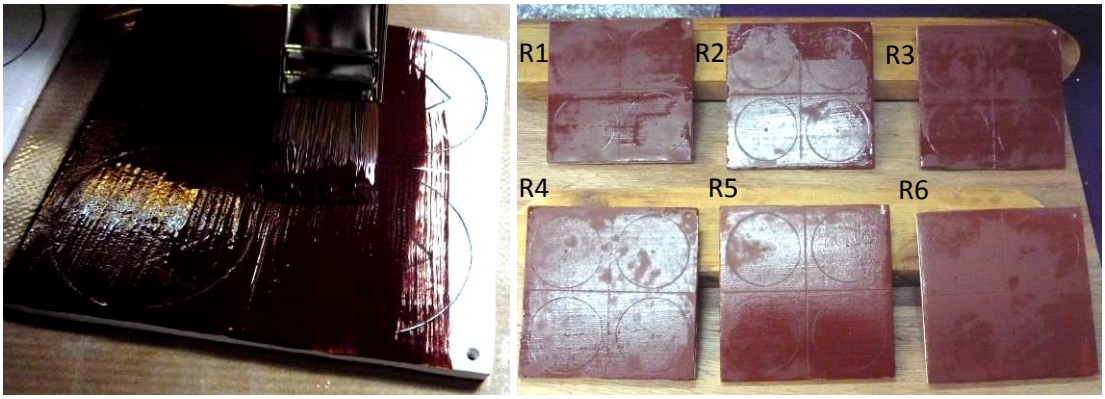

Fig. 72. Application of the red primer.

3.1.4. Application of the paint layers

The last step consisted in the application of the paint layers. For those, seven inorganic pigments that were used during the 16th century were selected:

- White lead (lead carbonate),
- Malachite,
- Yellow ochre (yellow iron oxide),
- Vermilion (mercury sulfide),
- Hematite or red ochre (red iron oxide),
- Azurite,
- Lead-tin yellow (type I).

The pigments were prepared in paste form using 50 wt% pigment and 50 wt% methyl alcohol except for the azurite which was mixed with egg yolk diluted in water. To prepare the binder, the yolk and the white were separated. Then, the yolk membrane was removed and the liquid was poured into a clean glass jar and diluted in water at the same proportion. The pigment pastes coalesced with the same proportion of diluted yolk before they were applied, using the same previous brushes, in the order set on each support (Fig.73, Tables 11 and 12). On supports B1, B3, R1 and R3, two layers of white lead were applied in opposite directions. Finally, no lake was applied.

Table 11. Description of the experimental sample.

Support name	Priming layer	1st pigment layer	2nd pigment layer	3rd pigment layer
B1	White lead	White lead	Malachite	Yellow ochre
B2	White lead	Lead-tin yellow	Hematite	Azurite
B3	White lead	White lead	Lead-tin yellow	Vermilion
B4	White lead	Hematite	Azurite	White lead
B5	White lead	Hematite	Vermilion	Lead-tin yellow
R1	Hematite	White lead	Malachite	Yellow ochre
R2	Hematite	Lead-tin yellow	Hematite	Azurite
R3	Hematite	White lead	Lead-tin yellow	Vermilion
R4	Hematite	Hematite	Azurite	White lead
R5	Hematite	Hematite	Vermilion	Lead-tin yellow

Table 12. Description of the experimental sample.

Support name	Priming layer	1st square	2nd square	3rd square	4th square
B6	White lead	Malachite	Azurite	Vermilion	Yellow ochre
R6	Hematite	Malachite	Azurite	Vermilion	Yellow ochre

Fig. 73. The experimental paint multilayers.

3.2. Comparison of the capabilities of the IRR cameras

Since the PhD thesis of J.R.J. Van Asperen de Boer, infrared reflectography (IRR) has become a classic image registration method in the technical examination of art [5]. This technique reveals the presence of preparatory drawings made of carbon black (infrared no-reflective material) as well as the artist's process of execution and his changes in the painting composition (*pentimenti*). Although little explored by an inherent issue due to the complexity of an artwork, it also provides information that helps to deduce the nature of some pigments present on the artwork's surface [6, 101].

At present, different kinds of IRR cameras are commercially recording a specific part of the IR spectrum depending on the detector technology used. The intensity and the wavelengths of the IR reflected by an artwork depend on the thickness of the paint layers and the kind of materials present (pigments, binding medium, etc.) as well as its quantity. If the IR spectrum recorded is different between the IRR cameras, the image obtained in a comparative study may show differences.

During this PhD, three different technologies of IRR cameras were used:

- a Si-CCD camera Power Phase model from Phase One,
- a Vidicon camera C2741-03 model with N2606-06 tube from Hamamatsu Photonics K.K.,
- two InGaAs cameras with *Xeva-XS-512* model (used in Seville) and, the most recent *Xeva-1.7-640* model (in Mexico); both from Xenics.

The characteristics of each system were previously explained (cf. Chapter 1.4).

As detailed in Chapter 1.4, the sensor response division scheme has been chosen to define the IR range of each camera (Table 13) [102]. It is important to note that both Si-CCD and Vidicon cameras register visible spectrum and Si-CCD also registers UV light. While the Vidicon camera from Hamamatsu uses a visible radiation cut-off filter, the Si-CCD camera from Phase One only works with a UV cut-off filter. Like no visible cut-off filter was used during the study, both visible spectrum radiations and near-infrared radiations participate in the image. This imaging method will be referred as visible-IR imaging. After that, there is a computing process converting the image into a grey scale image to make it appear like an IRR image. These considerations will be important to understand and interpret the results.

Table 13. Classification of the different technologies of IRR cameras based on the sensor response division scheme.

Camera type	Responsivity range (nm)	Sensor response division scheme
Si-CCD	300-1000	near-infrared
Vidicon	400-2200	near-infrared and short-wave infrared
InGaAs	900-1700	short-wave infrared

Consequently, the experimental paint multilayers previously presented were observed with the four IRR cameras in order to compare the results obtained. The IRR images were obtained under controlled lighting conditions, length and aperture of the cameras. The objectives were to:

- evaluate the performance of the different cameras,
- define the kind of information obtained by each camera,
- set the specific IR reflectivity of each material,
- evaluate the accuracy of a first diagnosis about the nature of the pigments presents based on IRR images; to do so, discrimination of different pigments with the same color was tried,
- identify the influence of overlapping layers of different materials.

3.2.1. IR reflectivity classification

At the beginning of this study, it was important to define a simplified, accurate and more objective classification for the description of images obtained by IRR which will be the foundation of the methodology proposed to differentiate the pigments present in the experimental samples. This classification is divided into three categories based on the characteristic IR reflectivity by the pigments:

- Transparent materials, which reflect a specific part of the IR spectrum,
- Opaque materials, which do not reflect IR radiation,
- Shiny materials, which reflect the most part of the IR spectrum reaching the saturation of the detector.

Thereafter, this variation of IR reflectivity will be used to evaluate pigments nature.

3.2.2. Si-CCD camera issue

The first result concerns the images obtained with Si-CCD camera. As mentioned before, the image is a combination of IR and visible spectrum information. For example, in Fig. 74, the three red pigments are distinguishable from the yellow one based on observed visible color contrast consideration. The visible spectrum contribution distorts the IR contrast and renders the quality evaluation scale proposed to discriminate pigments useless. With this device, the observation of drawings underneath the pigment is limited not only by shiny and opaque pigments but also by the color of the pigments which can mask the drawing signal (Fig.74 and Table 14). In order to solve this problem and suppress the visible spectrum information from the image, it would be necessary to use the Si-CCD camera coupled with a visible light cut-off filter. Meanwhile, the results obtained cannot be compared with those provided by Vidicon and InGaAs cameras.

Table 14. Description of R5 sample.

Support name	Priming layer	1st pigment layer	2nd pigment layer	3rd pigment layer
R5	Hematite	Hematite	Vermilion	Lead-tin yellow

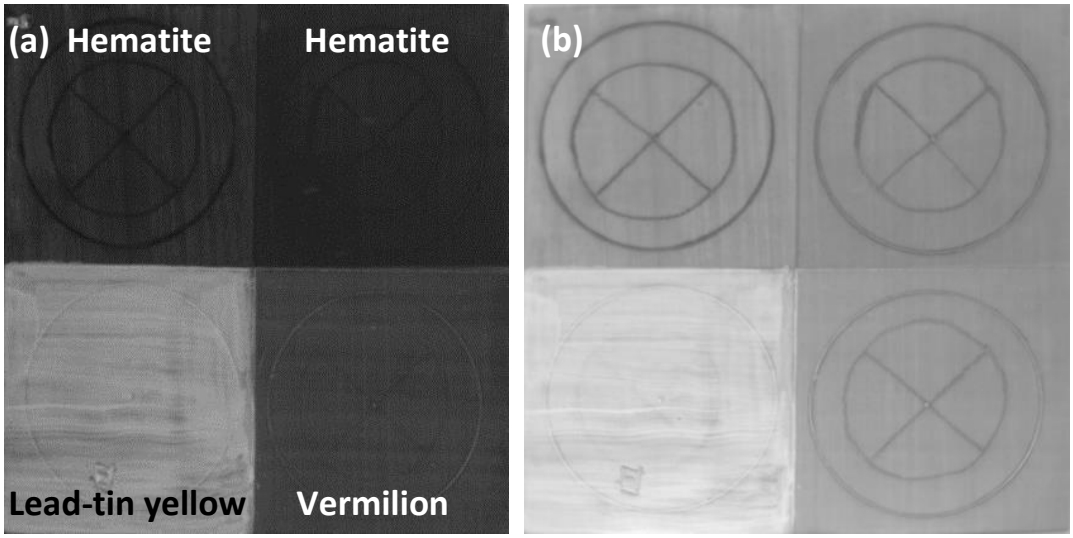

Fig. 74. Differences between the images obtained respectively with the Power Phase (near-infrared) (a) and with the Xeva-1.7-640 (short-wave infrared) (b).

3.2.3. Specific reflectivity of several inorganic pigments

Excluding the Si-CCD camera, specific IR reflectivities are observable with the other cameras. Regardless of the kind of priming (white or red), or the type of IR equipment (Vidicon or InGaAs), pigments studied show the same features on IR images (Table 15). There is one exception with yellow lead-tin. It looks shiny with the Vidicon camera while it looks transparent with InGaAs camera (Fig.75 and 77). This can be explained by the fact that yellow lead-tin is made of a material which reflects short-wave infrared better than other materials. The Vidicon camera registers a wider IR spectrum than InGaAs camera, and consequently the intensity of the IR reflection registered by the Vidicon detector is higher than that of the InGaAs detector. As a result, for all short-wave infrared reflecting materials, the images obtained with those two detectors show a difference of contrast. The Vidicon image will be shinier than the InGaAs one. This observable difference can be helpful to discriminate two categories of materials: those which reflect only near-infrared and those which reflect short-wave infrared as well like yellow lead-tin.

There are two possibilities in order to obtain identical results between Vidicon and InGaAs cameras:

- Use the Vidicon camera together with a short-wave infrared cut-off filter,
- Lighting the artwork only with near-infrared radiation.

Table 15. Table of characteristics IR reflectivity.

Pigments	Vidicon C2741-03	Xeva-XS-512	Xeva-1.7-640
White lead	Transparent	Transparent	Transparent
Vermilion	Shiny	Shiny	Shiny
Hematite	Transparent	Transparent	Transparent
Yellow lead-tin	Shiny	Transparent	Transparent
Yellow ochre	Transparent	Transparent	Transparent
Malachite	Opaque	Opaque	Opaque
Azurite	Transparent	Transparent	Transparent

3.2.4. Discrimination of inorganic pigments with the same color

Regarding our selection of pigments, the results obtained with two different yellow pigments (yellow lead-tin and yellow ochre) and two different red pigments (hematite and vermilion) can be compared. The objective is to observe if IRR images allow discrimination of those same color pigments.

Regardless of the type of IRR camera, lead-tin yellow is brighter than yellow ochre. This effect hinders the observation of preparatory drawing (Fig.75 and 77). In the case of white priming, the contrast between both pigments is low (Fig.75 and 76) thus obstructs the distinction of both pigments while, in the case of red priming, the contrast is apparent (Fig.77 and 78).

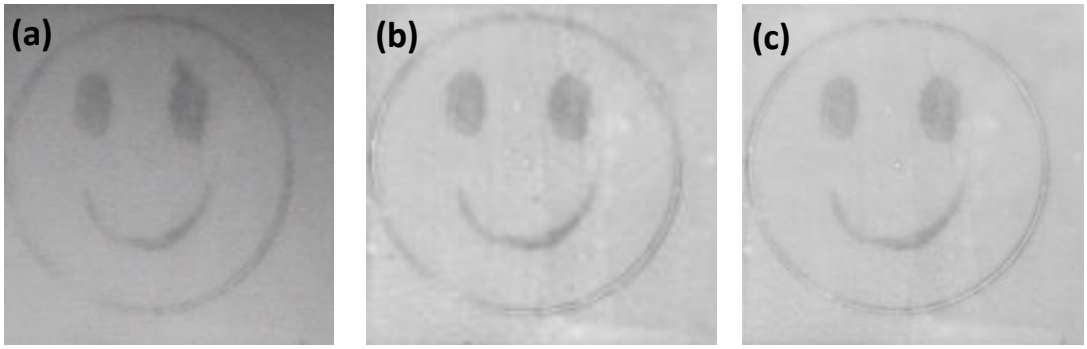

Fig. 75. Lead-tin yellow with white priming acquire with Hamamatsu (a), Xeva-XS-512 (b) and Xeva-1.7-640 (c).

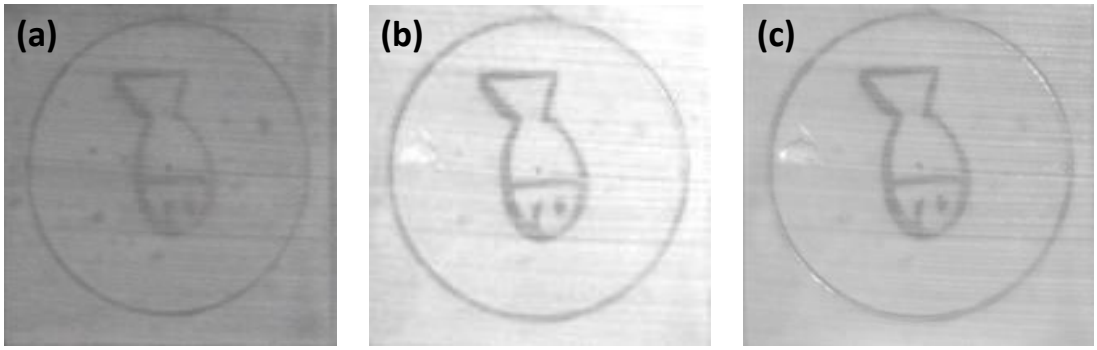

Fig. 76. Yellow ochre with white priming acquired with Hamamatsu (a), Xeva-XS-512 (b) and Xeva-1.7-640 (c).

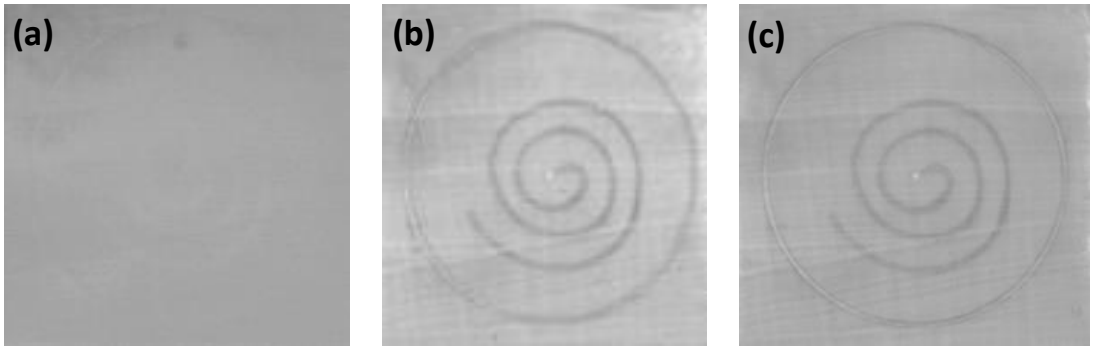

Fig. 77. Lead-tin yellow with red priming acquire with Hamamatsu (a), Xeva-XS-512 (b) and Xeva-1.7-640 (c).

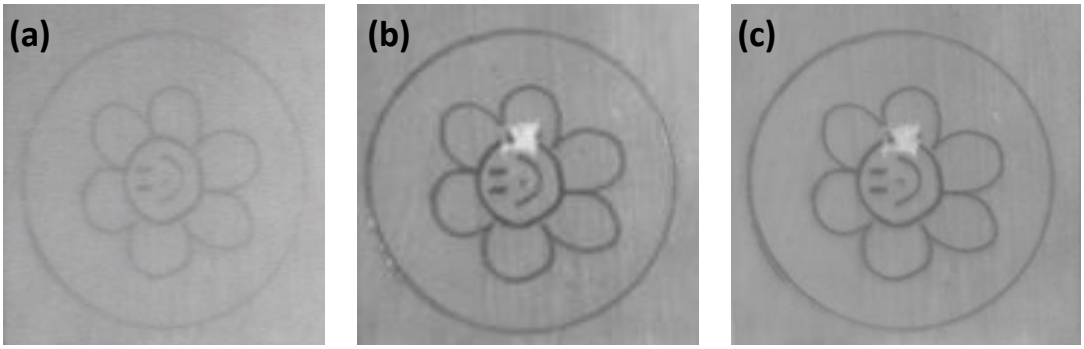

Fig. 78. Yellow ochre with red priming acquired with Hamamatsu (a), Xeva-XS-512 (b) and Xeva-1.7-640 (c).

In the case of the red pigments, regardless of the type of IRR camera, the vermilion is brighter than the hematite thus hindering, in the case of the vermilion, the observation of preparatory drawing. (Fig.79 and 81). Moreover, regardless of the kind of priming, the difference is apparent between the two pigments (Fig.79 to 82), so it is possible to discriminate them from IRR images.

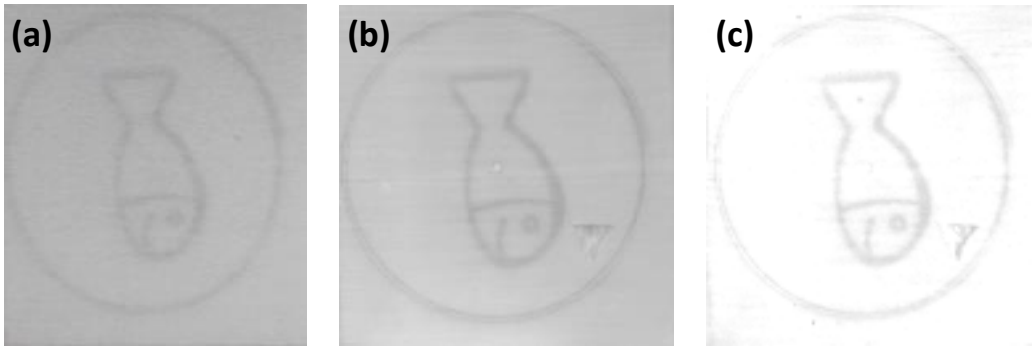

Fig. 79. Vermilion with white priming acquired with Hamamatsu (a), Xeva-XS-512 (b) and Xeva-1.7-640 (c).

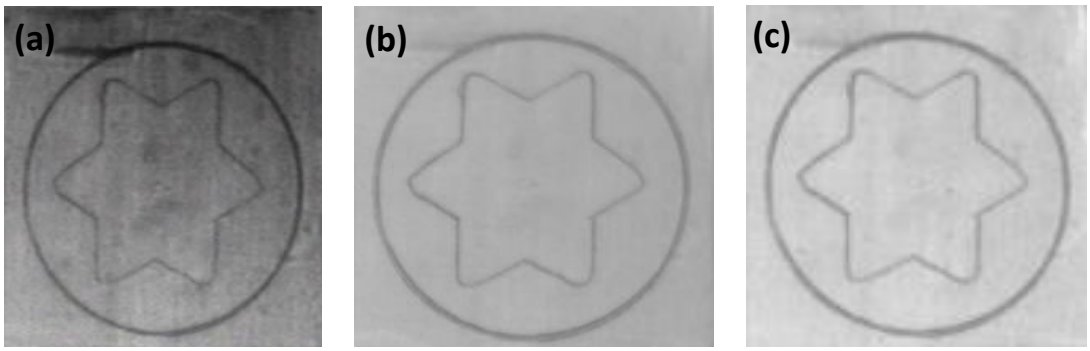

Fig. 80. Hematite with red priming acquired with Hamamatsu (a), Xeva-XS-512 (b) and Xeva-1.7-640 (c).

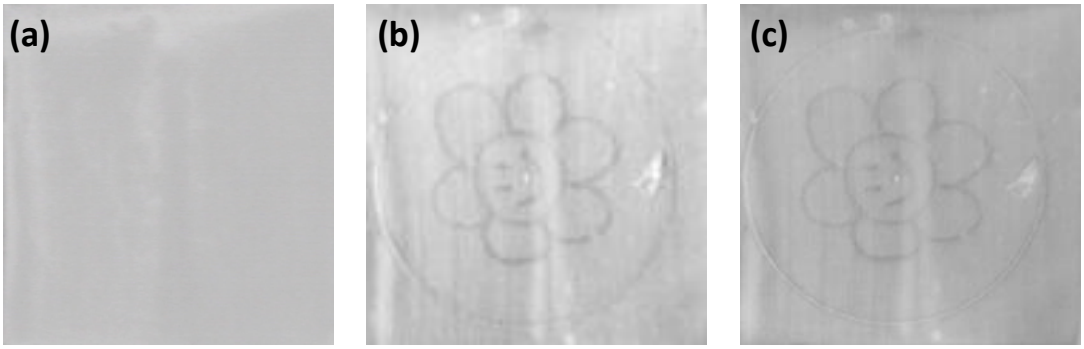

Fig. 81. Vermilion with red priming acquired with Hamamatsu (a), Xeva-XS-512 (b) and Xeva-1.7-640 (c).

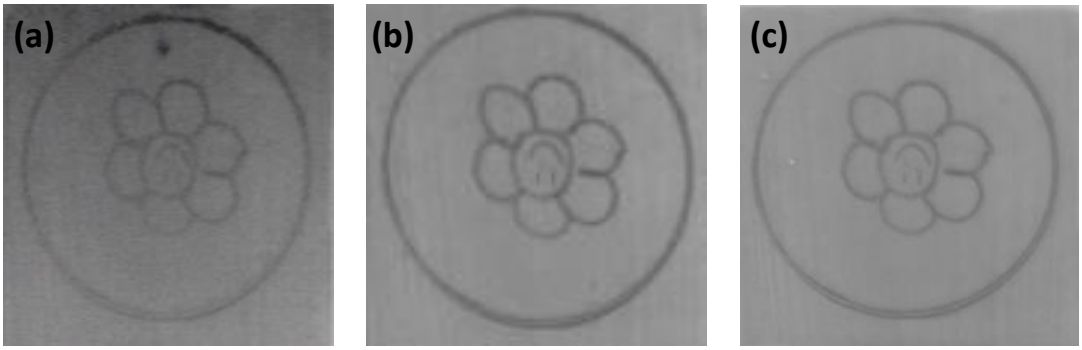

Fig. 82. Hematite with white priming acquired with Hamamatsu (a), Xeva-XS-512 (b) and Xeva-1.7-640 (c).

3.2.5. Influence of overlapping layers of different inorganic pigments

Several observations can be made about the influence of different overlapping layers. First of all, with all IRR cameras, juxtaposing up to three paint layers with "transparent" pigments did not prevent the observation of the preparatory drawing (Fig.83).

Secondly, if one “opaque” pigment layer composed the multilayer, preparatory drawings were not observable (Fig.84). As a result, when IRR studies looked at the preparatory drawings in artwork, it is expected that the areas containing malachite, for example, do not allow the detection of underdrawings.

On the other hand, the juxtaposition of paint layers using “shiny” pigments raises the brightness observed in the IRR images and also prevented any observation of preparatory drawings (Fig.85).

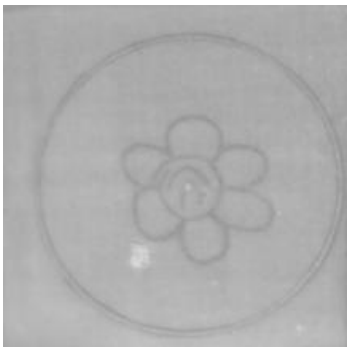

Fig. 83. Three-layer system with lead white, azurite and hematite with red priming acquired with Xeva-1.7-640.

Fig. 84. Bilayer with malachite under white lead (a) and three-layer with yellow ochre above lead white and malachite (b) both with red priming acquired with Xeva-1.7-640.

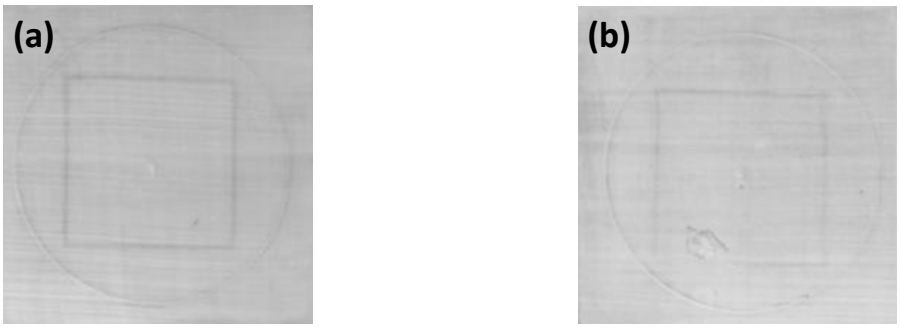

Fig. 85. Bilayer with yellow lead-tin and white lead (a) and three-layer with vermilion above yellow lead-tin and white lead (b) both with red priming acquired with Xeva-1.7-640.

3.2.6. Conclusions of the IRR study

The three technologies which were used to do IRR (Si-CCD, Vidicon and InGaAs) allowed the observation of preparatory drawings made in carbon black. To obtain results comparable to those provided by InGaAs and Vidicon cameras, the Si-CCD camera will have to be used together with a UV-visible light cut-filter.

A classification linked to IR reflectivity of material was established and applied to several inorganic pigments. White lead, hematite, yellow ochre and azurite are transparent. Malachite is opaque and vermilion is shiny. Yellow lead-tin proved to reflect near-infrared and short-wave infrared radiations. The pigments classified as opaque and shiny hindered the observation of preparatory drawings. Regardless of the type of IRR camera used (Vidicon or InGaAs), lead-tin yellow proved to be brighter than yellow ochre and vermilion showed to be brighter than hematite. So, it is possible to discriminate between those different inorganic pigments with the same color using IRR images.

The study of the influence of overlapping layers of different inorganic pigments gives yields information about the best way to observe preparatory drawings. The observation of preparatory drawings should be focused on the location on the artwork presenting only “transparent” pigments.

Considering these initial results, a methodology for the preliminary assessment of pigments used in ancient paintings can be proposed. The observation of a first global image of the artwork obtained with an IRR camera allows to focus on the area where detection of preparatory drawing is possible. Diagnosis of pigments used by the artist is also achievable. Obtaining a unique image of the entire artwork is a crucial first step in the methodology proposed in this project for the study of old paintings. Indeed, it

enhances the strategy applied in the analysis by other techniques such as X-ray fluorescence (XRF), Fourier transform infrared spectroscopy (FTIR) [138], Raman spectroscopy [139], confocal X-ray fluorescence spectrometry (CXRF), etc.

3.3. Multilayered samples CXRF study

In theory, confocal micro X-ray fluorescence (CXRF) provides compositional and spatial information without sampling (which is not the case with SEM-EDX sampling). CXRF extends the capabilities of the micro X-ray fluorescence to in depth of profiling multilayered materials, as previously explained (cf. Chapter 1.2).

In this part of the study, its functionality when studying controlled multilayered samples was tested. In order to do so, the depth resolution the µXRF-CONCHA set-up was measured as a function of the energy (see Fig. 46, Chapter 2.1.2). Besides, the depth resolution (FWHM) depends on the chemical composition of the sample. Moreover, the shape of the depth profile depends on the composition, density and thickness of the sample.

The results obtained with the µXRF-CONCHA set-up will be compared below with those obtained using two other CXRF systems. The aim of these measurements is to compare the composition and sequence information obtained by analyzing the same experimental paint layers using the three different setups outline in this thesis in order to determine if some differences inherent to those existing between the three devices appear.

3.3.1. Thin foil samples study with µXRF-CONCHA

The success of in-depth profiling of multilayered materials depends on several phenomena. To illustrate them, several experiments were performed. First, a superposition of three reference thin layers (Cr, Ni and Pb, 1 µm thick, from Goodfellow) was analyzed. The layers were separated by organic material (kapton polyimide film used in analog photography) with a thickness around 200 µm, superior to the depth resolution of the CXRF device (Fig. 86). The scan was obtained with 10 µm step size and a counting time of 120 s per point. The three layers in the depth profile were observable without any trouble (Fig. 86). The CXRF measurement objective was completed by determining the composition and sequence of the layers.

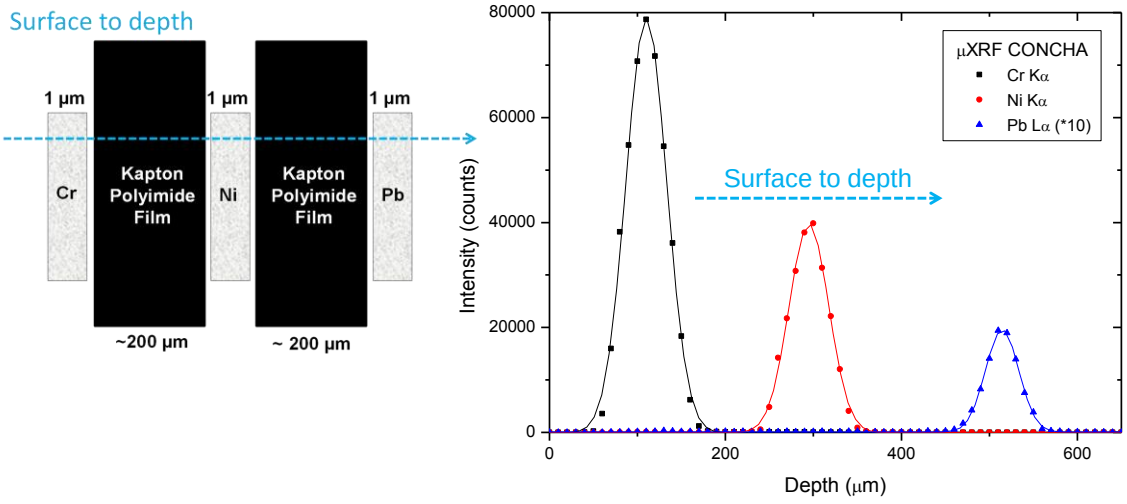

Fig. 86. Depth scan of a superposition of three reference thin layers (Cr, Ni and Pb, 1 µm thick).

3.3.2. Experimental paint multilayers study with µXRF-CONCHA

However, for more complex unknown samples, such as cultural heritage samples, it might be more difficult to differentiate the layers. To test this assertion, experimental paint multilayers were analyzed.

Paintings work on a layer-by-layer system basis. First, the artist prepares the ground layer, then the priming layer. He then adds one or several pigment layers, usually by melting several pigments (organic and inorganic) together and finally, but not always, applying a layer of varnish on the artwork. The interests of CXRF study of antique paintings resides in the definition of the chemical composition of every layer composed by inorganic pigments, with particular interest in the ground layer, the priming layer and the pigment layers.

Previously, cross sections of these samples were also studied using optical microscopy in order to evaluate the thickness of each layer and to check the accuracy of the CXRF analyses. The preparation and measurements of these cross sections were then made at the IIE of the UNAM with the invaluable help of Víctor Santos. The average thickness of the layers was measured with AxioVs40 software (version 4.8.2.0 copyright © 2006-2010 Carl Zeiss MicroImaging GmbH) and is summarized in Tables 16 and 17.

Table 16. Range of thickness of each layer of the experimental paint multilayers (error estimated ± 1 µm).

Support name	Priming layer	1st pigment layer	2nd pigment layer	3rd pigment layer
	Thickness (µm)			
B1	White lead	White lead	Malachite	Yellow ochre
	12-25		6-31	8-17
B2	White lead	Lead-tin yellow	Hematite	Azurite
	13-27	12-39	5-10	9-24
B3	White lead	White lead	Lead-tin yellow	Vermilion
	18-51		7-12	6-10
B4	White lead	Hematite	Azurite	White lead
	28-77	5-23	10-30	8-19
B5	White lead	Hematite	Vermilion	Lead-tin yellow
	30-50	3-7	8-14	10-25
R1	Hematite	White lead	Malachite	Yellow ochre
	19-39	9-38	12-38	8-20
R2	Hematite	Lead-tin yellow	Hematite	Azurite
	6-14	8-15	4-7	11-36
R3	Hematite	White lead	Lead-tin yellow	Vermilion
	6-17	5-16	10-31	11-15
R4	Hematite	Hematite	Azurite	White lead
	7-30		10-42	8-20
R5	Hematite	Hematite	Vermilion	Lead-tin yellow
	10-16		5-10	25-46

Table 17. Range of thickness of each layer of the experimental paint multilayers (error estimated ± 1 µm).

Support name	Priming layer	1st square	2nd square	3rd square	4th square
	Thickness (µm)				
B6	White lead	Malachite	Azurite	Vermilion	Yellow ochre
	20-56	21-35	11-32	12-17	6-11
R6	Hematite	Malachite	Azurite	Vermilion	Yellow ochre
	6-31	12-37	30-55	9-20	7-11

As illustrated in Fig.87 and Table 18, the CXRF depth profile resulted in the correct information about the sequence and composition of the layers. All the in-depth scans were composed of 40 spectra taken with 5 µm step size and a counting time of 120 s per point.

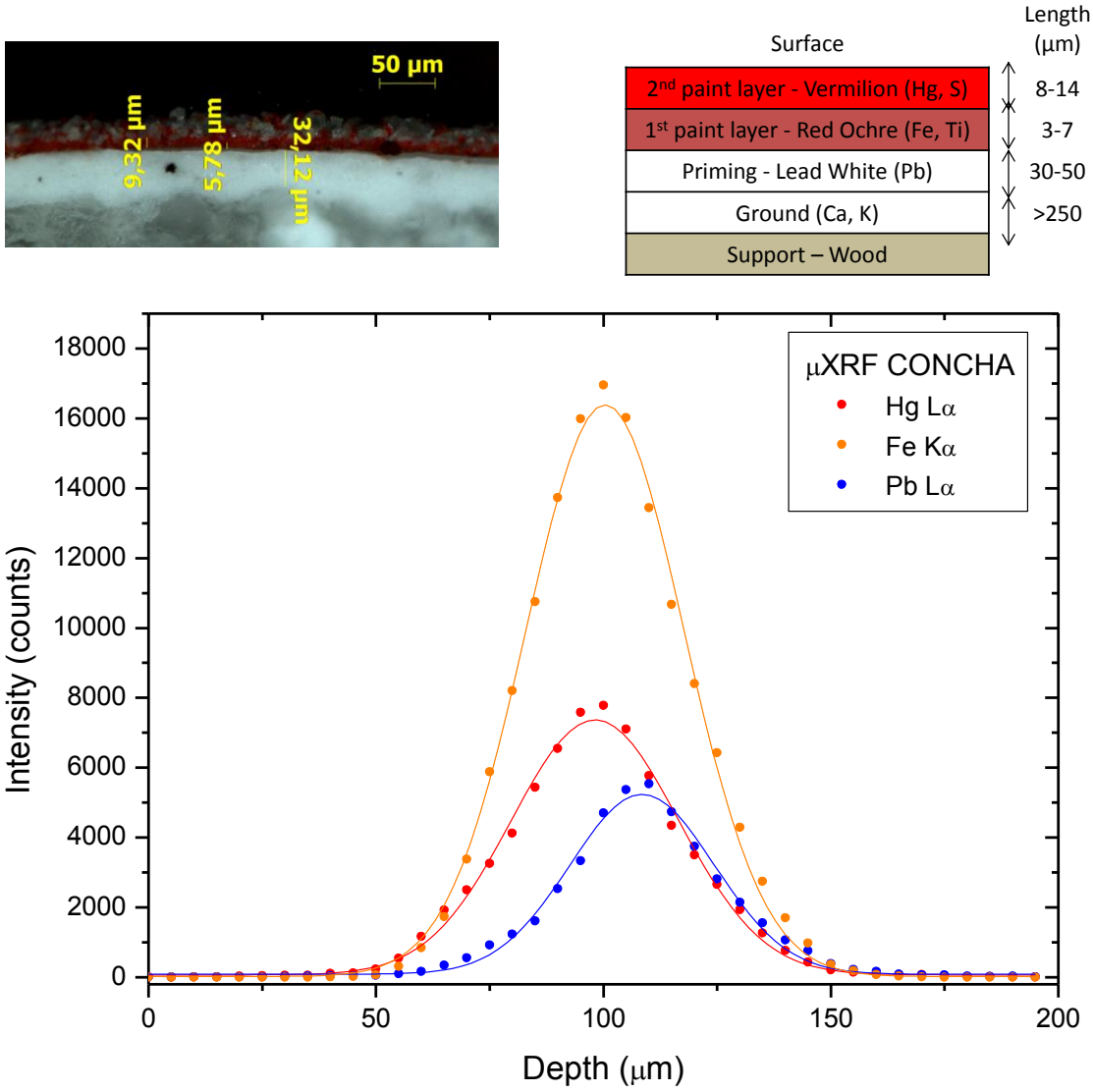

Fig. 87. Depth profile of an experimental paint multilayer.

Table 18. Results of depth profile of the experimental paint multilayer.

Layer	FWHM (µm)	Xc (µm)	Distance between Xc (µm)
Hg Lα	43 ± 3	98 ± 3	2 ± 3
Fe Kα	41 ± 3	100 ± 3	9 ± 3
Pb Lα	37 ± 3	109 ± 3	

X-ray interference effects must be taken into account in certain cases. Indeed, some pigments used in the 16th century were composed by heavy elements such as lead (Pb) or mercury (Hg), both very powerful X-ray absorbing elements. The occurrence of this effect is shown in Fig. 88 and 89 (Table 19). The second sample was composed of two successive layers of white lead, so the resulting white lead layer was thicker in this case. Consequently, the information about the ground layer has disappeared. The X-rays emitted by the calcium composing the ground layer were totally absorbed by the upper white lead layer and as a result could not reach the X-ray detector. Indeed, depth profile information showed to depend strongly on the absorption effect i.e. in the composition, density and thickness of different layers presented in the sample. Therefore, by using only CXRF, it is impossible to know if some elements and or layers are masked in the depth profile. For example, in Fig.87, in the depth profile of a four layered sample, the information about the ground layer is lost and only the first three layers are detected.

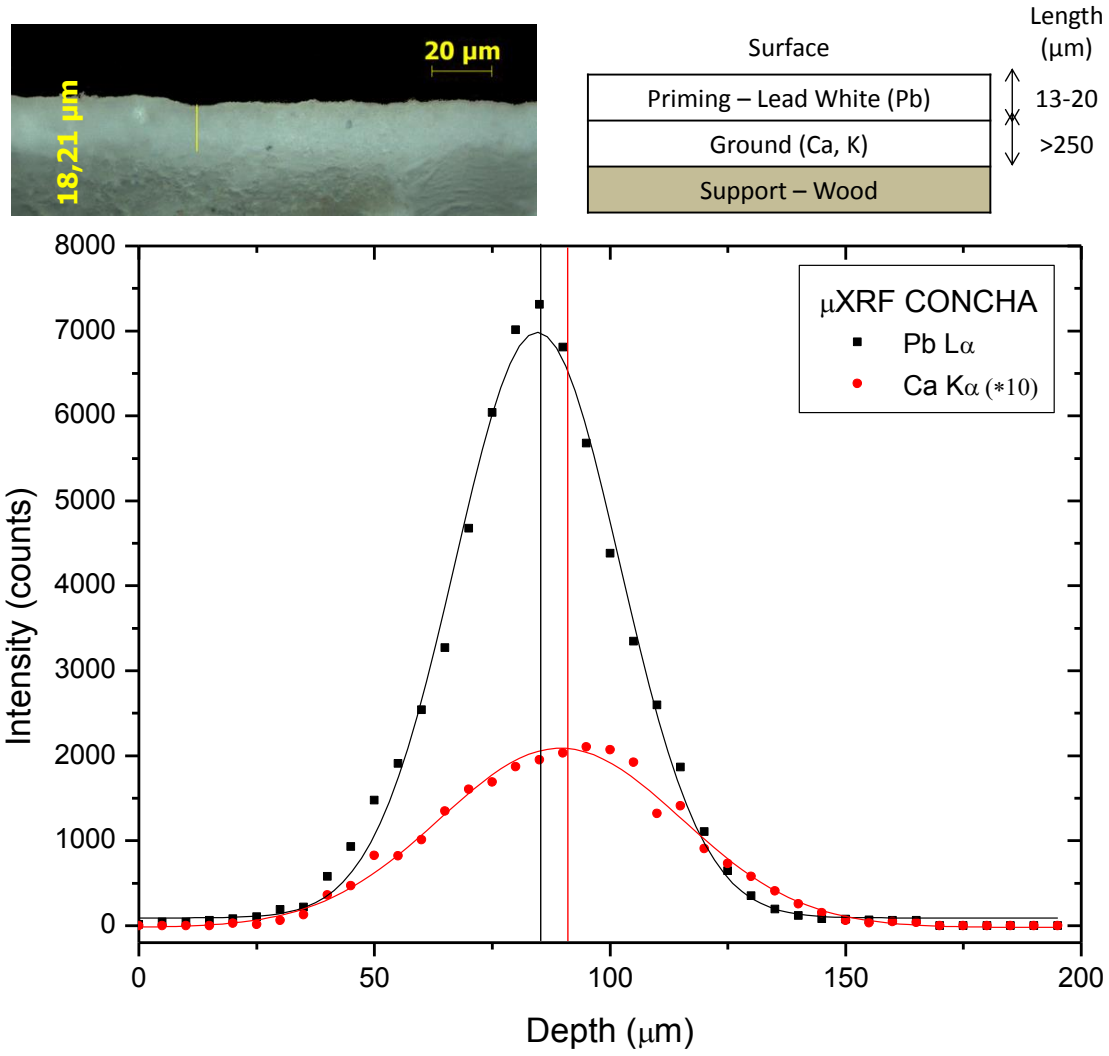

Fig. 88. Depth profile of an experimental paint multilayer.

Table 19. Results of depth profile of the experimental paint multilayer.

Layer	Xc (µm)	Distance between Xc (µm)
Pb Lα	85 ± 3	5 ± 3
Ca Kα	90 ± 3	

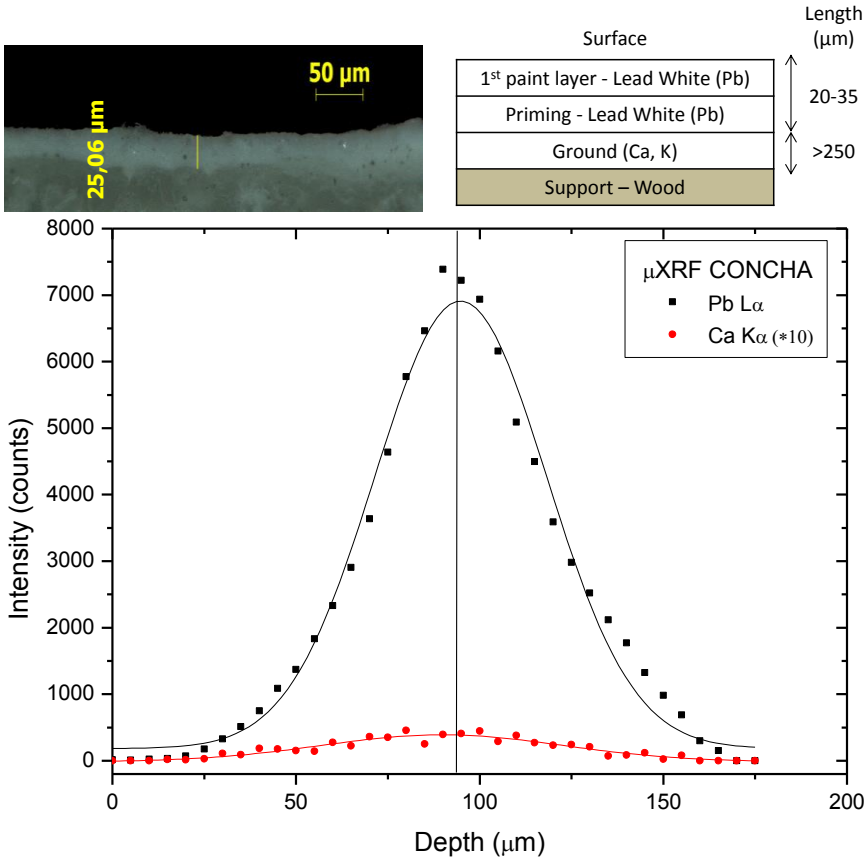

Fig. 89. Depth profile of an experimental paint multilayer with a white lead layer thicker than the previous example (Fig. 88). The depth information about the Ca layer is not registered due to absorption effect.

Nevertheless, the experimental paint multilayered samples are relatively simple compared with older paintings. They do not present a mixture of different pigments and are only composed with inorganic pigments. Still, it is possible to evaluate the difficulties inherent to old paintings by looking at samples presenting two or more layers composed and defined by the same chemical elements. This is the case presented in Fig. 90 where a five-layer sample shows two layers defined by the presence of lead (white lead) separated by two distinct pigments layers (azurite and red ochre). The lead depth profile presented a slightly distorted shape due to the presence of another layer in depth (in black, Fig. 90). The lead depth profile was fitted by two Gaussian curves (in green, Fig. 90). The distance between those two layers (~25 µm, value estimated by OM) is below the depth resolution (~37 µm for Pb Lα energy) which did not allow to separate them. On the other hand, the absorption effect was so strong that it made the detection of the second lead layer difficult. It should be noted that the observation of the deformation of the curve was possible only with previous knowledge about the exact composition and sequence of the sample. This is another important limitation of the CXRF technique which should be considered when interpreting depth profile results.

Moreover, the depth profile of the four-layer sample was measured (Fig. 91). This sample is identical to the five-layer sample without the second white lead layer. The accuracy of the double fitting on the Pb depth profile from the five-layer sample is confirmed comparing the distance between the centroids (Xc) obtained for both samples (Table 20). Finally, the FWHM of the second Pb layer (25±3 µm) is smaller than that of the first layer (37±3 µm) in agreement with the absorption effect (cf. Chapter 1.2.7).

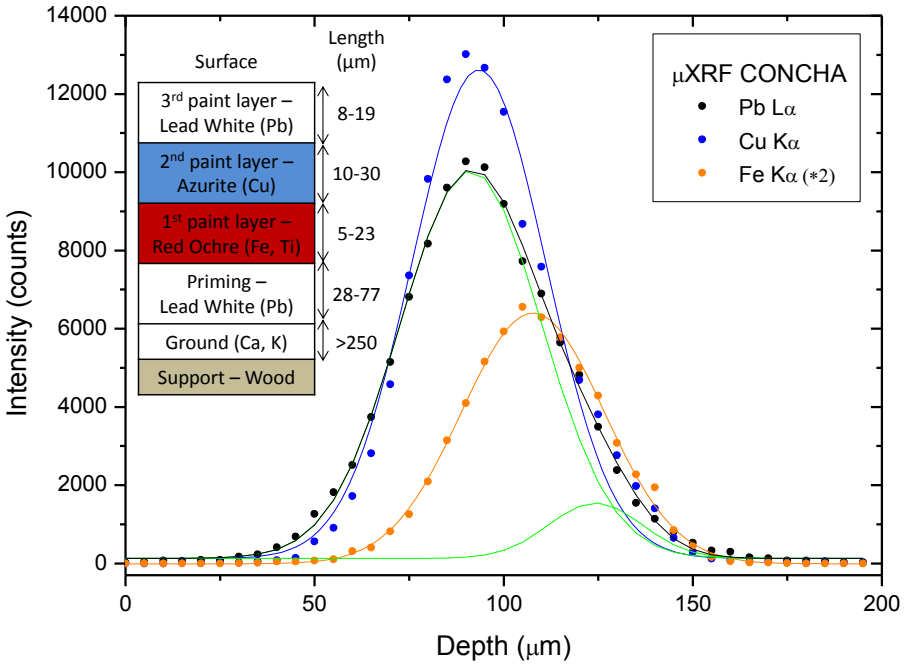

Fig. 90. Depth profile of the five-layer sample.

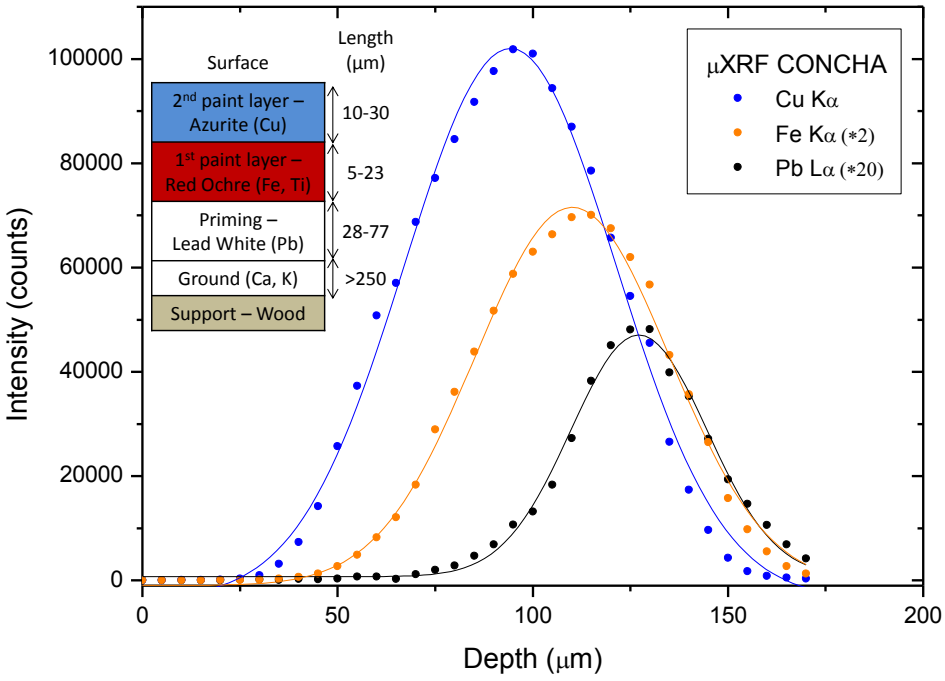

Fig. 91. Depth profile of the four-layer sample.

Table 20. Results of the depth profiling of the experimental paint multilayers.

Layer	Five-layer sample		Four-layer sample	
	Xc (μm)	Distance between Xc (μm)	Xc (μm)	Distance between Xc (μm)
Pb	91 ± 3	2 ± 3		
Cu	93 ± 3	15 ± 3	94 ± 3	16 ± 3
Fe	108 ± 3	16 ± 3	110 ± 3	17 ± 3
Pb	124 ± 3		127 ± 3	

3.3.3. Intercomparison of three CXRF systems

The intercomparison of the performance of CXRF systems is a mandatory step that will pave the way in international collaboration studies in the field of cultural heritage.

The results presented in this thesis were obtained using two other CXRF systems, on the one hand using the LouX^{3D} at the C2RMF laboratory in Paris [11] and on the other hand using the CXRF setup at AGH University of Science and Technology in Krakow [59]. These systems are comparable to those of the µXRF-CONCHA. Nevertheless, as previously presented (Chapter 2.2), the specifications of each set-up are slightly different.

The aim of these measurements was to compare the composition and sequence information obtained by analyzing the same experimental paint multilayered samples. The objective is to determine if any differences appeared to be inherent to those existing between the three devices. To evaluate the accuracy of the intercomparison, all the experimental samples were studied using the same conditions (50 kV, 600 µA, 5 µm steps and 120 s/point) with the exception of the Poland CXRF setup which measurements were performed with 1000 µA. A selection of the results can be seen in Appendix IX.

Previously, the depth resolution as a function of the energy was obtained for each setup using thin foils of different chemical elements (Fig.92, repetition of Fig. 51). The depth resolution depends on the applied optics and the analyzed element. It is specific to each CXRF system and might be affected by absorption effect. The FWHM measured in the paint samples (Table 21) presented the same behavior as the depth resolution graphics (Fig.92). In Table 21, the slight variation of the depth resolution for each element and each setup depending on the sample configuration is noted. The maximum deviance is also noted for Ti Kα with LouX^{3D} system (23 µm between the lowest and the highest measured value).

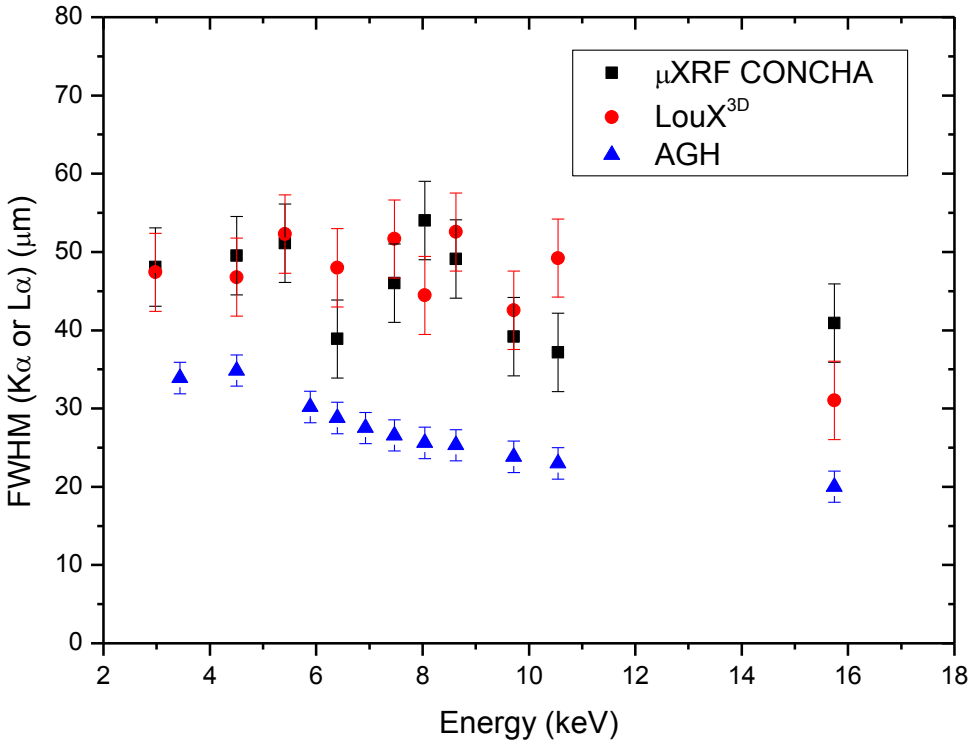

Fig. 92. Depth resolution of the three CXRF setups as a function of the emitted energy (repetition of Fig. 51).

Table 21. Lowest and highest FWHM values observed in the 12 paint multilayer samples.

Element	FWHM (μm)					
	Low	High	Low	High	Low	High
Sn-Lα	55±3	56±3	57±3	59±3	37±3	38±3
Ca-Kα	57±3	59±3	54±3	66±3	45±3	45±3
Ti-Kα	56±3	58±3	45±3	68±3	26±3	34±3
Fe-Kα	52±3	66±3	43±3	64±3	28±3	39±3
Cu-Kα	49±3	54±3	49±3	59±3	26±3	30±3
Pb-Lα	36±3	42±3	42±3	51±3	23±3	31±3
CXRF device	μXRF-CONCHA		LouX^{3D}		AGH CXRF set-up	

The results obtained analyzing the experimental paint multilayered samples show that, besides design differences between the three setups, measured depth profiles are similar (Fig. 93). They also provided the same chemical information and sequence of layers. Variations could be observed due principally to the sample nature. Finally, the differences of depth resolution between the CXRF devices do not affect the analytical results (Fig. 93).

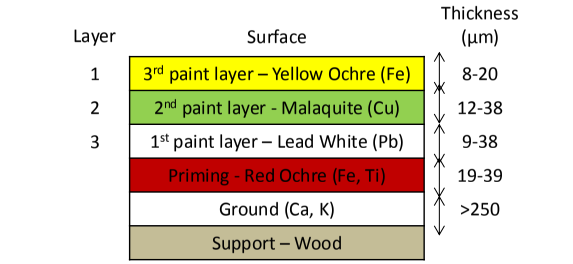

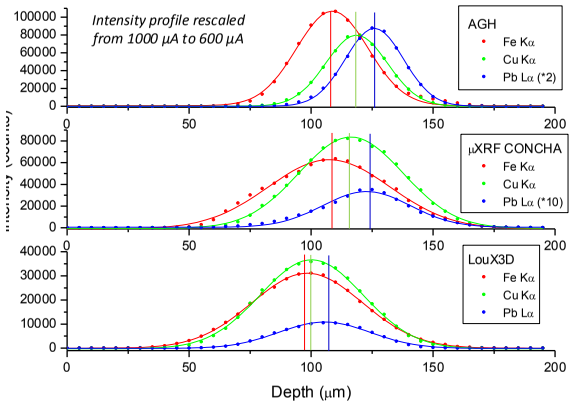

Distance b/w layers	ΔXc (μm) Concha	ΔXc (μm) LouX3D	ΔXc (μm) AGH
1-2	9 ± 3	2 ± 3	10 ± 3
2-3	7 ± 3	5 ± 3	7 ± 3

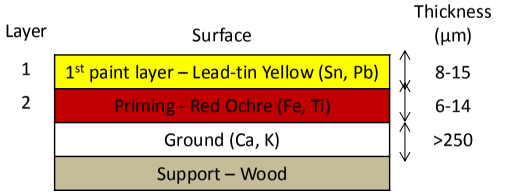

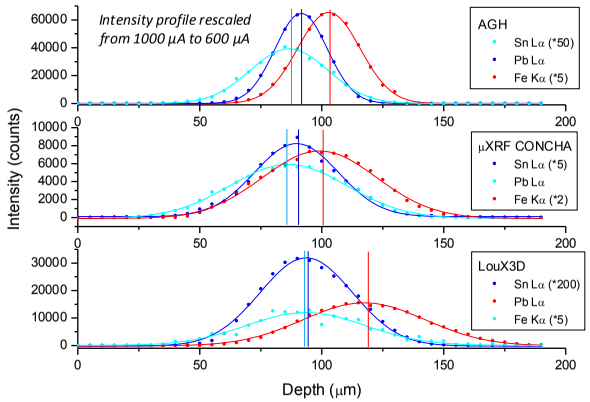

Distance b/w layers	ΔXc (μm) Concha	ΔXc (μm) LouX3D	ΔXc (μm) AGH
1a-1b	4 ± 3	1 ± 3	5 ± 3
1b-2	9 ± 3	23 ± 3	11 ± 3

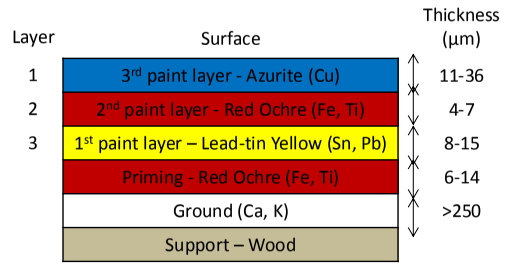

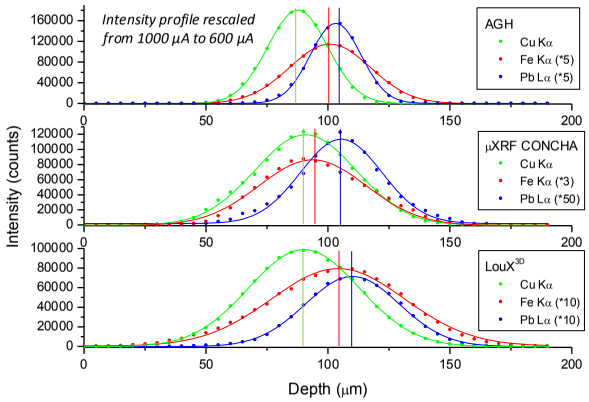

Distance b/w layers	ΔXc (μm) Concha	ΔXc (μm) LouX3D	ΔXc (μm) AGH
1-2	3 ± 3	14 ± 3	13 ± 3
2-3	11 ± 3	6 ± 3	2 ± 3

Fig. 93. Depth profiles of 3 of the 12 analyzed samples with the three CXRF devices.

3.3.4. Conclusions of the CXRF study

In conclusion, the μXRF-CONCHA set-up allows to carry out the compositional analysis with depth resolution in a nondestructive way. In the study of old paintings, it may provide complementary results to the classical extraction of stratigraphic micro-samples. This technique also gives access to depth compositional profiles of the pictorial layers for the purpose of identifying the inorganic pigments palette and techniques used by the artist. However, the data interpretation is not trivial.

The absorption effect is the principal limitation of this technique. Results obtained on experimental paint multilayered samples allowed us to propose a specific methodology to study original old paintings whose chemical constitution would be unknown and more complex.

In order to simplify the interpretation of a particular depth profile, the characterization of each specific layer must be achieved using a specific area on the painting. The principal problem when considering 16th century paintings is the use of pigments composed of heavy elements (e.g. Pb or Hg) which masked the signals given by the ground layer or the priming layer. As proposed, the first depth profile should be focused in a painting area free of heavy elements. To select this area, the results obtained previously with IRR and XRF should be used. Once ground and priming layers have been clearly defined by CXRF, the second step of the study should focus on pigment layers containing heavy elements. Finally, the CXRF analysis ends with study of interesting details such as *pentimenti* or a succession of pigments layers.

All this information can help to specify or compare the technique of the artist, the choices made during his or her execution, to detect the presence of original painting layers under restoration interventions or to evaluate its condition for conservation.

There exists another limitation inherent to the depth resolution. It has proven to be difficult to differentiate layers defined by the same chemical element when the layers are closer or thinner than the depth resolution. It is possible to reduce the depth resolution using polycapillary lenses with lower working distance, which is a safety issue when dealing with invaluable artwork.

Finally, the lack of organic material information might be emphasized. In the future, it would be interesting to develop and evaluate the fiber optic mid-Fourier transform infrared spectroscopy (FTIR) [140]. Depending on its usefulness and the technological possibilities, the design of a combined CXRF-fiber optic mid-FTIR setup working *in situ*, could be considered.

In light of the CXRF intercomparison study, it is possible to compare results obtained by different setups.

Chapter 4. Alonso Vázquez paintings study

In this chapter the study of seven paintings attributed to the artist Alonso Vázquez is presented. First, the painter and the seven artworks in question are presented. Then, the methodology applied is explained and each technique used in the study is illustrated with emblematic examples. In conclusion, a summary of the study of all paintings is proposed.

4.1. Alonso Vázquez and their artworks

Alonso Vázquez was a painter from Seville (Spain) who was one of the first Spanish artists to work in the New Spain in 1603. This part of the thesis is written in Spanish as required to claim the international PhD title. At the end of this chapter a synthesis of the seven artworks studied is available in English (cf. Chapter 4.1.8).

Sevilla se benefició de la importancia que adquirió el comercio con América. En las artes, afluyeron numerosos maestros foráneos en especial flamencos e italianos y muchas obras penetraron en la ciudad fundamentalmente a través de la actividad comercial del puerto del Guadalquivir. Esos maestros y esas obras contribuirán a configurar al peculiar desarrollo de la escuela pictórica sevillana [141].

La creación de riqueza facilitó la posibilidad de financiar numerosas actividades constructivas, escultóricas y pictóricas. Durante la segunda mitad del siglo XVI, se empieza a constatar la actividad de artistas locales dotados de cierto talento creativo. En la última generación de artistas sevillanos del siglo XVI destaca la presencia de Alonso Vázquez quien practicó una pintura de carácter manierista que, en su momento, tuvo una gran aceptación [142].

4.1.1. Vida del pintor (Life of the artist)

Su nombre completo era según las fuentes Alonso Vázquez Perea [143]. No obstante, no usaba su segundo apellido, lo que hace difícil distinguirlo en los documentos oficiales de homónimos. No se conoce la fecha ni el lugar de nacimiento de este pintor [144]. Lo más probable, debido a lo que se sabe de él con certeza, es que fuera originario de la ciudad de Sevilla. Se puede tener en cuenta que, en el preámbulo de su testamento, Vázquez se considera “natural de la ciudad de Sevilla” [145].

Se casó con Doña Inés de Mendoza el 25 de septiembre de 1588 en la parroquia de Omnium Sanctorum de Sevilla [145]. Tuvo con ella ocho hijos. En el momento de su testamento, les nombra como Diego, doña María de Vargas, Antonio y Alonso mientras cuatro habian ya fallecido: un varón (Juan) y tres mujeres (Francisca, Francisca y Melchora) [145].

No se sabe con quién pudo realizar su formación [144]. El historiador del arte Juan Miguel Serrera define su estilo dentro del Manierismo tardío [146]. El estilo manierista se caracterizó por el predominio de colores vivos artificiales y la representación de la figura humana desproporcionada y en posiciones poco naturales, pero siguiendo en cierto modo "la bella maniera", es decir, la habilidad técnica de los grandes maestros (Leonardo Da Vinci, Rafael Sanzio y Miguel Ángel). Serrera insiste también en su pertenencia al círculo

artístico del pintor flamenco Martín de Vos, proponiendo que las obras de Vázquez estén basadas en sus estampas [147]. El historiador del arte José Rogelio Ruiz Gomar Campos describe la tendencia de Vázquez a pintar cuerpos enormes y musculosos. Dice de él que "es un buen dibujante y anatomista que gusta de los escorzos; es poseedor de un eficaz colorido y revela fruición por imprimir a sus ropajes artificiosos pliegues" [148]. En su campo de especialidad como pintor se incluía el policromar retablos y esculturas [147] junto a su aptitud como decorador de techos y policromador de rejas [145].

La carrera artística de Alonso Vázquez se divide en dos etapas:

- en Sevilla hasta 1603, con el año 1588 como primera referencia al artista,
- en México desde 1603 hasta su muerte en 1607.

De la etapa sevillana se conocen gran número de referencias documentales y se conservan numerosas obras, unas documentadas y otras firmadas y fechadas [147]. La primera noticia de su trabajo en Sevilla data de 1588 mientras pintaba la "Sagrada Cena" de la Cartuja de Santa María de Las Cuevas [146]. Durante más de 15 años, Vázquez desarrolló una intensa labor, pintando al servicio de la mayoría de las órdenes religiosas y de los hospitales pertenecientes al Arzobispado sevillano, así como de mercaderes y nobles sevillanos [147]. Fue reconocido como uno de los maestros más importantes y representativos del último cuarto del siglo XVI sevillano junto con Vasco de Pereira y Francisco Pacheco [146] cuando fue contratado con ellos para pintar obras del túmulo levantado en 1598 en la catedral de Sevilla con motivo de las exequias del rey Felipe II [149].

Alonso Vázquez partió de Cádiz a la Nueva España con el virrey Juan de Mendoza y Luna, Marqués de Montesclaros, el 29 de junio de 1603 dejando su esposa y sus hijos en Sevilla [150].

A partir del 26 de octubre de 1603 [150], día en que el virrey y su séquito entraron en la ciudad de México, Alonso Vázquez realizó una serie de trabajos al servicio del virrey marqués de Montesclaros. De esas obras realizadas en México, la mayoría se han perdido o no se han identificado [144]. De hecho, se tiene pocas referencias documentales de su etapa mexicana [145, 147]. Basándose en la "Inmaculada" del Hospital de Jesús (México) y el "Martirio de San Hipólito" atribuidas a Alonso Vázquez, Serrera califica sus obras mexicanas como una prolongación de su etapa sevillana dentro del Manierismo tardío [147]. Alonso Vázquez falleció por causas naturales en la mañana del 13 de abril de 1607 en la ciudad de México [145]. Había permanecido en territorio mexicano 3 años, 7 meses y 1 semana [145].

Alonso Vázquez no fue el primer pintor español que trabajó en la Nueva España, pero sí fue de los primeros (según las fuentes bibliográficas, el primer pintor hubiera sido el andaluz Cristóbal de Quesada en 1538 o Juan de Najara o Nájera [151]). En esos pintores españoles, primeros llegados a Nueva España, se está buscando, hoy en día, los orígenes del arte pictórico colonial mexicano. Por lo tanto, el estudio de las obras de Alonso Vázquez resulta clave para los historiadores del arte para poder evaluar su influjo real sobre la evolución del arte en México. Pero antes de poder hacer ese trabajo, resulta ya necesario determinar qué obras de ese pintor existen todavía y efectuar un trabajo de identificación imprescindible, ya que no están firmadas.

El estudio realizado resulta de gran interés para poder comparar las obras mexicanas atribuidas a Vázquez con las de su anterior etapa sevillana. El análisis comparativo permitirá definir con mayor precisión las técnicas pictóricas y la paleta de ese pintor con aportes significativos para el estudio de la pintura Novohispana y la influencia de las

escuelas pictóricas españolas y europeas en el México colonial. A continuación, presentamos las siete obras estudiadas.

4.1.2. "Sagrada Cena"

La "Sagrada Cena" o "Ultima Cena" es un óleo sobre lienzo que mide 318 × 402 cm (Fig. 94) [142].

Según el historiador del arte Enrique Valdivieso, "la composición de esta obra parece derivar de varias estampas flamencas, de las que el artista ha extraído diferentes elementos, fundiéndolos después con notoria habilidad" [144]. Destaca en esta escena la última cena de Jesús junto a los apóstoles. Se puede apreciar los detalles de los alimentos y de las vajillas que se disponen sobre la mesa y en el suelo del cenáculo.

Es una pintura realizada en 1588 para el refectorio de la Cartuja de Santa María de las Cuevas de Sevilla [147, 152, 153]. Si su atribución es cierta [144], se trata de la obra más temprana conocida de Alonso Vázquez. Se conserva desde 1840 en el Museo de Bellas Artes de Sevilla [142].

4.1.3. "Virgen del Valle"

La "Virgen del Valle" o "Virgen del Pozo Santo" es un óleo sobre tabla que mide 213 × 123,5 cm (Fig. 95) [154].

La obra representa a la Virgen con el Niño en su regazo mientras es coronada por dos ángeles y acompañada por otros dos que portan instrumentos musicales. A sus pies se narra la milagrosa intervención de la Virgen para conseguir que salga indemne un niño del pozo al que había caído y en un segundo plano se presenta un paisaje de un valle [155].

En 1978, Valdivieso la atribuyó a Alonso Vázquez. Esa atribución fue corroborada por Serrera quien identificó esa obra como la de la "Virgen del Valle". La "Virgen del Valle" fue la pintura centrica del retablo que Doña Beatriz Pérez encargó a Vázquez el 2 de julio de 1597 para la iglesia del Convento de Santa María de Jesús de Sevilla [146]. La obra perdió su titulacion original al desmembrar el retablo y fue presentada como "Virgen del Pozo Santo". El hecho que esa obra fuera inicialmente parte de un retablo está confirmado con los daños observados durante su última restauración en 1999. Se notificó una intervención anterior en la que se modificó el formato original de la tabla de medio hexágono a rectángulo [155].

Si esa atribución es correcta, la obra fue ejecutada en 1597 según el contrato [146]. Fue comprada por el Deán Manuel López Cepero a raíz de la desamortización de los bienes eclesiásticos [146] y, finalmente, donada en 1860 por sus herederos al Cabildo de la Catedral de Sevilla, su ubicación actual [154].

Esa obra fue restaurada en 1999 por el Instituto Andaluz del Patrimonio Histórico con motivo de la exposición "Velázquez y Sevilla" del cual se tiene el informe de la investigación efectuada [155].

Fig. 94. “Sagrada Cena”.

Fig. 95. “Virgen del Valle”.

Fig. 96. "San Pedro Nolasco despidiéndose de Jaime I El Conquistador".

Fig. 97. "San Pedro Nolasco redimiendo cautivos".

4.1.4. La serie sobre la vida de San Pedro Nolasco ("Nolasco" series)

Pacheco relata en su "*Arte de la pintura*" que fray Juan Bernal, prior del convento de la Merced Calzada de Sevilla (actual edificio del Museo de Bellas Artes de Sevilla), lo contrató junto a Alonso Vásquez en 1600 para realizar una serie pictórica sobre la vida de San Pedro Nolasco y San Ramón Nonato destinadas a decorar el claustro principal [142, 144, 152]. Sólo se conservan dos de las obras que Vázquez pudo haber realizado. Permanecen en el Museo de Bellas Artes de Sevilla y representan a "San Pedro Nolasco redimiendo cautivos" y "San Pedro Nolasco despidiéndose de Jaime I El Conquistador" [144].

4.1.4.1. "San Pedro Nolasco despidiéndose de Jaime I El Conquistador"

Se trata de un óleo sobre lienzo que mide 208 × 250 cm (Fig. 96) [142].

Del conjunto de obras estudiadas, es la única firmada por Alonso Vázquez y fechada en el año 1601 [152].

La obra se divide horizontalmente en dos planos. En el superior, a la izquierda, aparece San Pedro Nolasco despidiéndose de Jaime I el Conquistador mientras que, a la derecha, se abre en la lejanía un paisaje marítimo con un puerto [156]. En el plano inferior, a la derecha, dos personajes sentados a una mesa cubierta con un mantel rojo parecen estar concluyendo un trato mientras que, en el ángulo inferior derecho, San Pedro Nolasco supervisa la maniobra de un grupo de porteadores [156].

4.1.4.2. "San Pedro Nolasco redimiendo cautivos"

Se trata de un óleo sobre lienzo que mide 206 × 250 cm (Fig. 97) [142].

Al contrario que el precedente, éste no está ni firmado ni fechado. Por lo tanto se propone una fecha de ejecución entre 1600 (año del contrato) y 1603 (año de su viaje a México).

Esta escena podría tratarse de una de las redenciones que San Pedro Nolasco efectuó en el Norte de África en la que se exalta a la Orden de la Merced como redentora de cautivos [142]. Se puede diferenciar tres planos distintos en la obra. En la parte superior izquierda, se representa el momento en el cual San Pedro Nolasco concluye el trato económico con un Sarraceno. La escena principal se desarrolla en el plano central con San Pedro Nolasco y el mismo Sarraceno supervisando al grupo de los cautivos representados en la zona inferior izquierda [142].

4.1.5. “Inmaculada”

La “Inmaculada” o “Virgen Inmaculada” es un óleo sobre lienzo que mide 283 × 206 cm (Fig. 98) [147].

El año de ejecución de la obra y su lugar de origen son desconocidos [147]. Sólo se sabe que fue desamortizada en 1840 y permanece en el Museo de Bellas Artes de Sevilla [142].

En esa obra, la Inmaculada aparece triunfante sobre el dragón demoniaco, acompañada de ángeles. En la parte inferior, está representado un paisaje donde se advierten los símbolos de las advocaciones marianas [142]. Fue atribuida estilísticamente a Alonso Vázquez por Serrera. La única referencia documental que se tiene a día de hoy sobre una Inmaculada pintada por Vázquez está mencionada por Palomero Páramo. Se trata de una pintura que interesaba el misionero agustino fray Pedro Solier [145]. Se refiere a un cuadro que debió de ser pintado en torno a 1605 en México del cual dice que ignora su destino final, que, “en caso de aparecer, resolvería el problema de atribución que hoy tienen las Vírgenes apocalípticas del Museo de Sevilla y del Hospital de Jesús, de México”.

Fig. 98. “Inmaculada”.

4.1.6. “Martirio de San Hipólito”

Se trata de un óleo sobre lienzo que mide 103 × 73 cm (Fig. 99) [147].

La obra conmemora la caída de la capital azteca México-Tenochtitlán ocurrida el 13 de agosto de 1521, justo el día de San Hipólito [157]. La composición se divide en dos planos. En el fondo se aprecia la plaza de una iglesia ocupada por soldados que portan escudos decorados con águilas bicéfalas doradas. En el centro del cuadro, San Hipólito yace de cabeza, sus pies están atados y va arrastrado por un caballo que corre en medio de observadores civiles y militares [157]. El santo mártir está flanqueado del lado izquierdo por un indio americano vestido con taparrabos y un tocado simple de plumas en el cabello atado. No se trata de una representación de un azteca sino una versión simbólica del indio salvaje de piel rojiza [157]. Al lado derecho del Santo, está representado Hernán Cortés hincado y con las manos unidas en gesto de oración [157]. En el frente del pilar que aparece detrás de la figura orante de Hernán Cortés quedan restos de una leyenda, de la que sólo son identificables el nombre de un mes y las cifras correspondientes a un día y año: el 13 de agosto de 1526, día de San Hipólito y de la conquista de la ciudad de México por Hernán Cortés [147]. Finalmente, encima del pilar, la escultura de un ángel sostiene un medallón de forma ovalada sobre el que se lee la inscripción “Salve Gloria” [157].

Serrera identifica esa obra como la que componia el triptico del altar mayor de la iglesia del Hospital de Jesús de la ciudad de México fundado por Hernán Cortés. Esa pintura estuvo desubicada a partir de 1657 y, hoy en día, está conservada en el Museo Nacional de Historia (MNH) del Castillo de Chapultepec en la ciudad de México [147]. Serrera destaca que debido a sus restauraciones es imposible precisar la autoría del “Martirio de San Hipólito” y que un estudio técnico contribuiría a confirmar tales suposiciones [147]. Si su atribución es correcta, esa obra fue realizada entre los años 1605 (año del contrato) y 1607 (año de su muerte) y la imagen de Hernán Cortes sería una de sus representaciones más antiguas hasta ahora conocida [147].

Esa obra tiene otra historia debido a su valor simbólico. Durante el siglo XIX, estuvo atribuida al artista Rodrigo de Cifuentes [151]. No obstante, Rodrigo de Cifuentes nunca existió y resultó ser un invento del conde de la Cortina, cuando, en 1853, escribió su biografía en el “*Diccionario Universal de Historia y Geografía*” [158]. En aquella época, en que la nación mexicana estaba creciendo y el nacionalismo se desarrollaba, el personaje de Rodrigo de Cifuentes encarnó el primer gran artista mexicano de la Nueva España en la propaganda nacionalista. El historiador del arte Pedro Ángeles expone las razones de la invención histórica de ese personaje fundamental para defender la idea del origen de la pintura mexicana [151]. Durante ese proceso de propaganda, se le atribuyeron varias obras de arte y hasta se falsificaron algunas cubriendo firmas originales con la supuesta suya o añadiéndola simplemente [157]. En 1983, el “Martirio de San Hipólito” fue restaurado y se eliminó la firma de Cifuentes por considerarla un falso histórico [157]. Esta acción radical borró un aspecto muy importante en la historia del objeto.

Más allá del estudio del pintor Alonso Vázquez, en el caso del “Martirio de San Hipólito”, se plantean otras preguntas:

- ¿La representación de Hernán Cortés es contemporánea a la representación de San Hipólito?
- ¿Las inscripciones ubicadas en la zona donde está representado Hernán Cortés son contemporáneas al resto de la obra o fueron añadidas posteriormente?

- ¿Quedan restos de alguna firma del pintor original (o sea, Alonso Vásquez) escondida en el momento de la falsificación del siglo XIX?
- ¿Quedan restos de la firma falsa de Rodrigo de Cifuentes?

4.1.7. "Virgen de las Uvas"

La "Virgen de las Uvas" o "Virgen apocalíptica" o "Inmaculada Concepción" es un óleo sobre lienzo que mide 145 x 103 cm (Fig. 100) [159].

El año de ejecución de la obra es desconocido. Solo se sabe que permanece hoy en día en la Sala Capitular de la Catedral Metropolitana de la ciudad de México [159].

La obra representa a la Virgen con el Niño en su regazo mientras es coronada por dos ángeles. El Niño sostiene uvas en su mano derecha. En la parte inferior, está representado un paisaje.

La historiadora del arte Nelly Sigaut atribuye estilísticamente esa obra a Alonso Vázquez [159]. Posteriormente dice: "Asumo el riesgo y no oculto que Ruiz Gomar me comunicó verbalmente que Serrera vio la obra de la catedral de México y desechó una posible atribución a Alonso Vázquez."

Fig. 99. “Martirio de San Hipólito”.

Fig. 100. “Virgen de las Uvas”.

4.1.8. Summary

Alonso Vázquez was not the first Spanish painter to work in New Spain, but he was among the first ones. For the notice, the first Spanish painter was probably the Andalusian Cristobal de Quesada in 1538 or Juan de Najara (or Nájera) [151]. Among these first Spanish painters arrived in New Spain, art historians search the origins and the influences of Mexican colonial painting. Therefore, the study of the Mexican artworks by Alonso Vázquez is important for Art History in order to assess their real influence on the evolution of art in Mexico. Nonetheless, before being able to do this work, it is necessary to identify still existing paintings from this artist and to do an unpredictable identification study for those that remain unsigned.

So far, there is no study published on the painting technique of Alonso Vázquez. The work presented is useful to compare the Mexican artworks attributed to Vázquez from his previous period painting in Seville. The comparative analysis will further define the pictorial techniques and palettes of this artist. It will bring significant contributions to the study of New Spanish paintings and the influence of Spanish and European painting schools on colonial Mexico.

The information about the seven artworks is summarized in Table 22. For the material study of these paintings, the artworks with confirmed authenticity will be taken as reference. They are the series of "San Pedro Nolasco". From these three paintings, a comparative study of the others will confirm their attribution in a material point of view.

Table 22. Summary about the seven artworks.

Artwork title	Alternative title	Year of execution	Authenticity
Sagrada Cena	Ultima Cena	1588	Attributed
Virgen del Valle	Virgen del Pozo Santo	1597	Attributed to an altarpiece with contract
San Pedro Nolasco despidiéndose de Jaime I El Conquistador	None	1601	Contract and artwork signed
San Pedro Nolasco redimiendo cautivos	None	1600-1603	Contract
La Inmaculada	Virgen Inmaculada	Unknown	Attributed
Martirio de San Hipólito	None	1605-1607	Attributed to an altarpiece with contract
Virgen de las Uvas	Virgen apocalíptica or Inmaculada Concepción	Unknown	Attributed

4.2. Methodology

The methodology used to analyze the seven artworks in Seville and Mexico was similar in order to normalize the results and allow comparison. The objective of these material analyses was to obtain concrete data on the artwork techniques and the pigments used. The study was carried out following an interdisciplinary methodology developed for the analysis of paintings which consisted of:

- Photographic record in the reflected visible light spectrum and UV-induced visible fluorescence photography. This work was performed and directed by Eumelia Hernández from LDOA (IIE-UNAM). The UV study allows for the detection of restored areas (cf. Chapter 4.2.1).
- IRR study to detect preparatory drawings, corrections (*pentimenti*) and to discern pigments (cf. Chapter 4.2.1).
- X-ray fluorescence study with portable setups in order to characterize the chemical elements associated with inorganic pigments (cf. Chapter **Erreur ! Source du renvoi introuvable.**).
- CXRF depth profiles were obtained in order to determine the sequence and number of layers composing each painting (in the case of the artworks from the Fine Arts Museum of Seville) (cf. Chapter 4.2.3).
- OM and SEM-EDX studies were carried out on micro-samples mounted in cross sections to obtain information on painting layers (in the case of Mexican artworks) (cf. Chapter 4.2.4).

4.2.1. UV-induced visible fluorescence photography and IRR

First, imaging techniques were applied. General and detailed photography of the artworks were made. Then, UV-induced visible fluorescence photography and IRR were applied. IRR mosaic of six artworks was obtained. In the case of "Martirio de San Hipólito", the Gigapan system was not available yet. IRR images of details of the painting were taken. It was possible to connect some of the images in order to obtain bigger pictures but it was not possible to complete a full view of the artwork.

From the visible light, UV and IRR images, points of analysis were selected for XRF. The selection was made to cover the palette of colors present in each artwork. The specific contrasts observed in the IRR image were also analyzed. A similar color in visible light can provide a different contrast in IRR which could be due to the use of a different pigment or a different mixture of pigments. Moreover, both UV and IRR images help to discern the original areas of the paintings from the restored areas.

4.2.2. XRF

Interpreting XRF results can be complicated due to the fact that this technique only provides information on inorganic compounds, but paintings are made of inorganic and organic materials. The incapacity to identify all the compounds present and the complexity of the material studied propose too many assumptions which made the information obtained too complex to be used in a comparative study.

In this sense, the methodology proposed in this PhD work has the benefit of simplifying the interpretation of the results and take advantage of the information obtained allowing comparison of the artworks.

First, elemental peak areas were obtained with PyMCA software. The values of the peak areas provided by the software correspond to the sum of all the peaks (α, β and, eventually, γ) from a level transition (K or L depending on the chemical element).

For all the artworks studied, a unique series of chemical elements (Al, K, Ca, Ti, Cr, Mn, Fe, Co, Ni, Cu, Zn, As, Sr, Sn, Ba, Hg and Pb) were systematically analyzed in all the spectra. The elements Zr, Mo or W were selected depending of the X-ray tube used to do the XRF study. This strategy allows the analysis of hundreds of spectra in a short time.

After compilation of the information, the data is processed in an Excel file. The peak area values are classified for each chemical element in order of magnitude and discriminated by a color scale. This scale is adapted for each setup and each artwork so as to provide comparable results. All the classification scales are available in Appendix X.

Based on those color scales, the results are classified. First, the analysis presenting restoration interventions were identified (presence of Ti, Zn, Ba and/or Co). Then, the major elements were related to the visible color observed on the analysis area. In more complex cases, the IRR contrast helped to explain the color. The interpretation of the spectra just took into account the inorganic elements known for being responsible for visible color in pigments (Pb, Hg, Cu, Mn, Fe and Sn). The low peak area values were ignored solving the problem of the presence of ghost peaks due to the systematic study made with PyMCA.

This methodology produced a simplified classification of the inorganic pigments used and the palette presented on each artwork was obtained (see

Table 27, Chapter 4.3.3). In the case in which the inorganic elements could not explain the visible color observed, the presence of an organic pigment was proposed.

In the case of the "Sagrada Cena" painting, 2D analysis profiles were also obtained on the surface of the artwork. Those analyses revealed the use of pigment mixtures in order to get different contrasts.

4.2.3. CXRF spectrometry

In the case of the artworks from the Fine Arts Museum of Seville, CXRF in-depth profiles have been chosen for two purposes:

- To define the priming and, eventually, the ground preparation of each painting.
- To solve specific problems highlighted by the comparison of XRF and IRR results.

4.2.4. Other techniques applied

In Mexico, several other techniques were applied:

- Radiography;
- Both OM and SEM-EDX were applied to micro-samples;
- Raman spectrometry and FTIR were used in the study of the "Virgen de las Uvas".

Those results are not presented in this thesis with an exception for the micro-samples studies.

In the case of the "Virgen de las Uvas", the SEM-EDX study is still in progress. The future results will characterize the pigments used, in order to confirm the hypothesis that it was not painted by Alonso Vázquez.

In the case of "Martirio de San Hipólito", the information offered by SEM-EDX about the ground preparation and the priming layers was compared to the CXRF in-depth profile results obtained at the Fine Arts Museum of Seville and to the SEM-EDX study

made by the IAPH during the restoration intervention of the "Virgen del Valle". The results of this comparison support the attribution of this Mexican painting to Alonso Vázquez.

In the case of the two Mexican artworks ("Martirio de San Hipólito" and "Virgen de las Uvas"), the samples taken were less than 3 mm in size. The preparation of the cross sections was conducted by Victor Santos from LDOA (IIE-UNAM). The study by OM with visible and ultraviolet light was done by Elsa Arroyo, Sandra Zetina and Tatiana Falcón. The study by SEM-EDX was performed by Manuel Espinosa Pesqueira from the National Nuclear Research Institute from Mexico (Instituto Nacional de Investigaciones Nucleares, ININ) using a scanning electron microscope model JEOL JSM 6610 in a low vacuum mode.

4.3. Alonso Vázquez paintings study

The most relevant cases are presented here, in order to illustrate the advantages of each technique applied. For the complete study of every artwork, the full report of each study is provided in Appendix XI.

4.3.1. UV-induced visible fluorescence photography

UV-induced visible fluorescence photography reveals the presence of the recent organic materials that often is connected to restoration interventions. This information can also be observed in the IRR results (Fig. 101) but not consistently (Fig. 102). The correlation between the two techniques is apparent when the restoration intervention is associated to the use of pigment with different IR reflection properties from the original one.

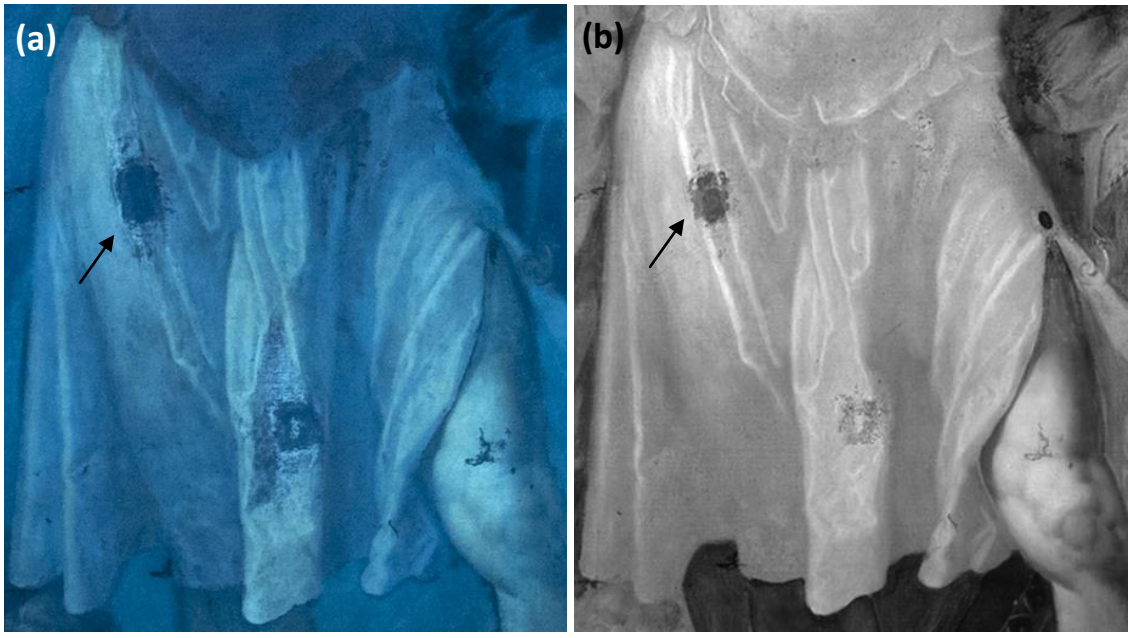

Fig. 101. UV image (a) and IRR image (b) of the same detail of "San Pedro Nolasco redimiendo cautivos".

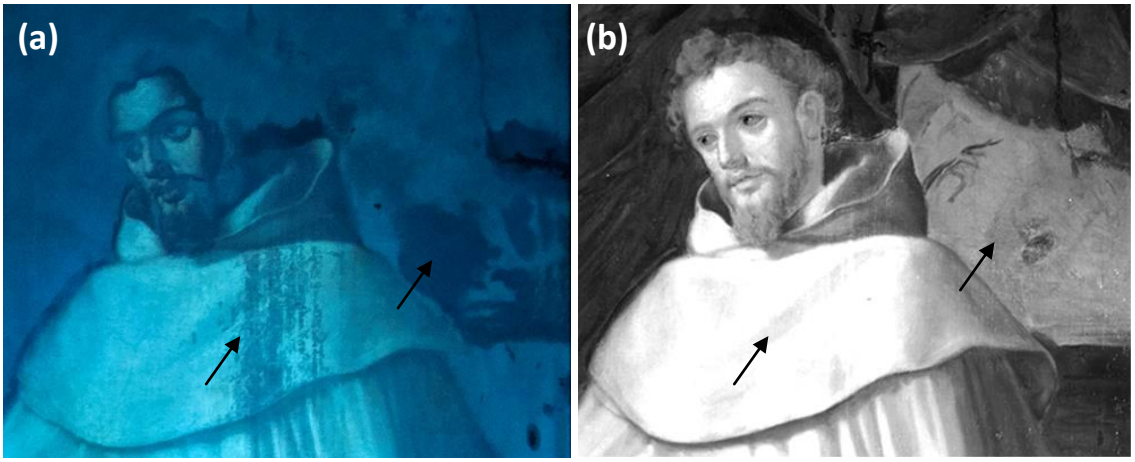

Fig. 102. UV image (a) and IRR image (b) of the same detail of "San Pedro Nolasco redimiendo cautivos".

Using a detail of the "Sagrada Cena" as an example (Fig. 103), the XRF study tries to avoid restored areas with the help of UV and IRR images (with the exception of XRF point 213 which was previously known to be part of a restoration intervention). The example illustrates the fact that the UV and IRR images help successfully avoiding restored areas. However it is not always easy to detect all later interventions as shown by XRF point 207 and 237 (Table 23).

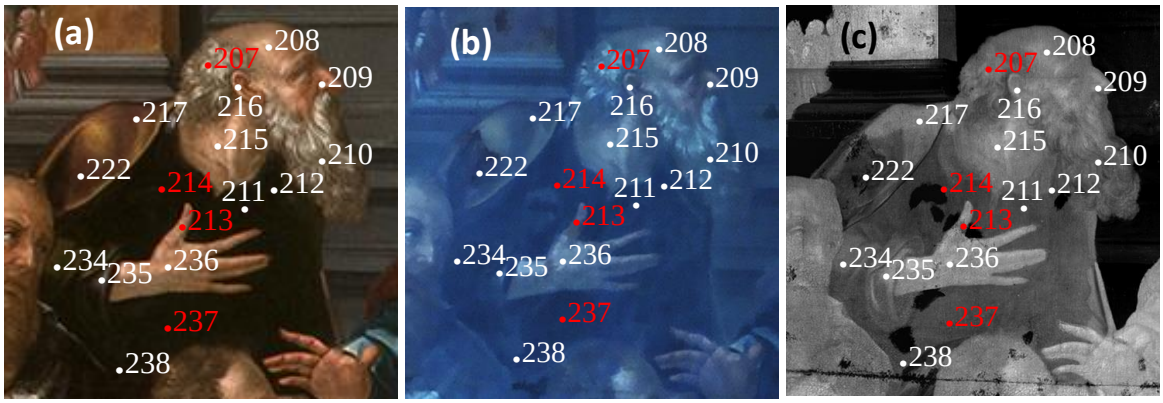

Fig. 103. Same detail of "Sagrada Cena" in visible light (a), UV light (b) and IRR (c). The XRF points in red show presence of modern pigments (restoration interventions).

Table 23. Net peak areas (in counts) of the elements detected by XRF in different restoration interventions found in selected points showed in Fig. 103.

Points	Ti-K	Co-K	Zn-K	Ba-L	Presence of restoration interventions
207	1528 ± 39	n.d.	9765 ± 99	112 ± 11	Ti and Zn
208	14 ± 4	43 ± 7	988 ± 31	124 ± 11	
209	42 ± 6	5 ± 2	963 ± 31	81 ± 9	
210	77 ± 9	22 ± 5	882 ± 30	30 ± 5	
211	65 ± 8	53 ± 7	838 ± 29	87 ± 9	
212	70 ± 8	220 ± 15	1553 ± 39	43 ± 7	
213	6427 ± 80	n.d.	29160 ± 170	308 ± 18	Ti and Zn
214	101 ± 10	n.d.	2190 ± 47	114 ± 11	Zn
215	25 ± 5	25 ± 5	977 ± 31	114 ± 11	
216	52 ± 7	39 ± 6	1042 ± 32	87 ± 9	
217	100 ± 10	13 ± 4	824 ± 29	181 ± 13	
222	60 ± 8	265 ± 16	1575 ± 40	60 ± 8	
234	4 ± 2	136 ± 12	949 ± 31	133 ± 12	
235	104 ± 10	115 ± 11	861 ± 29	64 ± 8	
236	12 ± 3	18 ± 4	1746 ± 42	104 ± 10	
237	79 ± 9	222 ± 15	2173 ± 47	18 ± 4	Zn
238	61 ± 8	188 ± 14	1623 ± 40	99 ± 10	

4.3.2. IRR

The first use of IRR in the study of paintings consisted in the observation of the carbon black preparatory underdrawings. Indeed, carbon black is visible in IRR images due to its non-IR reflective property. In the IRR mosaic of the "San Pedro Nolasco redimiendo cautivos", the underdrawings, done by the artist in order to guide him through the painting execution of the arched architecture and stairs, is visible (Fig. 104).

As mentioned before, IRR can also identify the presence of restored areas, when material with different IR reflectivity from the original material has been used (Fig. 103). Because of this ability, it is complementary to the observation by UV-induced visible fluorescence photography.

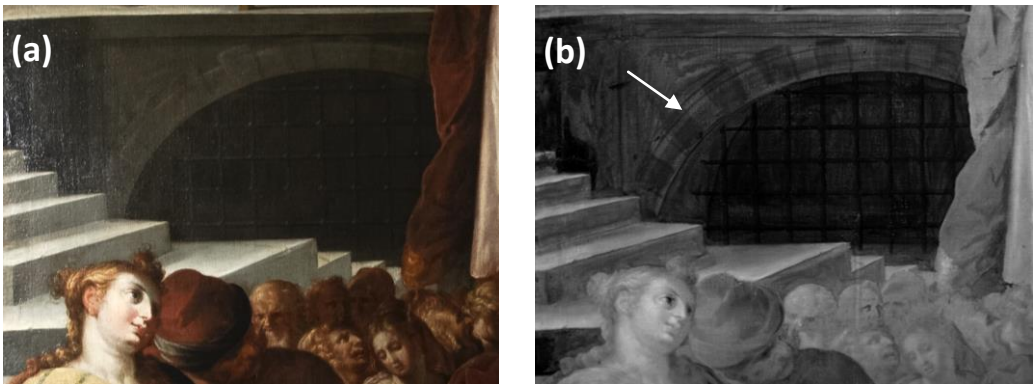

Fig. 104. Underdrawings of the arched architecture and stairs visible on the IRR mosaic of the "San Pedro Nolasco redimiendo cautivos" (b).

Fig. 105. IRR detail of the "Virgen del Valle" obtained with a manual tripod system. The little deviations and modifications of distance that occure during the capture of the IRR images hinder the stitching process.

The advantage of using an automatic device (e.g. Gigapan) instead of a manual tripod system in order to obtain a full mosaic of a great artwork is obvious as shown in the example of the "Virgen del Valle" (Fig. 105). The difficulty in using a tripod is too high for it to be chosen as a systematic method. It should be employed only in cases where an automatic device is unavailable. In the most difficult case studies (confined space, *in situ* studies, etc.), the Gigapan system is the most appropriate (cf. Chapter 2.4.1).

The concept of differentiating inorganic pigments using their different IR reflectivity properties is difficult to apply to artworks. The reason is that the artist may have used a mixture of carbon black or ochre to darken the tone of the pigment. In consequence, the resulting IR reflection of the mixture is different than the IR reflection of a pure pigment. Because of this, the characteristic IR reflection of the pigment is not consistent

In the detail of the "San Pedro Nolasco despidiéndose de Jaime I El Conquistador" (Fig. 106 and Table 24), the artist used, on one side, only vermilion for bright red (XRF points 15 and 34) and, secondly, red ochre to obtain a dark red (XRF points 33, 39 and 40). XRF point 15 presents a higher reflection rate according to the properties of the vermilion. Meanwhile, XRF point 34 is not as evident as the painter probably used a mixture that includes carbon black. The XRF points revealing a mixture of ochre with vermilion (33, 39 and 40) present similar IR reflection properties to ochre.

In the same painting, the difference between lead-tin yellow (XRF points 14 and 17) and yellowish ochre (XRF points 23, 25 and 26) is most obvious in IRR. This is due to the fact that, usually, the artist did not mix lead-tin yellow with any other pigment to get a brighter yellow (Fig. 106 and Table 24).

It has been observed (Chapter 3.2.3) that azurite presents a higher IR reflection rate than malachite. However, the IR reflection properties of other copper-based green pigments (e.g. copper resinate) have not been studied in this work.

In another detail of the "San Pedro Nolasco despidiéndose de Jaime I El Conquistador" (Fig. 107 and Table 25), azurite (detected in XRF points 50, 80 and 98) presents the IR

reflection property expected. However, this property is modified when azurite is underlay with black iron oxide in order to obtain dark blue (XRF point 99). XRF point 84 is more difficult to interpret. The presence of Cu detected by XRF probably belongs to a blue sub-layer (representing the sea) which was then covered by the upper layer (representing the railing) composed by white lead mixed with carbon black. This hypothesis will be confirmed by CXRF results (cf. Chapter 4.3.7).

Finally, the copper-green pigment observed in XRF point 82 presents a higher IR reflection rate than pure malachite. Due to the large amount of Cu observed in XRF, this different IR reflection could correspond to another kind of green copper-based pigment.

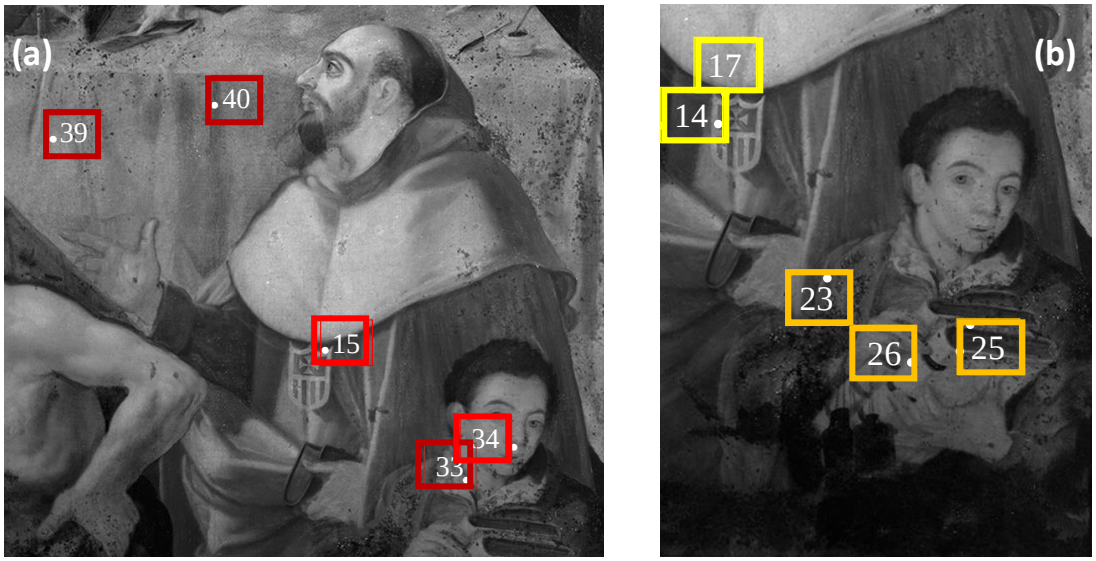

Fig. 106. IRR details of the "San Pedro Nolasco despidiéndose de Jaime I El Conquistador". XRF detection of vermilion is marked in bright red while red ochre is marked in dark red (a). Lead-tin yellow is marked in bright yellow while yellowish ochre is marked in orange (b).

Table 24. Net peak areas (in counts) of the elements detected by XRF in selected points showed in Fig. 106.

Pigments	Characteristic elements	Points	Fe-K	Sn-K	Hg-L	Pb-L
Lead-tin yellow	Pb, Sn	14	2904 ± 54	2298 ± 48	4017 ± 63	570600 ± 760
		17	9476 ± 97	2892 ± 54	13790 ± 120	605720 ± 780
Yellow ochre	Fe	23	38490 ± 200	903 ± 30	3990 ± 63	299530 ± 550
		25	57610 ± 240	301 ± 17	1215 ± 35	70610 ± 270
		26	22700 ± 150	281 ± 17	3040 ± 55	262650 ± 510
Vermilion	Hg	15	2511 ± 50	1280 ± 36	64680 ± 250	548930 ± 740
		34	29160 ± 170	306 ± 17	60140 ± 250	275640 ± 530
Red ochre	Fe	33	70050 ± 270	423 ± 21	201 ± 14	75850 ± 280
		39	59390 ± 240	218 ± 15	7883 ± 89	31430 ± 180
		40	69920 ± 260	217 ± 15	7468 ± 86	34690 ± 190

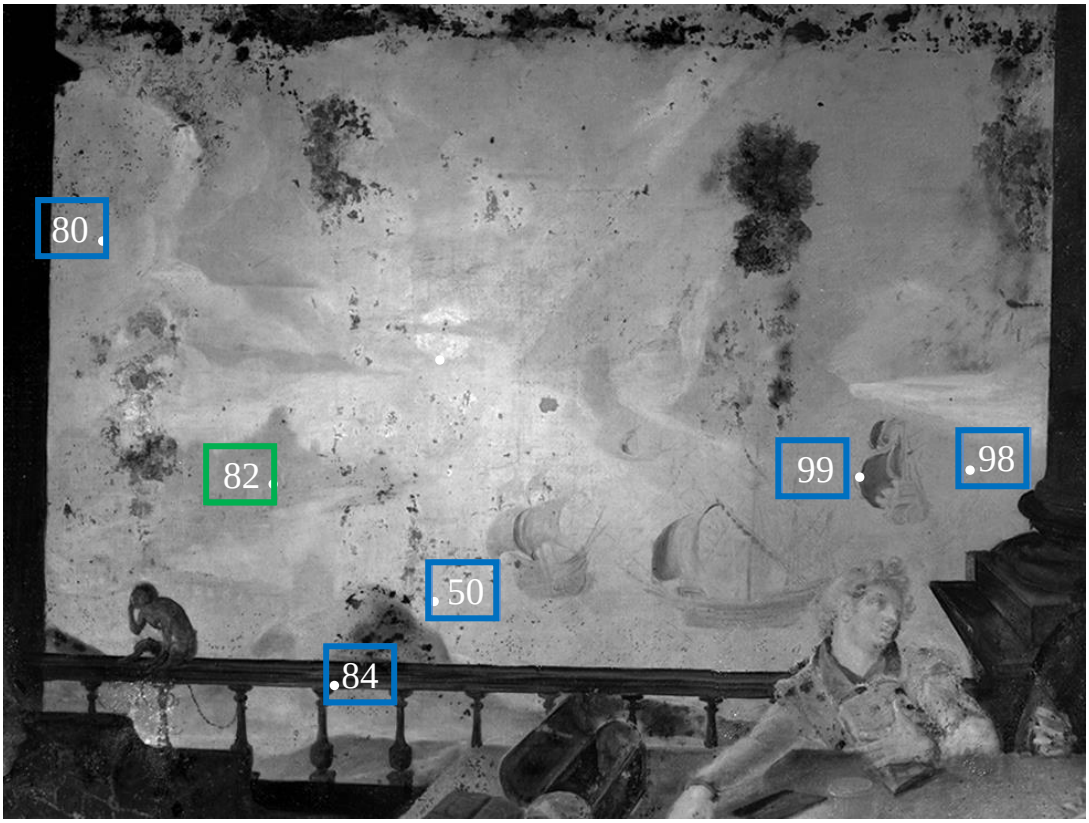

Fig. 107. IRR details of the "San Pedro Nolasco despidiéndose de Jaime I El Conquistador". XRF detection of azurite is marked in blue while green Cu-based pigment is marked in green.

Table 25. Net peak areas (in counts) of the elements detected by XRF in selected points showed in Fig. 107.

Pigments	Characteristic elements	Points	Fe-K	Cu-K
Azurite	Cu	50	6657 ± 82	194770 ± 440
		80	6264 ± 79	298620 ± 550
		84	7446 ± 86	180680 ± 430
		99	3100 ± 56	158630 ± 400
Azurite underlay with black iron oxide	Cu, Fe	98	31240 ± 180	318760 ± 570
Cu-based pigment	Cu	82	4168 ± 65	458170 ± 680

4.3.3.

4.3.4. Inorganic pigments study with XRF

XRF was used to study the palette of the artist. A novel methodology was applied to the treatment of the XRF data in order to compare the results measured. In fact, the studies of the seven artworks were made using three different XRF setups (cf. Chapter 2.5). Table 26 presents the conditions used for each device.

First, the presence of modern pigments resulting from restoration interventions (Ti, Zn, Co and Ba) was detected. As for the original pigments, 24 categories linking a pigment or pigment mixture to a certain color palette were defined (Table 27) [160, 161].

Table 26. Conditions used for each XRF device.

XRF device	Time per spectrum (s)	Voltage (kV)	Intensity (µA)
X-Panda	150	30	130
"Museum XRF device"	300	33.4	80
SANDRA	120	45	150

Table 27. Description of the 24 categories defined for XRF study.

Color palette	Pigments	Characteristic elements
White	Lead white	Pb
Flesh tones	Lead white with vermilion	Pb, Hg
	Lead white with lake	Pb
Yellow	Lead-tin yellow	Pb, Sn
	Massicot	Pb
Red	Vermilion	Hg
	Mixture of vermilion with ochre	Hg, Fe
	Red ochre	Fe
	Purple lake	/
Blue	Azurite	Cu
	Azurite underlay with black iron oxide	Cu, Fe
	Azurite underlay with umber	Cu, Fe, Mn
	Organic blue pigment	/
Green	Bright green Cu-based pigment	Cu
	Mixture of Cu-based pigment with ochre	Cu, Fe
	Organic green pigment	Fe
Ochre	Yellow ochre	Fe
	Ochre mixed with vermilion	Fe, Hg
Dark color	Black iron oxide	Fe
	Mixture of ochre with Cu-based pigment	Fe, Cu
	Umber	Fe, Mn
	Mixture of umber with Cu-based pigment	Fe, Mn, Cu
	Brown obtained with Cu-based pigment	Cu
	Organic black pigment	/

White was obtained with white lead (Pb). When mixed with vermilion, the artist gets flesh tones. Also, flesh tones obtained with lake were observed (only presence of Pb was detected). Yellow was obtained with lead-tin yellow (Pb and Sn) or massicot (Pb). The methodology distinguishes four kinds of red, three kinds of blue, two kinds of green, and two kinds of ochre. Finally, the pigments with hues from dark ochre to black through gray and blue-gray were separated into 6 categories.

In the case of the "Virgen de las Uvas", the presence of organic green and blue pigments was noted.

4.3.5. Accuracy of the methodology applied to the treatment of the XRF data

To determine the accuracy and efficiency of the methodology, radar charts were drawn. The homogeneity of each group of pigments has been verified from the XRF study of the "Sagrada Cena" done with the X-Panda setup. The ability to compare artworks has been tested in the case of the blue category comparing XRF spectra of each artwork obtained with different XRF setups.

The radar charts represent the net peak areas (in counts) of the six characteristic elements detected by XRF (Pb-L, Ca-K, Mn-K, Fe-K, Cu-K, Hg-L). This type of plot is a graphical method of displaying multivariate data in the form of a two-dimensional chart of several variables represented on axes starting from the same point. The maximum of each axis corresponds to the maximum value measured by one XRF set-up on one painting. Each spectrum is represented by a color area depending of the value of the net peak areas of the six elements selected. If the pigment category is well defined, the area resulting by the superposition of all spectra has to be homogeneous. Consequently, each pigment shows a specific pattern depending of its chemical composition.

In the case of the "Sagrada Cena" study, the maximum value chosen for each axis corresponds to the maximum value registered between all the XRF spectra measured in the painting.

Lead white (Pb) and every organic pigment mixed with lead white (e.g. organic black and red lake) exhibit similar patterns as they are all characterized by XRF by the presence of Pb (Fig. 108). Mixing lead white with vermilion, the artist gets flesh tones (Fig. 109). Red categories: the mixture of vermilion with ochre (Hg, Fe) presents more Fe than the vermilion (Hg) as expected (Fig. 110). Indeed, the mixture of vermilion with ochre (Hg, Fe) and the ochre mixed with vermilion (Fe, Hg) have the same pattern (Fig. 110). The patterns of yellow ochre (Fe) and of black iron oxide (Fe) are also similar (Fig. 111). The azurite (Cu) and the azurite underlay with black iron oxide (Cu, Fe) present similar patterns, with a higher content of Fe in the second, as expected (Fig. 112). The brown obtained with azurite (Cu) is similar to azurite (Cu) while the mixture of ochre with Cu-based pigment (Fe, Cu) is similar to the azurite underlay with black iron oxide (Cu, Fe) (Fig. 112 and 113). "Umber" (Fe Mn) and the mixture of umber with Cu-based pigment (Fe, Mn, Cu) show similar patterns, with a higher content of Cu for the second, as expected (Fig. 114). The bright green Cu-based pigment (Cu) and the mixture of Cu-based pigment with ochre (Cu, Fe) present similar patterns, with a higher content of Fe for the second (Fig. 115).

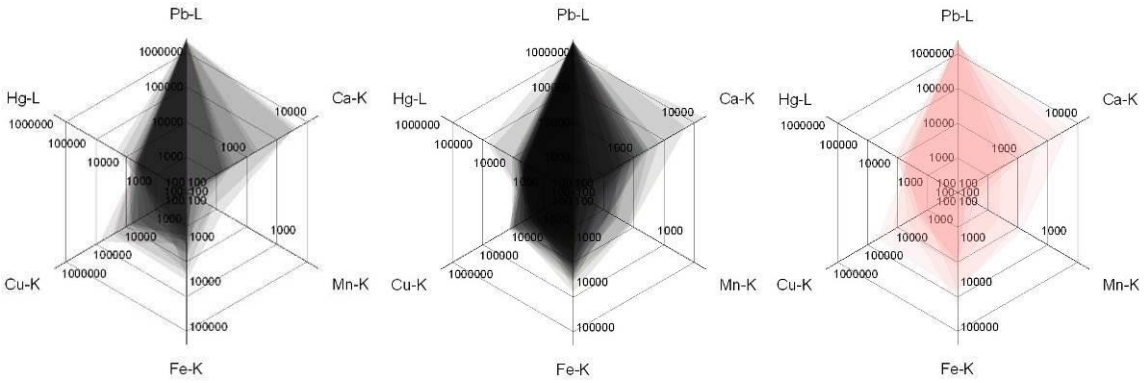

Fig. 108. Radar charts of the lead white (19 spectra) (a), the organic black (32 spectra) (b) and, the red and purple lakes (7 spectra) (c) categories.

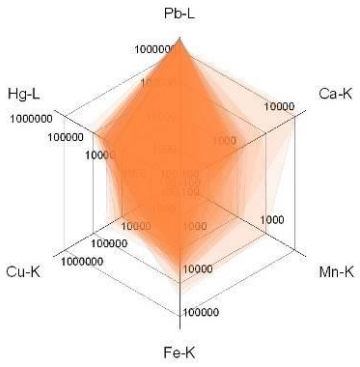

Fig. 109. Radar charts of the flesh tones category (Lead white with vermilion) (36 spectra).

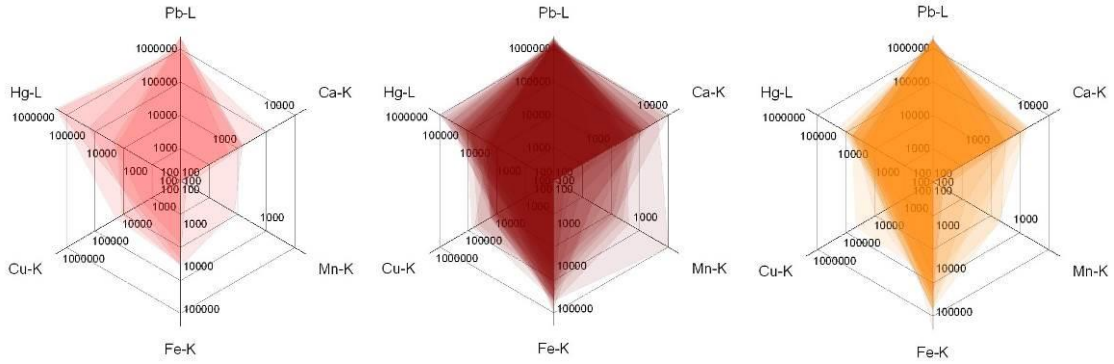

Fig. 110. Radar charts of vermilion (5 spectra) (a), the mixture of vermilion with ochre (24 spectra) (b) and the ochre mixed with vermilion (18 spectra) (c) categories.

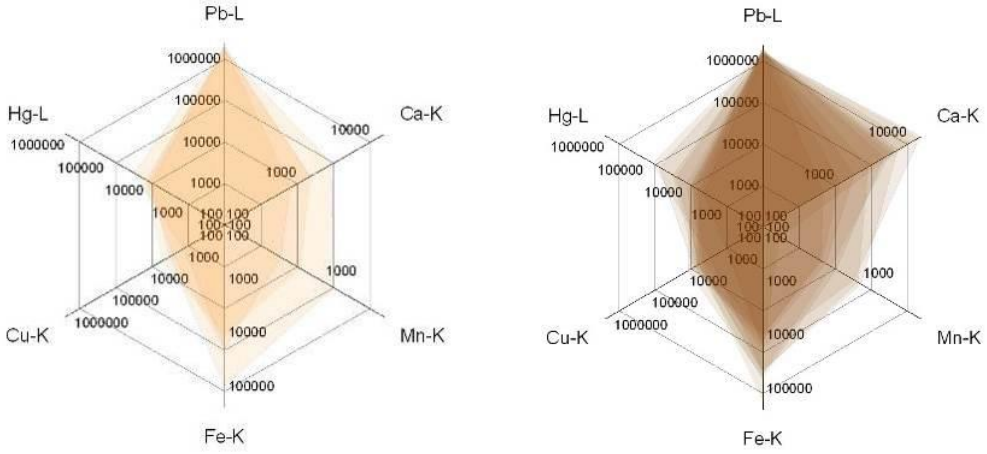

Fig. 111. Radar charts of the yellow ochre (4 spectra) (a) and the black iron oxide (12 spectra) (b) categories.

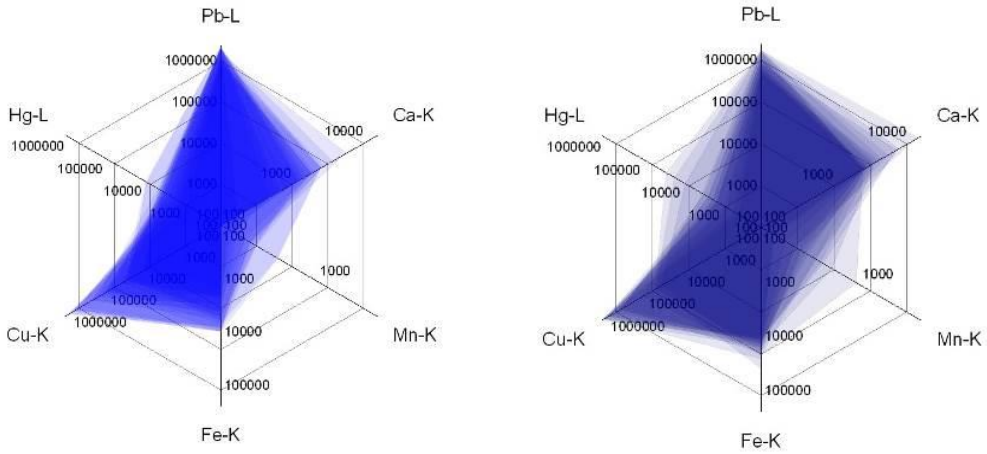

Fig. 112. Radar charts of the azurite (23 spectra) (a) and the azurite underlay with black iron oxide (16 spectra) (b) categories.

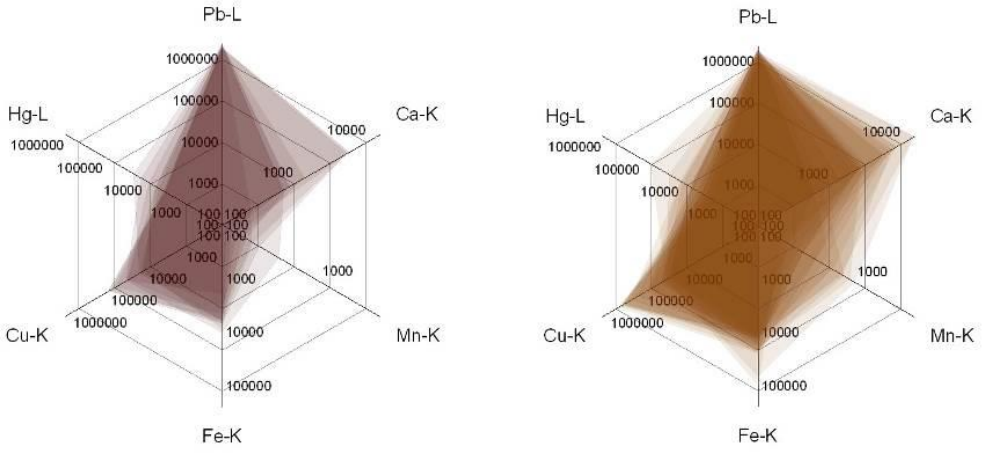

Fig. 113. Radar charts of the brown obtained with Cu-based pigments (10 spectra) (a) and the mixture of ochre with Cu-based pigment (21 spectra) (b) categories.

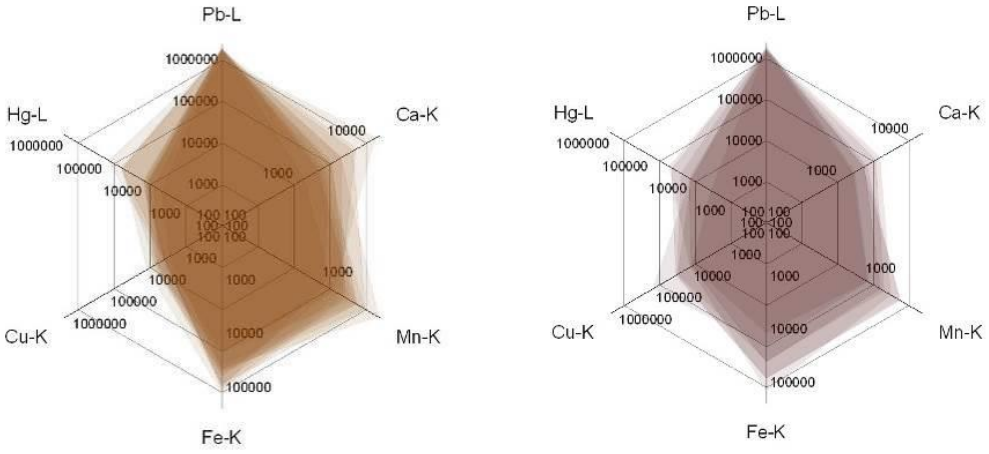

Fig. 114. Radar charts of the umber (13 spectra) (a) and the mixture of umber with Cu-based pigment (7 spectra) (b) categories.

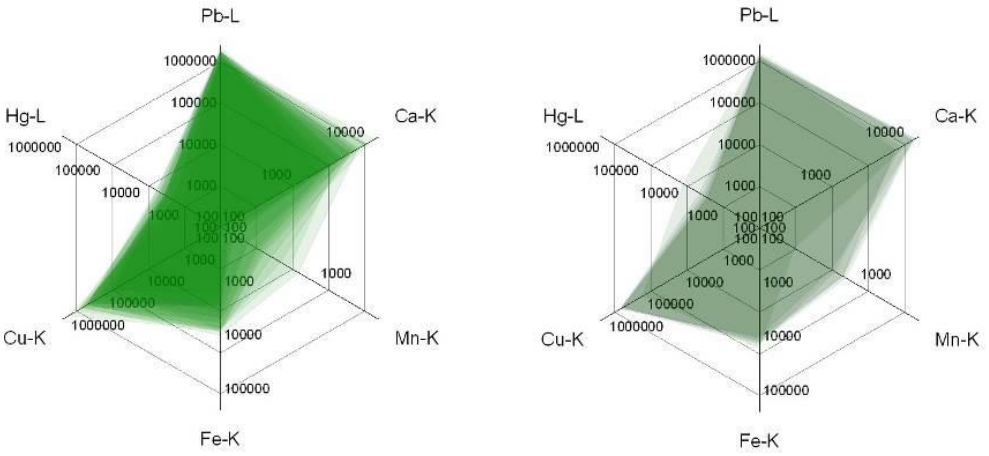

Fig. 115. Radar charts of the bright green Cu-based pigment (19 spectra) (a) and the mixture of Cu-based pigment with ochre (6 spectra) (b) categories.

For the blue category comparison, for each artwork, XRF spectra were obtained using different XRF setups. In this case, the maximum value chosen for each axis of the radar charts corresponds to the maximum value registered between all the XRF spectra measured in each painting with each setup.

Five of the six artworks (Fig. 116 to 118) show similar patterns with high content in Cu and Pb, and low content in Mn and Hg with the exception of the "Virgen del Valle" which presents a higher content in Hg due to the fact that the artist applied blue pigment above flesh tones (Hg, Pb) (XRF points 25, 33 and 34) (Fig. 117 and 188). Finally, the pattern of the "Virgen de las Uvas" is noticeably different (Fig. 118). This is because of the use, in this painting, of a blue organic pigment instead of azurite (i.e. indigo).

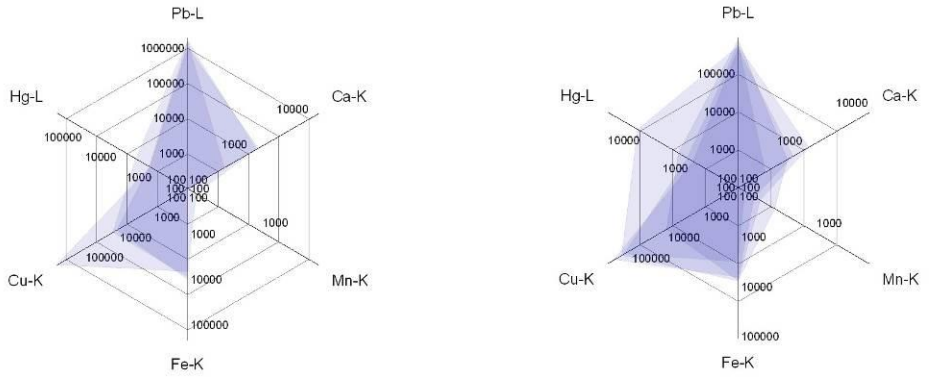

Fig. 116. Radar charts of "Bright blue" category of "San Pedro Nolasco redimiendo cautivos" (3 spectra) (a) and "San Pedro Nolasco despidiéndose de Jaime I El Conquistador" (4 spectra) (b).

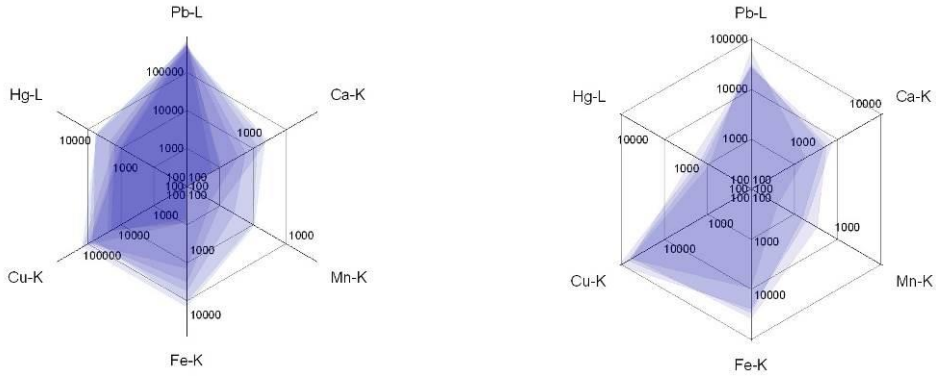

Fig. 117. Radar charts of "Bright blue" category of "Virgen del Valle" (8 spectra) (a) and "Martirio de San Hipólito" (4 spectra) (b).

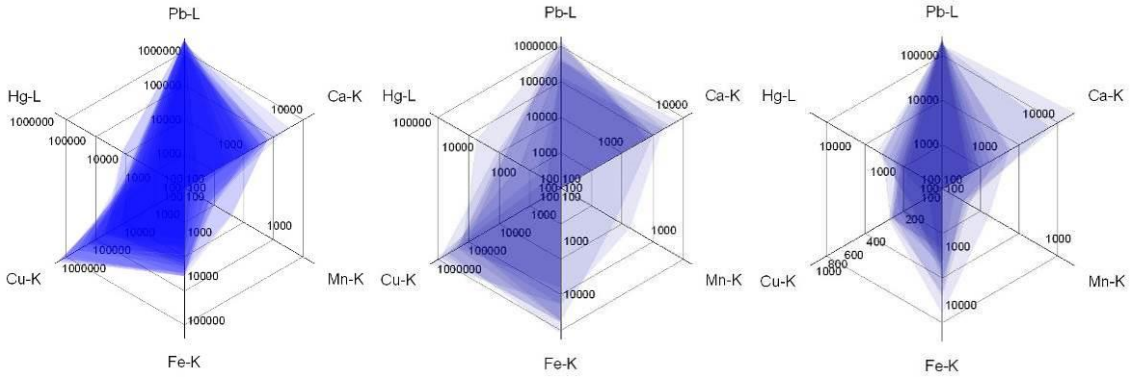

Fig. 118. Radar charts of "Bright blue" category of "Sagrada Cena" (23 spectra) (a), "Inmaculada" (8 spectra) (b) and "Virgen de las Uvas" (12 spectra) (c).

4.3.6. 1D analysis with XRF

In the case of the "Sagrada Cena", three 1D analyses with XRF using the 2D motion device at the Fine Arts Museum of Seville have been made. The objective was to test the device's ability to obtain 1D profile in areas that present interesting contrasts in IRR. All spectra of the lateral profiles were recorded during 10 s with 30 kV for 130 µA.

The first lateral profile illustrates the technique applied by the artist to paint the shadow of the apostle's leg on the gray floor. The IRR image shows an interesting

contrast on the border of the shadow which cannot be seen in visible light (Fig. 119). 60 spectra measured each 2 mm were taken for this profile.

The shadow was obtained with a mixture of ochre with Cu-based pigment (Fe, Cu) (Fig. 120, B). The painter used two kinds of mixture to produce the gray of the floor. The floor above the shadow is made of a brown with azurite (Cu) (Fig. 120, A) while the floor below the shadow is obtained with organic black pigment (Fig. 120, C). It is interesting to observe the disappearance of Cu on the border of the shadow which probably characterizes the technique of the artist and corresponds to the specific contrast observed on the IRR mosaic.

Fig. 119. IRR (a) and visible (b) images of the detail of the "Sagrada Cena" where the lateral profile was performed.

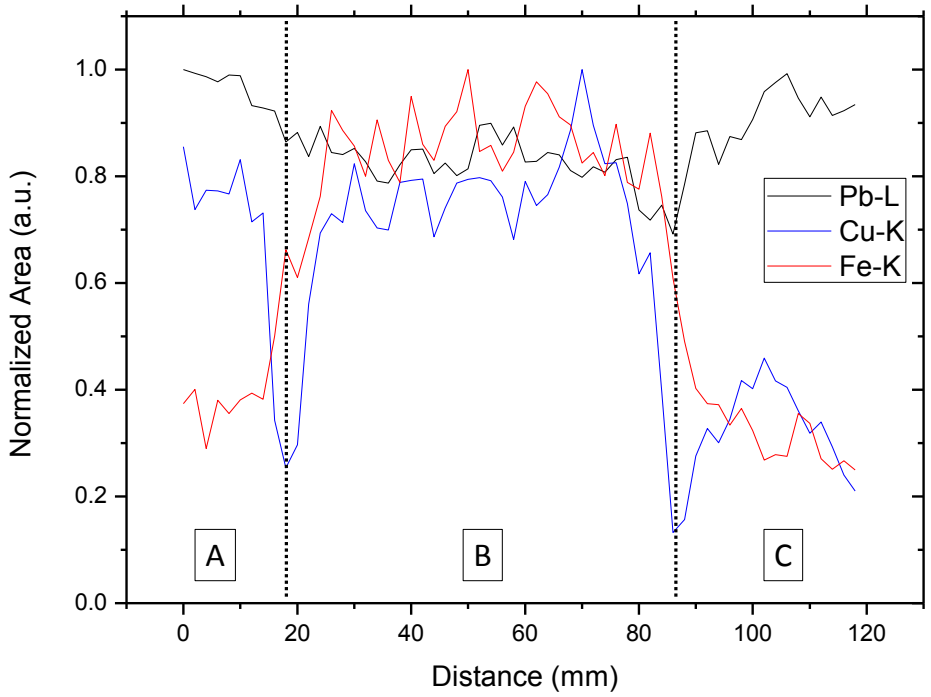

Fig. 120. Results of the lateral profile.

The second lateral profile illustrates a *pentimenti* of the artist in the angulation of the table. The IRR image (Fig. 121) shows the underdrawings of the original table. In his final execution, the painter decided to change its perspective. Between the two apostles three different IRR contrasts are observable, unlike in visible light (Fig. 121). The two areas on the left show a similar contrast, while the area on the right is totally opaque. The profile starts at the blue sleeve of the apostle on the left side of the painting and continues up to the brown hair of the apostle on the right side. 60 spectra measured every 3 mm were taken to create the profile.

The blue sleeve was painted with azurite (Cu) (Fig. 122, A). Then, the dark area between the original border of the table and the blue sleeve was painted using umber (Fe, Mn) (Fig. 122, B). The second dark area, between the original and the final borders of the table has been unfortunately restored (Zn), so the information about the mixture used by the artist was not registered (Fig. 122, C). The last dark area, totally opaque in IRR, was made of an organic black pigment (Fig. 122, D). Finally, the brown hair of the second apostle was carried out using umber (Fe, Mn) (Fig. 122, E). Maybe the original painting presented a color contrast between the final border of the table and the blue sleeve. For some reason, this contrast is no longer visible.

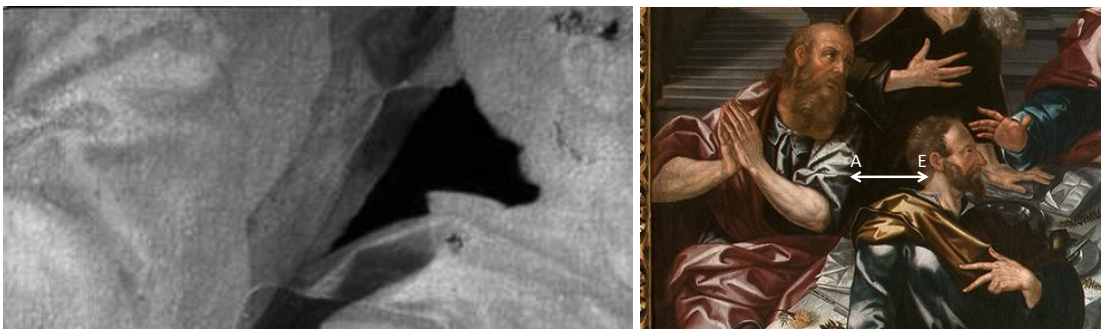

Fig. 121. IRR (a) and visible (b) images of the detail of the "Sagrada Cena" where the lateral profile was performed.

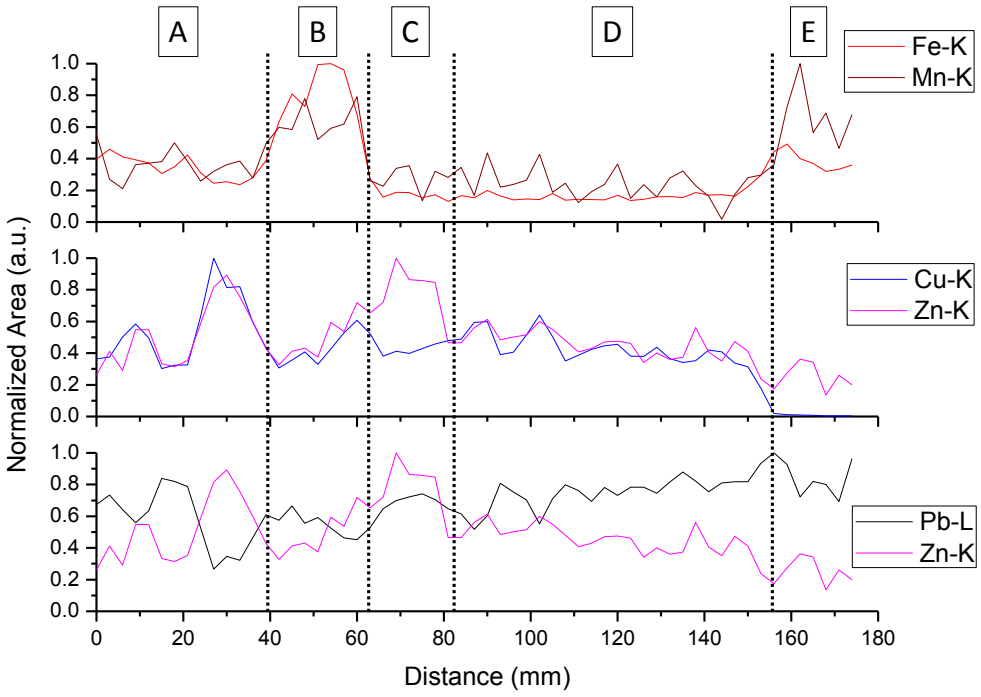

Fig. 122. Results of the lateral profile.

The last lateral profile includes several examples from the palette used in the artwork. In both visible light and IRR images (Fig. 123), the *pentimenti* of the table are visible like in the previous example. On the IRR mosaic, the original underdrawings of the corner of the table are visible as well. The profile starts on the purple tunic of the apostle and ends on the blue cloth of the second apostle. 200 spectra measured every 2 mm were taken for the profile.

The purple tunic of the apostle is a purple lake (Fig. 124, A). The grey handle of the vase is made of an organic black pigment (Fig. 124, A). The darkest red of the tunic was obtained with red ochre (Fe) and umber (Fe, Mn) (Fig. 124, B). The white tablecloth is lead white (Pb) (Fig. 124, C). The plant was made of Cu-based pigment (Cu) for the green part and umber (Fe, Mn) for the dark part (Fig. 124, D). Finally, the blue cloth of the second apostle was obtained with azurite (Cu) (Fig. 124, E).

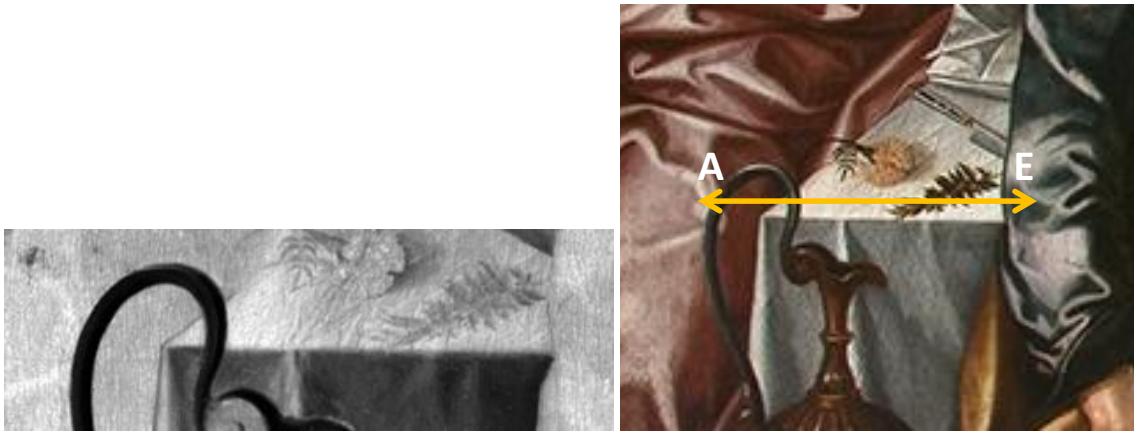

Fig. 123. IRR (a) and visible (b) images of the detail of the "Sagrada Cena" where the lateral scan was performed.

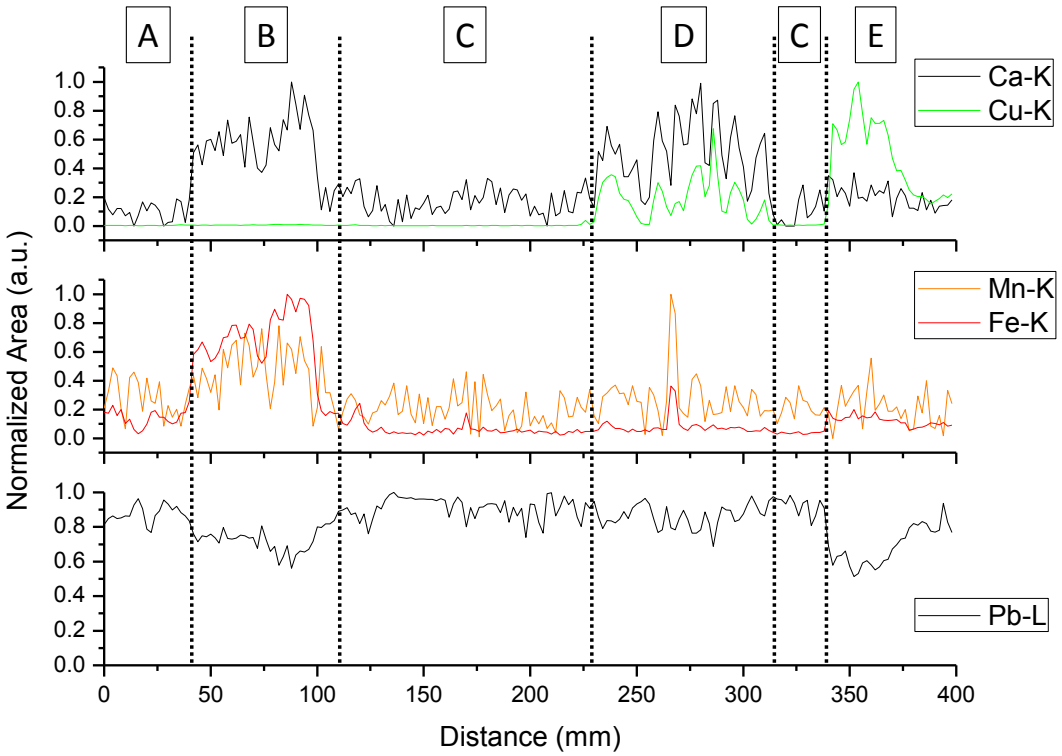

Fig. 124. Results of the lateral profile.

4.3.7. CXRF spectrometry

Nine in-depth scans were performed at the Fine Arts Museum of Seville (Table 28). One of the objectives was to test the μXRF-CONCHA device's ability to obtain *in situ* depth profiles. All spectra of the in-depth scans were recorded during 60 s with 50 kV for 600 μA.

CXRF in-depth profiles have been chosen for two purposes:

- To define the priming and, eventually, the ground preparation of each painting.
- To solve specific problems highlighted by the comparison of XRF and IRR results.

In the case of the "San Pedro Nolasco despidiéndose de Jaime I El Conquistador", two in-depth scans reveal the presence of a red priming layer (Fig. 125 and 126; Tables 29 and 30) and one of them shows the presence of the Ca ground layer (Fig. 125, Table 29). The first scan was performed on the red table while the second on the San Pedro Nolasco's white dress was on the right side of the painting (Fig. 96). As expected, the lead white present in the second point of analysis absorbs the XRF signal of the Ca ground layer. In the case of the first CXRF scan, the pigment layer and the priming layer are defined by the same chemical element (Fe) and appear together.

Table 28. List of the 9 in-depth scans performed at the Fine Arts Museum of Seville.

Artwork title	Number of scans	Step size (μm)
"San Pedro Nolasco despidiéndose de Jaime I El Conquistador"	3	5
"San Pedro Nolasco redimiendo cautivos"	1	10
"Sagrada Cena"	3	10
"Inmaculada"	2	5

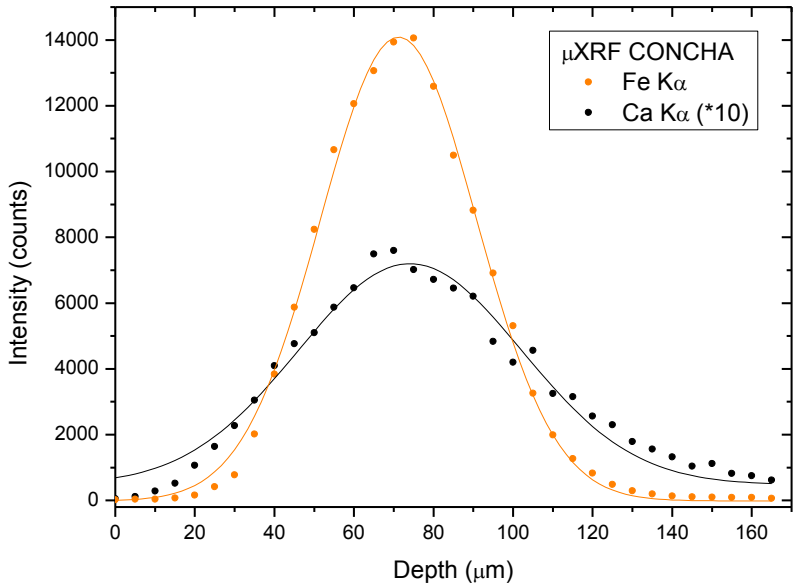

Fig. 125. First depth profile of the "San Pedro Nolasco despidiéndose de Jaime I El Conquistador".

Table 29. Results of in-depth scan (Fig.125).

Layer	Xc (μm)	Distance between Xc (μm)
Fe Kα	71 ± 3	3 ± 3
Ca Kα	74 ± 3	

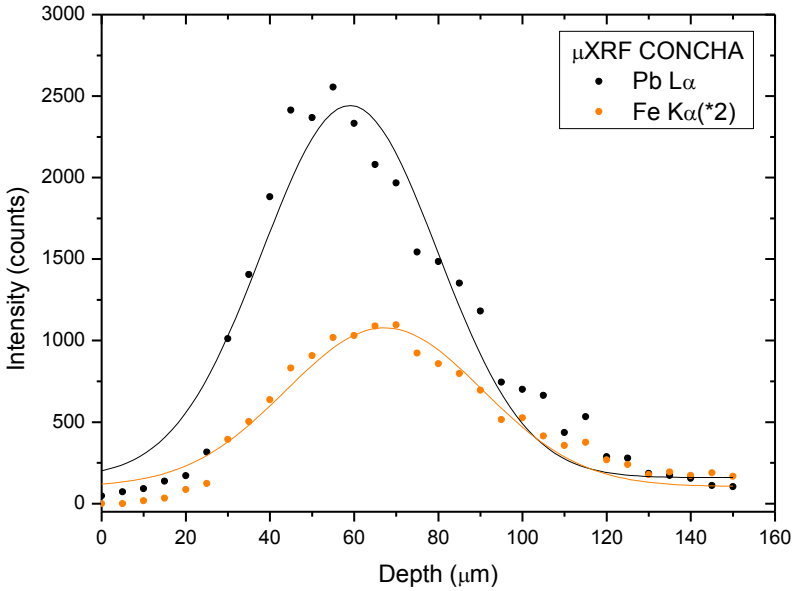

Fig. 126. Second depth profile of the "San Pedro Nolasco despidiéndose de Jaime I El Conquistador".

Table 30. Results of in-depth scan (Fig.126).

Layer	Xc (μm)	Distance between Xc (μm)
Pb Lα	59 ± 3	8 ± 3
Fe Kα	67 ± 3	

In the case of the "Sagrada Cena", three in-depth scans show the existence of two different priming layers (Fig. 127). These results confirm the hypothesis based on the observation of the IRR image (Fig. 128). A Pb-based priming was used for the representation of the apostles (Table 31, scans 1 and 2), while a red ochre priming (Fe) was used for the rest of the painting (Table 31, scan 3).

Fig. 127. In-depth scans position on the "Sagrada Cena".

Fig. 128. Details of the IRR image of the "Sagrada Cena" showing the contrast between the apostles and the rest of the artwork.

Table 31. Results of depth profiles obtained on the "Sagrada Cena" (Fig. 126).

In-depth scan	Layer	Xc (μm)	Distance between Xc (μm)
1	Fe Kα	115 ± 5	9 ± 5
	Pb Lα	124 ± 5	
2	Cu Kα	86 ± 5	5 ± 5
	Fe Kα	91 ± 5	12 ± 5
	Pb Lα	103 ± 5	
3	Cu Kα	138 ± 5	7 ± 5
	Pb Lα	145 ± 5	4 ± 5
	Fe Kα	149 ± 5	

Finally, in the case of the "San Pedro Nolasco despidiéndose de Jaime I El Conquistador", another in-depth scan was performed, in order to help the interpretation of the result obtained in XRF point 84 (cf. Chapter 4.3.2).

The hypothesis was that the presence of Cu detected by XRF probably belongs to a blue underlayer of the sea, which was overlaid by a dark color layer of the railing. This hypothesis was confirmed by CXRF depth profile showing a two layer-system (Table 32 and Fig. 129). The first layer is made of black iron oxide (Fe) while the second is made of azurite (Cu).

Table 32. Results of depth profile showed in Fig. 129.

Layer	Xc (μm)	Distance between Xc (μm)
Fe Kα	54 ± 3	4 ± 3
Cu Kα	58 ± 3	

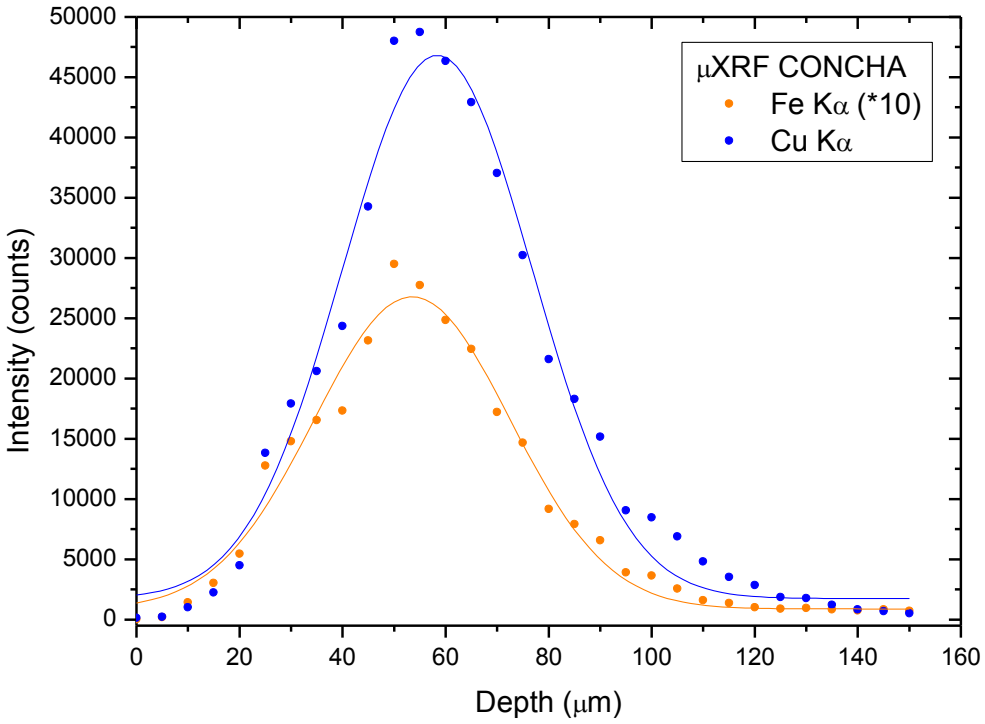

Fig. 129. Depth profile of the railing of the "San Pedro Nolasco despidiéndose de Jaime I El Conquistador".

4.4. Synthesis of the corpus studied

The study synthesis of the seven artworks is presented below. The artist's painting technique and the inorganic pigments of his palette are shown amongst other information provided through the archaeometric investigation.

4.4.1. Preparatory drawings

The IRR study revealed very few preparatory drawings carried out by carbon black. All these drawings were used in architectural areas such as stairs, grille (Fig. 104), windows or elements such as a table (Fig. 130). They are all geometric elements difficult to produce without drawing them first.

4.4.2. *Pentimenti*

Faces and hands of the characters show very few corrections. The paint application is sharp; the borders of the bodies and clothes were improved using a dark color mixture (Fig. 59, 128, 131 and 132). More *pentimenti* are observed on decorative items such as dishes, cutlery, pots, etc. In the case of the "Sagrada Cena", the presence of numerous *pentimenti* is probably unique due to the size and complexity of this painting. The modification of design of the calyx (Fig. 133) or the disappearance of a knife (Fig. 134) can be shown as examples. Besides *pentimenti*, the IRR mosaic reveals the different elaboration steps of some parts of the artwork. For example, the artist first painted the entire dish before he made the lamb, starting with his body, finishing with his feet (Fig. 133).

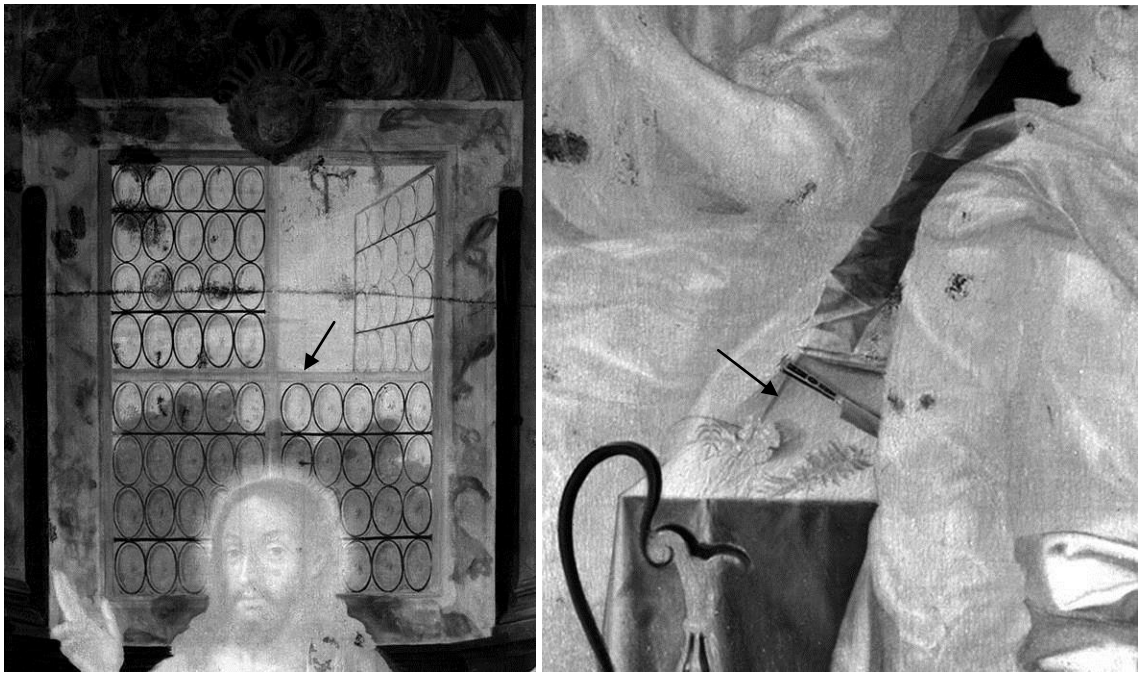

Fig. 130. Details of the IRR image of the "Sagrada Cena" showing the preparatory drawings of the window (a) and the modification of the table border (b).

Fig. 131. Details of the IRR (a) and visible (b) images of the "San Pedro Nolasco despidiéndose de Jaime I El Conquistador" showing how the border of the arms and hands were corrected using a dark mixture.

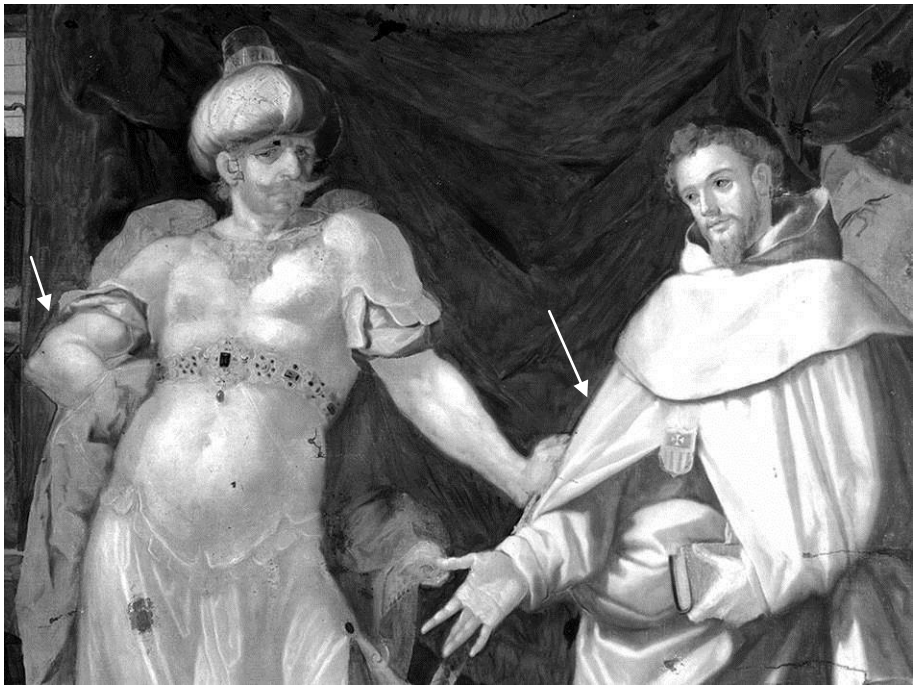

Fig. 132. Details of the IRR image of the "San Pedro Nolasco redimiendo cautivos".

Fig. 133. Details of the IRR (a) and visible (b) images of the "Sagrada Cena" showing the modification of design of the calyx and the different steps of construction used to represent the dish with the lamb.

Fig. 134. Details of the IRR (a) and visible (b) images of the "Sagrada Cena" showing the disappearance of a knife.

4.4.3. Pigments used on artworks produced in Seville.

From the XRF studies, based on the methodology proposed (cf. Chapter **Erreur ! Source du renvoi introuvable.**), a synthesis of the pigments detected on each artwork is presented (Table 33).

The modern pigments used for restoration interventions were zinc white (Zn), titanium white (Ti) and cobalt blue (Co). White barium sulfate (Ba) was detected in the case of the "Inmaculada".

The most complex palettes were detected in the "Sagrada Cena" (with 20 different pigments and mixtures). It is a logical conclusion as it is the largest artwork.

Comparing the five artworks from Seville, the palette of inorganic pigments used is very similar. The different tones were obtained by applying the same mixtures with some variations from one painting to another. For example, the dark blue was obtained by a layer of azurite underlay with umber on the "Inmaculada". Some brown color was obtained only with copper-based pigments most likely mixed with a black organic pigment on the "Sagrada Cena", the "San Pedro Nolasco redimiendo cautivos" and the "Virgen del Valle".

The use of organic pigments was suggested by the absence of inorganic elements able to explain the color observed in the artwork. The use of an organic black pigment (as lamp black for example) in the "Sagrada Cena" and in the "Virgen del Valle" was detected. This organic black pigment may have been used in the other artworks. However, the XRF study did not reveal any areas on those paintings where the absence of an inorganic element suggested its use. Purple lake (as carmine for example) was observed on all of the artworks (with the exception of "San Pedro Nolasco redimiendo cautivos"). It is possible that a similar lake served to produce some flesh tones on the "Sagrada Cena" and the "Virgen del Valle".

Finally, both the "Inmaculada" and the "Sagrada Cena", attributed to Alonso Vázquez by Serrano, present a palette of pigments and mixtures coherent with those observed on his confirmed artworks carried out in Seville. In the case of the "Sagrada Cena", IRR observations are also coherent while the "Inmaculada" displays too much deterioration and restoration interventions to obtain any useful observation from the IRR mosaic.

4.4.4. The Mexican artworks

The pigments' palette detected on the "Martirio de San Hipólito" is consistent with the artworks from Seville, while the palette on the "Virgen de las Uvas" differs drastically. The blue and green colors cannot be explained by the use of inorganic Cu-based pigments as observed on the artworks from Seville. The future Mexican SEM-EDX study of the micro-samples extracted from this painting may confirm the presence of organic pigments (as indigo for the blue color and a mixture of indigo with ochre for the green color for example).

In the case of "Martirio de San Hipólito", IRR images revealed the *pentimenti* of the pediment above Hernán Cortes as well as the angel and the shield. The pigments and mixtures detected are similar to those from the rest of the painting. It suggests that the representation of Hernán Cortés, as well as the inscriptions, are contemporary with the representation of San Hipólito. If Serrera's attribution is correct, this portrait may be one of the oldest known from the Spanish conqueror. Finally, IRR images did not show remains of the signature of Alonso Vásquez nor of the fictional Rodrigo de Cifuentes.

Table 33. Synthesis of the pigments detected on the seven artworks.

Color palette	Pigments	Characteristic elements	Inmaculada	Sagrada Cena	Nolasco, cautivos	Nolasco, Jaime I	Virgen, Valle	San Hipolito	Virgen, Uvas
White	Lead white	Pb	1	1	1	1	1	1	1
Flesh tones	Lead white with vermilion	Pb, Hg	1	1	1	1	1		1
	Lead white with lake	/		1			1	1	1
Yellow	Lead-tin yellow	Pb, Sn	1		1	1	1		
	Massicot	Pb		1				1	1
Red	Vermilion	Hg	1	1	1		1	1	1
	Mixture of vermilion with ochre	Hg, Fe	1	1	1	1		1	
	Red ochre	Fe		1		1		1	
	Purple lake	/	1	1	1		1	1	1
Blue	Azurite	Cu	1	1	1	1	1	1	
	Azurite underlay with black iron oxide	Cu, Fe	1	1	1	1		1	
	Azurite underlay with umber	Cu, Fe, Mn	1						
	Organic blue pigment	/							1
Green	Bright green Cu-based pigment	Cu	1	1	1	1	1	1	
	Mixture of Cu-based pigment with ochre	Cu, Fe		1			1	1	
	Organic green pigment	Fe							1
Ochre	Yellow ochre	Fe	1	1	1	1	1	1	1
	Ochre mixed with vermilion	Fe, Hg	1	1		1			
Dark color	Black iron oxide	Fe	1	1	1	1	1		1
	Mixture of ochre with Cu-based pigment	Fe, Cu	1	1	1		1	1	
	Umber	Fe, Mn	1	1	1	1		1	1
	Mixture of umber with Cu-based pigment	Fe, Mn, Cu		1	1	1	1	1	
	Brown obtained with Cu-based pigment	Cu		1	1		1		
	Organic black pigment	/		1			1	1	1
Number of categories			15	20	15	13	15	16	12
Restoration	Zinc white	Zn							
	Titanium white	Ti							
	Cobalt blue	Co							
	White barium sulfate	Ba							

4.4.5. CXRF results

From the nine in-depth scans performed at the Fine Arts Museum of Seville (Table 28), one of the objectives was to define the priming and, eventually, the ground preparation of each painting. As example, Figure 135 and Table 34 show the in-depth profile obtained on a blue area of the "Inmaculada". The results show a first layer of dark blue, azurite underlay with black iron oxide (Fe and Cu), sustained by a Pb-based layer and a red priming layer (Fe).

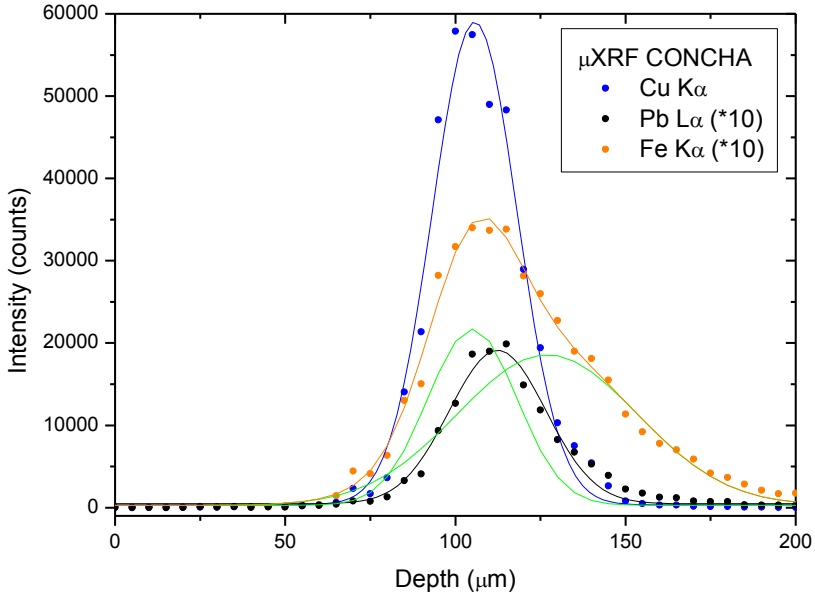

Fig. 135. Depth profile of the "Inmaculada".

Table 34. Results of depth profile presented Fig. 134.

Layer	Xc (μm)	Distance between Xc (μm)
Fe Kα	105± 3	1 ± 3
Cu Kα	106± 3	6 ± 3
Pb Lα	112 ± 3	15 ± 3
Fe Kα	127 ± 3	

Table 35. Synthesis of the information obtained with CXRF about priming and ground layers.

Artwork title	Priming layer	Ground layer
"San Pedro Nolasco despidiéndose de Jaime I"	Fe	Ca
"Sagrada Cena"	Fe or Pb	ND
"Inmaculada"	Fe	ND

The other results obtained were presented in the Chapter 4.3.7 and are summarized in Table 35. The three paintings show the presence of a red priming layer. In the case of the "Sagrada Cena", a second kind of priming layer was detected. This second Pb-based priming is used in the area with the representation of the apostles. Based on the observation of the IRR image (Fig. 132), it is possible to suggest that this technique, which uses two different kinds of priming layer, is also present in the "San Pedro Nolasco redimiendo cautivos". Nevertheless, the CXRF results were not conclusive on this last artwork and more CXRF analyses have to be done in the future to answer this question.

4.4.6. SEM-EDX results

Micro-sampling was done on three artworks. The IAPH restorers took six samples during the restoration intervention of the "Virgen del Valle" in 1999. Five and six samples were extracted respectively on the "Martirio de San Hipólito" and on the "Virgen de las Uvas" by Mexican researchers from LDOA (IIE-UNAM).

The results report from IAPH is available. The results of the SEM-EDX study of the "Martirio de San Hipólito" samples were communicated in 2012 [157] while the study of the "Virgen de las Uvas" is still in progress and results are not yet available.

The XRF study of the "Virgen del Valle" includes analysis of the areas next to the sampling made by the restorers of the IAPH, in order to compare the XRF results with the SEM-EDX results from the IAPH (Table 36). The IAPH report does not propose interpretation of the results. However, the similarity of the information obtained for Val2, Val3 and Val4 can be observed.

The IAPH report concludes that the white ground preparation consists of white calcium sulphate mixed with animal glue [162]. The thickness of the layer is from 100 to 450 µm. The reddish/pink priming layer is a mixture of lead white, calcite and ochres with a thickness from 15 to 60 µm.

Table 36. Comparison of the results obtained with SEM-EDX and XRF studies of "Virgen del Valle".

Observed color	SEM-EDX study		XRF study		
	IAPH sample name	Characteristic elements	Spectrum name	Characteristic elements	Pigment or mixture determined
Dark green	Val1	Pb, Fe	51	Pb, Cu	Cu-based pigment (Cu)
Flesh tones	Val2	Pb, lake	43	Pb, Ca	Lead white with lake (Pb)
Purple	Val3	Pb, Ca, lake	62	Pb, Ca	Purple lake (Pb)
Blue	Val4	Pb, Ca, Cu	50	Pb, Cu	Azurite (Cu)
Dark ochre	Val5	Ca, Pb, Fe	27	Pb, Ca, Mn, Fe	Umber (Mn, Fe)
Dark brown	Val6	Ca, Pb, Fe, Cu	60	Pb, Ca, Cu	Brown obtained with azurite (Cu)

Table 37. Comparison of the results obtained with SEM-EDX and XRF studies of "Martirio de San Hipólito".

Observed color	SEM-EDX study		XRF study		
	LDOA sample name	Characteristic elements	Spectrum name	Characteristic elements	Pigment or mixture determined
White	M1	Pb	59	Pb	Lead white
Red	M2	Red lake, Pb	35	Fe	Red ochre
Brown red	M3	Lamp black, Fe	64	Fe, Mn	Umber
Dark color	M4	Lamp black, Pb	67	Pb	Organic black pigment
Green	M5	Cu	3	Cu	Cu-based pigment

The XRF study of the "Martirio de San Hipólito" includes analysis of the areas next to the sampling made by researchers from LDOA in order to compare the XRF results with

the SEM-EDX results obtained (Table 37). The similarity of the results for M1, M4 and M5 can be observed.

The LDOA results report concludes that the dark red ground preparation consists of red clay (iron oxides with quartz, feldspars, igneous rock fragments with iron and titanium, calcite, silica and aluminum as impurities) mixed with hematite and barium sulfate or barite. The presence of barite in red ground preparation has already been identified in various examples of New Spanish paintings [163] as well as in 17th French paintings [164]. The thickness of the layer is more or less 100 µm. The dark gray priming layer is a mixture of the previous ground preparation with white lead oxide and copper presenting a thickness from 20 to 50 µm. The LDOA report points out that literature does not mention any previous examples of the use of Cu-based pigments in the priming layer during the 17th century [157].

Finally, in the case of "Martirio de San Hipólito", the chemical information obtained by SEM-EDX about the ground preparation and the priming layers is similar to the CXRF in-depth profiles results obtained at the Fine Arts Museum of Seville and to the SEM-EDX study made by the IAPH during the restoration intervention of the "Virgen del Valle", supporting the authorship attribution to Alonso Vázquez (Table 38).

Table 38. Summary of the results obtained with SEM-EDX and CXRF studies.

Artwork title	Study	Ground preparation	Ground color	Priming	Priming color
Sagrada Cena	CXRF	ND	ND	Fe or Pb	Red or white
Virgen del Valle	SEM-EDX (IAPH)	Ca, S	White	Pb, Ca, Fe	Reddish/pink
San Pedro Nolasco despidiéndose de Jaime I	CXRF	Ca	White	Fe	Red
San Pedro Nolasco redimiendo cautivos	CXRF	In progress			
La Inmaculada	CXRF	ND	ND	Fe	Red
Martirio de San Hipólito	SEM-EDX (LDOA)	Fe, Ca, Ba, S	Dark red	Fe, Pb, Ca, Ba, Cu, S	Dark gray
Virgen de las Uvas	SEM-EDX (LDOA)	In progress			

4.5. Conclusions of the Alonso Vazquez's artworks study

Alonso Vázquez was among the first Spanish painters to work in New Spain. Therefore, the study of the Mexican paintings of Alonso Vázquez is important for the Art History in order to assess their real influence on the evolution of art in Mexico. Nonetheless, before being able to carry out this work, it is necessary to identify artworks of this painter that still exist and to do an unpredictable identification study for those that remain unsigned.

The present study was used to compare the artworks attributed to Vázquez during his period in Mexico and his previous stay in Seville. The comparative analysis defined the pictorial techniques and palette of this artist. The information about the seven artworks is summarized in Table 39. For the material study of these paintings, the artworks with

confirmed authenticity were taken as reference. They are from the series of "San Pedro Nolasco". A comparative study of other paintings allowed to discuss their attribution from the material point of view.

The methodology used to analyze the seven artworks in Seville and Mexico was similar in order to normalize the results and be able to compare them. The study was carried out following an interdisciplinary methodology developed for the analysis of paintings which consisted of:

- Photographic record in the reflected visible light spectrum and UV-induced visible fluorescence photography,
- IRR study,
- XRF study,
- CXRF study (in the case of the artworks from the Fine Arts Museum of Seville),
- OM and SEM-EDX studies of micro-samples mounted in cross sections (in the case of Mexican artworks).

The accuracy and efficiency of the methodology applied to XRF data treatment and interpretation was verified. Its ability to compare artworks was also demonstrated. From the XRF studies, based on the methodology proposed, a synthesis of the pigments detected on each artwork was presented. The technique of the artist and his palette in terms of inorganic pigments was shown amongst other information provided by the archaeometric investigation.

The IRR study revealed very few preparatory drawings made of carbon black. All these drawings were used in architectural areas (e.g. stairs, grille, windows) or elements such as the table. They are all geometric elements difficult to produce without drawing them first. Faces and hands of the characters show very few corrections. The paint application is sharp, the border of the bodies and clothes were corrected using the same mixture of dark pigments used in the decorated adjacent parts. More *pentimenti* are observed on decorative items such as dishes, cutlery, pots, etc.

In XRF, the most complex palettes were detected in the "Sagrada Cena" and the "San Pedro Nolasco despidiéndose de Jaime I El Conquistador", followed by "San Pedro Nolasco redimiendo cautivos" and the "Inmaculada". It is a logical conclusion as they are the greatest artworks. Comparing the five artworks from Seville, the palette of inorganic pigments used is very similar. The different tones were obtained by applying the same mixtures with some variations from one painting to another.

The use of organic pigments was suggested by the absence of inorganic elements able to explain the color observed in the artwork. The use of an organic black pigment in the "Sagrada Cena" and in the "San Pedro Nolasco redimiendo cautivos" was detected. This organic black pigment may have been used in the other artworks. Purple lake was observed on all the artworks. It is possible that the same or similar lake served to produce some flesh tones on the "Sagrada Cena". Finally, both the "Inmaculada" and the "Sagrada Cena", attributed to Alonso Vázquez by Serrano, present a palette of pigments and mixtures coherent with those observed on his confirmed artworks done in Seville.

Finally, the results obtained from the two Mexican paintings were compared to the five artworks analyzed in Seville. The palette of pigments detected on the "Martirio de San Hipólito" is consistent with the artworks from Seville, while the palette on the "Virgen de las Uvas" differs drastically. The blue and green colors cannot be explained by the use of inorganic Cu-based pigments as observed on the artworks from Seville. The future Mexican SEM-EDX study of the micro-samples extracted from this painting may confirm the presence of organic pigments. In the case of "Martirio de San Hipólito", IRR images

revealed the *pentimenti* of the pediment above Hernán Cortes as well as the *pentimenti* of the angel and the shield. The pigments and mixtures detected are similar to those from the rest of the painting. It suggests that the representations of Hernán Cortés and San Hipólito are contemporary. If Serrera's attribution is correct, this portrait may be one of the oldest known of the Spanish conqueror.

To conclude this study, Table 39 presents the new synthesis of the corpus excluding "Virgen de las Uvas" by material study and confirming the attribution of four paintings including "Martirio de San Hipolito" as the first Mexican painting attributed to Alonso Vazquez by both material and art history studies.

Table 39. Summary about the seven artworks.

Artwork title	Alternative title	Year of execution	Authenticity
Alonso Vazquez paintings			
Sagrada Cena	Ultima Cena	1588	Attributed by material and art history studies
Virgen del Valle	Virgen del Pozo Santo	1597	Attributed to an altarpiece with contract and by material study
San Pedro Nolasco despidiéndose de Jaime I El Conquistador	None	1601	Contract and artwork signed
San Pedro Nolasco redimiendo cautivos	None	1600-1603	Contract
La Inmaculada	Virgen Inmaculada	Unknown	Attributed by material and art history studies
Martirio de San Hipólito	None	1605-1607	Attributed to an altarpiece with contract and by material study
Unknown artist painting			
Virgen de las Uvas	Virgen apocalíptica or Inmaculada Concepción	Unknown	Excluded by material study

CONCLUSIONS

The main goal of this research was to design and characterize the capabilities of a portable confocal μXRF system that allows the noninvasive *in situ* analysis of easel paintings in combination with other spectroscopic and multispectral techniques, more specifically, XRF, IRR and UV-induced visible fluorescence. The potential of this device was proved in a particular problem in the fields of Cultural Heritage and Art History: the characterization of the techniques and the palette of the 16th century Spanish painter Alonso Vázquez and the confirmation of the authorship of some unsigned paintings, on the basis of material study. For this purpose, a methodology involving those techniques was proposed.

The first part of this PhD thesis was dedicated to the design, development and *in situ* application of several setups (PIRR, X-Panda and μXRF-CONCHA devices). A big effort was made to design *in situ* working setups allowing the study of artworks directly in the places of exhibition. It provides access to unique items that cannot leave their storage or exposition room. This work concerned not only the methodological application of the techniques and characterization of the setups but also the mechanical engineering and computing developments.

Several routines based on LabVIEW platform were developed in order to control the portable devices. A particular interest was focused on the treatment of the obtained data. A specific methodology was applied in order to achieve the analysis of XRF spectra obtained by CXRF using PyMCA software. Moreover, particular attention was paid to the production of mosaics of up to hundreds of IRR images comparing three software packages (VARIM, Autopano Giga and Microsoft ICE). In fact, obtaining a unique image of the entire artwork showed to be crucial in order to enhance the strategy applied in the analysis by other techniques such as XRF and CXRF.

The constructed μXRF-CONCHA device is the first of its kind in Spain and one of a few available around the world. It is also probably the first CXRF setup with the ability to perform *in situ* analysis.

Before to start the analysis of artworks, a series of experimental paint multilayers made like old paintings were studied with IRR and CXRF setups. The second part of the research consisted in developing specific methodologies in order to analyze more complex paintings.

On one hand, a comparison study of the performance of three IRR technologies (Si-CCD, InGaAs and Vidicon tube) was done. The Si-CCD camera have to be used together with a UV-visible light cut-filter in order to provide results comparable to those obtained with InGaAs and Vidicon cameras. The results obtained proved that the three IRR technologies allowed the observation of preparatory drawings made in carbon black.

This study also achieved the classification of the IR reflectivity of several inorganic pigments. The results showed that it is possible to discriminate different inorganic pigments with the same color observing IRR images. They confirmed the possibility of a first interpretation about the pigments presents based on IRR images.

On other hand, the experimental samples were studied with the μXRF-CONCHA device. The results were successfully compared with two other CXRF systems, the LouX^{3D} at the C2RMF in Paris and the CXRF set-up at AGH University of Science and Technology in Krakow. This intercomparison study confronted the composition and

sequence information obtained. The results achieved with the three devices are similar in spite of some technical differences.

The in-depth measurements showed that the µXRF-CONCHA set-up allows to carry out the compositional analysis with depth resolution in a nondestructive way. In most of the cases, it was possible to characterize the composition and sequence information of the multilayered samples. However, sometimes the data interpretation revealed to be quite complex. Absorption effect is the principal limitation of this technique. The problem when considering 16th century paintings is the use of pigments composed of heavy elements (e.g. Pb or Hg) which masked the signals from the ground layer or the priming layer.

As the last part of this PhD, seven paintings attributed to Alonso Vázquez were studied. This artist left paintings on both sides of the Atlantic, although unfortunately, several examples preserved, particularly in Mexico, are decontextualized and remain unsigned. As Alonso Vázquez was among the first Spanish painters to work in New Spain, the study of his Mexican artworks is important to Art History in order to assess his real influence on the evolution of the art in Mexico. In order to compare the paintings, this study took as reference the artworks with confirmed authenticity defining the techniques and palette of this artist.

The IRR study revealed very few preparatory drawings carried out by carbon black. All these drawings were used in geometric elements difficult to produce without drawing them first. The paint application revealed to be sharp, the border of the bodies and clothes were corrected using the same mixture of dark pigments used in the decorated adjacent parts. More *pentimenti* are observed on decorative items such as dishes, cutlery, pots, etc. The complementary results obtained with UV and IRR were used in order to select the area study of XRF and CXRF.

A novel methodology was proposed and validated in the XRF data interpretation in order to normalize the results and be able to compare them. The XRF results allowed a synthesis of the pigments detected on each artwork (lead white, vermilion, tin-lead yellow, massicot, ochres, azurite, green Cu-based pigment, umber). The different tones were obtained by applying the same mixtures with some variations from one painting to another. Comparing the five artworks from Seville, the palette of inorganic pigments used is very similar. This study confirmed the attribution of both the “Inmaculada” and the “Sagrada Cena”. Based on the Sevillan study, the results obtained from the two Mexican paintings showed that the palette detected on the “Martirio de San Hipólito” is consistent with the artworks from Seville while the palette on the “Virgen de las Uvas” differs drastically. In the case of the “Virgen de las Uvas”, the blue and green colors cannot be explained by the use of inorganic Cu-based pigments as observed on the artworks from Seville. The results excluded “Virgen de las Uvas” and confirmed the attribution of the “Martirio de San Hipolito” as the first Mexican painting attributed to Alonso Vazquez by both archaeometric and art historical studies. Moreover the integrity of the composition showed by IRR and XRF suggested that the representation of Hernán Cortés is contemporary to the “Martirio de San Hipolito”. Consequently the portrait of the Spanish conqueror may be the oldest known.

In-depth profiles were focused on painting areas free of heavy elements. The presence of ground and priming layers revealed by in-depth CXRF scans were compared to SEM-EDS study. The ground layers were made of Ca. In the case of the priming layer, both techniques revealed the use of red ochre priming with exception of the “Sagrada Cena” which in-depth scans showed the presence of a second Pb-based priming layer. The use of

two kinds of priming in a same artwork may be present in other artworks of Alonso Vazquez and could be studied in future.

CXRF demonstrated its usefulness when the interpretation of XRF results is not trivial due to the presence of several pigment layers.

Finally, CXRF was proven to be a very promising technique for performing depth-resolved chemical analyses. Although some limitations could appear when heavy element based pigments are present. In the study of old paintings, it can provide complementary results to the classical extraction of stratigraphic micro-samples providing an alternative noninvasive analysis. CXRF combined with IRR and XRF gives to the archaeometric study the ability to define the inorganic pigments palette and techniques used by painters.

APPENDIX

I. Specifications of the micro-focus X-ray source

DATENBLATT / DATA SHEET
Datum / Date: 21.12.2006

MCBM 50-0,6B W

METALL-KERAMIK RÖNTGENRÖHRE — METAL-CERAMIC X-RAY TUBE

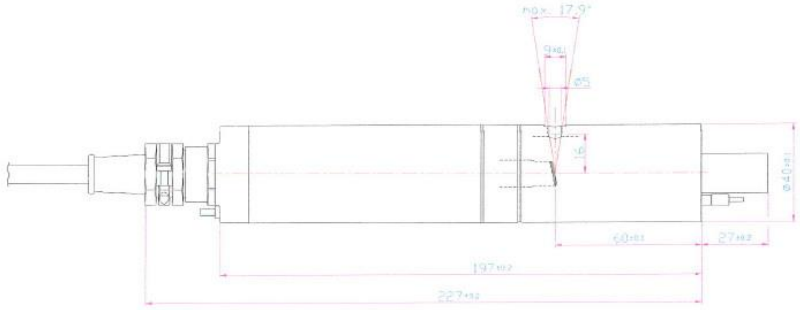

Alle Maße in mm / Grad — All Dimensions in mm / Degrees

Allgemeine Daten		**General Data**
Targetmaterial (andere auf Anfrage)	**W**	Target material (others on request)
Brennfleckgröße vermessen nach DIN EN 12543-5	**50 µm x 50 µm**	Focal spot size in accordance to DIN EN 12543-5
Anodenwinkel	**12°**	Anode angle
Ausstrahlungswinkel	**8°**	Emission angle
Eigenfilterung	**0,1 mm Be**	Inherent filtration
Masse	**~1 kg**	Mass
Absolute Grenzwerte		**Absolute maximum ratings**
Konstante Gleichspannung	**+ 50 kV**	Constant DC voltage
Anodenbelastung	**30 W**	Anode load
Heizfadenbelastung	**3,2 A (~3,2 V)**	Filament current
Temperatur	**60 °C**	Temperature

kV	50	40	35	30	25	20	15	10	5
mA	0,6	0,7	0,8	0,68	0,55	0,4	0,3	0,2	0,1

Masse ca.	**1 kg**	**Mass approx.**
Kontaktierung		**Contacting**
Katodenanschluß auf Erdpotential	**incl.**	Cathode at ground potential
Gedämpftes Polyolefin-Hochspannungskabel, im Keramikisolator fest verklebt	**incl.**	Polyolefine high voltage cable with inherent surge resistor bonded into ceramic isolator
Min. Biegeradius	**100 mm**	Min. bending radius
Min. Biegeradius, stationär	**50 mm**	Min. bending radius at fixed position
Luftisolierter Stecker	**65 kV**	Air insulated ht plug
Strahlenschutz	**Ohne/ Without**	**Radiation shielding**
Kühlung		**Cooling**
Luftkühler	**No.: 0606**	Air cooler
Wasserkühler	**No.: 1910**	Water cooler
Konduktionskühlung	**No.: -------**	Conduction cooling
Bei Bestellung bitte angeben	Kabellänge/ Cable length	**Please specify with order**

rtw RÖNTGEN-TECHNIK DR. WARRIKHOFF GmbH & Co. KG

Fig. 136. Specifications of the micro-focus X-ray source.

II. Specifications of the two polycapillary lenses of the µXRF-CONCHA device

IFG Institute for Scientific Instruments

Polycapillary X-Ray mini-lens
for micro-XRF
GEOMETRICAL PARAMETERS
OF LENS **167mkl05***)

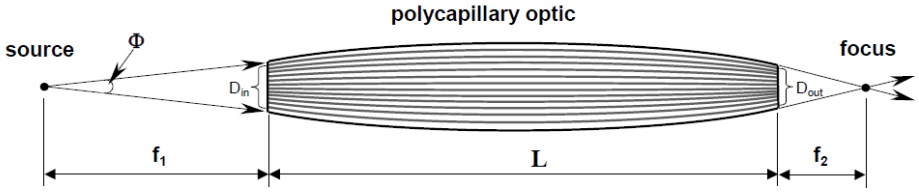

f_1, mm	80 +/- 0.5
f_2, mm	7.3 +/- 0.1
L, mm	47.7
D_{in}, mm	3.9
D_{out}, mm	1.55
D_{max}, mm	4.5
Φ, rad	0.075
R =f_1+f_2+L , mm	135 +/- 0.5

PARAMETERS OF FOCUS

E, keV	3-5	5-7.5	7.5-10	10-15	15-20	20-25	25-30
Focus size *, µm	29	28	28	25	19	17	17
Intensity gain**	907	2347	2923	3277	3045	1351	269

* - FWHM, scanning by 5µm pinhole
** - Intensity gain = Intensity through 5µm pinhole at lens focus/ Intensity of direct beam through
5µm pinhole

XRF Intensity:
from plexiglas: 9 000 cps
from Cu: 78 000 cps
from RC 36/16: 60 000 cps
Source: Mo, Ua=40kV, Ia=700µA
Detector: X-Flash Röntec 5mm^2
Distance Sample - Detector: 16mm

Tested: 07.02.2012 **S. Bjeoumikhova**

*) Be window, He filling

WARNING NOTE: The delivered optics device includes parts of beryllium. The delivered configuration is in no respect toxic.
In case of damaging it can be different! Uncovered beryllium parts can be very toxic for the health.
For this reason please inform all involved persons about this possibility preventative!
Please look at the safety instructions at the following websites:
http://www.brushwellman.com/EHS/Safety%20Facts/SF201.pdf http://www.brushwellman.com/EHS/Safety%20Facts/SF200.pdf

Fig. 137. Specifications of the full-lens of the µXRF-CONCHA device.

IFG Institute for Scientific Instruments

Polycapillary Semi-lens 137mkl03

GEOMETRICAL PARAMETERS

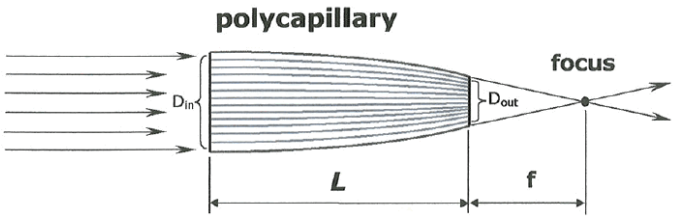

f, mm	**6.5 +/- 0.1**
L, mm	**35**
D_{in}, mm (cover/structure)	**4.6/4**
D_{out}, mm (cover/structure)	**1.8/1.4**

Source: Mo, 50µm - Warrikhoff
Ua=40kV, Ia=200µA
Detector - X-Flash (Röntec)

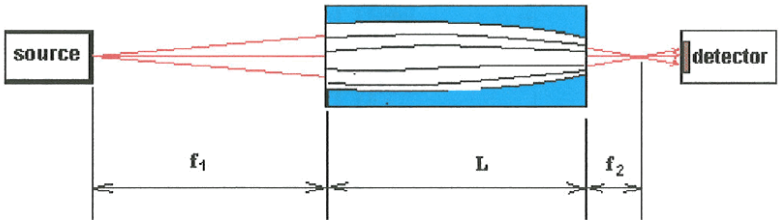

PARAMETERS OF FOCUS

E, keV	3-5	5-7.5	7.5-10	10-15	15-20	20-25
Focus size *, µm	36	35	33	27	20	19
Intensity gain**	47	444	429	328	210	75

* - FWHM, scanning by 5µm pinhole
** - Intensity gain = Intensity through 5µm pinhole at lens focus/ Intensity of direct beam through 5µm pinhole

Tested: 01.07.2010 **S.Bjeoumikhova**

Fig. 138. Specifications of the half-lens of the µXRF-CONCHA device.

III. Resolution of SDD detectors

The resolution of the Amptek SDD detectors used for the µXRF-CONCHA device and the X-Panda set-up were measured. The specifications of each detector are resumed in Table 40. The nominal resolution given by the manufacturer depends on measurement time and temperature.

The resolution of both detectors was measured with a manganese target using the X-Panda setup with a voltage of 30 kV and a current of 120 µA during 60 seconds. Table 40 shows the resolutions *R* calculated using the formula:

$$R(eV) = \frac{FWHM}{C} * E_{Mn}(eV) \quad (14)$$

with *FWHM* for the full width at half maximum and *C* for the centroid, both from the X-ray peak of Mn Kα, and E_{Mn} for the energy of excitation of the Mn Kα (5,894 eV).

Table 40. Information about SDD detectors.

Model detector	Active area (mm^2)	Si crystal thickness (µm)	FWHM	Centroid	Resolution (eV)
Super 123SDD	25	500	5,044	215,21	138
123SDD	7	450	4,1	163,14	148

IV. Specifications of the X-123SDD model detector from Amptek

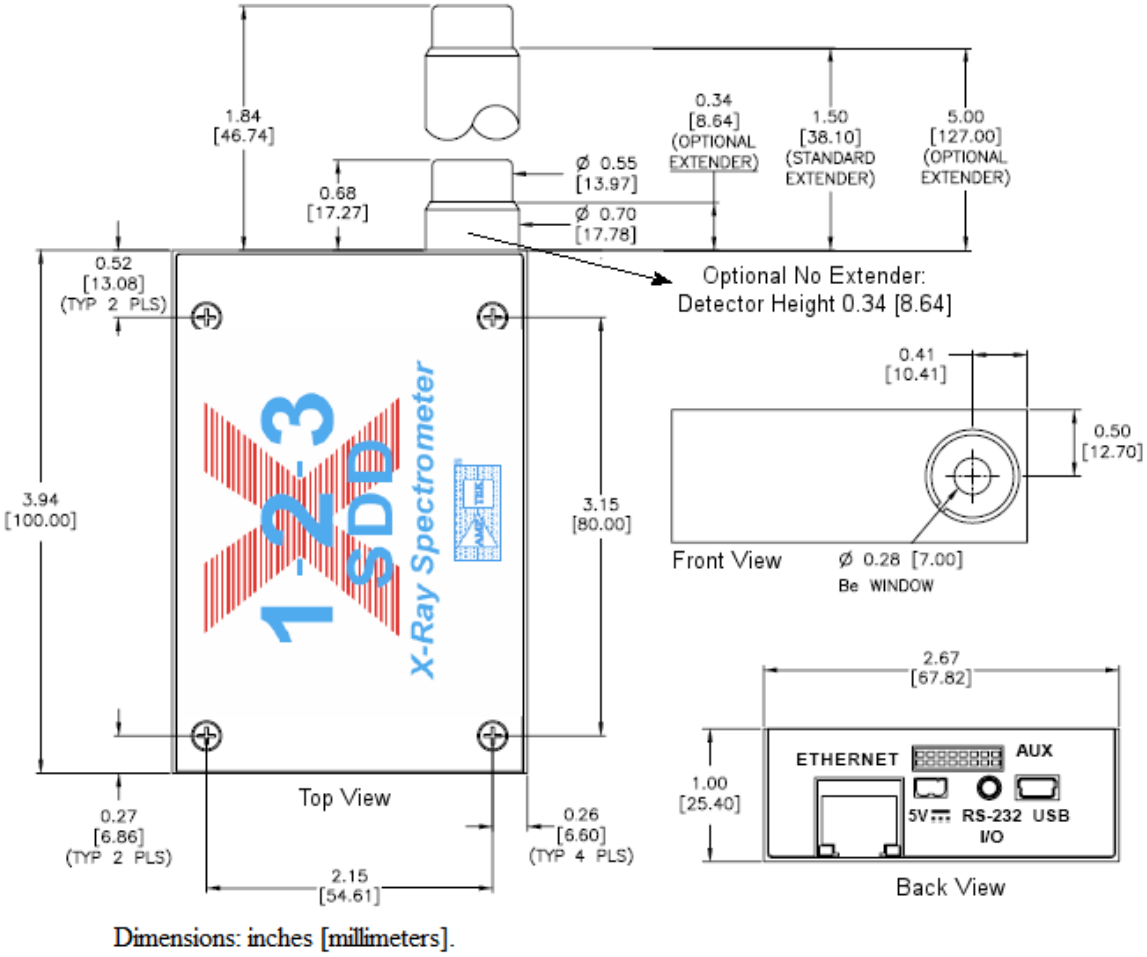

Fig. 139. Dimensions of the X-123SDD detector [33].

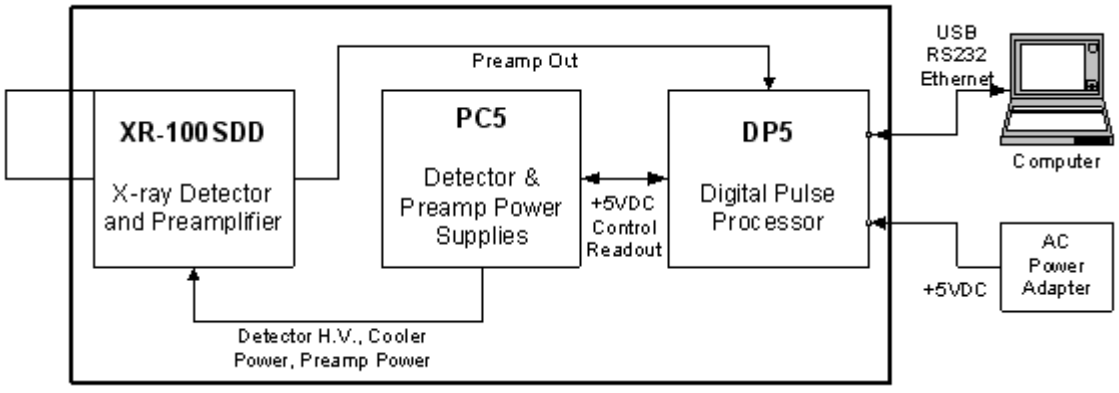

Fig. 140. Architecture and conexion diagram of the X-123SDD detector [33].

V. Treatment of the data obtained with CXRF and XRF setups using PyMca software

This appendix explains the use of PyMca software and its sub-programs to analyze the XRF spectra obtained with µXRF-CONCHA, LouX^{3D} and the three XRF devices. A detailed manual (about 75 pages in French) about the CXRF data processing by mean of PyMCA software was produced during PhD internship at the C2RMF.

The first step consists in obtain the EDF file compiling all the spectra from an analysis. In the case of the LouX^{3D} device, the software named "Convertisseur Multiformat AGLAE" (version "Octobre 2012") converts the MSA files to EDF. It was conceived by Ing. Laurent Pichon. In the case of the µXRF-CONCHA and XRF setups, "Mca to Edf Conversion" PyMca routine is used to convert the MCA files to EDF.

Then, the fit of the XRF spectra is made using "ROI Imaging Tool" PyMca routine (Fig. 141). In order to do that, configuration file were registered for each setup depending of their characteristics (X-ray detector, X-ray tube, fit parameters, etc.) including the calibration. For each EDF file, the chemical elements present were selected.

In the case of CXRF setup, all the peaks from a level transition were selected separately due to the fact that their proportions are strongly affected by absorption effect (Fig. 142).

To improve the fit, a layer of Pb (1 µm thick) was selected as approximation of the matrix. This specific Pb layer was created using "Material Editor".

Finally, the EDF files are analyzed with "PyMca Batch" PyMca routine. The software creates a DAT file including all the information about the peak area. This file is then used with Excel software and, eventually, OriginPro.

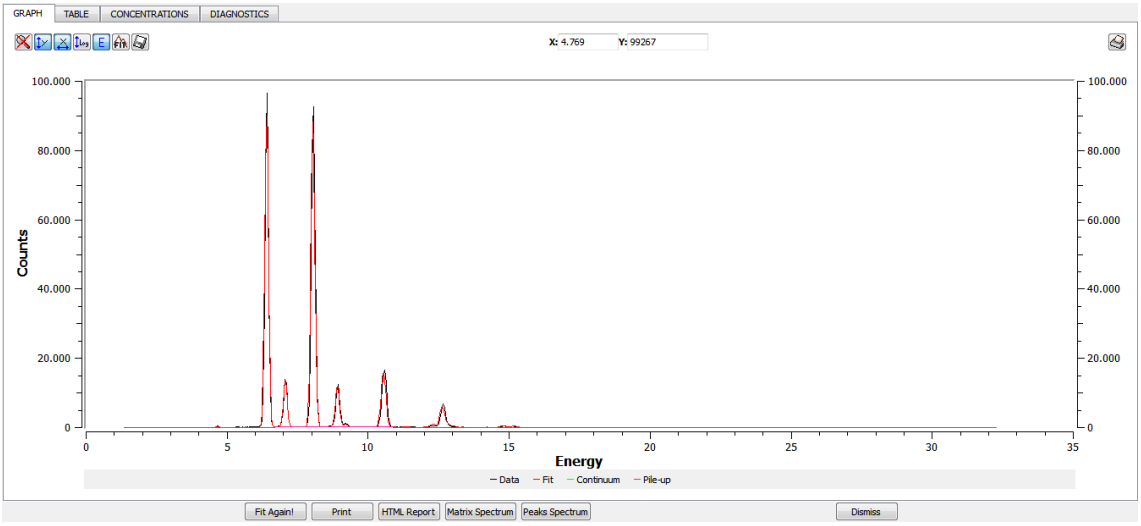

Fig. 141. Detail of the windows named « PyMca – McaAdvancedFit » showing the fit of a XRF spectrum represented in linear scale.

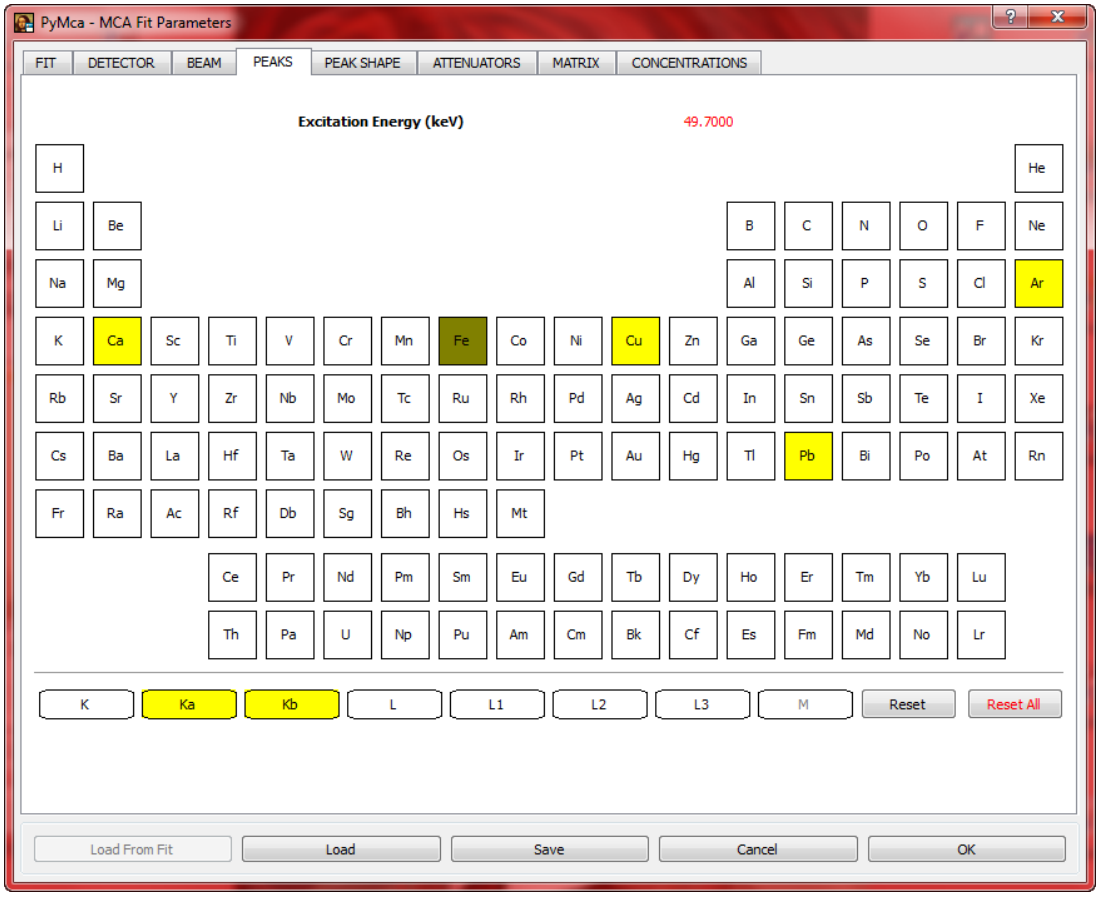

Fig. 142. Windows « PyMca – MCA Fit Parameters » showing the selection of the element.

VI. Specifications of the two polycapillary lenses of the LouX^{3D} device

IFG Institute for Scientific Instruments

Polycapillary X-Ray mini-lens

GEOMETRICAL PARAMETERS
OF LENS **51mls06**

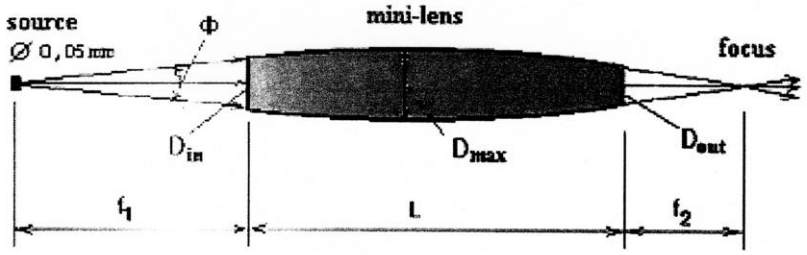

f_1, mm	53 +/- 0.1
f_2, mm	11 +/- 0.1
L, mm	100.3
D_{in}, mm	5.4
D_{out}, mm	2
D_{max}, mm	7
Φ, rad	0.101
R =f_1+f_2+L, mm	164.3 +/- 1

PARAMETERS OF FOCUS

E, keV	3-5	5-7.5	7.5-10	10-15	15-20	20-25	25-30
Focus size *, µm	42	43	45	43	34	29	30
Intensity gain**	1336	3426	4019	4438	4393	2591	675

*** - FWHM, scanning by 5µm pinhole**
**** -Intensity gain = Intensity through 5µm pinhole at lens focus/ Intensity of direct beam through 5µm pinhole**

XRF Intensity:

from plexiglas: 5 500 cps
from Cu: 45 000 cps
from RC 36/16: 29 000 cps

Tested: 23.11.2006 **S. Bjeoumikhova**

Fig. 143. Specifications of the full-lens of the LouX^{3D} device.

IFG Institute for Scientific Instruments

Polycapillary conic collimator POLY-CCC for micro-XRF

58mkl09*)

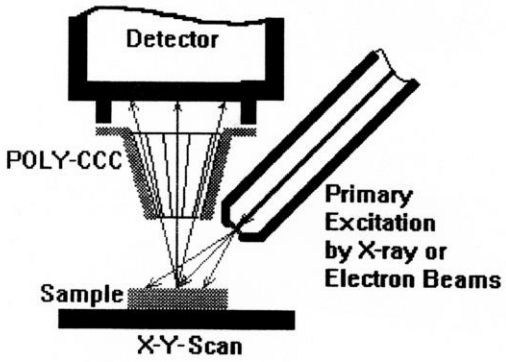

Principle: Fluorescence radiation capture from a local area of the sample surface.

Geometrical parameters:

Length, mm	13.52
Entrance size, mm	1.3/2.0
Exit size, mm	2.0/3.4
Sample-entrance distance, mm	6.2
F_2, mm	79.0
Capture angle (effectively), deg.	11.8

Physical parameters:

Spatial resolution (10μm stripe scanning in focal plane, CrKα-line and FeKα–line, FWHM), μm	**40**

*) Be window, He filling

Tested: 13.11.2006 **S. Bjeoumikhova**

WARNING NOTE: The delivered optics device includes parts of beryllium. The delivered configuration is in no respect toxic. In case of damaging it can be different! Uncovered beryllium parts can be very toxic for the health. For this reason please inform all involved persons about this possibility preventative! Please look at the safety instructions at the following websites: http://www.brushwellman.com/EHS/Safety%20Facts/SF201.pdf http://www.brushwellman.com/EHS/Safety%20Facts/SF200.pdf

Fig. 144. Specifications of the Poly-CCC of the LouX3D device.

VII. "Louvre0" acquisition software of LouX^{3D} set-up (in French)

During my PhD internship at the C2RMF, a user manual of the LouX^{3d} device and its acquisition software named "Louvre0" was written in French. The original document is about 63 pages. It proposes a methodology to obtain depth profile as well as lateral scan. This appendix only transcribes the part about the "Louvre0" use and specifically the way to obtain depth profile, in French. The software version used was dated from October 19, 2007.

Cette notice est informative. Nul ne pourra tenir pour responsable l'auteur de cette notice. Elle n'autorise pas une personne non autorisée, non formée, à utiliser l'équipement. Les protocoles présentés sont des protocoles parmi d'autres et ne prétendent pas être les protocoles de références. Ils ont pour objectifs de permettre un usage facile et efficace du logiciel.

Le dispositif est commandé à travers un logiciel intitulé « Louvre0 » développé par l'Institute for Scientific Instruments (IfG) [112]. La fenêtre principale du programme est présentée Fig. 145.

Les valeurs indiquées sous l'intitulé « Actual Position » correspondent aux valeurs de position des moteurs X, Y et Z dans cet ordre de haut en bas. Avant tout déplacement, il faut savoir que :

- le moteur X gère les déplacements horizontaux. Les valeurs négatives déplacent l'échantillon vers la gauche et, les positives, vers la droite (Fig. 146),
- le moteur Y gère les déplacements verticaux. Les valeurs négatives déplacent l'échantillon vers le haut et, les positives, vers le bas,
- le moteur Z gère les déplacements en profondeur. Les valeurs négatives rapprochent le support du dispositif d'analyse et, les positives, l'éloignent.

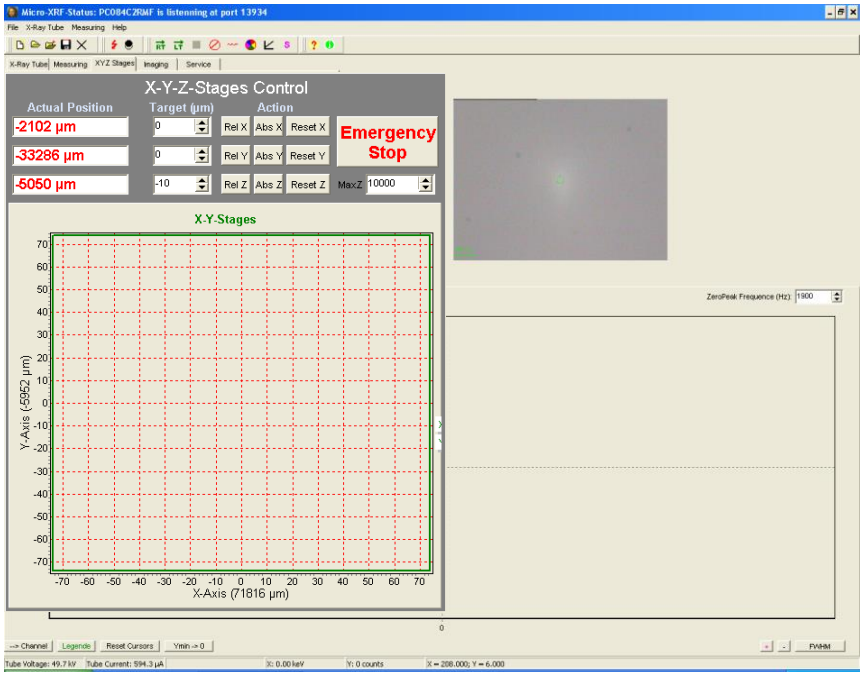

Fig. 145. Fenêtre principale avec l'onglet "XYZ Stages".

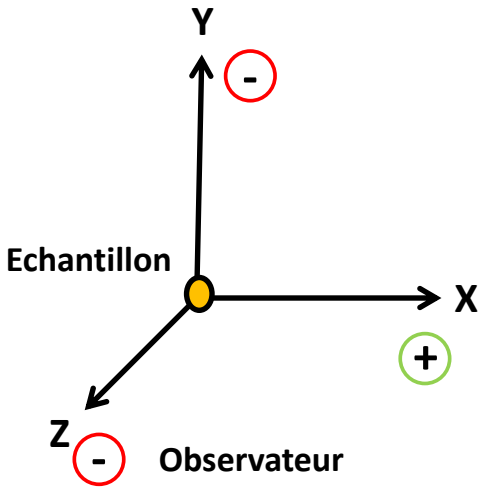

Fig. 146. Sens de déplacement de l'échantillon vis-à-vis de l'observateur.

On peut positionner l'échantillon sur le support lorsque celui-ci est suffisamment éloigné du dispositif. Une fois fixé, on approche manuellement le support du dispositif jusqu'à ce que l'échantillon se situe à 2-4 cm de la tête d'analyse (Figure 147).

Une fois l'échantillon à analyser positionné, on doit le rapprocher du dispositif, via le logiciel cette fois-ci, jusqu'à obtenir une image nette via le microscope. Pour se faire, on utilise les déplacements relatifs correspondants aux boutons Rel X, Rel Y et Rel Z dessous l'intitulé « Action » (Fig. 145). L'utilisateur doit fixer une distance de déplacements dans les cases situées sous l'intitulé «Target (µm)». Pour positionner l'échantillon, les déplacements en X et Y peuvent être amples (de 100 à 1000 µm). En Z, il est préférable d'avancer prudemment (de 50 à 100 µm). Le sens du déplacement dépend de la valeur positive ou négative du chiffre entré. Le déplacement s'effectue de la distance choisie chaque fois que l'utilisateur actionne le bouton « Rel » correspondant (les boutons Rel X, Rel Y ou Rel Z).

Remarque : Dans un premier temps, un repère rouge dessiné au marqueur sur l'écran de télévision (Fig. 148) retransmettant l'image enregistrée par une caméra placée sur le dispositif permet à l'utilisateur de positionner l'échantillon dans l'axe du microscope via les déplacements en X et Y.

Fig. 147. Mise en place de l'échantillon et rapprochement manuel du support au dispositif.

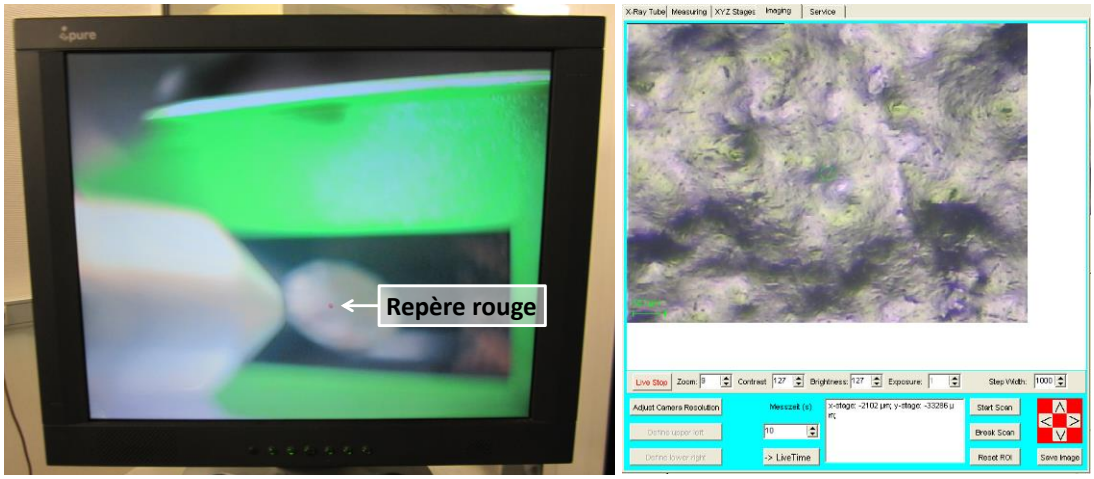

Fig. 148. Repère rouge sur l'écran (à gauche). Onglet "Imaging" (à droite).

Par la suite, l'utilisateur doit rapprocher l'échantillon du dispositif jusqu'à obtenir une image nette en s'aidant de l'image du microscope dans la fenêtre principale du logiciel. Une fois obtenu le focus avec le microscope, on peut sauvegarder l'image en cliquant sur Save Image dans l'onglet « Imaging » (Fig. 148). La sauvegarde de l'image permet de fixer dès le départ le dossier par défaut où toutes les données seront sauvegardées. Par commodité, le nom de l'image d'un échantillon correspond au nom du premier fichier MSA (c'est-à-dire de la première mesure du jour).

Une fois enregistrée l'image, on retourne dans l'onglet « XYZ Stages ». On avance le support de 400 µm en Z en rentrant la valeur « -400 » dans Target (µm) et en cliquant sur Rel Z (Fig. 149). Puis, on remet la valeur de déplacement à zéro.

On clique sur l'onglet « Measuring ». Il est préférable de lancer un premier profil en profondeur rapide pour vérifier que l'échantillon est correctement positionné vis-à-vis du profil mesuré. Dans ce cas, on conseille de faire un profil avec un pas de 10 ou 20 µm en Z sur une distance de 400 µm (soit respectivement 40 ou 20 spectres) pour un temps de mesure de 10 ou 20 secondes par spectre. Ce premier profil permet de définir la zone d'intérêt à analyser pour le profil lent.

Dans le cas présent, on choisit d'effectuer un profil avec un pas de 10 µm en Z sur une distance de 300 µm (soit 30 spectres) pour un temps de mesures de 10 secondes par spectre. Pour plus de sûreté, il serait préférable d'effectuer un scan sur une distance de 400 µm. Pour se faire, dans l'encadré intitulé « Measuring Control », on écrit « 10 » dans la case « Time (s) : » et « 30 » dans la case « No of Z Pos : » et on clique sur le bouton Live Start (s) (Fig. 149).

Puis apparaît une fenêtre intitulée « X-Y-Z-Scan Start Parameter » récapitulant les paramètres choisis pour le profil. Dans la case correspondant à « Z-Direction » du paramètre « Step Width » (dimension du déplacement ou du pas), on rentre la valeur positive « 10 » car on souhaite que l'échantillon s'éloigne du dispositif lors du profil (Fig. 150). Puis, on clique sur Start XYZ-Scan, une fois tous les paramètres vérifiés.

On revient sur la fenêtre principale et le profil est en train de s'enregistrer. On peut observer l'avancée du profil dans une petite barre de progression (Fig. 151).

Remarque : Il est possible d'arrêter une série de mesure en cours de route dans le cas où, par exemple, l'on s'aperçoit que l'on n'enregistre plus de données intéressantes ou que le scan déjà effectué est suffisant. Pour cela, il suffit de cliquer sur le bouton Break.

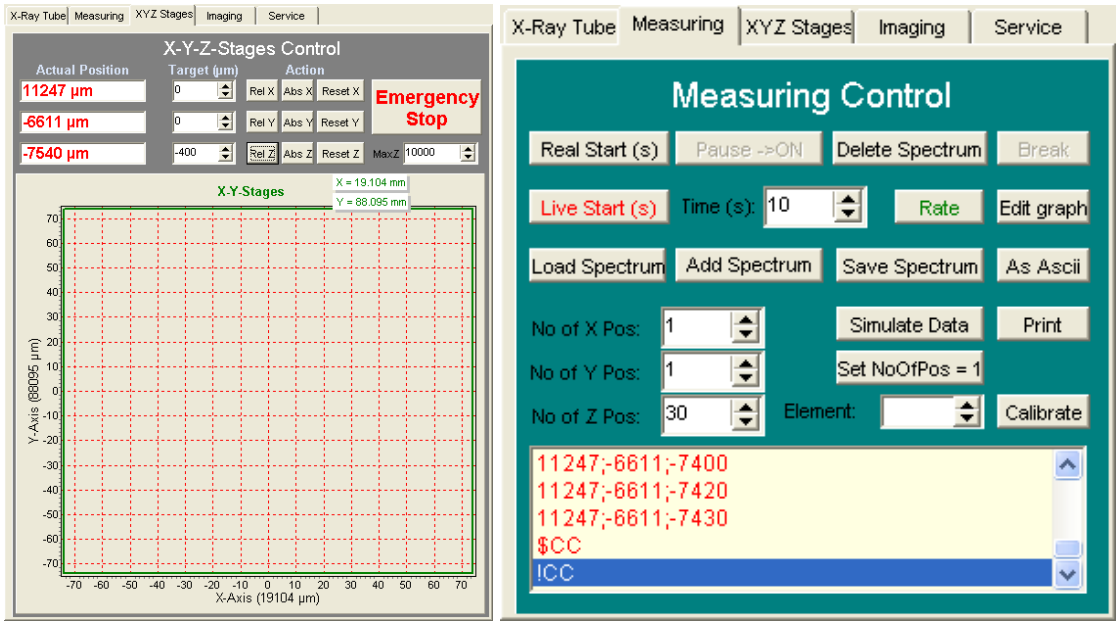

Fig. 149. Onglet "XYZ Stages" (à gauche). Onglet "Measuring" (à droite).

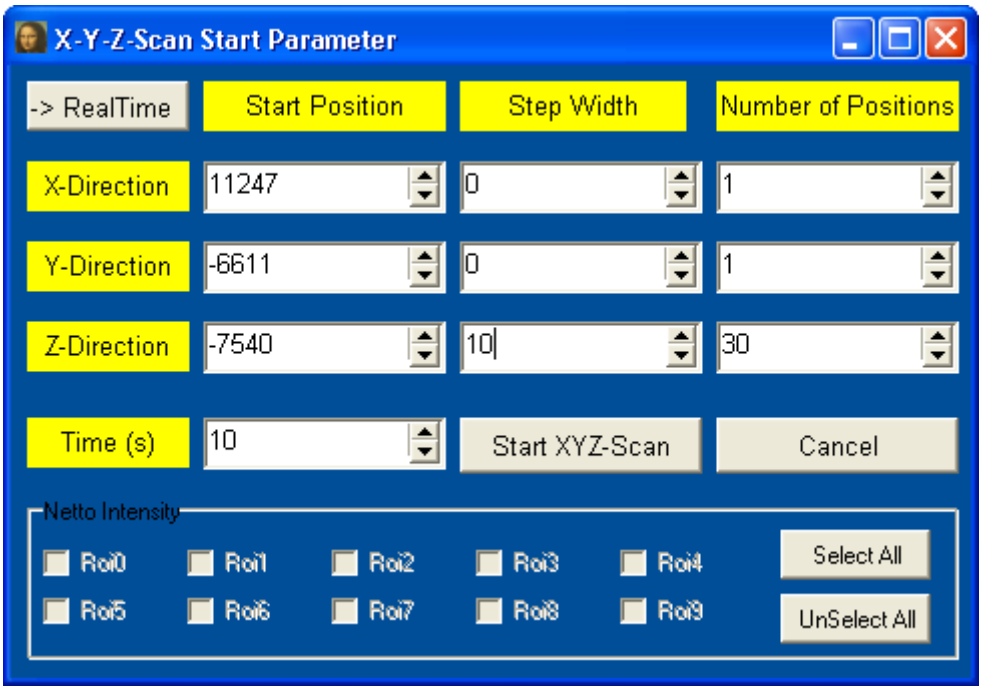

Fig. 150. Fenêtre "X-Y-Z-Scan Start Parameter".

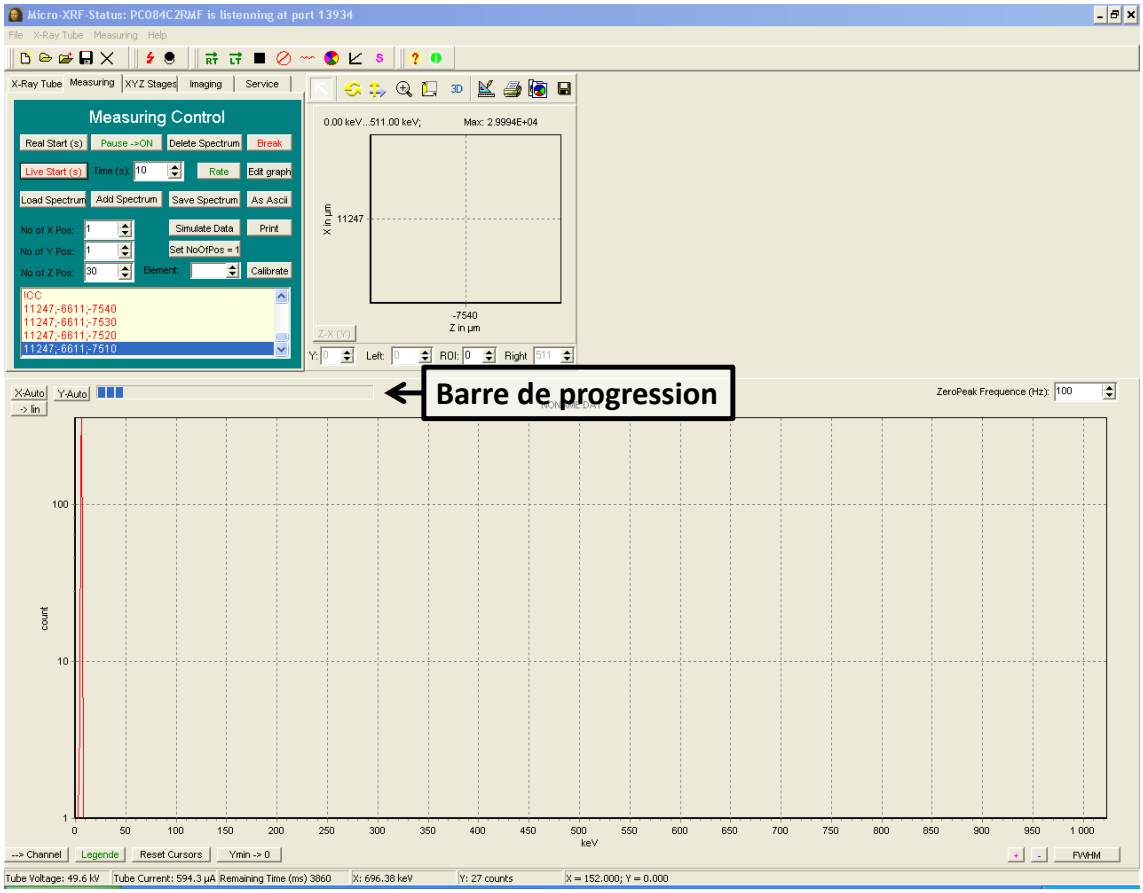

Fig. 151. Fenêtre principale lors d'une mesure en cours.

Pour avoir une bonne appréciation du déroulement des mesures, il est préférable de passer le graphique, présent en bas de l'écran, en échelle logarithmique en cliquant sur le bouton -> log.

Une fois la série de mesures terminée, on voit apparaître dans la zone du graphique, en bas, la somme des spectres enregistrés ainsi qu'un aperçu de l'évolution de l'intensité du spectre en fonction de la profondeur (Fig. 152).

En double-cliquant avec le clic gauche de la souris autour des pics du spectre, on peut sélectionner une zone d'intérêt qui apparaît par la suite dans l'aperçu d'intensité en fonction de la profondeur, en haut de la fenêtre principale, pour la zone sélectionnée. On peut déplacer les lignes de sélections de pics en cliquant avec le clic gauche de la souris sur une ligne et en déplaçant le curseur sur le spectre tout en maintenant le clic (Fig. 153). Il est aussi possible de supprimer toutes les sélections en cliquant sur Reset Cursors. En cliquant avec le clic gauche de la souris sur l'aperçu d'intensité en fonction de la profondeur, on fait apparaître à sa droite, en lieu et place de l'aperçu du microscope, un nouvel encadré qui représente le profil en profondeur de la zone sélectionnée (Fig. 153).

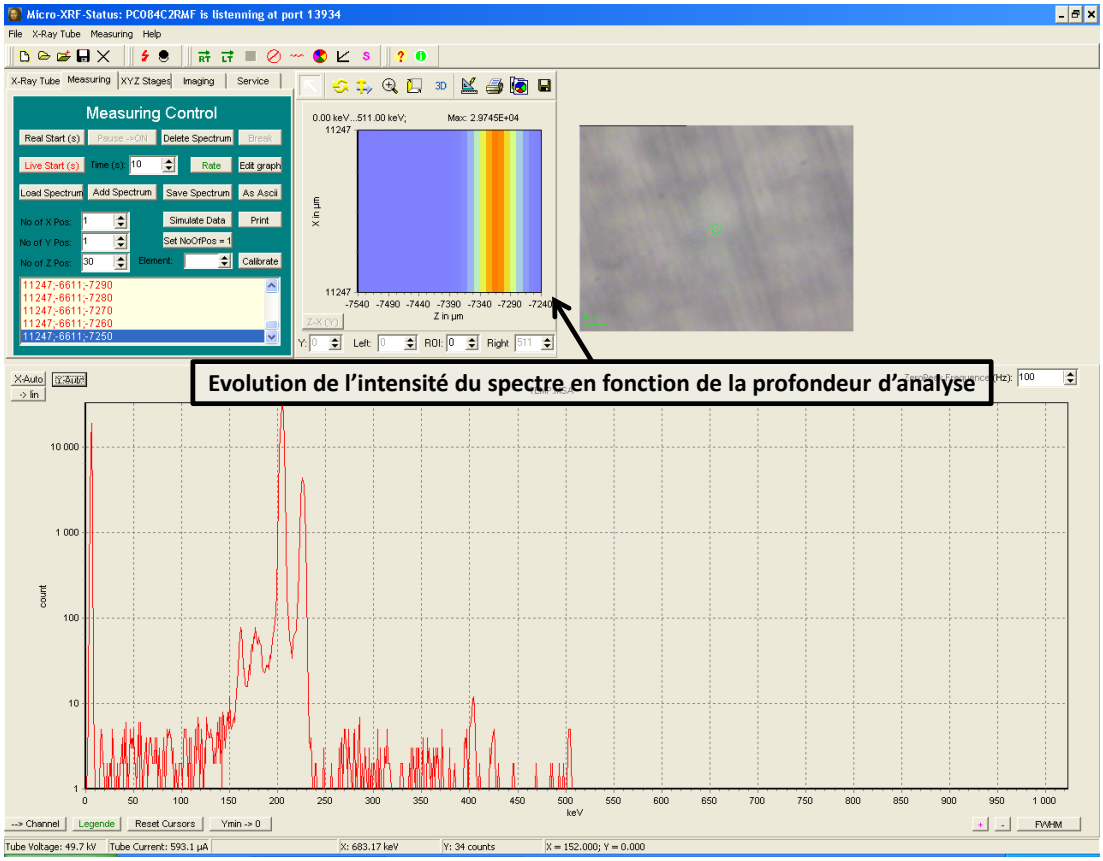

Fig. 152. Fenêtre principale, visualisation du profil en profondeur des pics Kα et Kβ du Cu.

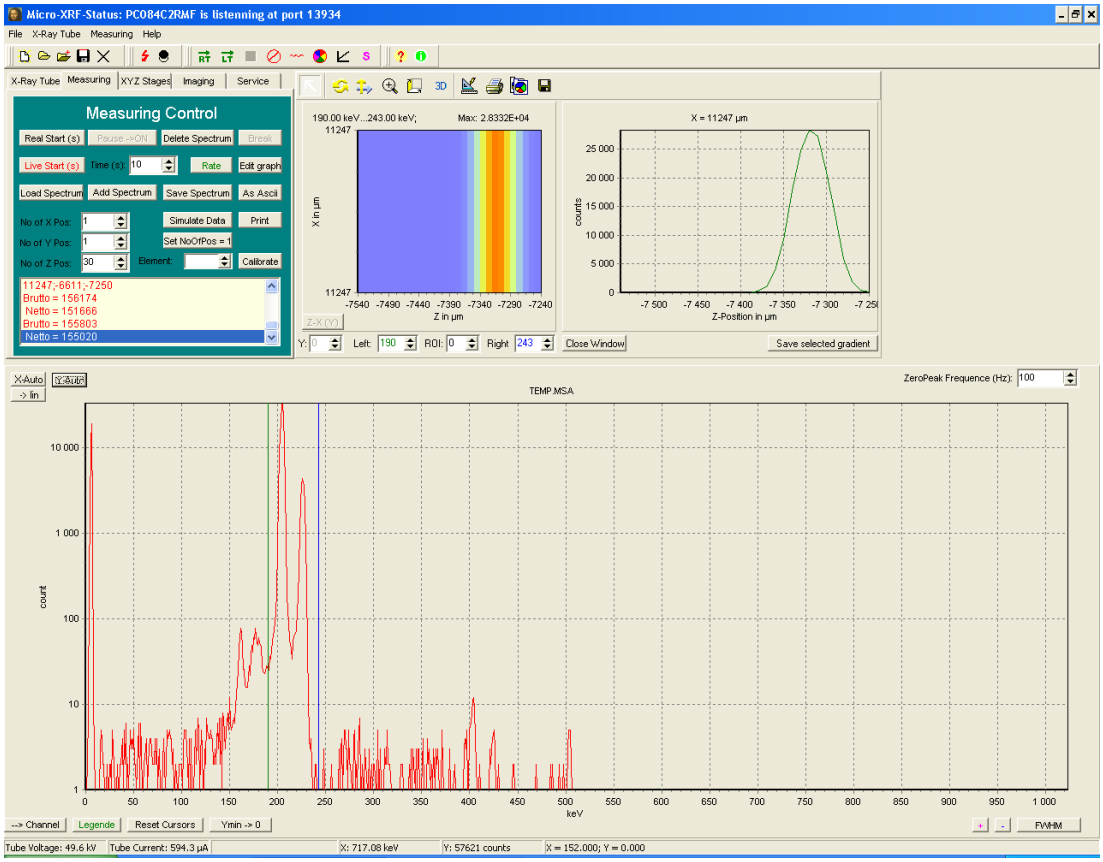

Fig. 153. Fenêtre principale.

On observe, dans la Fig. 153, que la zone d'intérêt se situe entre les positions Z « -7400 » et « -7200 ». Avant de redémarrer une mesure, on peut vider la zone du graphique et les données du profil en appuyant sur le bouton Delete Spectrum dans l'encadré « Measuring Control ». On retourne dans l'onglet « XYZ Stages » et on positionne l'échantillon à « -7400 » avec Rel Z.

Maintenant, on peut effectuer un profil en profondeur lent. On choisit d'effectuer un profil avec un pas de 10 µm en Z sur une distance de 200 µm (soit 20 spectres) pour un temps de mesures de 120 secondes par spectre. Pour se faire, dans l'encadré intitulé « Measuring Control », on écrit « 120 » dans la case « Time (s) : » et « 20 » dans la case « No of Z Pos : » et on clique sur le bouton Live Start (s). Puis, une nouvelle fenêtre intitulée « X-Y-Z-Scan Start Parameter » apparaît récapitulant les paramètres choisis pour le profil (Fig. 154). Dans la case correspondant à « Z-Direction » du paramètre « Step Width » (dimension du déplacement ou du pas), on rentre la valeur positive « 10 » car on souhaite que l'échantillon s'éloigne du dispositif lors du profil. Puis on clique sur Start XYZ-Scan, une fois tous les paramètres vérifiés.

Une fois la série de mesures terminée, on voit apparaître dans la zone du graphique en bas, la somme des spectres enregistrés ainsi qu'un aperçu de l'évolution de l'intensité du spectre en fonction de la profondeur (Fig. 155).

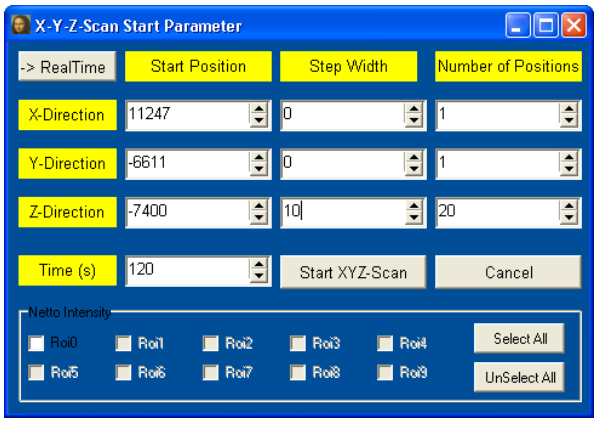

Fig. 154. Fenêtre "X-Y-Z-Scan Start Parameter".

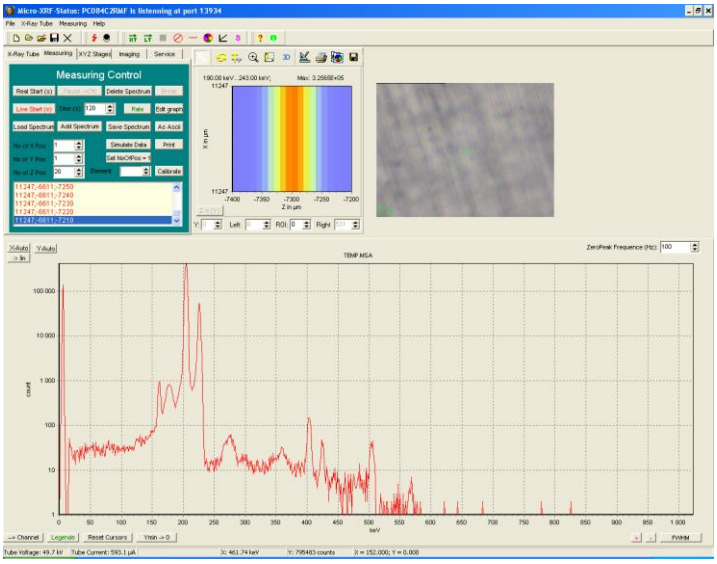

Fig. 155. Fenêtre principale à la fin de la série de mesures.

Voici un exemple de profil en profondeur d'un système multicouche Cr-Ni-Pb de 1 µm chacun (cf. Fig. 86, Chapitre 3.3.1).

Remarque : Ce profil en profondeur a été effectué en sens inverse (en rapprochant le support au dispositif), pour autant les pics apparaissent de la gauche vers la droite. Dans un profil en profondeur effectué dans le sens normal conseillé, les pics doivent apparaître de la droite vers la gauche (la surface de l'échantillon se situant à l'extrême droite du graphique).

En cliquant sur le spectre avec le clic gauche de la souris, on sélectionne d'abord les pics Kα et Kβ du Cr qui apparaît par la suite dans l'aperçu en haut, puis on clique sur l'aperçu d'intensité en fonction de la profondeur pour le voir s'ajouter à la fenêtre de droite. Ensuite, on sélectionne les pics Kα et Kβ du Ni qui apparaît par la suite dans l'aperçu en haut. Puis, on clique avec le clic gauche de la souris sur l'aperçu d'intensité en fonction de la profondeur pour le voir s'ajouter à la fenêtre de droite (Fig. 156). Finalement, on sélectionne les pics Lα et Lβ du Pb qui apparaît par la suite dans l'aperçu en haut. Puis, on clique avec le clic gauche de la souris sur l'aperçu d'intensité en fonction de la profondeur pour le voir s'ajouter à la fenêtre de droite (Fig. 157). On obtient ainsi le profil en profondeur du système multicouche analysé (Fig. 158).

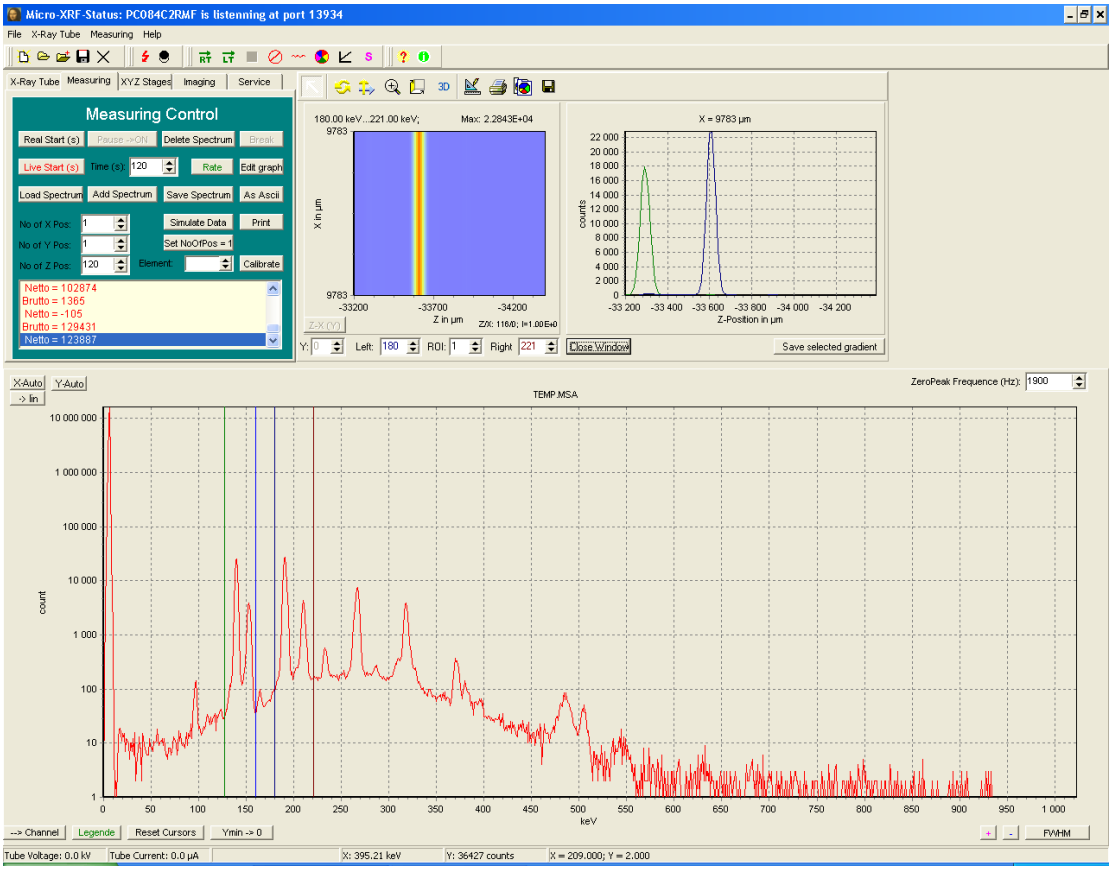

Fig. 156. Fenêtre principale, visualisation des profils en profondeur du Cr et du Ni.

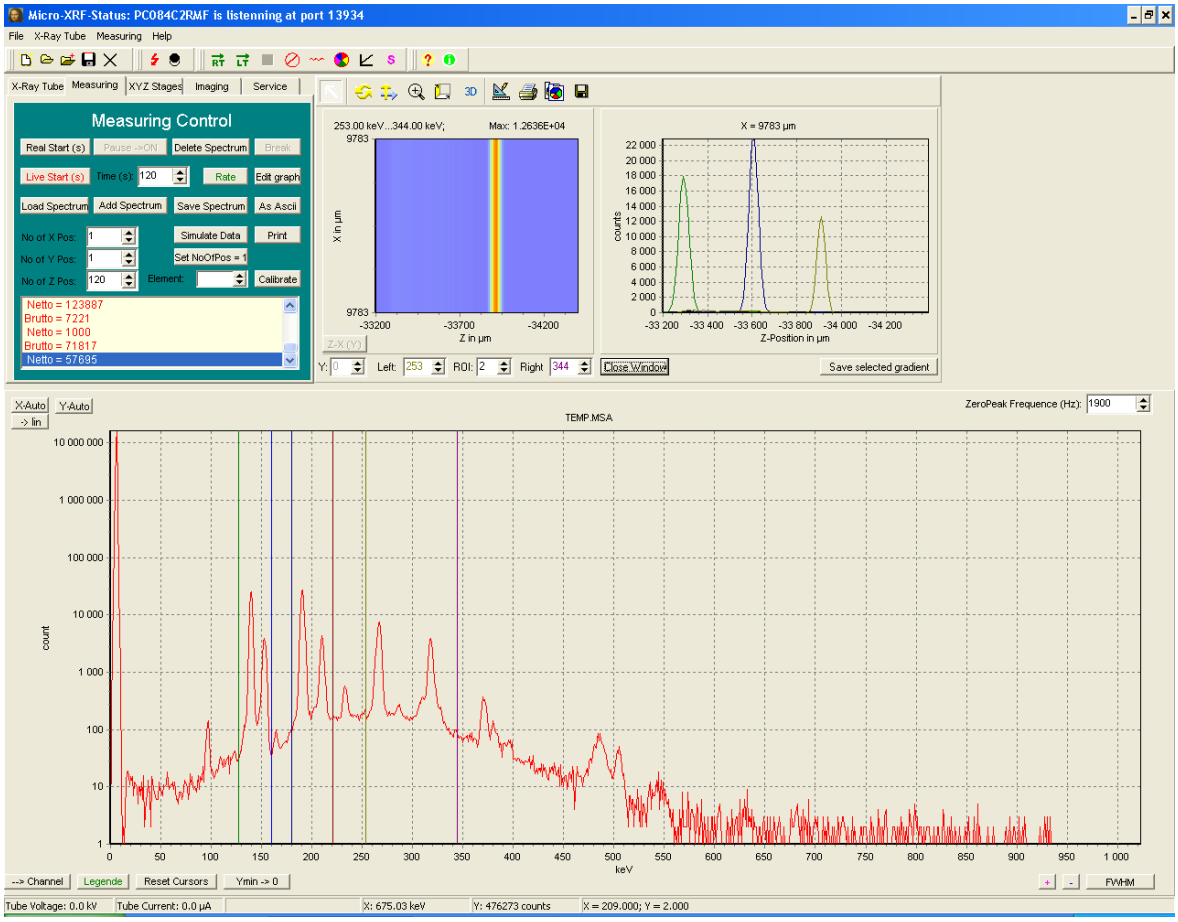

Fig. 157. Fenêtre principale, visualisation des profils en profondeur du Cr, du Ni et du Pb.

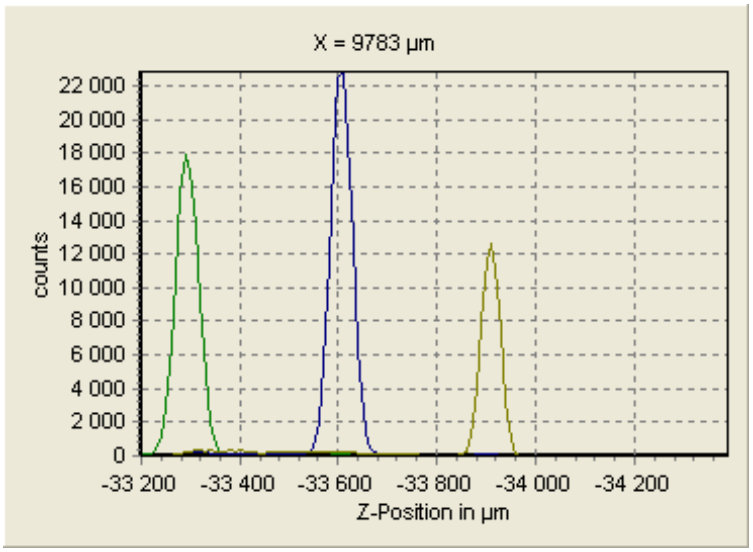

Fig. 158. Profil en profondeur du système multicouche analysé.

VIII. Specifications of X-ray tube Mini-X model from Amptek

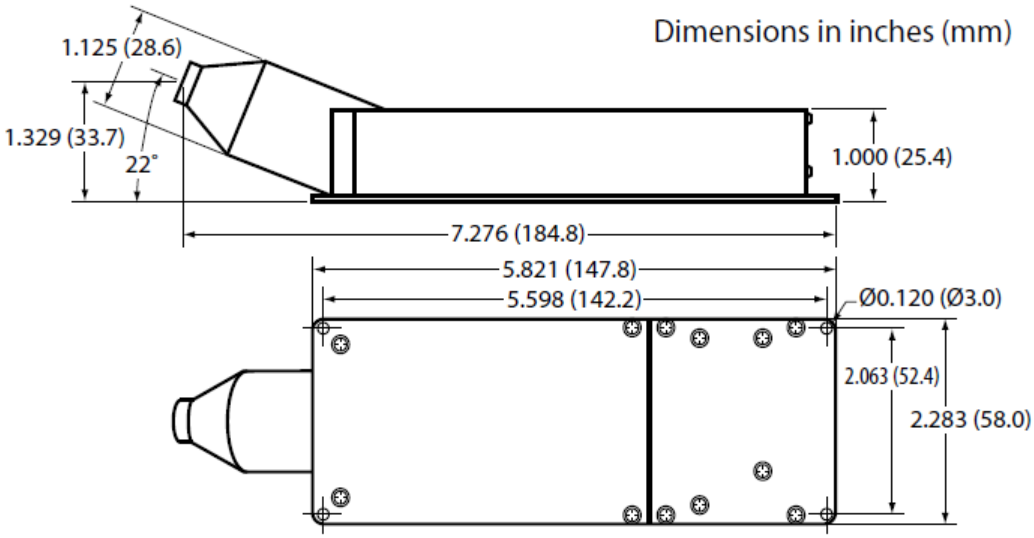

Fig. 159. Dimensions of the *Mini-X* X-ray tube [33].

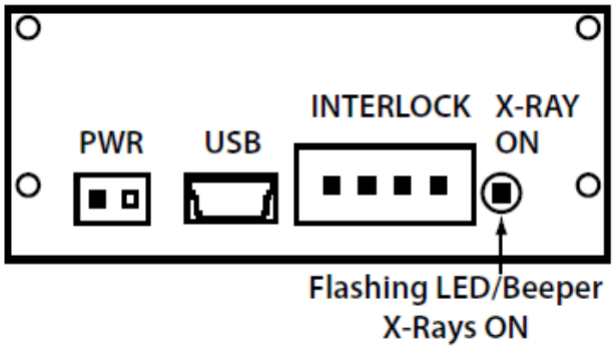

Fig. 160. Exit of the different connectors of the *Mini-X* X-ray tube [33].

IX. In-depth scan results with the three CXRF devices

This appendix presents six more in-depth scans obtained of experimental paint multilayers with µXRF-CONCHA, LouX3D and AGH CXRF devices (Fig. 161 to Fig. 171 and Table 41 to Table 46). All the experimental paint layers were studied using the same conditions (50 kV, 600 µA, 5 µm steps and 120 s/point, with the exception of the Poland CXRF setup which measurements were performed with 1000 µA).

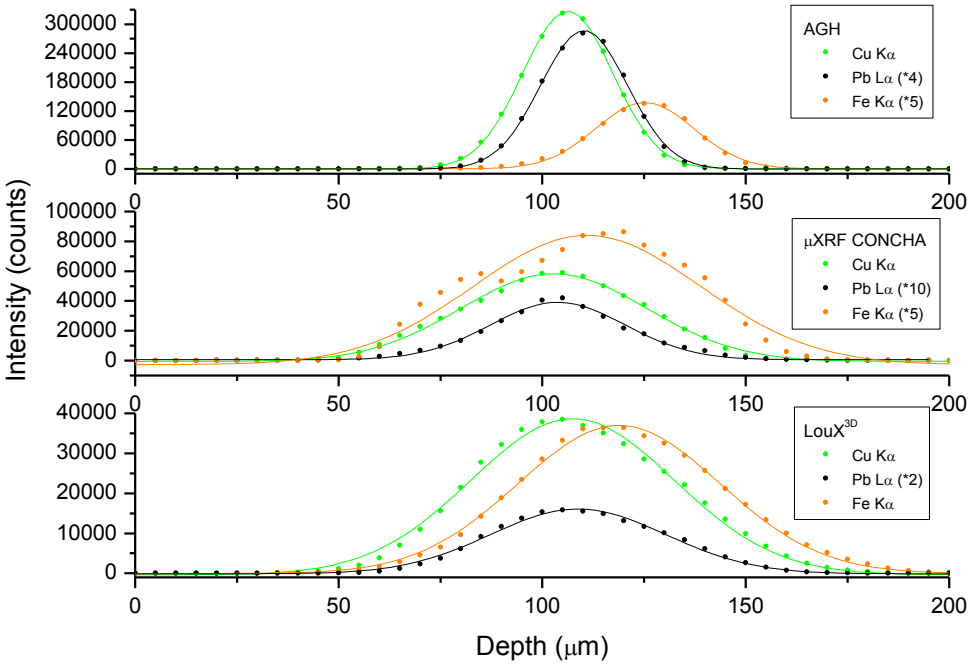

Fig. 161. Depth profile of an experimental paint multilayer.

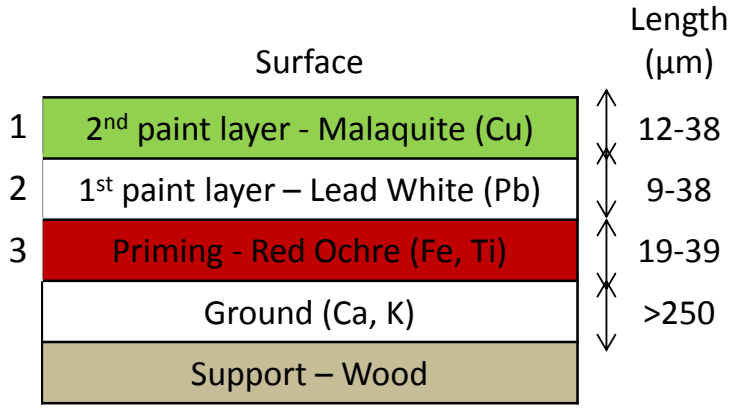

Fig. 162. Scheme of the experimental paint multilayer (Fig. 161).

Table 41. Results of in-depth scan presented Fig. 161.

Distance b/w layers	ΔXc (µm) Concha	ΔXc (µm) LouX^{3D}	ΔXc (µm) AGH
1-2	1 ± 3	2 ± 3	4 ± 3
2-3	7 ± 3	10 ± 3	15 ± 3

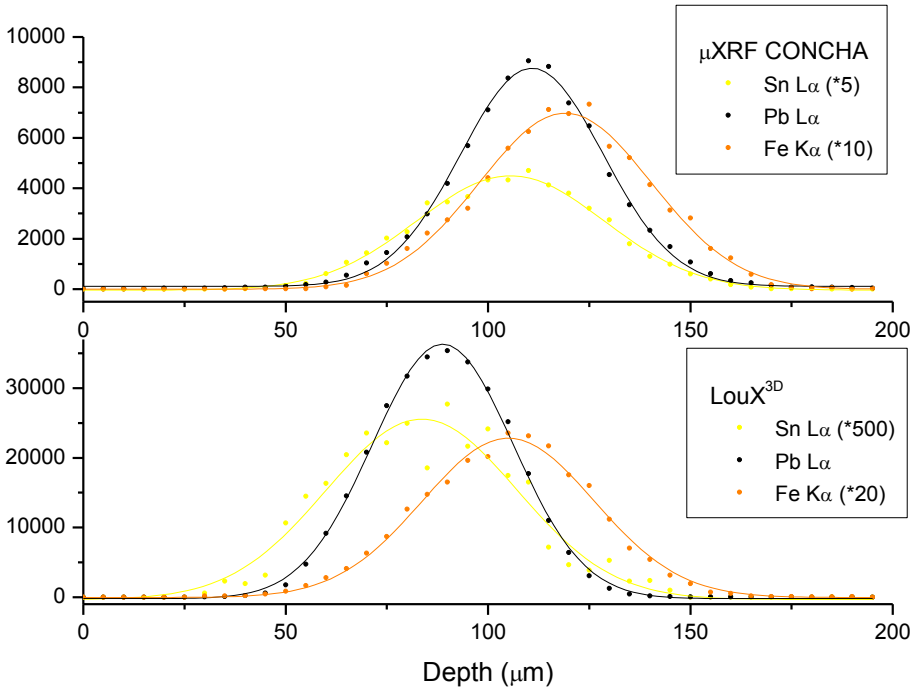

Fig. 163. Depth profile of an experimental paint multilayer.

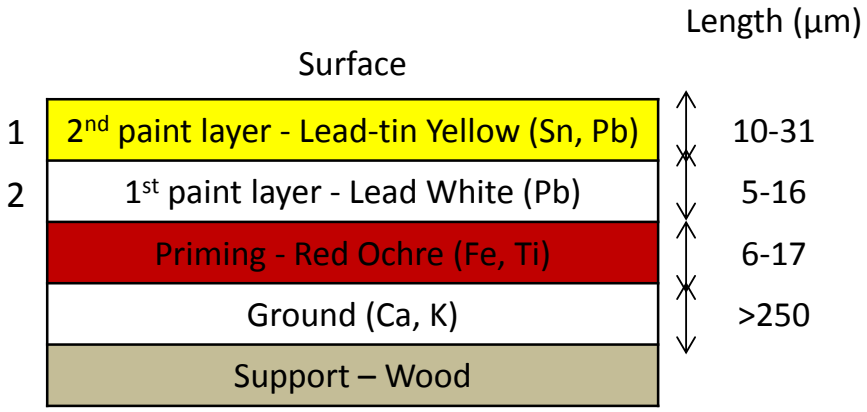

Fig. 164. Scheme of the experimental paint multilayer (Fig. 163).

Table 42. Results of in-depth scan presented Fig. 163.

Distance b/w layers	ΔXc (μm) Concha	ΔXc (μm) LouX^{3D}
1a-1b	5 ± 3	5 ± 3
1b-2	8 ± 3	16 ± 3

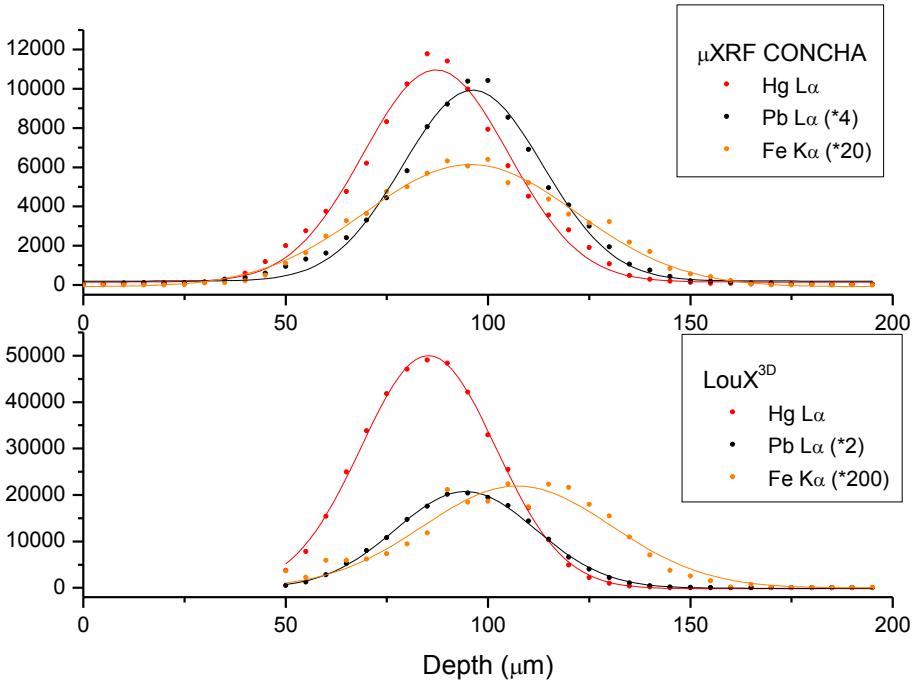

Fig. 165. Depth profile of an experimental paint multilayer.

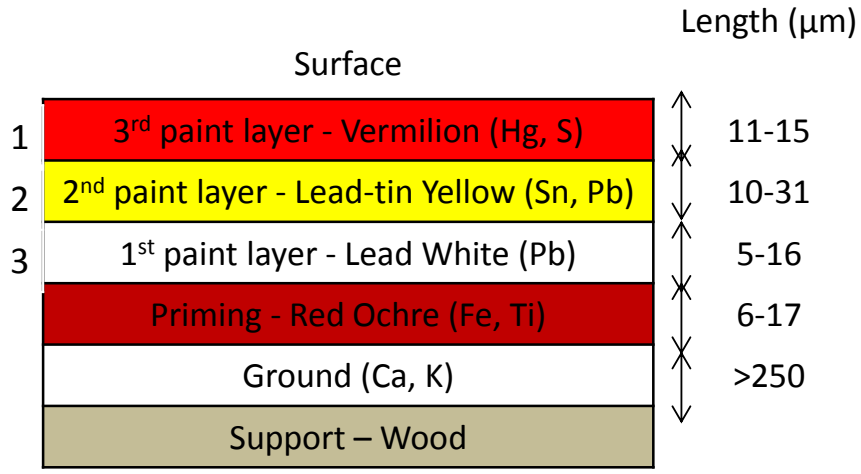

Fig. 166. Scheme of the experimental paint multilayer (Fig. 165).

Table 43. Results of in-depth scan presented Fig. 165.

Distance b/w layers	ΔXc (μm) Concha	ΔXc (μm) LouX^{3D}
1-2	7 ± 3	9 ± 3
2-3	3 ± 3	13 ± 3

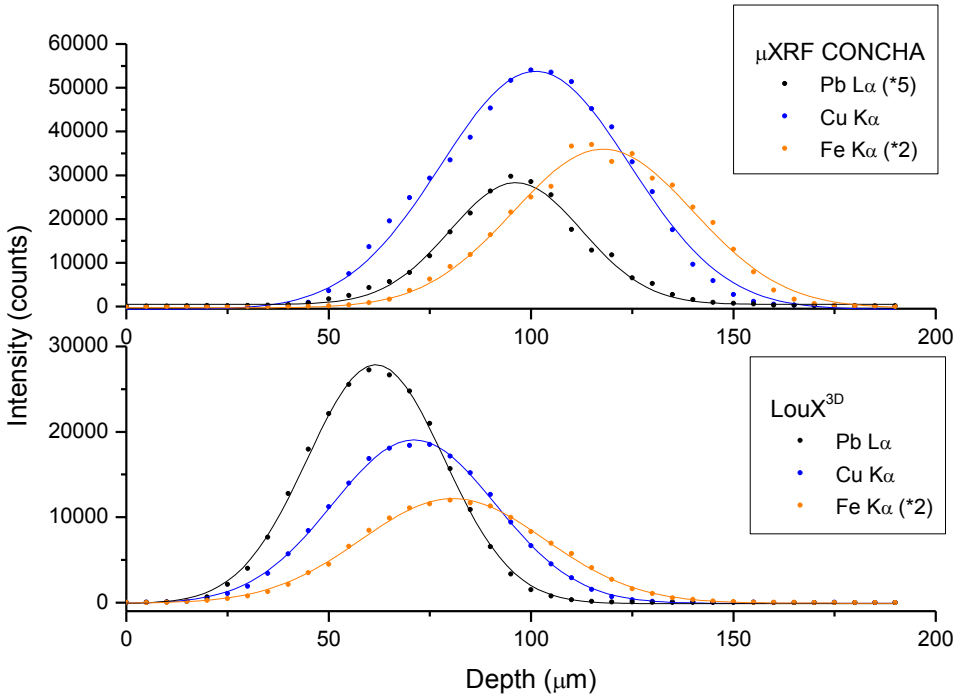

Fig. 167. Depth profile of an experimental paint multilayer.

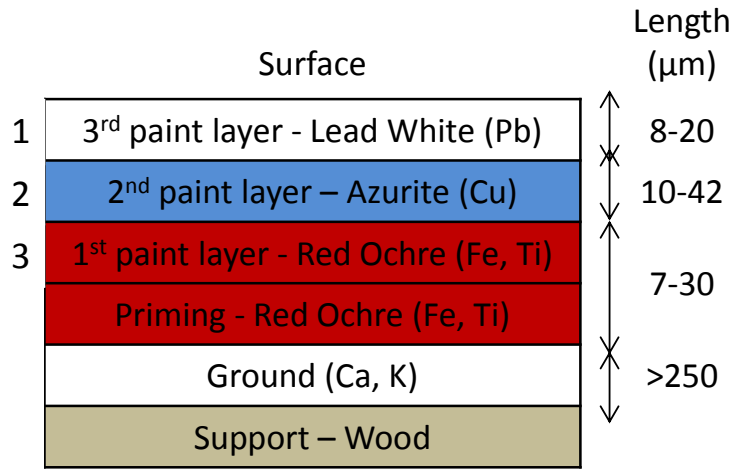

Fig. 168. Scheme of the experimental paint multilayer (Fig. 167).

Table 44. Results of in-depth scan presented Fig. 167.

Distance b/w layers	ΔXc (μm) Concha	ΔXc (μm) LouX^{3D}
1-2	5 ± 3	9 ± 3
2-3	17 ± 3	10 ± 3

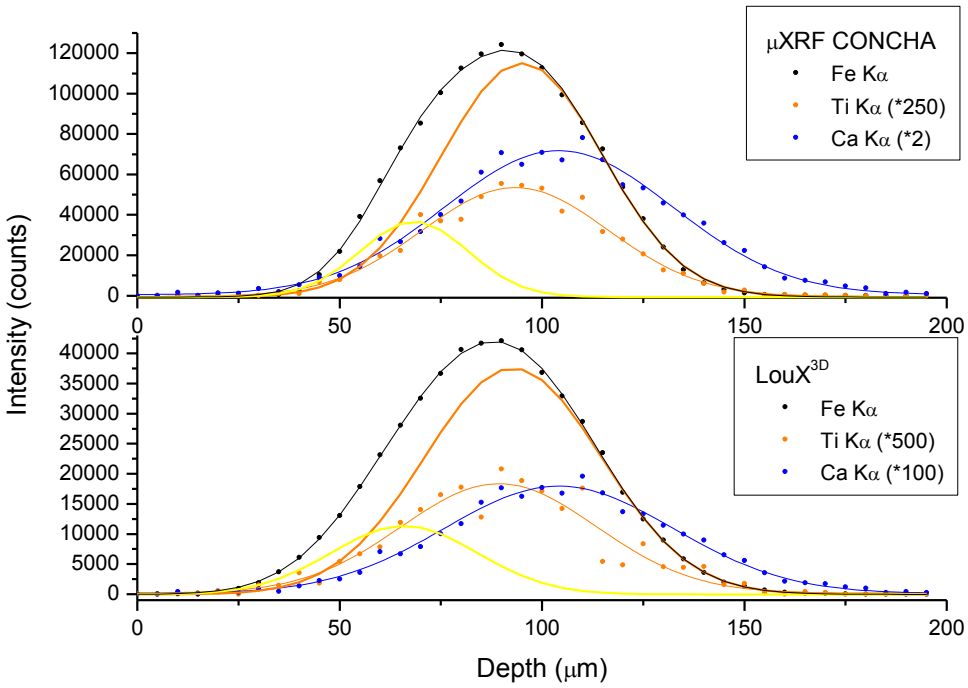

Fig. 169. Depth profile of an experimental paint multilayer.

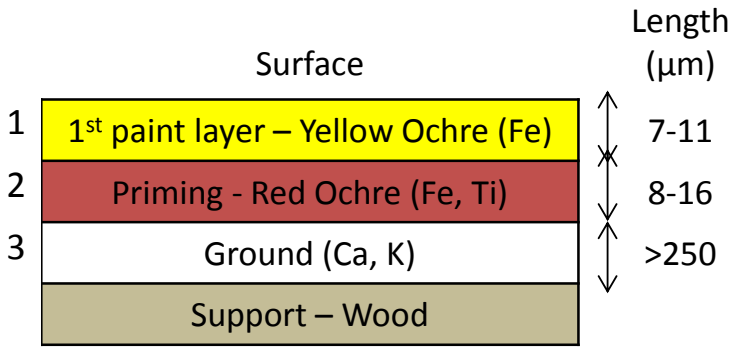

Fig. 170. Scheme of the experimental paint multilayer (Fig. 169).

Table 45. Results of in-depth scan presented Fig. 169.

Distance b/w layers	ΔXc (μm) Concha	ΔXc (μm) LouX^{3D}
1-2b	27 ± 3	27 ± 3
2a-2b	2 ± 3	4 ± 3
2-3	9 ± 3	11 ± 3

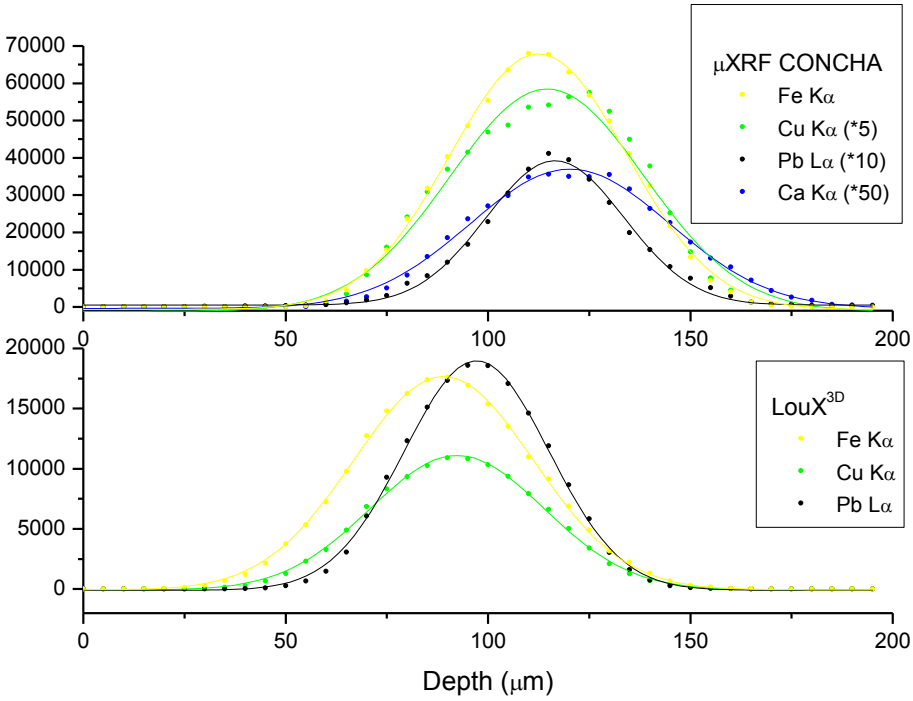

Fig. 171. Depth profile of an experimental paint multilayer.

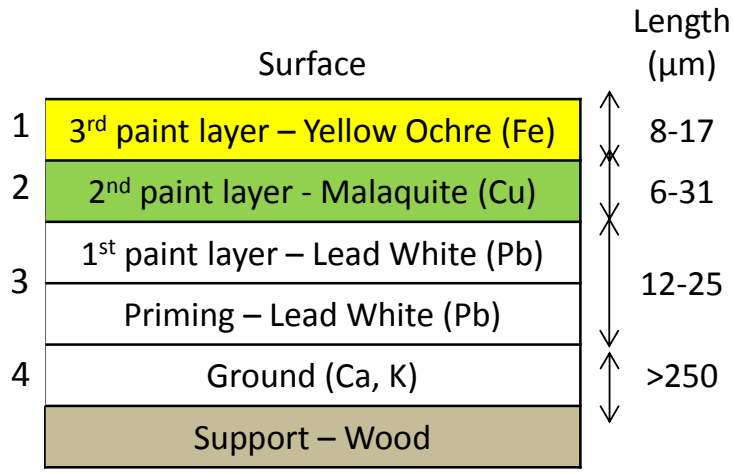

Fig. 172. Scheme of the experimental paint multilayer (Fig. 171).

Table 46. Results of in-depth scan presented Fig. 171.

Distance b/w layers	ΔXc (μm) Concha	ΔXc (μm) LouX^{3D}
1-2	3 ± 3	3 ± 3
2-3	2 ± 3	5 ± 3
3-4	3 ± 3	ND

X. Color scale classification of XRF peak area values by order of magnitude

The XRF peak area values are classified for each chemical element in order of magnitude and discriminated by a color scale. This scale is adapted for each setup and each artwork so as to provide comparable results. All the classification scales are available in Table 47 and Table 48.

Table 47. XRF classification scales.

"San Pedro Nolasco despidiéndose de Jaime I El Conquistador" - X-Panda - Seville - (123SDD detector)												
Ca-K	Ti-K	Cr-K	Mn-K	Fe-K	Co-K	Cu-K	Zn-K	As-K	Sn-K	Ba-L	Hg-L	Pb-L
0	0							0		0	0	
	$<10^2$	$<10^2$	$<10^2$	10^2-10^3	$<10^2$	10^2-10^3		10^2-10^3		$<10^2$	10^2-10^3	10^2-10^3
10^2-10^3	10^2-10^3	10^2-10^3	10^2-10^3	10^3-10^4	10^2-10^3	10^3-10^4	10^2-10^3	10^3-10^4	10^2-10^3	10^2-10^3	10^3-10^4	
10^3-10^4			10^3-10^4	10^4-10^5	10^3-10^4	10^4-10^5	10^3-10^4	10^4-10^5	10^3-10^4		10^4-10^5	10^4-10^5
				$>10^5$		$>10^5$	10^4-10^5					$>10^5$

"San Pedro Nolasco despidiéndose de Jaime I El Conquistador" - Museum XRF device - Seville												
Ca-K	Ti-K	Cr-K	Mn-K	Fe-K	Co-K	Cu-K	Zn-K	As-K	Sn-K	Ba-L	Hg-L	Pb-L
	0	0	0		0			0		0		
	$<10^2$	$<10^2$	$<10^2$	10^2-10^3	$<10^2$	10^2-10^3	$<10^2$			$<10^2$	10^2-10^3	
10^2-10^3	10^2-10^3	10^2-10^3	10^2-10^3	10^3-10^4	10^2-10^3	10^3-10^4	10^2-10^3	10^3-10^4	10^2-10^3	10^2-10^3	10^3-10^4	
10^3-10^4			10^3-10^4	10^4-10^5	10^3-10^4	10^4-10^5	10^3-10^4	10^4-10^5	10^3-10^4		10^4-10^5	10^4-10^5
						$>10^5$		$>10^5$				$>10^5$

"San Pedro Nolasco rendimiendo cautivos" - X-Panda - Seville - (Super 123SDD detector)												
Ca-K	Ti-K	Cr-K	Mn-K	Fe-K	Co-K	Cu-K	Zn-K	As-K	Sn-K	Ba-L	Hg-L	Pb-L
0	0		0		0			0				
$<10^2$	$<10^2$	$<10^2$	$<10^2$		$<10^2$	10^2-10^3	$<10^2$			$<10^2$	10^2-10^3	
10^2-10^3	10^2-10^3	10^2-10^3	10^2-10^3	10^3-10^4	10^2-10^3	10^3-10^4	10^2-10^3	10^3-10^4	10^2-10^3	10^2-10^3	10^3-10^4	
10^3-10^4	10^3-10^4	10^3-10^4	10^3-10^4	10^4-10^5	10^3-10^4	10^4-10^5	10^3-10^4	10^4-10^5	10^3-10^4		10^4-10^5	
$>10^5$				$>10^5$		$>10^5$	10^4-10^5				$>10^5$	10^5-10^6
												$>10^6$

"San Pedro Nolasco rendimiendo cautivos" - Museum XRF device - Seville												
Ca-K	Ti-K	Cr-K	Mn-K	Fe-K	Co-K	Cu-K	Zn-K	As-K	Sn-K	Ba-L	Hg-L	Pb-L
	0	0	0		0		0	0		0	0	
	$<10^2$	$<10^2$	$<10^2$		$<10^2$	10^2-10^3	$<10^2$	10^2-10^3		$<10^2$	10^2-10^3	
10^2-10^3	10^2-10^3	10^2-10^3	10^2-10^3	10^3-10^4	10^2-10^3	10^3-10^4	10^2-10^3	10^3-10^4	10^2-10^3	10^2-10^3	10^3-10^4	
10^3-10^4			10^3-10^4	10^4-10^5	10^3-10^4	10^4-10^5	10^3-10^4	10^4-10^5	10^3-10^4		10^4-10^5	10^4-10^5
						$>10^5$					$>10^5$	$>10^5$

"Virgen del Valle" - Museum XRF device - Seville												
Ca-K	Ti-K	Cr-K	Mn-K	Fe-K	Co-K	Cu-K	Zn-K	As-K	Sn-K	Ba-L	Hg-L	Pb-L
	0	0			0		0	0		0		
$<10^2$	$<10^2$	$<10^2$	$<10^2$	10^2-10^3	$<10^2$	10^2-10^3	$<10^2$	10^2-10^3		10^2-10^3	10^2-10^3	
10^2-10^3	10^2-10^3	10^2-10^3	10^2-10^3	10^3-10^4	10^2-10^3	10^3-10^4	10^2-10^3	10^3-10^4	10^2-10^3	10^3-10^4	10^3-10^4	
10^3-10^4			10^3-10^4	10^4-10^5	10^3-10^4	10^4-10^5	10^3-10^4	10^4-10^5	10^3-10^4		10^4-10^5	
						$>10^5$						$>10^5$

Table 48. XRF classification scales.

"Sagrada Cena" - Museum XRF device - Seville												
Ca-K	Ti-K	Cr-K	Mn-K	Fe-K	Co-K	Cu-K	Zn-K	As-K	Sn-K	Ba-L	Hg-L	Pb-L
	0				0		0	0				
	$<10^{2}$	$<10^{2}$	$<10^{2}$		$<10^{2}$	10^{2}-10^{3}	$<10^{2}$					
10^{2}-10^{3}	10^{2}-10^{3}	10^{2}-10^{3}	10^{2}-10^{3}	10^{3}-10^{4}	10^{2}-10^{3}	10^{3}-10^{4}	10^{2}-10^{3}	10^{3}-10^{4}	10^{2}-10^{3}	10^{2}-10^{3}	10^{3}-10^{4}	
10^{3}-10^{4}				10^{4}-10^{5}		10^{4}-10^{5}	10^{3}-10^{4}	10^{4}-10^{5}	10^{3}-10^{4}		10^{4}-10^{5}	
						$>10^{5}$					$>10^{5}$	$>10^{5}$

"Sagrada Cena" - X-Panda - Seville - (123SDD detector)												
Ca-K	Ti-K	Cr-K	Mn-K	Fe-K	Co-K	Cu-K	Zn-K	As-K	Sn-K	Ba-L	Hg-L	Pb-L
0	0	0			0			0		0	0	
$<10^{2}$	$<10^{2}$	$<10^{2}$	$<10^{2}$	10^{2}-10^{3}	$<10^{2}$	10^{2}-10^{3}				$<10^{2}$	10^{2}-10^{3}	10^{2}-10^{3}
10^{2}-10^{3}	10^{2}-10^{3}	10^{2}-10^{3}	10^{2}-10^{3}	10^{3}-10^{4}	10^{2}-10^{3}	10^{3}-10^{4}	10^{2}-10^{3}		10^{2}-10^{3}	10^{2}-10^{3}	10^{3}-10^{4}	
10^{3}-10^{4}	10^{3}-10^{4}	10^{3}-10^{4}	10^{3}-10^{4}	10^{4}-10^{5}		10^{4}-10^{5}	10^{3}-10^{4}		10^{3}-10^{4}		10^{4}-10^{5}	
						$>10^{5}$	10^{4}-10^{5}					$>10^{5}$

"Sagrada Cena" - X-Panda - Seville - (Super 123SDD detector)												
Ca-K	Ti-K	Cr-K	Mn-K	Fe-K	Co-K	Cu-K	Zn-K	As-K	Sn-K	Ba-L	Hg-L	Pb-L
0	0		0	0	0			0			0	
$<10^{2}$	$<10^{2}$	$<10^{2}$	$<10^{2}$	$<10^{3}$	$<10^{2}$	10^{2}-10^{3}				$<10^{2}$	10^{2}-10^{3}	
10^{2}-10^{3}	10^{2}-10^{3}	10^{2}-10^{3}	10^{2}-10^{3}	10^{3}-10^{4}	10^{2}-10^{3}	10^{3}-10^{4}	10^{2}-10^{3}		10^{2}-10^{3}	10^{2}-10^{3}	10^{3}-10^{4}	
10^{3}-10^{4}	10^{3}-10^{4}	10^{3}-10^{4}	10^{3}-10^{4}	10^{4}-10^{5}	10^{3}-10^{4}	10^{4}-10^{5}	10^{3}-10^{4}	10^{4}-10^{5}	10^{3}-10^{4}	10^{3}-10^{4}	10^{4}-10^{5}	
$>10^{5}$		$>10^{5}$		$>10^{5}$		10^{5}-10^{6}	10^{4}-10^{5}				10^{5}-10^{6}	10^{5}-10^{6}
						$>10^{6}$	$>10^{5}$				$>10^{6}$	$>10^{6}$

"Inmaculada" - Museum XRF device - Seville												
Ca-K	Ti-K	Cr-K	Mn-K	Fe-K	Co-K	Cu-K	Zn-K	As-K	Sn-K	Ba-L	Hg-L	Pb-L
	0	0			0		0	0		0		
	$<10^{2}$	$<10^{2}$	$<10^{2}$	10^{2}-10^{3}	$<10^{2}$	10^{2}-10^{3}	$<10^{2}$	10^{2}-10^{3}		$<10^{2}$	10^{2}-10^{3}	
10^{2}-10^{3}	10^{2}-10^{3}	10^{2}-10^{3}	10^{2}-10^{3}	10^{3}-10^{4}	10^{2}-10^{3}	10^{3}-10^{4}	10^{2}-10^{3}	10^{3}-10^{4}	10^{2}-10^{3}	10^{2}-10^{3}	10^{3}-10^{4}	
10^{3}-10^{4}	10^{3}-10^{4}		10^{3}-10^{4}	10^{4}-10^{5}	10^{3}-10^{4}	10^{4}-10^{5}	10^{3}-10^{4}	10^{4}-10^{5}	10^{3}-10^{4}	10^{3}-10^{4}	10^{4}-10^{5}	10^{4}-10^{5}
						$>10^{5}$						$>10^{5}$

"Inmaculada" - X-Panda - Seville - (Super 123SDD detector)												
Ca-K	Ti-K	Cr-K	Mn-K	Fe-K	Co-K	Cu-K	Zn-K	As-K	Sn-K	Ba-L	Hg-L	Pb-L
			0					0		0		
	$<10^{2}$	$<10^{2}$	$<10^{2}$		$<10^{2}$					$<10^{2}$	10^{2}-10^{3}	
10^{2}-10^{3}	10^{2}-10^{3}	10^{2}-10^{3}	10^{2}-10^{3}	10^{3}-10^{4}	10^{2}-10^{3}	10^{3}-10^{4}	10^{2}-10^{3}	10^{3}-10^{4}	10^{2}-10^{3}	10^{2}-10^{3}	10^{3}-10^{4}	
10^{3}-10^{4}	10^{3}-10^{4}		10^{3}-10^{4}	10^{4}-10^{5}	10^{3}-10^{4}	10^{4}-10^{5}	10^{3}-10^{4}	10^{4}-10^{5}	10^{3}-10^{4}	10^{3}-10^{4}	10^{4}-10^{5}	10^{4}-10^{5}
$>10^{5}$						$>10^{5}$	10^{4}-10^{5}	$>10^{5}$			$>10^{5}$	10^{5}-10^{6}
												$>10^{6}$

"Martirio de San Hipólito" - SANDRA - Mexico												
Ca-K	Ti-K	Cr-K	Mn-K	Fe-K	Co-K	Cu-K	Zn-K	As-K	Sn-K	Ba-L	Hg-L	Pb-L
	0	0			0			0				
	$<10^{2}$	$<10^{2}$	$<10^{2}$		$<10^{2}$	10^{2}-10^{3}	$<10^{2}$	10^{2}-10^{3}	$<10^{2}$	$<10^{2}$	10^{2}-10^{3}	10^{2}-10^{3}
10^{2}-10^{3}	10^{2}-10^{3}	10^{2}-10^{3}	10^{2}-10^{3}	10^{3}-10^{4}	10^{2}-10^{3}	10^{3}-10^{4}	10^{2}-10^{3}	10^{3}-10^{4}	10^{2}-10^{3}	10^{2}-10^{3}	10^{3}-10^{4}	10^{3}-10^{4}
10^{3}-10^{4}	10^{3}-10^{4}		10^{3}-10^{4}	10^{4}-10^{5}	10^{3}-10^{4}	10^{4}-10^{5}	10^{3}-10^{4}	10^{4}-10^{5}		10^{3}-10^{4}	10^{4}-10^{5}	10^{4}-10^{5}
												$>10^{5}$

"Virgen de las Uvas" - SANDRA - Mexico												
Ca-K	Ti-K	Cr-K	Mn-K	Fe-K	Co-K	Cu-K	Zn-K	As-K	Sn-K	Ba-L	Hg-L	Pb-L
	0	0			0		0	0				
	$<10^{2}$	$<10^{2}$	$<10^{2}$	10^{2}-10^{3}	$<10^{2}$	10^{2}-10^{3}	$<10^{2}$		$<10^{2}$	$<10^{2}$	10^{2}-10^{3}	
10^{2}-10^{3}	10^{2}-10^{3}	10^{2}-10^{3}	10^{2}-10^{3}	10^{3}-10^{4}	10^{2}-10^{3}	10^{3}-10^{4}	10^{2}-10^{3}		10^{2}-10^{3}	10^{2}-10^{3}	10^{3}-10^{4}	
10^{3}-10^{4}	10^{3}-10^{4}		10^{3}-10^{4}	10^{4}-10^{5}			10^{3}-10^{4}				10^{4}-10^{5}	10^{5}-2*10^{5}
$>10^{4}$												>2*10^{5}

XI. Brief report of each artwork analyzed

This appendix shows for each artwork studied the UV image, the IRR images, the XRF points and a selection of one example of each category detected during the XRF study. The error applied to the XRF data is the standard deviation. Following the IUPAC recommendation to XRF [165], the standard deviation s_N for counting of photons emitted at completely random intervals of time t obeys for an average number of accumulated counts N to the equation:

$$s_N = \sqrt{N} \quad (15)$$

Table 49 summarizes the number of IRR reflectograms and of XRF spectra for each artwork.

Table 49. Number of IRR images and XRF spectra per each artwork.

Artwork title	Number of IRR images	Number of XRF spectra
Sagrada Cena	525	353
Virgen del Valle	296	62
San Pedro Nolasco despidiéndose de Jaime I El Conquistador	238	99
San Pedro Nolasco redimiendo cautivos	210	101
La Inmaculada	196	87
Martirio de San Hipólito	82	89
Virgen de las Uvas	35	58

i. “San Pedro Nolasco despidiéndose de Jaime I el Conquistador”

Fig. 173. UV image of "San Pedro Nolasco despidiéndose de Jaime I".

Fig. 174. IRR image of "San Pedro Nolasco despidiéndose de Jaime I".

Fig. 175. XRF points of "San Pedro Nolasco despidiéndose de Jaime I".

Table 50. Net peak areas (in counts) of the elements detected by XRF in different pigments found in selected points of "San Pedro Nolasco despidiéndose de Jaime I".

Pigments	Characteristic elements	Point	Ca-K	Mn-K	Fe-K	Cu-K	Sn-K	Hg-L	Pb-L
Lead white	Pb	16	714 ± 27	122 ± 11	883 ± 30	357 ± 19	807 ± 28	3626 ± 60	702900 ± 840
Lead white with vermilion	Pb, Hg	20	1391 ± 37	68 ± 8	5560 ± 75	3975 ± 63	978 ± 31	75630 ± 280	376310 ± 610
Lead-tin yellow	Pb, Sn	17	1108 ± 33	ND	9476 ± 97	518 ± 23	2892 ± 54	13790 ± 120	605720 ± 780
Mixture of vermilion with ochre	Hg, Fe	34	1834 ± 43	764 ± 28	29160 ± 170	5850 ± 76	306 ± 17	60140 ± 250	275640 ± 530
Red ochre	Fe	33	2749 ± 52	760 ± 28	70050 ± 270	2446 ± 49	423 ± 21	201 ± 14	75850 ± 280
Azurite	Cu	50	570 ± 24	71 ± 8	6657 ± 82	194770 ± 440	374 ± 19	1737 ± 42	339410 ± 580
Azurite underlay with black iron oxide	Cu, Fe	10	2017 ± 45	23 ± 5	29380 ± 170	238340 ± 490	305 ± 17	2512 ± 50	103390 ± 320
Bright green Cu-based pigment	Cu	82	1009 ± 32	99 ± 10	4168 ± 65	458170 ± 680	291 ± 17	1080 ± 33	344870 ± 590
Yellow ochre	Fe	64	1622 ± 40	899 ± 30	47980 ± 220	3531 ± 59	496 ± 22	1227 ± 35	348050 ± 590
Ochre mixed with vermilion	Fe, Hg	48	3695 ± 61	519 ± 23	66560 ± 260	3538 ± 59	521 ± 23	70190 ± 270	64550 ± 250
Black iron oxide	Fe	9	1917 ± 44	ND	13020 ± 110	1049 ± 32	457 ± 21	1116 ± 33	330850 ± 580
Umber	Fe, Mn	36	2320 ± 48	1434 ± 38	56000 ± 240	7108 ± 84	425 ± 21	1886 ± 43	111990 ± 340
Mixture of umber with Cu-based pigment	Fe, Mn, Cu	1	2588 ± 51	2358 ± 49	51030 ± 230	26220 ± 160	276 ± 17	3284 ± 57	149120 ± 390

ii. “San Pedro Nolasco redimiendo cautivos”

Fig. 176. UV image of "San Pedro Nolasco redimiendo cautivos".

Fig. 177. IRR image of "San Pedro Nolasco redimiendo cautivos".

Fig. 178. XRF points of "San Pedro Nolasco redimiendo cautivos".

Table 51. Net peak areas (in counts) of the elements detected by XRF in different pigments found in selected points of "San Pedro Nolasco redimiendo cautivos".

Pigments	Characteristic elements	Point	Ca-K	Mn-K	Fe-K	Cu-K	Sn-K	Hg-L	Pb-L
Lead white	Pb	46	723 ± 27	66 ± 8	2307 ± 48	549 ± 23	986 ± 31	1806 ± 42	569650 ± 760
Lead white with vermilion	Pb, Hg	17	864 ± 29	75 ± 9	1807 ± 43	2130 ± 46	417 ± 20	12070 ± 110	663250 ± 810
Lead-tin yellow	Pb, Sn	5	1106 ± 33	24 ± 5	1370 ± 37	925 ± 30	2346 ± 48	3571 ± 60	598440 ± 770
Vermilion	Hg	41	756 ± 27	95 ± 10	6089 ± 78	428 ± 21	277 ± 17	135930 ± 370	305730 ± 550
Mixture of vermilion with ochre	Hg, Fe	89	4678 ± 68	650 ± 25	67610 ± 260	5181 ± 72	394 ± 20	582560 ± 760	253480 ± 500
Purple lake	Pb	23	677 ± 26	194 ± 14	8022 ± 90	516 ± 23	212 ± 15	1553 ± 39	435830 ± 660
Azurite	Cu	31	885 ± 30	23 ± 5	5004 ± 71	57350 ± 240	391 ± 20	2009 ± 45	492780 ± 700
Azurite underlay with black iron oxide	Cu, Fe	59	2629 ± 51	571 ± 24	47850 ± 220	78710 ± 280	914 ± 30	1599 ± 40	1100300 ± 1000
Bright green Cu-based pigment	Cu	6	1360 ± 37	150 ± 12	3308 ± 58	76620 ± 280	1774 ± 42	3652 ± 60	505090 ± 710
Yellow ochre	Fe	7	7327 ± 86	594 ± 24	19610 ± 140	872 ± 30	332 ± 18	273 ± 17	30170 ± 170
Black iron oxide	Fe	13	3438 ± 59	832 ± 29	26090 ± 160	5348 ± 73	224 ± 15	1257 ± 35	173410 ± 420
Mixture of ochre with Cu-based pigment	Fe, Cu	29	1664 ± 41	352 ± 19	26250 ± 160	25350 ± 160	351 ± 19	3649 ± 60	218010 ± 470
Umber	Fe, Mn	22	1542 ± 39	1663 ± 41	31080 ± 180	793 ± 28	292 ± 17	1843 ± 43	124300 ± 350
Mixture of umber with Cu-based pigment	Fe, Mn, Cu	10	1386 ± 37	1319 ± 36	24650 ± 160	46630 ± 220	166 ± 13	5536 ± 74	185820 ± 430
Brown obtained with Cu-based pigment	Cu	64	51 ± 7	84 ± 9	4157 ± 64	34410 ± 190	2023 ± 45	4321 ± 66	1956800 ± 1400

iii. “Sagrada Cena”

Fig. 179. UV image of "Sagrada Cena".

Fig. 180. IRR image of "Sagrada Cena".

Fig. 181. IRR image of "Sagrada Cena".

Fig. 182. IRR image of "Sagrada Cena".

Fig. 183. IRR image of "Sagrada Cena".

Fig. 184. XRF points of "Sagrada Cena".

Table 52. Net peak areas (in counts) of the elements detected by XRF in different pigments found in selected points of "Sagrada Cena".

Pigments	Characteristic elements	Point	Ca-K	Mn-K	Fe-K	Cu-K	Sn-K	Hg-L	Pb-L
Lead white	Pb	44	436 ± 21	85 ± 9	804 ± 28	353 ± 19	378 ± 19	1676 ± 41	976040 ± 990
Lead white with vermilion	Pb, Hg	26	107 ± 10	122 ± 11	2173 ± 47	2690 ± 52	330 ± 18	13030 ± 110	861990 ± 930
Lead white with lake	Pb	25	2530 ± 50	126 ± 11	6211 ± 79	1348 ± 37	334 ± 18	9970 ± 100	695970 ± 830
Massicot	Pb	9	933 ± 31	53 ± 7	729 ± 27	784 ± 28	662 ± 26	1931 ± 44	958650 ± 980
Vermilion	Hg	178	3014 ± 55	119 ± 11	6452 ± 80	2740 ± 52	784 ± 28	916490 ± 960	836130 ± 910
Mixture of vermilion with ochre	Hg, Fe	131	3060 ± 55	ND	123960 ± 350	3398 ± 58	1245 ± 35	112040 ± 340	1400000 ± 1200
Red ochre	Fe	227	4686 ± 68	96 ± 10	30820 ± 180	3778 ± 61	2410 ± 49	4966 ± 70	1593900 ± 1300
Purple lake	Pb	42	360 ± 19	92 ± 10	2106 ± 46	615 ± 25	409 ± 20	2085 ± 46	902390 ± 950
Azurite	Cu	55	1131 ± 34	325 ± 18	8156 ± 90	250190 ± 500	348 ± 19	2497 ± 50	482930 ± 700
Azurite underlay with black iron oxide	Cu, Fe	318	2756 ± 52	293 ± 17	11990 ± 109	951230 ± 980	888 ± 30	1327 ± 36	823080 ± 910
Bright green Cu-based pigment	Cu	45	1246 ± 35	72 ± 8	1197 ± 35	42630 ± 210	291 ± 17	1528 ± 39	922000 ± 960
Mixture of Cu-based pigment with ochre	Cu, Fe	337	7074 ± 84	688 ± 26	10850 ± 100	423130 ± 650	1138 ± 34	2121 ± 46	1178700 ± 1100
Yellow ochre	Fe	1	3122 ± 56	445 ± 21	28980 ± 170	8380 ± 92	419 ± 20	9466 ± 97	571250 ± 760
Ochre mixed with vermilion	Fe, Hg	17	1752 ± 42	670 ± 26	55640 ± 240	1655 ± 41	347 ± 19	23370 ± 150	679550 ± 820
Black iron oxide	Fe	61	534 ± 23	678 ± 26	14270 ± 120	3065 ± 55	509 ± 23	5025 ± 71	746940 ± 860
Mixture of ochre with Cu-based pigment	Fe, Cu	72	8298 ± 91	579 ± 24	11160 ± 100	518690 ± 720	886 ± 30	1880 ± 43	903170 ± 950
Umber	Fe, Mn	4	1035 ± 32	1992 ± 45	50910 ± 230	1641 ± 41	431 ± 21	7538 ± 87	625280 ± 790
Mixture of umber with Cu-based pigment	Fe, Mn, Cu	76	3301 ± 57	1601 ± 40	38960 ± 200	23640 ± 150	1252 ± 35	8664 ± 93	1448700 ± 1200
Brown obtained with Cu-based pigment	Cu	10	3053 ± 55	127 ± 11	5850 ± 76	26590 ± 160	311 ± 18	2876 ± 54	749590 ± 870
Organic black pigment	Pb	40	842 ± 29	96 ± 10	3915 ± 63	1242 ± 35	300 ± 17	4057 ± 64	872820 ± 930

iv. “Inmaculada”

Fig. 185. UV image (a) and XRF points (b) of "Inmaculada".

Fig. 186. IRR images of "Inmaculada".

Table 53. Net peak areas (in counts) of the elements detected by XRF in different pigments found in selected points of "Inmaculada".

Pigments	Characteristic elements	Point	Ca-K	Mn-K	Fe-K	Cu-K	Sn-K	Hg-L	Pb-L
Lead white	Pb	11	3013 ± 55	9 ± 3	7270 ± 85	3424 ± 59	381 ± 20	273 ± 17	149150 ± 390
Lead white with vermilion	Pb, Hg	60	644 ± 25	80 ± 9	1259 ± 35	418 ± 20	417 ± 20	22120 ± 150	672280 ± 820
Lead-tin yellow	Pb, Sn	52	231 ± 15	29 ± 5	608 ± 25	2007 ± 45	1344 ± 37	3255 ± 57	692590 ± 830
Vermilion	Hg	55	836 ± 29	93 ± 10	2537 ± 50	351 ± 19	392 ± 20	66720 ± 260	533280 ± 730
Mixture of vermilion with ochre	Hg, Fe	15	4913 ± 70	124 ± 11	25420 ± 160	1851 ± 43	285 ± 17	18630 ± 140	41730 ± 200
Purple lake	Pb	25	2155 ± 46	113 ± 11	9334 ± 97	697 ± 26	346 ± 19	1621 ± 40	393260 ± 630
Azurite	Cu	14	1349 ± 37	ND	6336 ± 80	138320 ± 370	373 ± 19	1405 ± 37	295270 ± 540
Azurite underlay with black iron oxide	Cu, Fe	85	3803 ± 62	600 ± 24	14950 ± 120	1501400 ± 1200	641 ± 25	361 ± 19	137600 ± 370
Azurite underlay with umber	Cu, Fe, Mn	84	9273 ± 96	1222 ± 35	38000 ± 200	409840 ± 640	651 ± 26	1320 ± 36	230110 ± 480
Bright green Cu-based pigment	Cu	45	1034 ± 32	15 ± 4	8406 ± 92	44090 ± 210	421 ± 21	490 ± 22	284520 ± 530
Yellow ochre	Fe	59	3678 ± 61	497 ± 22	32670 ± 180	5026 ± 71	453 ± 21	1600 ± 40	67340 ± 259
Ochre mixed with vermilion	Fe, Hg	31	2442 ± 49	669 ± 26	16940 ± 130	5327 ± 73	453 ± 21	13200 ± 120	316360 ± 560
Black iron oxide	Fe	44	2921 ± 54	211 ± 15	11600 ± 110	3758 ± 61	538 ± 23	1938 ± 44	395770 ± 630
Mixture of ochre with Cu-based pigment	Fe, Cu	1	3121 ± 56	457 ± 21	11400 ± 110	67783 ± 260	896 ± 30	2583 ± 51	194770 ± 440
Umber	Fe, Mn	32	2236 ± 47	1479 ± 38	25980 ± 160	3094 ± 56	330 ± 18	1868 ± 43	206910 ± 460

v. “Virgen del Valle”

Fig. 187. UV (a) and IRR (b) images of "Virgen del Valle".

Fig. 188. XRF points of "Virgen del Valle".

Table 54. Net peak areas (in counts) of the elements detected by XRF in different pigments found in selected points of "Virgen del Valle".

Pigments	Characteristic elements	Point	Ca-K	Mn-K	Fe-K	Cu-K	Sn-K	Hg-L	Pb-L
Lead white	Pb	38	63 ± 8	41 ± 6	233 ± 15	2113 ± 46	466 ± 22	4572 ± 68	733700 ± 860
Lead white with vermilion	Pb, Hg	26	469 ± 22	115 ± 11	469 ± 22	1759 ± 42	562 ± 24	28720 ± 170	664600 ± 820
Lead white with lake	Pb	24	376 ± 19	74 ± 9	353 ± 19	3404 ± 58	510 ± 23	9400 ± 97	750370 ± 870
Lead-tin yellow	Pb, Sn	46	1059 ± 33	77 ± 9	406 ± 20	2411 ± 49	3342 ± 58	3530 ± 59	715590 ± 850
Vermilion	Hg	20	572 ± 24	67 ± 8	938 ± 31	2524 ± 50	495 ± 22	40950 ± 200	610160 ± 780
Purple lake	Pb	3	912 ± 30	181 ± 13	2515 ± 50	4417 ± 66	391 ± 20	3162 ± 56	489750 ± 700
Azurite	Cu	48	463 ± 22	174 ± 13	1890 ± 43	64670 ± 250	567 ± 24	2611 ± 51	533530 ± 730
Bright green Cu-based pigment	Cu	4	1104 ± 33	212 ± 15	3037 ± 55	54810 ± 230	666 ± 26	2379 ± 49	413690 ± 640
Mixture of Cu-based pigment with ochre	Cu, Fe	29	2791 ± 53	674 ± 26	18990 ± 140	175420 ± 420	521 ± 23	5380 ± 73	277070 ± 530
Yellow ochre	Fe	44	2941 ± 54	801 ± 28	21480 ± 150	7726 ± 88	1006 ± 32	3105 ± 56	418330 ± 650
Black iron oxide	Fe	45	1301 ± 36	494 ± 22	10910 ± 100	9670 ± 98	613 ± 25	1946 ± 44	490020 ± 700
Mixture of ochre with Cu-based pigment	Fe, Cu	8	1632 ± 40	739 ± 27	15930 ± 130	20480 ± 140	497 ± 22	4165 ± 65	413350 ± 640
Mixture of umber with Cu-based pigment	Fe, Mn, Cu	23	1256 ± 35	1052 ± 32	16550 ± 130	42700 ± 210	455 ± 21	6353 ± 80	578250 ± 760
Brown obtained with Cu-based pigment	Cu	33	576 ± 24	294 ± 17	4198 ± 65	63320 ± 250	461 ± 21	8269 ± 91	528890 ± 730
Organic black pigment	Pb	31	777 ± 28	250 ± 16	5227 ± 72	7015 ± 84	938 ± 31	9980 ± 100	585720 ± 770

vi. “Martirio de San Hipólito”

Fig. 189. UV (a) and IRR (b) images of “Martirio de San Hipólito”.

Fig. 190. XRF points of “Martirio de San Hipólito”.

Table 55. Net peak areas (in counts) of the elements detected by XRF in different pigments found in selected points of "Martirio de San Hipólito".

Pigments	Characteristic elements	Point	Ca-K	Mn-K	Fe-K	Cu-K	Sn-K	Hg-L	Pb-L
Lead white	Pb	4	445 ± 21	155 ± 12	2618 ± 51	1339 ± 37	194 ± 14	735 ± 27	91180 ± 300
Lead white with lake	Pb	44	537 ± 23	228 ± 15	6984 ± 84	1031 ± 32	194 ± 14	330 ± 18	85090 ± 290
Massicot	Pb	21	486 ± 22	326 ± 18	9069 ± 95	1260 ± 35	173 ± 13	1287 ± 36	84970 ± 290
Vermilion	Hg	57	566 ± 24	250 ± 16	4329 ± 66	1443 ± 38	113 ± 11	26220 ± 160	62740 ± 250
Mixture of vermilion with ochre	Hg, Fe	22	1031 ± 32	449 ± 21	16310 ± 130	1889 ± 43	72 ± 8	40630 ± 200	36050 ± 190
Red ochre	Fe	35	2759 ± 53	601 ± 25	23610 ± 150	7653 ± 87	87 ± 9	1836 ± 43	38070 ± 200
Purple lake	Pb	65	1106 ± 33	326 ± 18	8084 ± 90	2384 ± 49	168 ± 13	3456 ± 59	82070 ± 290
Azurite	Cu	39	674 ± 26	211 ± 15	7529 ± 87	53690 ± 230	132 ± 12	675 ± 26	58920 ± 240
Azurite underlay with black iron oxide	Cu, Fe	37	1256 ± 35	417 ± 20	21460 ± 150	59630 ± 240	82 ± 9	859 ± 29	31190 ± 180
Bright green Cu-based pigment	Cu	2	741 ± 27	571 ± 24	9034 ± 95	19750 ± 140	96 ± 10	603 ± 25	64290 ± 250
Mixture of Cu-based pigment with ochre	Cu, Fe	5	1620 ± 40	711 ± 27	24160 ± 160	52780 ± 230	61 ± 8	559 ± 24	33220 ± 180
Yellow ochre	Fe	29	740 ± 27	528 ± 23	20450 ± 140	4191 ± 65	101 ± 10	1243 ± 35	61600 ± 250
Mixture of ochre with Cu-based pigment	Fe, Cu	62	922 ± 30	748 ± 27	21370 ± 150	17350 ± 130	83 ± 9	1012 ± 32	54370 ± 230
Umber	Fe, Mn	9	977 ± 31	2681 ± 52	34900 ± 190	3446 ± 59	89 ± 9	638 ± 25	46370 ± 220
Mixture of umber with Cu-based pigment	Fe, Mn, Cu	81	2456 ± 50	1101 ± 33	25450 ± 160	10450 ± 100	109 ± 10	2349 ± 48	40750 ± 200
Organic black pigment	Pb	70	529 ± 23	641 ± 25	8098 ± 90	2453 ± 50	168 ± 13	838 ± 29	80830 ± 280

vii. “Virgen de las Uvas”

Fig. 191. UV (a) and IRR (b) images of "Virgen de las Uvas".

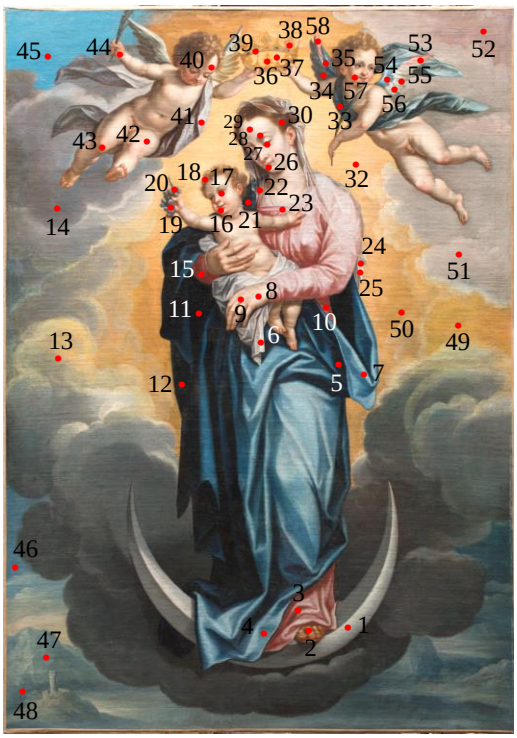

Fig. 192. XRF points of "Virgen de las Uvas".

Table 56. Net peak areas (in counts) of the elements detected by XRF in different pigments found in selected points of "Virgen de las Uvas".

Pigments	Characteristic elements	Point	Ca-K	Mn-K	Fe-K	Cu-K	Sn-K	Hg-L	Pb-L
Lead white	Pb	24	535 ± 23	102 ± 10	2831 ± 53	208 ± 14	218 ± 15	616 ± 25	220440 ± 470
Lead white with vermilion	Pb, Hg	57	474 ± 22	102 ± 10	4134 ± 64	137 ± 12	190 ± 14	29080 ± 170	194800 ± 440
Lead white with lake	Pb	8	313 ± 18	77 ± 9	771 ± 28	258 ± 16	291 ± 17	2088 ± 46	239680 ± 490
Massicot	Pb	50	757 ± 28	220 ± 15	8068 ± 90	123 ± 11	261 ± 16	2271 ± 48	211510 ± 460
Vermilion	Hg	16	895 ± 30	508 ± 23	9068 ± 95	1081 ± 33	102 ± 10	50760 ± 230	155380 ± 390
Purple lake	Pb	3	1900 ± 44	155 ± 12	4570 ± 68	364 ± 19	190 ± 14	1613 ± 40	187120 ± 430
Yellow ochre	Fe	36	1992 ± 45	622 ± 25	28990 ± 170	175 ± 13	153 ± 12	3316 ± 58	160440 ± 400
Black iron oxide	Fe	11	1560 ± 40	462 ± 22	20560 ± 140	258 ± 16	204 ± 14	809 ± 28	165790 ± 410
Umber	Fe, Mn	17	4815 ± 69	1457 ± 38	15520 ± 130	323 ± 18	202 ± 14	4804 ± 69	181380 ± 430
Organic black pigment	Pb	14	491 ± 22	206 ± 14	4289 ± 65	247 ± 16	232 ± 15	851 ± 29	224370 ± 470
Organic blue pigment	Pb	46	434 ± 21	62 ± 8	1052 ± 32	269 ± 16	291 ± 17	702 ± 26	233790 ± 480
Organic green pigment	Fe	39	13210 ± 120	399 ± 20	12930 ± 110	174 ± 13	227 ± 15	1451 ± 38	150680 ± 390

INTERNATIONAL CONGRESSES AND AWARD

The results obtained during this PhD thesis were presented in several international congresses:

27-31 October 2014 **México DF (Mexico)**
Invited Oral Title: "First non-destructive *in situ* easel painting analysis by confocal micro X-ray fluorescence (CXRF) with µXRF-CONCHA system". Conference: 4th Latin-American Congress of Archaeometry. Authors: K. Laclavetine, F.J. Ager, M. del Valme Muñoz, M. Vega and M.A. Respaldiza.

Poster Title (in Spanish): "Multispectral and spectroscopic techniques applied to non-destructive *in situ* study of a set of artworks attributed to Alonso Vázquez". Authors: K. Laclavetine, E. Arroyo, E. Hernández, A. Kriznar, M.V. Muñoz, M. Vega, J.L. Ruvalcaba Sil and M.A. Respaldiza.

20-22 October 2014 **Seville (Spain)**
Oral Title (in Spanish): "Characterization of the new confocal micro X-ray fluorescence (CXRF) system for non-destructive cultural heritage analysis at the CNA: µXRF-CONCHA". Conference: VI CPAN Days. Authors: K. Laclavetine, F.J. Ager, J. Arquillo, T. Calligaro, M. Eveno, K. Müller, I. Reiche, M.A. Respaldiza and M. Menu.

15-20 June 2014 **Bologna (Italy)**
Poster Title: "Intercomparison of three confocal micro X-ray fluorescence (CXRF) systems for the non-destructive characterization of experimental paint layers". Conference: European Conference on X-Ray Spectrometry. Authors: K. Laclavetine, P. Wrobel, F.J. Ager, J. Arquillo, T. Calligaro, M. Eveno, M. Lankosz, K. Müller, I. Reiche, M.A. Respaldiza and M. Menu.

11-13 June 2014 **Madrid (Spain)**
Oral Title: "Infrared reflectography (IRR) for large formats: comparison of various capture and mosaic assembly methodologies for large format easel paintings". Conference: 11th International Conference on non-destructive investigations and microanalysis for the diagnostics and conservation of cultural and environmental heritage. Authors: E. Hernández, K. Laclavetine, R. Alvarado, A. Kriznar, M. del Valme Muñoz, M. Vega, E. Arroyo, J.L. Ruvalcaba Sil and M.A. Respaldiza.

16-18 October 2013 **Bogotá (Colombia)**
Oral Title (in Spanish): "Analysis of experimental paint samples made following XVI century recipes by infrared reflectography (IRR)". "Conference: 4th Latin-American symposium on physics and chemistry applied to archaeology, art and cultural heritage conservation (LASMAC). Authors: K. Laclavetine, E. Hernandez, J. Arquillo, E. Arroyo and M.A. Respaldiza.

2-6 September 2013 **Hamburg (Germany)**
Oral y Poster Title: "Characterization of the new confocal micro X-ray fluorescence (CXRF) system for non-destructive cultural heritage analysis at the CNA: µXRF-CONCHA". Conference: 22th International Congress on X-ray Optics and Micro

Analysis. Authors: K. Laclavetine, F.J. Ager, J. Arquillo, T. Calligaro, M. Eveno, K. Müller, I. Reiche, M.A. Respaldiza and M. Menu.

22-26 April 2013 **Caen (France)**
Oral Title (in French): "Non-destructive characterization of experimental paint layers using the LOUX^{3D} and the µXRF-CONCHA confocal micro X-ray fluorescence (CXRF) systems". Conference: 19th Symposium of GMPCA "*Archéométrie2013"*. Authors: K. Laclavetine, F.J. Ager, J. Arquillo, T. Calligaro, M. Eveno, K. Müller, I. Reiche, M.A. Respaldiza and M. Menu.

Finally, the poster presented at the European Conference on X-ray Spectrometry, in Bologna, in 2014, received the Second Poster Price Award by the Organizing Committee.

BIBLIOGRAPHY

1. Janssens K., Dik J., *et al., Photon-Based Techniques for Nondestructive Subsurface Analysis of Painted Cultural Heritage Artifacts.* Accounts of Chemical Research, 2010. **43**(6): p. 814-825.

2. Longoni A., Fiorini C., *et al., A portable XRF spectrometer for non-destructive analyses in archaeometry.* Nuclear Instruments and Methods in Physics Research Section A: Accelerators, Spectrometers, Detectors and Associated Equipment, 1998. **409**(1–3): p. 407-409.

3. Kanngießer B., Malzer W., *et al., A deep view in cultural heritage—confocal micro X-ray spectroscopy for depth resolved elemental analysis.* Applied Physics A, 2012. **106**(2): p. 325-338.

4. Mairinger F., *UV-, IR- and X-ray imaging*. 2004: Comprehensive Analytical Chemistry XLII. p. 15-71.

5. van Asperen de Boer J.R.J., *Infrared Reflectography: a Method for the Examination of Paintings.* Applied Optics, 1968. **7**(9): p. 1711-1714.

6. Casini A., Lotti F., *et al., Image spectroscopy mapping technique for noninvasive analysis of paintings.* Studies in Conservation, 1999. **44**(1): p. 39-48.

7. Nakano K. and Tsuji K., *Nondestructive elemental depth profiling of Japanese lacquerware 'Tamamushi-nuri' by confocal 3D-XRF analysis in comparison with micro GE-XRF.* X-Ray Spectrometry, 2009. **38**(5): p. 446-450.

8. Ding X., Gao N., *et al., Monolithic polycapillary x-ray optics engineered to meet a wide range of applications*. 2000. p. 174-182.

9. Kanngießer B., Malzer W., *et al., A new 3D micro X-ray fluorescence analysis set-up – First archaeometric applications.* Nuclear Instruments and Methods in Physics Research Section B: Beam Interactions with Materials and Atoms, 2003. **211**(2): p. 259-264.

10. Eveno M., Ravaud E., *et al., The Louvre Crucifix by Giotto - Unveiling the original decoration by 2D-XRF, X-ray radiography, Emissiography and SEM-EDX analysis.* Heritage Science, 2014. **2**(1): p. 1-17.

11. Reiche I., Muller K., *et al., Depth profiling reveals multiple paint layers of Louvre Renaissance paintings using non-invasive compact confocal micro-X-ray fluorescence.* Journal of Analytical Atomic Spectrometry, 2012. **27**(10): p. 1715-1724.

12. Valdivieso Gonzalez E., *Historia de la pintura sevillana*. Guadalquivir ed. 2002. 525 p.

13. Wrobel P., *Development of Integrated Measurement Control/Data Processing Algorithms and Interfering Effects Reduction Methods for X-Ray Fluorescence Confocal Microscopy*. 2013, AGH University of Science and Technology: Cracow. p. 90.

14. Bertin E.P., *Principles and Practice of X-Ray Spectrometric Analysis*. Plenum Press ed. 1970. 679 p.

15. Broll N., *Quantitative x-ray fluorescence analysis. Theory and practice of the fundamental coefficient method.* X-Ray Spectrometry, 1986. **15**(4): p. 271-285.

16. Garrison E.G., *Technique in Archaeological Geology*. Springer ed. 2003. p. 215-230.

17. Moens L., Von Bohlen A., *et al.*, *X-Ray Fluorescence*, in *Modern Analytical Methods in Art and Archaeology*. 2000. p. 55-79.

18. Ruvalcaba Sil J.L. and Gonzalez Tirado C., *Análisis in situ de documentos históricos mediante un sistema portátil de FRX*, in *La Ciencia de Materíales y su Impacto en la Arqueología*. 2005. p. 55-77.

19. Milazzo M. and Cicardi C., *Simple Methods for Quantitative X-Ray Fluorescence Analysis of Ancient Metal Objects of Archaeological Interest.* X-Ray Spectrometry, 1997. **26**(4): p. 211-216.

20. Mantler M. and Schreiner M., *X-ray analysis of objects of art and archaeology.* Journal of Radioanalytical and Nuclear Chemistry, 2001. **247**(3): p. 635-644.

21. Mantler M. and Schreiner M., *X-ray fluorescence spectrometry in art and archaeology.* X-Ray Spectrometry, 2000. **29**(1): p. 3-17.

22. Roldán C. and Juanes D., *Fluorescencia de rayos-X mediante equipo portátil aplicada al estudio y conservación del patrimonio cultural*, in *La Ciencia y el Arte. Ciencias experimentales y conservación del Patrimonio Histórico*. 2008. p. 140-151.

23. Mathis F., *Croissance et propriétés des couches d'oxydation et des patines à la surface d'alliages cuivreux d'intérêt archéologique ou artistique.* 2005, Université de Paris-Sud U.F.R. Scientifique d'Orsay, France: Paris. p. 210.

24. Scrivano S., *Caracterizacion no-destructiva de joyas arqueologicas de oro mediante Micro Fluorescencia de Rayos X (Non-destructive characterization of archaeological gold jewels by Micro X-Ray Fluorescence)* 2015, Universidad de Sevilla: Sevilla. Under press.

25. Moseley H.G.J., *The High Frequency Spectra of the Elements.* Philosophical Magazine, 1913: p. 1024.

26. Markowicz A.A., *X-ray Physics*, in *Handbook of X-ray Spectrometry: Methods and Techniques.* 1993. p. 1-73.

27. Janssens K., *X-ray based methods of analysis chapter book*. 2004: Comprehensive Analytical Chemistry XLII. p. 129-226.

28. Verma H.R., *Atomic and nuclear analytical methods: XRF, Mossbauer, XPS, NAA and ion-beam spectroscopic techniques.* Springer ed. 2007. 376 p.

29. Gilardoni A., Orsini A.O., *et al.*, *X-Rays in Art*. Grafica & Arte Bergamo ed. 1994. 342 p.

30. Ferretti M., *X-ray Fluorescence applications for the Study and conservation of cultural heritage*, in *Radiation in Art and Archeometry*. 2000. p. 285-296.

31. Skoog D.A., Crouch S.R., *et al.*, *Principios de análisis instrumental.* Cengage Learning ed. 2008. 1038 p.

32. Jaklevic J.M. and Giauque R.D., *Energy-Dispersive X-ray Fluorescence Analysis Using X-ray Tube Excitation*, in *Handbook of X-ray Spectrometry: Methods and Techniques.* 1993. p. 151-180.

33. *Amptek.* 2014; Available from: www.amptek.com.

34. Gatti E. and Rehak P., *Semiconductor drift chamber — An application of a novel charge transport scheme.* Nuclear Instruments and Methods in Physics Research, 1984. **225**(3): p. 608-614.

35. Rehak P., Gatti E., *et al.*, *Semiconductor drift chambers for position and energy measurements.* Nuclear Instruments and Methods in Physics Research Section A: Accelerators, Spectrometers, Detectors and Associated Equipment, 1985. **235**(2): p. 224-234.

36. Kemmer J., Lutz G., *et al.*, *Low capacity drift diode.* Nuclear Instruments and Methods in Physics Research Section A: Accelerators, Spectrometers, Detectors and Associated Equipment, 1987. **253**(3): p. 378-381.

37. Carini G.A., Wei C., *et al.*, *Performance of a Thin-Window Silicon Drift Detector X-Ray Fluorescence Spectrometer.* Nuclear Science, IEEE Transactions on, 2009. **56**(5): p. 2843-2849.

38. Fiorini C., Gola A., *et al.*, *A CMOS pulsed-reset preamplifier for silicon drift detectors with on-chip JFET*, in *Nuclear Science Symposium Conference Record, 2007. NSS '07. IEEE*. 2007. p. 2519-2521.

39. Rehak P., Wei C., *et al.*, *Comparison of two different methods to produce thin-window silicon drift detectors*, in *Nuclear Science Symposium Conference Record (NSS/MIC), 2009 IEEE*. 2009. p. 1777-1782.

40. Zampa G., Rashevsky A., *et al.*, *The X-Ray Spectroscopic Performance of a Very Large Area Silicon Drift Detector.* Nuclear Science, IEEE Transactions on, 2009. **56**(3): p. 832-835.

41. Gibson W.M. and Kumakhov M.A., *Applications of X-ray and neutron capillary optics*, in *X-ray Detector Physics Applications*. 1993, Proceedings of SPIE. p. 172-189.

42. Bjeoumikhov A., Bjeoumikhova S., *et al.*, *A new method of depth sensitive micro-X-ray fluorescence analysis.* Nuclear Instruments and Methods in Physics Research Section B: Beam Interactions with Materials and Atoms, 2006. **248**(1): p. 142-149.

43. *Portable μ-XRF Spectrometer - ARTAX*. 2014; Available from: http://www.bruker.com/products/x-ray-diffraction-and-elemental-analysis/micro-xrf-and-txrf/artax/overview.html.

44. Dik J., van Leeuwenhook A., *et al. Non-destructive Analysis of Historical Paintings with Spatially Resolved XRF - M6 JETSTREAM*. 2014; Available from: http://www.bruker.com/fr/service/education-training/webinars/xrf/non-destructive-analysis-of-historical-paintings-with-spatially-resolved-xrf.html.

45. Mantouvalou I., Malzer W., *et al.*, *Reconstruction of Thickness and Composition of Stratified Materials by Means of 3D Micro X-ray Fluorescence Spectroscopy.* Analytical Chemistry, 2008. **80**(3): p. 819-826.

46. Vincze L., Vekemans B., *et al., Three-Dimensional Trace Element Analysis by Confocal X-ray Microfluorescence Imaging.* Analytical Chemistry, 2004. **76**(22): p. 6786-6791.

47. Woll A.R., Mass J., *et al., Development of confocal X-ray fluorescence (XRF) microscopy at the Cornell high energy synchrotron source.* Applied Physics A, 2006. **83**(2): p. 235-238.

48. Kanngießer B., Malzer W., *et al., Three-dimensional micro-XRF investigations of paint layers with a tabletop setup.* Spectrochimica Acta Part B: Atomic Spectroscopy, 2005. **60**(1): p. 41-47.

49. Mantouvalou I., Lange K., *et al., A compact 3D micro X-ray fluorescence spectrometer with X-ray tube excitation for archaeometric applications.* Journal of Analytical Atomic Spectrometry, 2010. **25**(4): p. 554-561.

50. Rindby A., *Applications of fiber technique in the X-ray region.* Nuclear Instruments and Methods in Physics Research Section A: Accelerators, Spectrometers, Detectors and Associated Equipment, 1986. **249**(2–3): p. 536-540.

51. Carpenter D.A., *Improved laboratory X-ray source for microfluorescence analysis.* X-Ray Spectrometry, 1989. **18**(6): p. 253-257.

52. Rindby A., Engström P., *et al., Microbeam technique for energy-dispersive x-ray fluorescence.* X-Ray Spectrometry, 1989. **18**(3): p. 109-112.

53. Kumakhov M.A., *Channeling of photons and new X-ray optics.* Nuclear Instruments and Methods in Physics Research Section B: Beam Interactions with Materials and Atoms, 1990. **48**(1–4): p. 283-286.

54. Kumakhov M.A. and Komarov F.F., *Multiple reflection from surface X-ray optics.* Physics Reports, 1990. **191**(5): p. 289-350.

55. Markowicz A., Wegrzynek D., *et al., Activities in the IAEA X-ray fluorescence laboratory at Seibersdorf.* X-Ray Spectrometry, 2006. **35**(4): p. 207-214.

56. Smolek S., Pemmer B., *et al., Confocal micro-x-ray fluorescence spectrometer for light element analysis.* Review of Scientific Instruments, 2012. **83**(8): p. 1-6.

57. Nakano K. and Tsuji K., *Development of laboratory confocal 3D-XRF spectrometer and nondestructive depth profiling.* Journal of Analytical Atomic Spectrometry, 2010. **25**(4): p. 562-569.

58. Tsuji K. and Nakano K., *Development of confocal 3D micro-XRF spectrometer with dual Cr-Mo excitation.* X-Ray Spectrometry, 2007. **36**(3): p. 145-149.

59. Wrobel P., Czyzycki M., *et al., LabVIEW control software for scanning micro-beam X-ray fluorescence spectrometer.* Talanta, 2012. **93**(0): p. 186-192.

60. Patterson B. and Havrilla G., *Confocal Micro X-ray Fluorescence A New Paradigm in 3D Elemental Imaging for Materials Characterization.* Microscopy and Microanalysis, 2008. **14**(SupplementS2): p. 1088-1089.

61. Patterson B.M. and Havrilla G.J., *Three-Dimensional Elemental Imaging Using a Confocal XRay Fluorescence Microscope.* American Laboratory, 2006. **38**(8): p. 15-22.

62. Camacho A.L. and Mederos F.J.J., *Alcances de la técnica de Fluorescencia de Rayos X (FRX) aplicada al estudio de la distribución estratigráfica de pigmentos en la*

pintura de caballete novohispana. Caso de estudio: la pintura "San Fernando y San Luis entre papas, obispos y doctores seráficos" del templo de San Fernando de la Ciudad de México. 2011, Escuela de Conservación y Restauración de Occidente, México.: Guadalajara. p. 197.

63. de Viguerie L., Sole V.A., *et al.*, *Multilayers quantitative X-ray fluorescence analysis applied to easel paintings.* Analytical and Bioanalytical Chemistry, 2009. **395**(7): p. 2015-2020.

64. Neelmeijer C., Brissaud I., *et al.*, *Paintings— a challenge for XRF and PIXE analysis.* X-Ray Spectrometry, 2000. **29**(1): p. 101-110.

65. Campanella L., Ferretti M., *et al.*, *Non-destructive Approach to Multilayer Objects: XRF Analysis of Gilt and Enamelled Metals of the Medieval Cross of Rosciolo.* Procedia Chemistry, 2013. **8**(0): p. 284-291.

66. Polese C., Dabagov S.B., *et al.*, *Experimental study for the feasibility of using hard x-rays for micro-XRF analysis of multilayered metals.* AIP Advances, 2014. **4**(7): p. 077128.

67. Karydas A.-G., Sokaras D., *et al.*, *3D Micro PIXE-a new technique for depth-resolved elemental analysis.* Journal of Analytical Atomic Spectrometry, 2007. **22**(10): p. 1260-1265.

68. Sokaras D. and Karydas A.-G., *Secondary Fluorescence Enhancement in Confocal X-ray Microscopy Analysis.* Analytical Chemistry, 2009. **81**(12): p. 4946-4954.

69. Nakano K., Nishi C., *et al.*, *Depth Elemental Imaging of Forensic Samples by Confocal micro-XRF Method.* Analytical Chemistry, 2011. **83**(9): p. 3477-3483.

70. Tsuji K. and Nakano K., *Development of a new confocal 3D-XRF instrument with an X-ray tube.* Journal of Analytical Atomic Spectrometry, 2011. **26**(2): p. 305-309.

71. Leroy S., Simon R., *et al.*, *First examination of slag inclusions in medieval armours by confocal SR-[small micro]-XRF and LA-ICP-MS.* Journal of Analytical Atomic Spectrometry, 2011. **26**(5): p. 1078-1087.

72. Sun T., Ding X., *et al.*, *Characterization of a confocal three-dimensional micro X-ray fluorescence facility based on polycapillary X-ray optics and Kirkpatrick–Baez mirrors.* Spectrochimica Acta Part B: Atomic Spectroscopy, 2008. **63**(1): p. 76-80.

73. Derrick M., Souza L., *et al.*, *Embedding paint cross-section samples in polyester resins: problems and solutions.* Journal of the American Institute for Conservation, 1994. **33**(3): p. 227 to 245.

74. Mantouvalou I., Wolff T., *et al.*, *3D Micro-XRF for Cultural Heritage Objects: New Analysis Strategies for the Investigation of the Dead Sea Scrolls.* Analytical Chemistry, 2011. **83**(16): p. 6308-6315.

75. Tsuji K., Nakano K., *et al.*, *Development of confocal micro X-ray fluorescence instrument using two X-ray beams.* Spectrochimica Acta Part B: Atomic Spectroscopy, 2007. **62**(6–7): p. 549-553.

76. Tsuji K., Yonehara T., *et al.*, *Application of Confocal 3D Micro-XRF for Solid/Liquid Interface Analysis.* Analytical Sciences, 2008. **24**(1): p. 99-103.

77. Mazel V., Busignies V., *et al.*, *The surface layer of pharmaceutical compacts: The role of the punch surface and its impact on the mechanical properties of the compacts.* International Journal of Pharmaceutics, 2013. **442**(1–2): p. 42-48.

78. Mazel V., Reiche I., *et al.*, *Confocal micro-X-ray fluorescence analysis as a new tool for the non-destructive study of the elemental distributions in pharmaceutical tablets.* Talanta, 2011. **85**(1): p. 556-561.

79. Patterson B.M., DeFriend Obrey K.A., *et al.*, *Three-dimensional density measurements of ultra low density materials by X-ray scatter using confocal micro X-ray fluorescence spectroscopy.* X-Ray Spectrometry, 2012. **41**(4): p. 253-258.

80. Nakazawa T. and Tsuji K., *Depth-selective elemental imaging of microSD card by confocal micro XRF analysis.* X-Ray Spectrometry, 2013. **42**(3): p. 123-127.

81. Cosslett V.E. and Nixon W.C., *The X-Ray Shadow Microscope.* Journal of Applied Physics, 1953. **24**(5): p. 616.

82. Arndt U., Long J., *et al.*, *X-ray generator*. 2001: USA.

83. Alfeld M., Pedroso J.V., *et al.*, *A mobile instrument for in situ scanning macro-XRF investigation of historical paintings.* Journal of Analytical Atomic Spectrometry, 2013. **28**(5): p. 760.

84. Nielsen J. and McMorrow D., *Elements of modern X-ray physics.* John Wiley ed. 2011. 434 p.

85. Jones K.W., *Synchrotron Radiation-Induced X-ray Emission*, in *Handbook of X-ray Spectrometry: Methods and Techniques.* 1993. p. 411-452.

86. Taylor M., Bytheway R., *et al.*, *Micro X-ray Sources*, in *X-ray spectrometry: recent technological advances*. 2004. p. 13-27.

87. Gibson D. and Gibson W., *Polycapillary optics: an enabling technology for new applications.* Advances in X-ray Analysis, 2002. **45**: p. 286-297.

88. Gao N. and Ponomarev I.Y., *Polycapillary x-ray optics: manufacturing status, characterization and the future of the technology.* X-Ray Spectrometry, 2003. **32**(3): p. 186-194.

89. Macdonald C.A., *Focusing Polycapillary Optics and Their Applications.* X-Ray Optics and Instrumentation, 2010: p. 1-17.

90. Lin X., Wang Z., *et al.*, *Characterization and applications of a new tabletop confocal micro X-ray fluorescence setup.* Nuclear Instruments and Methods in Physics Research Section B: Beam Interactions with Materials and Atoms, 2008. **266**(11): p. 2638-2642.

91. Mantouvalou I., Malzer W., *et al.*, *Quantification for 3D micro X-ray fluorescence.* Spectrochimica Acta Part B: Atomic Spectroscopy, 2012. **77**(0): p. 9-18.

92. Czyzycki M., Bielewski M., *et al.*, *Quantitative elemental analysis of individual particles with the use of micro-beam X-ray fluorescence method and Monte Carlo simulation.* X-Ray Spectrometry, 2009. **38**(6): p. 487-491.

93. Czyzycki M., Wrobel P., *et al.*, *The perspective of new multi-layer reference materials for confocal 3D micro X-ray fluorescence spectroscopy.* X-Ray Spectrometry, 2012. **41**(4): p. 273-278.

94. Pérez R.D., Sánchez H.J., *et al., Quantification of Multilayer Samples by Confocal μXRF.* AIP Conference Proceedings, 2009. **1092**(1): p. 107-111.

95. Pérez R.D., Sánchez H.J., *et al., Analysis of thin intermediate layers by confocal μ-XRF*. X-Ray Spectrometry, 2011. **40**(1): p. 19-23.

96. Wegrzynek D., Mroczka R., *et al., Experimental evaluation of X-ray optics applied for microanalysis.* X-Ray Spectrometry, 2008. **37**(6): p. 635-641.

97. Wolff T., Malzer W., *et al., A new fundamental parameter based calibration procedure for micro X-ray fluorescence spectrometers.* Spectrochimica Acta Part B: Atomic Spectroscopy, 2011. **66**(2): p. 170-178.

98. Carney C.B. *Be Smart When Dealing With Art: Ultraviolet Light Inspection*. 2014; Available from: http://www.gainsboroughproducts.com/uvl_inspection.html.

99. *UVP*. 2014; Available from: http://www.uvp.com/.

100. Webber S.L. *Technical Bulletin - Williamstown Art Conservation Center*. 2014; Available from: http://www.williamstownart.org/techbulletins/images/WACC%20Imaging%20of%20Paintings.pdf.

101. Laclavetine K., Hernández E., *et al., Análisis de estándares de pintura según recetas del siglo XVI mediante reflectografía infrarroja (IRR)*, in *4th Latin-American Symposium on Physical and Chemical Methods in Archaeology, Art and Cultural Heritage Conservation (LASMAC2013)*. 2013: Bogota, Colombia. p. 1-6.

102. Miller J.L., *Principles of Infrared Technology: A Practical Guide to the State of the Art*. Van Nostrand Reinhold ed. 1994, New york. 596 p.

103. Boyle W. and Smith G., *Buried channel charge coupled devices*. 1974.

104. *Nobelprize.org*. 2014; Available from: http://www.nobelprize.org/nobel_prizes/physics/laureates/2009/.

105. *Nikon Microscopy U*. 2014; Available from: http://www.microscopyu.com/.

106. *Nikon Microscopy U-2*. 2014; Available from: http://www.microscopyu.com/articles/digitalimaging/ccdintro.html.

107. Pearsall T.P. and Hopson R.W., *Growth and characterization of lattice-matched epitaxial films of GaxIn1−xAs/InP by liquid-phase epitaxy*. Journal of Electronic Materials, 1978. **7**(1): p. 133-146.

108. *What are ingaas detectors*. 2013; Xenics:[Available from: http://www.xenics.com/en/infrared_technology/what_are_ingaas_detectors.asp.

109. *Technical Note - Introduction to scientific InGaAs FPA cameras - Princeton Instruments* 2014; Available from: http://www.princetoninstruments.com/Uploads/Princeton/Documents/TechNotes/PI_InGaAs_Tech_Note_revA0.pdf.

110. Consolandi L. and Bertani D., *A prototype for high resolution infrared reflectography of paintings.* Infrared Physics & Technology, 2007. **49**(3): p. 239-242.

111. *Technical Data Sheet - Super Infrared Vidicons N2606 Series*. 1994, Hamamatsu Photonics K.K. p. 1-4.

112. *Institute for Scientific Instruments GmbH (IfG) (Berlin, Germany).* 2014; Available from: www.ifg-adlershof.de.

113. Bjeoumikhov A., Langhoff N., *et al., A modular system for XRF and XRD applications consisting of a microfocus X-ray source and different capillary optics.* X-Ray Spectrometry, 2004. **33**(4): p. 312-316.

114. Chan G.C.Y. and Hieftje G.M., *A LabVIEW program for determining confidence intervals of Abel-inverted radial emission profiles.* Spectrochimica Acta Part B: Atomic Spectroscopy, 2005. **60**(11): p. 1486-1501.

115. Hosek P., Prykäri T., *et al., Application of LabVIEW: Complex Software Controlling of System for Optical Coherence Tomography.* Journal of the Association for Laboratory Automation, 2009. **14**(2): p. 59-68.

116. Wagner C., Armenta S., *et al., Developing automated analytical methods for scientific environments using LabVIEW.* Talanta, 2010. **80**(3): p. 1081-1087.

117. Wrobel P., Laclavetine K., *et al. Reconstruction of paint layers thickness and composition by confocal micro X-ray fluorescence*. in *European Conference on X-Ray Spectrometry*. 2014. Bologna, Italy.

118. Flannery B.P., Deckman H.W., *et al., Three-Dimensional X-ray Microtomography.* Science, 1987. **237**(4821): p. 1439-1444.

119. Wegrzynek D., *Computer microtomography using a laboratory x-ray fluorescence microbeam spectrometer—A feasibility study.* X-Ray Spectrometry, 2001. **30**(6): p. 413-418.

120. Del Federico E., Centeno S., *et al., In Situ Unilateral 1H-NMR Studies of the Interaction Between Lead White Pigments and Collagen-Based Binders.* Applied Magnetic Resonance, 2012. **42**(3): p. 363-376.

121. Di Tullio V., Capitani D., *et al., Non-invasive NMR stratigraphy of a multi-layered artefact: an ancient detached mural painting.* Analytical and Bioanalytical Chemistry, 2013. **405**(26): p. 8669-8675.

122. Oligschläger D., Waldow S., *et al., Moisture dynamics in wall paintings monitored by single-sided NMR.* Magnetic Resonance in Chemistry, 2015. **53**(1): p. 48-57.

123. Solé V.A., Papillon E., *et al., A multiplatform code for the analysis of energy-dispersive X-ray fluorescence spectra.* Spectrochimica Acta Part B: Atomic Spectroscopy, 2007. **62**(1): p. 63-68.

124. Cosentino A., *Panoramic Infrared Reflectography. Technical Recommendations.* International Journal of Conservation Science, 2014. **5**(1): p. 51-60.

125. Torres J., Posse A., *et al., VARIM, A Useful System for Acquiring and Composing Images in Painting Analysis Techniques.* E_conservation, 2008(4): p. 27-42.

126. Kriznar A., Muñoz M.V., *et al., Pigment identification using x-ray fluorescence in a polychromated sculpture by Pedro Millán.* X-Ray Spectrometry, 2008. **37**(4): p. 355-359.

127. Križnar A., Muñoz M.V., *et al., XRF analysis of two terracotta polychrome sculptures by Pietro Torrigiano.* X-Ray Spectrometry, 2009. **38**(3): p. 169-174.

128. Kriznar A., Muñoz M.V., *et al., Portable XRF study of pigments applied in Juan Hispalense's 15th century panel painting.* X-Ray Spectrometry, 2011. **40**(2): p. 96-100.

129. Kriznar A., Muñoz M.V., *et al., A Comparison of Pigments Applied in an Original Painting by El Greco and in a Copy by an Anonymous Follower.* E-Preservation Science, 2011. **8**: p. 49-54.

130. Ager F.J., Moreno-Suárez A.I., *et al., Silver surface enrichment in ancient coins studied by micro-PIXE.* Nuclear Instruments and Methods in Physics Research Section B: Beam Interactions with Materials and Atoms, 2013. **306**(0): p. 241-244.

131. Respaldiza M.A., Barranco F., *et al., Combining PIXE and XRF with gamma-ray transmission to get accurate analysis of archaeological bronzes.* Nuclear Instruments and Methods in Physics Research Section B: Beam Interactions with Materials and Atoms, 1990. **50**(1–4): p. 226-230.

132. Scrivano S., Gómez-Tubío B., *et al., Identification of soldering and welding processes in ancient gold jewelry by micro-XRF spectroscopy.* X-Ray Spectrometry, 2013. **42**(4): p. 251-255.

133. Alonso M.P., Capel F., *et al., Stained-glass windows of the Huelgas Monastery. Process of conservation-restoration. Characterization of the medieval red glass.* Boletín de la Sociedad Española de Cerámica y Vidrio, 2009. **48**(4): p. 179-186.

134. *MP Mecánica de Precisión*. 2014; Available from: www.mecapres.com.

135. Laclavetine K., *Caracterizacion de pigmentos en obras de arte mediante analisis por fluorescencia de rayos X*. 2011, Universidad de Sevilla: Sevilla. p. 79 p.

136. Ruvalcaba Sil J.L., Ramírez Miranda D., *et al., SANDRA: a portable XRF system for the study of Mexican cultural heritage.* X-Ray Spectrometry, 2010. **39**(5): p. 338-345.

137. Arroyo E., Zetina S., *et al., XVI Century Colonial Panel Paintings from New Spain: Material Reference Standards and Non-Destructive Analysis for Mexican Retablos*, in *Art 2008, 9th International Conference on Nondestructive Testing of Art*. 2008: Jerusalem, Israel. p. 1-10.

138. Buti D., Rosi F., *et al., In-situ identification of copper-based green pigments on paintings and manuscripts by reflection FTIR.* Analytical and Bioanalytical Chemistry, 2013. **405**(8): p. 2699-711.

139. García Bucio M.A., *Desarrollo y aplicación de la espectroscopia Raman aplicada en superficie (SERS) para estudio no destructivo de pintura novohispana.* 2013, UNAM: México. p. 133.

140. Ricci C., Miliani C., *et al., Non-invasive identification of surface materials on marble artifacts with fiber optic mid-FTIR reflectance spectroscopy.* Talanta, 2006. **69**(5): p. 1221-1226.

141. Serrera J.M., *Velázquez y la pintura Sevillana de su tiempo*, in *Velázquez y Sevilla*, Luis Méndez Rodríguez, J.L.R.T., Editor. 1999, Junta de Andalucía, Consejería de Cultura. p. 51-59.

142. Valdivieso González E., *La pintura en el Museo de Bellas Artes de Sevilla*. 1993. 448 p.

143. Pérez Escolano V., *Los túmulos de Felipe II y de Margarita de Austria en la Catedral de Sevilla.* Archivo Hispalense: revista histórica, literaria y artística, 1977(185): p. 149-176

144. Valdivieso E., *Historia de la pintura sevillana*. Guadalquivir ed. 1986, Sevilla.

145. Palomero Páramo J.M., *Las últimas voluntades y el inventario de bienes del pintor Alonso Vázquez.* Anales del Instituto de Investigaciones Estéticas, 2005. **27**(86): p. 169-202.

146. Serrera J.M., *La catedral de Sevilla. Pinturas y pintores del siglo XVI en la catedral de Sevilla*. 1984. p. 353-404.

147. Serrera J.M., *Alonso Vásquez en México*. Espejo de Obsidiana ed. 1991, México. 64 p.

148. Rogelio Ruiz Gomar Campos J., *Las pinturas atribuidas a Alonso Vazquez en Mexico.* Anuario de Estudios Americanos, Publicaciones de la Escuela de Estudios Hispano-Americanos de Sevilla, 1981. **38**: p. 659-671.

149. Serrera Contreras J.M., *Alonso Vázquez: el Retablo Mayor del Hospital de las Cinco Llagas.* Archivo Hispalense: revista histórica, literaria y artística, 1991(227): p. 139-183.

150. Rogelio Ruiz Gomar J., *Noticias referentes al paso de algunos pintores a la Nueva España.* Anales del Instituto de Investigaciones Estéticas, 1983 **14**(53): p. 65-73.

151. Ángeles Jiménez P. *Rodrigo de Cifuentes y el conde de la Cortina: un invento de la historiografía de la pintura novohispana*. 2008; Available from: http://pedroangeles.wordpress.com/2008/04/30/cifuentes/.

152. Navarrete Prieto B., *Precisiones y adiciones al catálogo de Alonso Vázquez y Francisco Pacheco.* Archivo Hispalense: revista histórica, literaria y artística, 1995(78): p. 149-159.

153. Serrera J.M., *Dos nuevos cuadros del pintor Alonso Vázquez.* Archivo Hispalense: revista histórica, literaria y artística, 1977(184).

154. *IAPH - Consejería de Cultura - Virgen del Valle o del Pozo Santo* 2014; Available from: http://www.iaph.es/sys/productos/Velazquez/velazquezSevilla/exposicion/lienzoVirgenDelValle.html.

155. *IAPH - Consejería de Cultura - Virgen del Valle o del Pozo Santo - Catedral de Sevilla*. 2014; Available from: http://www.iaph.es/web/canales/conservacion-y-restauracion/catalogo-de-obras-restauradas/contenido/Virgen_del_Valle_o_del_pozo_santo_Catedral_de_Sevilla.

156. *Colecciones en Red - Ministerio de Educación, Cultura y Deporte* 2014; Available from: http://ceres.mcu.es/pages/ResultSearch?txtSimpleSearch=Convento%20de%20la%20Merced%20Calzada&simpleSearch=0&hipertextSearch=1&search=simpleSelection&MuseumsSearch=MBASE%7C&MuseumsRolSearch=2&listaMuseos=%5BMuseo%20de%20Bellas%20Artes%20de%20Sevilla%5D.

157. Arroyo E., Hernández E., *et al.*, *El Martirio de San Hipólito. Informe de técnica y análisis material*. 2012, Laboratorio de Diagnóstico de Obras de Arte, Instituto de Investigaciones Estéticas, UNAM. p. 1-43.

158. Alamán L., Andrade J.M., *et al.*, in *Diccionario universal de historia y geografía*. 1853-1856, Tipografía de Rafael, Librería de Andrade: México.

159. Sigaut N., *José Juárez. Recursos y discursos del arte de pintar*. 2002. 82 p.

160. Feller R.L. and Roy A., *Artist's pigments - A handbook of their history and characteristics*. National Gallery of Art Washington, Cambridge University Press ed. Vol. 1. 1986, Cambridge. 300 p.

161. Roy A., *Artists' pigments: a handbook of their history and characteristics*

1993. **2**: p. 234p.

162. Martín García L., *Virgen del Valle - Análisis químico - Julio 1999*. 1999, IAPH, Junta de Andalucía, Consejería de Cultura. p. 1-27.

163. Arroyo E., Espinosa M., *et al.*, *Variaciones celestes para pintar el manto de la Virgen.* Anales del Instituto de Investigaciones Estéticas, 2012(100): p. 85-117.

164. Duval A.R., *Les préparations colorées de tableaux de l'Ecole Française des dix-septième et dix-huitième siècles.* Studies in Conservation, 1992. **37**(4): p. 239-258.

165. van Espen P.J.M. and Janssens K.H.A., *Spectrum Evaluation*, in *Handbook of X-ray Spectrometry: Methods and Techniques.* 1993. p. 181-293.